

University of Nevada, Reno

**Patterns of Lithology, Structure, Alteration, Trace Elements, Carbonate Mineralogy, and
Stable Isotopes around High-Grade Carlin-type Gold Deposits: Turquoise Ridge
Deposit, Getchell District, Nevada**

A thesis submitted in partial fulfillment of the
requirements for the degree of Master of Science in
Geology

by

Michael D. Cassinerio

Dr. John Muntean/Thesis Advisor

May, 2010

© by Michael Cassinerio

All Rights Reserved



University of Nevada, Reno
Statewide • Worldwide

THE GRADUATE SCHOOL

We recommend that the thesis
prepared under our supervision by

MICHAEL DOMINIC CASSINERIO

entitled

**Patterns Of Lithology, Structure, Alteration, Trace Elements, Carbonate Mineralogy,
And Stable Isotopes Around High-Grade Carlin-Type Gold Deposits: Turquoise Ridge
Deposit, Getchell District, Nevada**

be accepted in partial fulfillment of the
requirements for the degree of

MASTER OF SCIENCE

John Muntean, Advisor

Greg Arehart, Committee Member

John Bell, Graduate School Representative

Marsha H. Read, Ph. D., Associate Dean, Graduate School

May, 2010

Abstract

Few data sets have been published that depict the extent of hydrothermal features surrounding high-grade ore bodies in Carlin-type gold deposits (CTGDs) in Nevada, making exploration, development, and production difficult, especially where visually unaltered, unmineralized rocks occur in close proximity to ore. This thesis, which is divided into 3 standalone chapters, investigates several hydrothermal features associated with the high-grade Turquoise Ridge CTGD in the Getchell District. Traditional exploration tools such as patterns of lithology, structure, visible hydrothermal alteration, trace elements, and clay mineralogy are presented in Chapter 1 to test for the presence of haloes that can potentially be used as vectoring tools in honing in on high-grade ore zones at the Turquoise Ridge CTGD. Carbonate staining was utilized to determine differences in carbonate mineralogy associated with more reactive and non-reactive carbonate host-rocks (Chapter 2). Stable isotopes ($\delta^{18}\text{O}$ and $\delta^{13}\text{C}$) are presented in Chapter 3 to test for the presence of potentially more pervasive cryptic alteration haloes relative to visible hydrothermal alteration and trace element anomalies. Closely-spaced diamond drill holes along two cross-sections across the High Grade Bullion (HGB) ore zone at the north end of Turquoise Ridge were logged in detail. The logging information, gold assays, multi-element analyses, and spectral reflectance analyses were plotted on a 1:600 scale cross-section, from which controls on gold (Au) grade and haloes to ore zones were interpreted.

The Eocene-age Turquoise Ridge CTGD is hosted within a complexly deformed package of Cambrian-Ordovician sedimentary and volcanic rocks that is characterized by

rapid facies changes and soft-sediment deformation. The lowermost unit comprises variably calcareous, carbonaceous mudstones and limestones that are overlain by a series of sedimentary debris flow breccias. Above the breccias are deformed tuffaceous mudstones and limestones, which inter-finger to the northeast with a thick sequence of pillow basalt. Both the sedimentary debris flow breccias and the basalt pinch out to the south, and are interpreted to be controlled by a Cambrian-Ordovician, west-northwest trending, northeast-facing, basin margin. Further up section the rocks are mainly mudstone, basalt, and chert. The rocks are intruded by Cretaceous dacite porphyry dikes. The Turquoise Ridge deposit occurs in the hanging wall of the east-dipping, north-northwest-striking Getchell fault zone, which is the main fault in the district.

Much of the HGB ore zone occurs along complex intersections between steep, small-displacement faults, folds, and fractured calcareous lithologies, especially within the series of sedimentary breccias. The Au grades commonly show abrupt variations, locally changing from ≥ 17 ppm to < 0.34 ppm within a few meters. Zones of ≥ 0.34 ppm Au extend up to 120 meters above and up to 150 meters below the HGB; occur within the Getchell fault; and occur along several steep, small-displacement, antithetic faults in the hanging wall of the Getchell fault. Visible alteration, consisting of decalcification, argillization, and silicification, strongly correlates with Au grades of > 0.34 ppm.

Correlation matrices and factor analysis of downhole multi-element data show Au is strongly associated with Hg, As, W, S, Tl, Sb, and Te, but has a strong negative correlation with Ca, Mg, and Sr that is consistent with decalcification being the main alteration type. Values of ≥ 100 ppm As form a halo up to 30 m beyond the 0.34 ppm Au

contour and visible alteration, whereas the 5 ppm Sb contour forms a halo up to 12 m wide. With the possible exception of Hg, other features derived from the multi-element data, including Tl, Te, degree of sulfidation (DOS), Au factor scores (derived from factor analysis), and Ca (to monitor decalcification) do not form significant, coherent haloes to the 0.34 ppm Au contour or visible alteration.

Kaolinite and illite commonly occur in zones of ≥ 0.34 ppm Au. Inspection of samples from ore zones using an SEM show they are intimately intergrown with arsenian pyrite. Kaolinite- and illite-bearing fractures surfaces form incoherent haloes extending up to 20 m beyond visible alteration in otherwise unaltered rocks. Limited analyses of these fractures using a Niton handheld XRF show the fractures can contain significantly higher As than the adjacent wall rock.

Carbonate staining was utilized to determine the spatial distribution of carbonate mineralogy relative to high-grade gold ore at the Turquoise Ridge Carlin-type gold deposit. Specifically, dilute hydrochloric acid containing both alizarin red S and potassium ferricyanide was utilized to differentiate between calcite, ferroan calcite, ferroan dolomite and dolomite in the Cambrian-Ordovician carbonate host rocks at Turquoise Ridge. Detailed carbonate staining was conducted on 31 drill holes throughout the north end of Turquoise Ridge. Results reveal a distinct spatial relationship between gold mineralization, ferroan calcite, and the southern margin of a thick basalt within the Cambrian-Ordovician stratigraphic package that is referred to as the northern pillow basalt (NPB). High-grade gold ore (≥ 17 ppm Au) within the HGB ore zone occurs exclusively within ferroan calcite-bearing host rocks. The transition from

ferroan calcite to calcite with depth occurs at the base of the HGB ore zone. Non-ferroan calcite is distal to the NPB, both laterally and with depth.

A close spatial association between the distribution of ferroan calcite and the NPB suggests iron was likely liberated from the basalt during seawater alteration of the basalts, and/or the emplacement of the Cretaceous intrusions and was mobilized into adjacent limestones, forming ideal host rocks for subsequent gold mineralization. Acidic, sulfur-rich, auriferous hydrothermal fluids dissolved ferroan carbonates, which liberated iron. Aqueous sulfide in the fluid reacted with the iron, which destabilized aqueous gold-sulfide complexes, resulting in the formation of auriferous pyrite and marcasite. The presence of interlayered basalts and ferroan carbonates could be important exploration criteria in the identification of future target areas in the Getchell District and throughout Nevada. Furthermore and most importantly, careful carbonate staining should be routinely employed, given that it provides inexpensive, real-time data.

Analyses of carbonates from both visibly altered and unaltered rocks at Turquoise Ridge yielded $\delta^{18}\text{O}$ values from 13.5‰ to 21.6‰ and $\delta^{13}\text{C}$ values from -8.2‰ to 1.2‰. Most of the $\delta^{18}\text{O}$ values associated with visibly unaltered recrystallized micrite are between 17.6‰ and 19.0‰, well below typical $\delta^{18}\text{O}$ values associated with unaltered Paleozoic carbonates (22‰ to 28‰). The spatial distribution of $\delta^{18}\text{O}$ values along an east-west cross-section through the northern portion of the Turquoise Ridge deposit reveal the lowest $\delta^{18}\text{O}$ and $\delta^{13}\text{C}$ values occur within visibly altered wall rocks associated with ore zones and defined fluid pathways. Stable isotopic alteration haloes

are limited to visible alteration and do not extend beyond hydrothermal alteration into adjacent unaltered wallrocks. Similarly, elevated trace element concentrations (e.g., Au, As, Hg, Te, Sb, and Tl) are largely limited to visibly altered wall rocks, with elevated concentrations associated with bleached clay/calcite-lined fractures extending beyond continuous hydrothermal alteration in otherwise visibly unaltered wall rocks.

The lack of wide, coherent haloes of various hydrothermal features surrounding ore at Turquoise Ridge is suggestive of a restrictive, fracture-controlled fluid flow network, rather than large-scale, pervasive, lithologically-controlled fluid flow. Ore fluids likely ascended along the pre-existing Getchell fault zone and into the steep, small-displacement, antithetic faults in the hanging wall and the main dacite porphyry dike before encountering highly fractured, reactive carbonate-bearing lithologies, especially the sedimentary breccias and deformed mudstones and limestones adjacent to the basalt. Increased surface area in these zones allowed more fluid:rock interaction, which resulted in more pervasive carbonate dissolution, sulfidation, and Au deposition in the HGB. A large zone <25% RQD values that surrounds ore supports exploitation of these pre-existing fracture networks and as well as fracturing caused by collapse during carbonate dissolution associated with ore formation.

The results of this study show that few hydrothermal features extend beyond visible alteration (decalcification, argillization, and/or silicification) or low-grade gold assays. The features that do only form narrow, discontinuous haloes that are mostly restricted to fractures. None of the features investigated in this study, including visible alteration and low-grade gold assays, form pervasive haloes to ore on the scale of tens

to hundreds of meters, suggesting widespread alteration haloes associated with CTGDs is a common misperception, especially high-grade CTGDs.

Acknowledgements

There are a large number of individuals to whom I owe a great deal of appreciation. First and foremost being my project advisor, John Muntean for providing me the opportunity to work on such a challenging project. Your guidance, motivation, and enthusiasm throughout the duration of this project have been greatly appreciated. I would also like to express my appreciation to Barrick Gold for funding of my trace element geochemical data, two summer internships, database access, drill core, core shed space, and unlimited access to the Getchell property. Special thanks goes to Karl Marlowe, Keith Wood, Rich Histed, Don MacKerrow, Dawn Martin, Kevin Wilson, Crystal Jordan, and Nick Orlando for their valuable input, ideas, and assistance provided during the duration of the field season and subsequent visits to the mine property.

Several individuals deserve recognition for their knowledge and assistance provided during this project. Special thanks goes to Greg Arehart, John Bell, Tommy Thompson, John McCormack, Gina Temple, and Paula Noble who provided support in both my academic and thesis endeavors. I also want to express my appreciation to Simon Poulson and Chris Sladek, from the Nevada Stable Isotope Laboratory for their assistance collecting the carbon and oxygen isotope data. Special thanks to the Gary Johnson, Jennifer Mauldin, Heather Armeno, and Mario Desilets of the Nevada Bureau of Mines and Geology for cartography and XRD assistance. Thanks to Sean Mulcahy and Aaron Bell from the University of Nevada, Las Vegas Electron Microanalysis and Imaging Laboratory for their assistance with the SEM and microprobe.

In closing I would like to thank my family, friends, and colleagues that have provided great support during the length of this project.

Table of Contents

Page

i **Abstract**

vii **Acknowledgements**

viii **Table of Contents**

x **List of Tables**

xi **List of Figures**

Chapter 1

Patterns of Lithology, Structure, Alteration, and Trace Elements around High-grade Ore Zones at the Turquoise Ridge Gold Deposit, Getchell District, Nevada

1	Abstract
4	Introduction
5	District History
9	District Geology
13	Geology of the North End of Turquoise Ridge
26	Alteration and Gold Mineralization
38	Multi-Element Data
39	Statistics
43	Distribution of Ore-Related Trace Elements
56	Sulfidation
60	Decalcification
65	Spectral Reflectance Data
76	Discussion
82	Recommendations

Chapter 2

Spatial Distribution of Ferroan Carbonates around a High-Grade Carlin-type deposit: Getchell District, Nevada

85	Abstract
87	Introduction
89	District Geology
92	Geology of the Turquoise Ridge Deposit
101	Carbonate Staining Techniques
101	Stock Solutions
102	Application of Stains

103	Stain Interpretation
104	Precautions
108	Results of Carbonate staining at Turquoise Ridge
115	Potential Causes for Ferroan Calcite Distribution
120	Comparison to other CTGDs
123	Conclusions

Chapter 3

Oxygen and Carbonate Isotope Characteristics associated with Carlin-type gold Deposits at the Turquoise Ridge Gold Deposit, Getchell District Nevada

127	Abstract
129	Introduction
131	District Geology
133	Geology, Mineralization, and Alteration of the Turquoise Ridge Deposit
141	Oxygen and Carbon Isotope Whole-rock Data
141	Sampling and analytical methods
143	Isotopic compositions of Cambrian-Ordovician carbonates
159	Fluid flow dynamics relative to whole-rock composition of carbonate rocks
168	Cathodoluminescence
170	Trace Element Distribution
173	Spatial distribution of Trace Elements relative to $\delta^{18}\text{O}$
176	Niton Results
191	Discussion
197	Conclusions
199	References
210	Appendix

List of Tables

42	Table 1.1	Results of Factor Analysis showing Loadings for 6 Factors.
45	Table 1.2	Background Multi-Element Geochemistry.
75	Table 1.3	ASD and Niton XRF Results on Rock and Fracture Surfaces.
77	Table 1.4	Summary of the Extent of Haloes of Features at Turquoise Ridge.
80	Table 1.5	Characteristics of hydrothermal haloes surrounding ore in other CTGDs.
102	Table 2.1	Colors of common carbonate minerals after staining.
107	Table 2.2	Carbonate Staining Recommendations.
124	Table 2.3	Characteristics of ferroan carbonates surrounding ore in other CTGDs.
145-151	Table 3.1	Oxygen and Carbon isotope and trace element compositions of carbonate-bearing Cambrian-Ordovician samples.
167	Table 3.2	Fracture Transects.
178	Table 3.3	Results of Factor Analysis showing Loadings for 7 Factors.
179-182	Table 3.4	Niton Portable XRF analyses.
195-197	Table 3.5	Characteristics of isotopic haloes in carbonates surrounding ore in CTGDs.

List of Figures

5	Figure 1.1	Location map of the Getchell District.
8	Figure 1.2	Geologic map of the Getchell District.
15-16	Figure 1.3	3370 N55°E geologic cross-section.
20	Figure 1.4	Lithologies of the north end of the Turquoise Ridge deposit.
23	Figure 1.5	Examples of crenulation cleavage.
24	Figure 1.6	Schematic Interpretation of Cambrian-Ordovician basin margin development.
28	Figure 1.7	Comparison of unaltered vs. decalcified carbonate rocks.
33-37	Figure 1.8	Distribution of hydrothermal alteration, late-stage realgar mineralization, Au-grade, and RQD along the 3370 N55°E cross-section.
40	Figure 1.9	Correlation matrix and scatter plots.
47-50	Figure 1.10	Distribution of Hg, Sb, and As relative to Au-grade.
51-55	Figure 1.11	Distribution of Tl, Te, Au-factor scores, and DOS relative to Au-grade.
58	Figure 1.12	Weight percent S Leco vs. weight percent S ICP-MS-AES.
59	Figure 1.13	Total weight % S vs. total weight % Fe.
61-64	Figure 1.14	Distribution of Ca, Ca/Au, and Ca/Au-factor score relative to Au-grade.
67-71	Figure 1.15	Distribution of clay minerals within wall rock and fracture surfaces relative to Au-grade.
73	Figure 1.16	Clay coated fracture surface.
74	Figure 1.17	BSE image of kaolinite and illite intergrown with auriferous pyrite.
91	Figure 2.1	Location map of Getchell District.
93	Figure 2.2	Simplified geologic map of the Getchell District.
96-97	Figure 2.3	East-west geologic cross-section.
98-99	Figure 2.4	3370 N55°E geologic cross-section.
100	Figure 2.5	Interpreted fluid pathways along east-west geologic cross-section.
105	Figure 2.6	Photo of non-ferroan calcite.
105	Figure 2.7	Photo of ferroan calcite.
106	Figure 2.8	Photo of ferroan dolomite replacing non-ferroan calcite.
110	Figure 2.9	District carbonate staining map.
111	Figure 2.10	Carbonate rock matrix staining along east-west cross-section.
112	Figure 2.11	Carbonate vein staining along east-west cross-section.
113	Figure 2.12	Carbonate rock matrix and vein staining along N55°E cross-section.

116	Figure 2.13	Spatial distribution of calcite vs ferroan calcite within Turquoise Ridge corridor.
134	Figure 3.1	Location map of Getchell District.
135	Figure 3.2	Simplified geologic map of the Getchell District.
137-138	Figure 3.3	East-west geologic cross-section.
140	Figure 3.4	Interpreted fluid pathways along east-west geologic cross-section.
152	Figure 3.5	$\delta^{18}\text{O}$ and $\delta^{13}\text{C}$ cumulative distribution curves.
152	Figure 3.6	Spatial distribution of background $\delta^{18}\text{O}$ values.
153	Figure 3.7	Spatial distribution of background $\delta^{13}\text{C}$ values.
154	Figure 3.8	$\delta^{18}\text{O}$ vs. $\delta^{13}\text{C}$ values from skarn, calc-silicate, and marble samples.
156	Figure 3.9	$\delta^{18}\text{O}$ vs. $\delta^{13}\text{C}$ from recrystallized unaltered and hydrothermally altered limestone samples.
157	Figure 3.10	Spatial distribution of $\delta^{13}\text{C}$ along the east-west cross-section.
158	Figure 3.11	Spatial distribution of $\delta^{18}\text{O}$ along the east-west cross-section.
164	Figure 3.12	Modeling of whole-rock isotope composition of carbonate rocks.
166	Figure 3.13	Photo of mini-isotope transect.
170	Figure 3.14	Photomicrograph of cathodoluminescence.
174	Figure 3.15	Correlation matrix and associated scatter plots.
175	Figure 3.16	Plots of trace elements (Au, As, Hg, Sb, Te, and Tl) versus $\delta^{18}\text{O}$.
183-189	Figure 3.17	Spatial distribution of trace elements (Au, As, Hg, Sb, Te, and Tl) along east-west cross-section.
190	Figure 3.18	Photo of typical paired fracture-rock samples that were analyzed with the Niton portable XRF.

Chapter 1

Patterns of Lithology, Structure, Alteration and Trace Elements around High-grade Ore Zones at the Turquoise Ridge Gold Deposit, Getchell District, Nevada

ABSTRACT

Few data sets have been published that depict the extent of hydrothermal features surrounding high-grade ore bodies in Carlin-type gold deposits (CTGDs), making exploration, development, and production difficult, especially where visually unaltered, unmineralized rocks occur in close proximity to ore. Patterns of lithology, structure, visible hydrothermal alteration, trace elements, and clay mineralogy are presented to test for the presence of haloes that can potentially be used as vectoring tools in honing in on high-grade ore zones at the Turquoise Ridge CTGD. Closely-spaced diamond drill holes along a cross-section across the High Grade Bullion (HGB) ore zone at the north end of Turquoise Ridge were logged in detail. The logging information, gold assays, multi-element analyses, and spectral reflectance analyses were plotted on a 1:600 scale cross-section, from which controls on gold (Au) grade and haloes to ore zones were interpreted.

The Eocene-age Turquoise Ridge CTGD is hosted within a complexly deformed package of Cambrian-Ordovician sedimentary and volcanic rocks that is characterized by rapid facies changes and soft-sediment deformation. The lowermost unit comprises variably calcareous, carbonaceous mudstones and limestones that are overlain by a series of sedimentary debris flow breccias.

Above the breccias are deformed tuffaceous mudstones and limestones, which inter-finger to the northeast with a thick sequence of pillow basalt. Both the sedimentary debris flow breccias and the basalt pinch out to the south, and are interpreted to be controlled by a Cambrian-Ordovician, west-northwest trending, northeast-facing, basin margin. Further upsection the rocks are mainly mudstone, basalt, and chert. The rocks are intruded by Cretaceous dacite porphyry dikes. The Turquoise Ridge deposit occurs in the hanging wall of the east-dipping, north-northwest-striking Getchell fault zone, which is the main fault in the district.

Much of the HGB ore zone occurs along complex intersections between steep, small-displacement faults, folds, and fractured calcareous lithologies, especially within the series of sedimentary breccias. The Au grades commonly show abrupt variations, locally changing from ≥ 17 ppm to < 0.34 ppm within a few meters. Narrow zones of ≥ 0.34 ppm Au extend up to 120 meters above and up to 150 meters below the HGB; occur within the Getchell fault; and occur along several steep, small-displacement, antithetic faults in the hanging wall of the Getchell fault. Visible alteration, consisting of decalcification, argillization, and silicification, strongly correlates with Au grades of > 0.34 ppm.

Correlation matrices and factor analysis of downhole multi-element data show Au is strongly associated with Hg, As, W, S, Tl, Sb, and Te, but has a strong negative correlation with Ca, Mg, and Sr that is consistent with decalcification being the main alteration type. Values of ≥ 100 ppm As form a halo up to 30 m beyond the 0.34 ppm Au contour and visible alteration, whereas the 5 ppm Sb contour forms a halo up to 12 m

wide. With the possible exception of Hg, other features derived from the multi-element data, including Tl, Te, degree of sulfidation (DOS), Au factor scores (derived from factor analysis), and Ca (to monitor decalcification) do not form significant, coherent haloes to the 0.34 ppm Au contour or visible alteration.

Kaolinite and illite commonly occur in zones of ≥ 0.34 ppm Au. Inspection of samples from ore zones using an SEM show they are intimately intergrown with arsenian pyrite. Kaolinite- and illite-bearing fractures surfaces form incoherent haloes extending up to 20 m beyond visible alteration in otherwise unaltered rocks. Limited analyses of these fractures using a Niton handheld XRF show the fractures can contain significantly higher As than the adjacent wall rock.

The lack of wide, coherent haloes of various hydrothermal features surrounding ore at Turquoise Ridge is suggestive of a restrictive, fracture-controlled fluid flow network, rather than large-scale, pervasive, lithologically-controlled fluid flow. Ore fluids likely ascended along the pre-existing Getchell Fault Zone and into the steep, small-displacement, antithetic faults in the hanging wall and the main dacite porphyry dike before encountering highly fractured, reactive carbonate-bearing lithologies, especially the sedimentary breccias and deformed mudstones and limestones adjacent to the basalt. Increased surface area in these zones allowed more fluid:rock interaction, which resulted in more pervasive carbonate dissolution, sulfidation, and Au deposition in the HGB. A large zone of <25% RQD values that surrounds the ore supports exploitation of these pre-existing fracture networks and as well as fracturing caused by collapse during carbonate dissolution associated with ore formation.

INTRODUCTION

Carlin-type gold deposits (CTGDs) in Nevada represent one of the largest concentrations of gold (Au) deposits in the world (Fig. 1.1). Nearly 200 Moz of Au in CTGDs have either been produced or occur as remaining reserves and resources. Current production accounts for 60% of annual U.S. Au production and 6.5% of annual global production, making the U.S. the 4th largest Au producing nation in the world (NBMG, 2009). CTGDs are epigenetic, disseminated auriferous pyrite deposits characterized by carbonate dissolution, argillic alteration, and silicification of typically Paleozoic calcareous sedimentary rocks (Hofstra and Cline, 2000; Cline et al., 2005). Au occurs as solid solution in pyrite and less commonly as submicron native Au particles in pyrite (Well and Mullens, 1973; Arehart et al., 1993a; Simon et al., 1999; Reich et al., 2005). Late ore-stage minerals commonly include orpiment, realgar, stibnite, and barite (Hofstra and Cline, 2000; Cline et al., 2005). CTGDs commonly occur in clusters along linear “trends” and formed mainly during the late Eocene (Hofstra et al., 1999; Arehart et al., 2003; Cline et al., 2005).

District-scale exploration for CTGDs has traditionally targeted zones of anomalous gold assays and elevated associated trace elements, namely arsenic, mercury, antimony and thallium, as well as favorable alteration, especially jasperoids because of their resistant nature. In addition, exploration has targeted structural culminations and intersections between calcareous stratigraphic horizons and high-angle structures. Future discoveries will undoubtedly focus on covered, deep ore bodies, requiring costly drilling. Continued research documenting not only mappable

macroscopic features, but also cryptic features, proximal and distal to known ore bodies could very well provide tools to assist in zeroing in on an unexposed ore body and mitigate exploration costs by gaining more vectoring information from each drill hole.

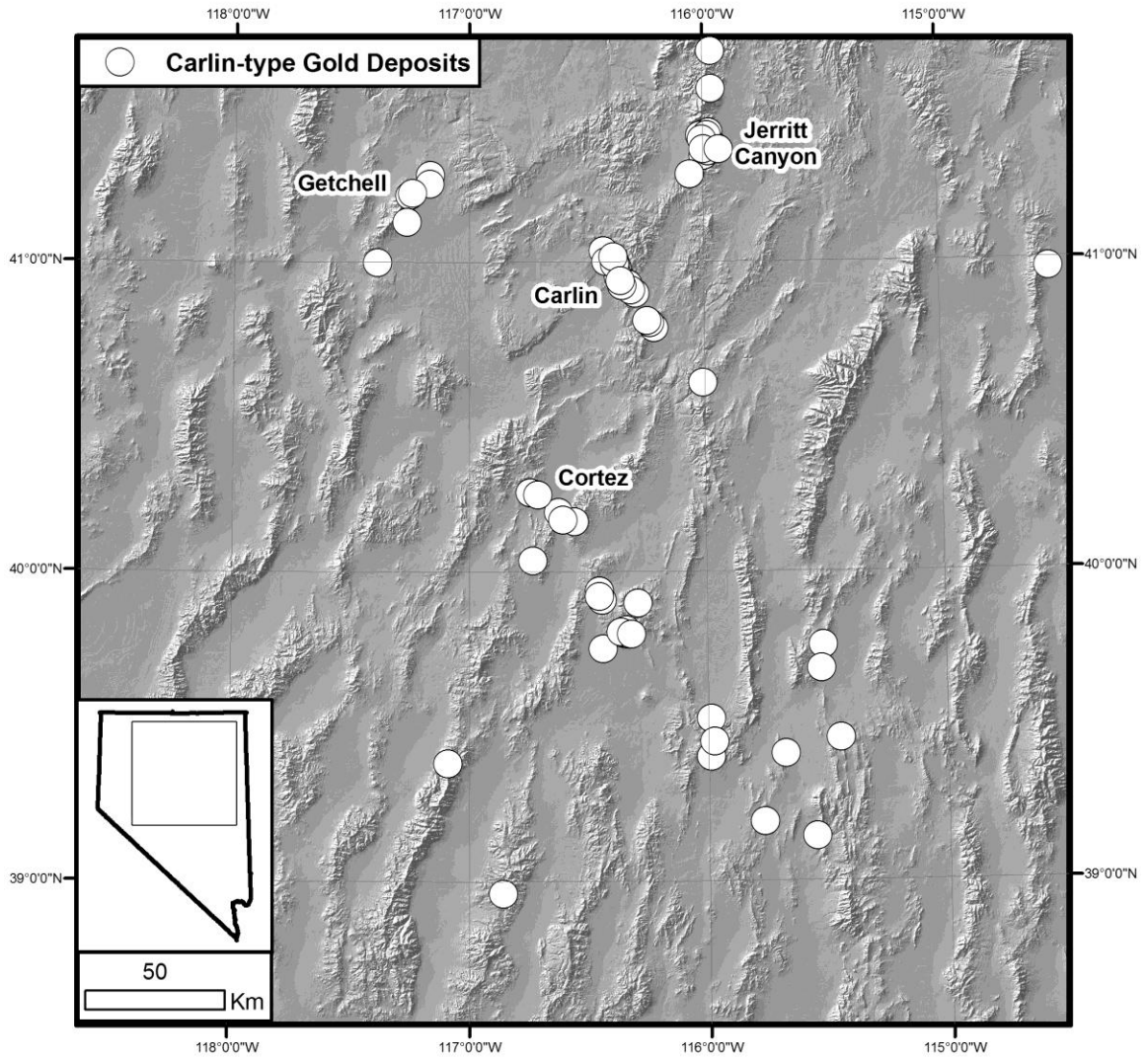


Figure 1.1. Digital elevation model of northern Nevada, showing locations of CTGDs and the locations of the four large clusters of large CTGDs, including Getchell.

Understanding of the vertical and lateral extent of Carlin-type hydrothermal systems has lagged behind porphyry and epithermal deposits (cf. Lowell and Guilbert, 1970; Gustafson and Hunt, 1975; Seedorff et al., 2005; Buchanan, 1981; Hedenquist et al., 2000; Simmons, et al., 2005). Published studies that mapped the relationship between gold grade and lithology, structure, alteration and trace elements at the scale of individual CTGDs include those at the Carlin (Bakken and Einaudi, 1986; Kuehn and Rose, 1992), Deep Star (Heitt et al., 2003), Gold Quarry (Harlan et al., 2002), Alligator Ridge (Ilchik, 1990) and Twin Creeks deposits (Stenger et al., 1998). Increasingly, exploration for CTGDs is being focused on underground targets that require high grades to be mined. Grades in known underground deposits can vary from >5-20 ppm Au in the ore to <0.5 ppm within a few meters peripherally (e.g., Deep Star, Heit et al., 2003), making exploration, development and mining very difficult. Few maps or cross-sections have been published showing patterns of hydrothermal features around individual high-grade ore zones.

This paper presents patterns of lithology, structure, hydrothermal alteration, Au grade, trace element concentrations, degree of sulfidation, and clay minerals around the High Grade Bullion (HGB) ore zone along a cross-section through the underground Turquoise Ridge CTGD in the Getchell District. This study takes advantage of closely spaced underground and surface core holes that allow assessment of patterns around the HGB at an appropriate scale. By focusing on a single cross-section, the haloes around the HGB ore zone presented below admittedly do not take into account the third dimension in and out of the plane of the section. In addition, there is no supergene

oxidation in any of the holes in the cross-section, thus eliminating weathering as a possible explanation for any of the patterns presented below.

DISTRICT HISTORY

The Getchell District is located along the northeastern flank of the Osgood Mountains, 70 km northeast of Winnemucca, Nevada (Figs. 1.1, 1.2). It includes the Getchell, Twin Creeks and Pinson mines, which have produced approximately 15.5 Moz of gold. The Getchell mine, which comprises several open pits along the Getchell fault; the Getchell underground deposit in the footwall of the Getchell fault, and the underground Turquoise Ridge deposit in the hanging wall of the Getchell fault, has produced approximately 4.7 Moz of gold from ore containing an average grade of 10 g/t Au. At the end of 2009, proven and probable reserves were 10.7 million tons grading 17.4 g/t Au, almost entirely in the Turquoise Ridge deposit.

Getchell was discovered in 1934 and represents one of the first Carlin-type gold deposits mined in Nevada, 27 years prior to the discovery of the Carlin deposit. Open pit mining along the Getchell fault commenced in 1938 with the production of 788,875 ounces of Au, initially from oxide ores and then from sulfide ores, until reserves were depleted in 1951. Episodic exploration and mining continued throughout the property until 1983 when First Mississippi Corp. acquired Getchell, discovered 1,346,000 oz of minable reserves, and formed FirstMiss Gold to put the mine back into production in 1987, first from open pits and then from underground (Horten, 1999). In 1991 low-grade production of oxide ore from open pits in the Turquoise Ridge Oxide Zone commenced in the hanging wall of the Getchell Fault. Subsequent deep drilling below

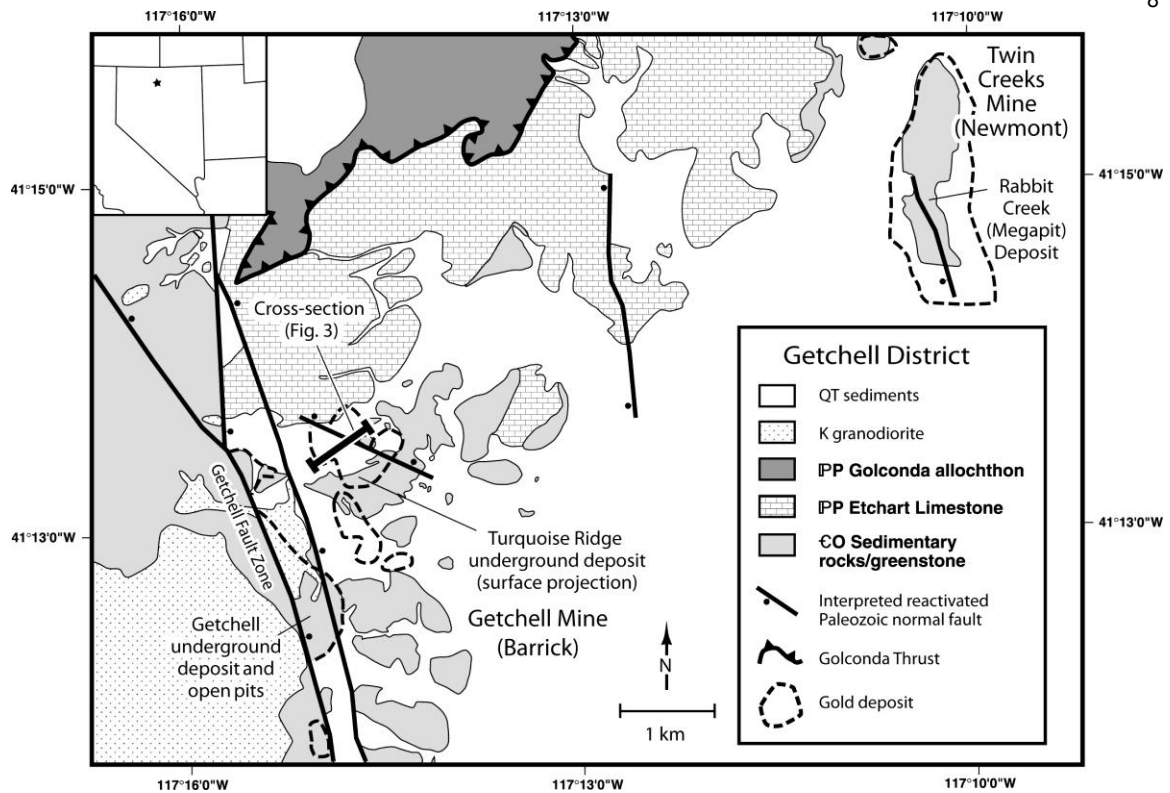


Figure 1.2. Simplified geologic map of the Getchell district (modified from Hotz and Wilden, 1964 and unpublished Placer Dome data). Shows trace of N55°E trending cross-section relative to the surface projection of the Turquoise Ridge underground deposit, Getchell underground deposit, and the Getchell open pits.

the Turquoise Ridge open pits penetrated high-grade sulfide ore. Continued drilling produced multiple high-grade intercepts resulting in the sinking of a production shaft in 1996. In 1998 Placer Dome became the operator after a merger with Getchell Gold Inc, a subsidiary of FirstMiss Gold. Between 2001 and 2003, work focused on the development of the Turquoise Ridge North Zone. Underground production began in 2004 shortly after a joint venture between Placer Dome (75%) and Newmont Mining Corp. (25%) was established. Barrick Gold Corp. acquired Placer Dome in 2005 and currently operates the mine, which it now refers to as its Turquoise Ridge mine.

DISTRICT GEOLOGY

The geology of the Getchell mine area and the northern Osgood Mountains has been discussed in many publications (Joralemon, 1951; Hotz and Willden, 1964; Chevillon et al., 2000; Crafford, 2000; McLachlan et al., 2000; Boskie, 2001; Breitt et al., 2005; Marlowe et al., 2007) and is summarized here. Ore bodies in the Getchell mine area are primarily hosted within a sequence of Cambrian-Ordovician carbonate and clastic rocks containing interlayered basalts that, in the past, have been mapped as Preble, Comus, and Valmy Formations (lumped together as Cambrian-Ordovician rocks in [Fig. 1.2](#)). Facies changes, gradational contacts, lack of age control, and lack of marker units in the mine area, discussed below, hamper assignment of these rocks into these established formations.

The primary ore-controlling structure in the district is the Getchell Fault Zone, which runs along the northeastern flank of the Cretaceous Osgood granodiorite stock. The fault zone dips between 30° and 80° east, mainly between 40° and 55°, and has a complex history with evidence for normal, reverse, and strike-slip motion. The Getchell fault and other faults highlighted in [Figure 1.2](#) were proposed by Cline et al. (2005) and Muntean et al. (2007) to be Paleozoic normal faults that formed prior to the Late Devonian-Early Mississippian Antler Orogeny. They propose the Paleozoic normal faults are linked to underlying basement faults that originated during rifting of western North America during the Proterozoic.

The Cambrian-Ordovician rocks were complexly deformed, likely during the Antler Orogeny, prior to the deposition of the Pennsylvanian-Permian Etchart

Formation. Basalt, chert, and siltstone, which have been historically assigned to the Valmy Formation, commonly have tight, locally recumbent, east to southeast-verging folds (e.g., Summer Camp Pit, Megapit at Twin Creeks) consistent with thin-skinned tectonics. On the other hand, the underlying rocks, which have more carbonate and have been traditionally assigned to the Preble and Comus Formations, commonly show west-verging more upright folds at Getchell and elsewhere in the Osgood and Edna Mountains (Madden-McGuire and Marsh, 1991; Crafford, 2000), including the Pinson Anticline at the Pinson mine, located just south of Getchell (McLachlan et al., 2000). These west-verging folds are also well expressed in seismic lines across the Getchell fault and its hanging wall (Cline et al., 2008). The west-verging structures are consistent with thick-skinned tectonics and are interpreted by Cline et al. (2005) and Muntean et al. (2007) to be the result of inversion of east-dipping normal faults, including the Getchell Fault Zone. The contact between the rocks historically assigned to the Valmy Formation and the underlying Preble and Comus Formations is locally expressed as a thrust fault that has been correlated with the Roberts Mountains thrust (e.g., Lopear thrust at Twin Creeks, Breit et al., 2005). However, in the Getchell mine area the thrust contact is not always apparent, the contact locally appears gradational, and no older-over-younger relationships have been documented, casting doubt whether it represents a regional thrust fault such as the Roberts Mountains thrust.

North of the Getchell mine area, the complexly deformed Cambrian-Ordovician sequence is unconformably overlain by the Pennsylvanian-Permian Etchart Formation, which is composed of variably sandy/silty limestone, calcareous siltstone/sandstone and

conglomerate. Conglomerates with quartzite cobbles derived from the Cambrian-Ordovician sequence locally occur near the base of the Etchart, indicating a period of uplift and erosion after the Antler orogeny prior to or during the earliest deposition of the Etchart (Breit et al., 2005; Muntean et al., 2007). The siliciclastic and basaltic rocks of the Mississippian-Permian Havallah Formation occur northwest of the Getchell mine area and were emplaced over Etchart Formation along the Golconda thrust during the late Permian to early Triassic Sonoma Orogeny. Broad, northeast-trending folds in the Etchart Formation are interpreted to have occurred during the Sonoma and/or subsequent Mesozoic orogenies.

The Paleozoic rocks were intruded by the Cretaceous Osgood stock, which consists predominantly of medium-grained equigranular to porphyritic granodiorite and related dikes and sills of dacite porphyry, which were commonly emplaced along structures sub-parallel to the Getchell Fault Zone (Berger and Taylor, 1980). $^{40}\text{Ar}/^{39}\text{Ar}$ dates on hornblende and biotite indicate emplacement between 91 and 98 Ma (Groff et al., 1997). The contact metamorphic aureole extends up to 3 km from the stock and, in carbonate rocks, zones outward from calcite-wollastonite-diopside-garnet-tremolite skarnoids to marble. Siliciclastic rocks, depending upon the protolith, can contain cordierite, andalusite, muscovite, and/or biotite. Metasomatic skarn associated with the stock is expressed mainly by tungsten mineralization (scheelite) associated with andraditic garnet and iron-rich diopside and retrograde tremolite/actinolite-epidote-quartz-sulfides. Later and/or more distal metasomatic mineralization is expressed by quartz veins that contain variable amounts of carbonate, pyrite, pyrrhotite,

arsenopyrite, and base metal sulfides. The Osgood stock appears to be part of a protracted magmatic-hydrothermal event ranging from 115-80 Ma based on $^{40}\text{Ar}/^{39}\text{Ar}$ dates and a U-Pb zircon date from Twin Creeks (Hall et al., 2000; Breit et al., 2005) and $^{40}\text{Ar}/^{39}\text{Ar}$ dates on hydrothermal K-feldspar and sericite at Getchell (Groff et al., 2005).

The Summer Camp, Hanson Creek, Getchell, and North open pits form a linear array of mined-out deposits along the Getchell fault. The Getchell underground development exploited ore in footwall splays and sympathetic fracture zones and dike contacts. The Getchell open pits and underground developments were within the contact metamorphic aureole of the Osgood stock, as defined by the presence of significant calc-silicates. The Turquoise Ridge oxide pits and the deep Turquoise Ridge refractory ore bodies occur in the hanging wall of the Getchell fault and straddle the margin of the metamorphic contact aureole. Mineralization at Turquoise Ridge extends discontinuously from the surface to a depth of over 1100 m. The main ore body plunges north, and the highest grades and tonnages are located at the north end at depths greater than 500 m. Ores in the Getchell District are largely devoid of supergene oxidation, which, although detrimental to economics, aids geologic studies. Gold grade is most closely correlated with the abundance of fine-grained gold-bearing arsenian pyrite associated with variable amounts of decalcification, argillization and silicification. Mineralization is Eocene in age, based on a 39.0 ± 2.1 Ma Rb-Sr age on galkhaite (Tretbar et al., 2000).

Present normal separation along the Getchell Fault Zone is indicated in the North pit by juxtaposition of basalts and cherts, historically assigned to the Valmy Formation,

against limestone and carbonaceous mudstone, historically assigned to the Comus and Preble Formations. Seismic data and limited drilling indicate apparent normal displacement could be as much as 300 m. How much of this normal movement is post-ore is uncertain; some of it could be synchronous with the deposition of the Etchart Formation (Muntean et al., 2007). However, post-ore movement on the fault is indicated by smeared orpiment and fine-grained pyrite along right-oblique and horizontal slickenlines (Boskie, 2001). Further post-ore normal movement is evidenced by steeply plunging slickenlines that overprint horizontal to very gently north- and south-dipping mullions and slickenlines. Post-ore rocks in the hanging wall of the Getchell fault include an Oligocene felsic tuff (27.1 ± 1.3 Ma, $^{40}\text{Ar}/^{39}\text{Ar}$, biotite, Ken Hickey, written communication, 2008), about 15 to 20 m thick, in the North Pit as well as alluvium up to about 5 to 10 m thick.

GEOLOGY OF THE NORTH END OF TURQUOISE RIDGE

The geology of the north end of the Turquoise Ridge deposit is characterized by a Cambrian-Ordovician sedimentary-volcanic package that has undergone a complex depositional, tectonic, metamorphic, and hydrothermal history. The complex depositional history of the package is compounded by rapid facies changes and a lack of marker units. Sediments within the deposit record multiple compressive and extensional deformational features, including both syn-sedimentary and tectonic. Pre-ore metamorphism related to the tectonic deformation and contact metamorphism, and hydrothermal activity related to emplacement of the Osgood stock further hampers

unraveling the geologic history. Given these complexities, understanding of the stratigraphy and structure of Turquoise Ridge continues to evolve.

The geologic framework presented here is based mainly on an underground cross-section that trends N55°E and cuts the north part of the Turquoise Ridge deposit through the HGB, the largest and highest-grade ore zone in the deposit at Turquoise Ridge (Fig. 1.2). The section was constructed from detailed logging of four surface diamond drill holes, spaced 60 m apart, and a fan of underground diamond drill holes (Fig. 1.3). A color-coded logging scheme similar to that used by the Anaconda Company in the 1960s was employed, in which lithology, structure, alteration, vein types, and mineralization was graphically recorded at a scale of 1:120. The logging information was transferred by hand onto a 1:600 scale cross-section. Interpretive overlays were done by hand and then digitized using ArcGIS. The closely spaced drilling has allowed for detailed interpretation. The lithologic units in Figure 1.3 represent a series of lithologic packages. Each of the individual lithologies described below can be seen in various proportions within each lithologic package. Unit designations at the deposit scale are assigned based on the most prominent rock types within a given unit.

The lowermost unit in the cross-section (unstippled purple unit in Fig. 1.3) is composed of carbonaceous mudstone and limestone (Fig. 1.4A). The mudstone varies from siliceous and non-calcareous to argillaceous and variably calcareous. The carbonaceous mudstones are composed of quartz and/or calcite, muscovite (formed during metamorphism), biotite (formed during contact metamorphism), carbonaceous material (>0.5 wt % organic C based on downhole assays), minor pyrite, and trace

pyrrhotite. The strata are commonly planar laminated with local disruption of bedding, which presumably resulted from soft-sediment deformation. The limestones within this unit consist of dark grey to black recrystallized micrite containing variable amounts of quartz silt and organic carbon. Sporadic turbidite sequences up to tens of centimeters thick occur locally. The turbidites consist of graded beds of light gray, coarse-grained, recrystallized calcarenite.

Figure 1.3. Underground cross-section through the Turquoise Ridge deposit oriented N55°E (section 3370, drill station 3). Shows the traces of the four surface core holes and five underground cores and interpreted geology. The top of the section is roughly 550 m below the surface while the bottom of the section is at a depth of approximately 975 m. The section's length is about 720 m. The panel above the cross-section is a map view, with a 60 m north-south grid, showing the surface projection of the traces of the holes relative to location of the cross-section (the red line in the center).

A sedimentary breccia unit overlies the carbonaceous mudstones and limestones and contains similar lithologies as the lower planar sediments, but contains abundant breccias and features consistent with soft-sediment deformation that were later overprinted by tectonic deformation. The breccias consist of subrounded to subangular limestone fragments, supported by a carbonaceous, non-calcareous mudstone matrix (Fig. 1.4B-C). In thin section, the limestone fragments are composed of fine-grained massive recrystallized micrite, and the mudstone matrix is composed of unoriented muscovite and biotite, organic carbon, and trace pyrite. The limestone fragments commonly contain calcite veinlets that are truncated along the fragment margins. The unit is divided into a lower and upper member (Fig. 1.3). The lower member consists of thick sections of limestone beds that have been stretched into disc-shaped clasts, which are typically several millimeters thick and several centimeters long (Fig. 1.4B). The clasts can have consistent orientations in a given drill hole for several tens of meters. The disc-shaped clasts are interpreted to be parallel to bedding and are analogous to pinch and swell structures, or boudins, which form in layers showing strong contrasts in ductility. In addition, the lower unit contains breccias with cm-sized limestone fragments that are commonly larger (up to at least 8 cm), rotated, and unoriented. The breccias in the lower member are difficult to correlate between drill holes, even between the closely-spaced underground holes in Figure 1.3. The upper member consists of about 70% breccia that is composed of finer-grained fragments than those in the lower member (Fig. 1.4C). These upper, finer-grained breccias can commonly be correlated from hole to hole. The fragments are commonly elongated and oriented,

and, the muddy matrix has a foliation, which in thin section, is accentuated by carbonaceous material. However, the foliation varies, and, in some thin sections, the muddy matrix has common tortuous whirls. None of the fragments contain recrystallized tails (i.e., pressure shadows) as would be expected if the breccias were related to brecciation during ductile, tectonic deformation. As pointed out by Muntean et al. (2007), the sedimentary breccia unit pinches out to the south, about 150 m south of the southeast corner of the cross-section in Figure 3. The pinch-out to the south has a fairly sharp margin that trends N80°W.

Above the sedimentary breccia unit lies a sequence of thin-bedded, light grey, recrystallized micritic limestones and massive to poorly bedded, non-calcareous, brown mudstones containing less organic carbon content than the underlying carbonaceous mudstones (<0.2 wt % organic carbon) (Fig. 1.4D). The brown mudstones contain foliated muscovite, unoriented biotite, and trace amounts of pyrite, pyrrhotite and rutile. The biotite, and possibly some of the muscovite, formed during contact metamorphism related to the emplacement of the Cretaceous Osgood stock and indicates a likely tuffaceous mudstone protolith. The limestone beds are commonly complexly, ductilely folded. These folds are interpreted to be slump folds formed from soft-sediment deformation that were then variably overprinted by tectonic folding.

A thick section of basalt, referred to as the “northern pillow basalt” (NPB) overlies the sequence of deformed limestones and brown mudstone on the eastern half of the cross-section in Figure 1.3. The basalt is greenish gray, commonly aphanitic, and non-vesicular (Fig. 1.4E). Pillow structures are locally abundant. The basalt contains

tabular plagioclase phenocrysts that are commonly 0.2 to 1 mm in length. The fine-grained groundmass consists of primary orthopyroxene and magnetite that are partially to completely replaced by chlorite, epidote, and/or actinolite. The replacement of primary magnetite has resulted in a low, flat magnetic signature in surface magnetic surveys conducted at Turquoise Ridge (K. Wood, personal commun., 2008). Note the blunt southwestern margin of the NPB in [Figure 1.3](#). The margin strikes N65°W, almost perpendicular to the cross-section. The contact between the northern pillow basalts and underlying sediments is frequently broken, but is locally depositional ([Fig. 1.4E](#)), suggesting that the basalt erupted onto the underlying sediments, rather than being tectonically emplaced.

Overlying the NPB are predominantly brown mudstones with thin, interlayered basalt flows and diabase sills, as well as minor limestone. Further upward and toward the present surface, above the cross-section in [Figure. 1.3](#), basalt, tuffaceous siltstones and chert become more abundant with no definitive evidence for a major thrust fault as mentioned above. Overall, the carbonate and organic carbon content decreases upward in the stratigraphic section at Turquoise Ridge. Features consistent with soft-sediment deformation and the southward linear pinch-outs of the sedimentary breccia unit and the NPB support the hypothesis originally proposed by Placer Dome geologists and published by Muntean et al. (2007) that there was a west-northwest trending active basin margin during deposition of the sedimentary host rocks at Turquoise Ridge. Based on bedding trends, the lowermost carbonaceous mudstones and limestones form a northwest-trending monocline that is interpreted to have originated by syn-depositional

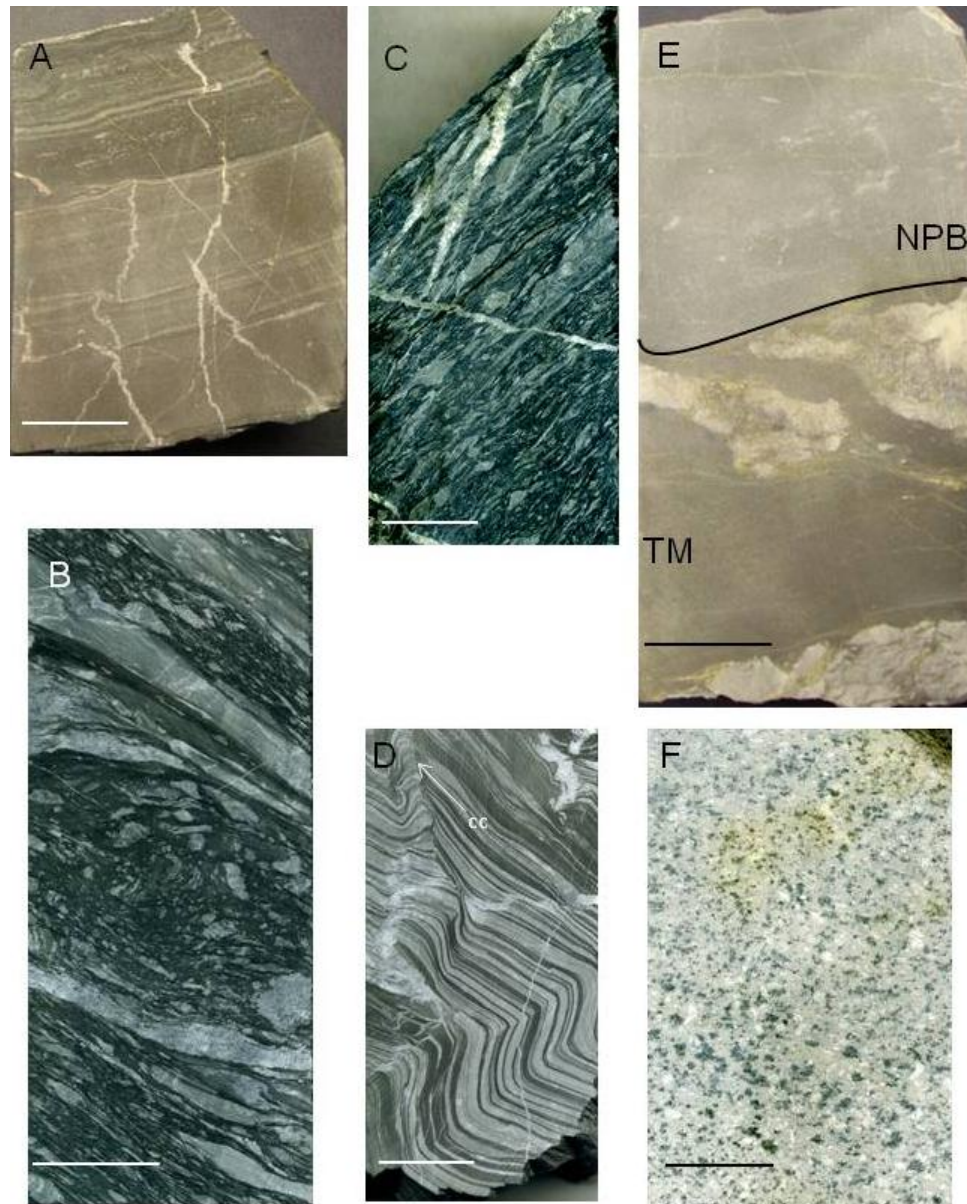


Figure 1.4. Sawed drill core of lithologies present at the north end of the Turquoise Ridge deposit. A. The lower interbedded carbonaceous mudstone (CM) and limestone (LS) unit (hole 99NZ015). B. Example of the lower member of the sedimentary breccia unit (hole TU01164A). C. Example of the upper member of the sedimentary breccia unit (hole TU01166). D. Interbedded brown tuffaceous mudstone and limestone showing complex folding overprinted by incipient crenulation cleavage (cc) (hole TU01164). E. Depositional contact between northern pillow basalt (NPB) and brown tuffaceous mudstone (TM) (hole TU01167). F. Least altered example of the main dacite porphyry dike (hole TU01167). Shows weak propylitic alteration characterized by the replacement of primary hornblende and biotite by chlorite and epidote and the replacement of plagioclase by albite and calcite.

normal movement along a buried west-northwest-striking, northeast-dipping fault (Fig. 1.2). The buried fault zone is interpreted to be linked to underlying basement rift faults of the same orientation that formed during the Proterozoic (Muntean et al., 2007). The normal faulting caused local topographic instability and the emplacement of slide blocks and sedimentary debris flow breccias, mainly of carbonaceous mud and partially lithified limestone. In addition, blocks of less carbonaceous limestone and tuffaceous mudstone slid northward over the breccia unit. Similar sedimentary debris flow breccias and slide blocks in Cambrian-Ordovician rocks have been documented in the Tybo district in the Hot Creek Range in central Nevada by Cook and Taylor (1977). Basalt then erupted and flowed up against the west-northwest-trending topographic barrier, forming the thick NPB. The submarine eruptions do not appear to have occurred along the basin margin, as evidenced by the lack of basaltic dikes in the vicinity of the margin. The transition from relatively deep quiet water sediments to disturbed sediments to volcanic rocks represents the onset of Cambrian-Ordovician extension in the Getchell area, which has been proposed for rocks of similar age in the Roberts Mountain Allochthon elsewhere in north-central Nevada (e.g., Madrid, 1987).

Rocks at Turquoise Ridge were later tectonically deformed by compression, primarily during the Antler Orogeny. The deformation is well-expressed in the cross-section in Figure 1.3 by a zone of folding along the blunt southwestern margin of the NPB. Several of the folds appear to be associated with west-northwest-striking, northeast-dipping, low-displacement faults along the margin. The faults now show either apparent normal or reverse separation. The blunt southwestern margin of the

thick NPB reflects a major competency contrast with the surrounding mudstone and limestone. Similar compressional deformation is seen in a diabase sill overlying the tuffaceous mudstones and limestones, near the top and just above the cross-section in [Figure 1.3](#). A definite tectonic cleavage is variably developed in the rocks at Turquoise Ridge. It occurs as a spaced crenulation cleavage that is generally oriented at a high angle to bedding ([Fig. 1.5A](#)) The crenulation cleavage is defined by sub-parallel wispy planes of carbonaceous material ([Fig. 1.5B](#)) and muscovite as well as kinking of muscovite grains in some samples.

[Figure 1.6](#) schematically illustrates the interpretation of the development of the Cambrian-Ordovician basin margin and its subsequent deformation during the Antler Orogeny. The contact between the NPB and underlying sediments was originally a depositional contact, representing an angular unconformity of about 20°. This suggests the underlying sediments were tilted up to 20° during the formation of the extensional monocline. Basalt then flowed up against the steepened slope and inter-fingered with mudstone and limestone toward the top of the basalt. During the Antler and subsequent orogenies, the angular unconformity between the NPB and the underlying sediments significantly steepened near the margin of the NPB. The sediments along the margin of the competent basalt took up the strain by folding like an accordion, whereas strain in the basalt was accommodated by minor thrust faults.

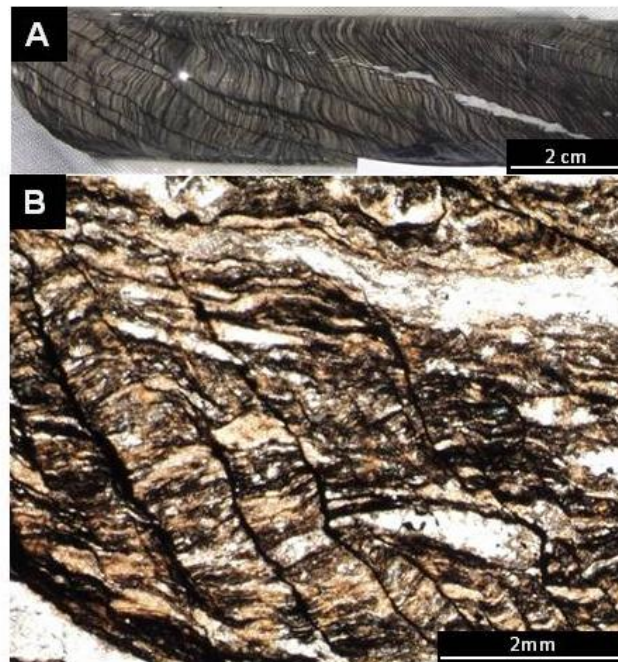


Figure 1.5. Examples of crenulation cleavage. A. Cleavage at high angle to bedding (sawed drill core, hole 00NZ135, located very close to cross-section in Fig. 3). B. Thin section photomicrograph showing cleavage defined by wispy planes of carbonaceous material (hole TU001165).

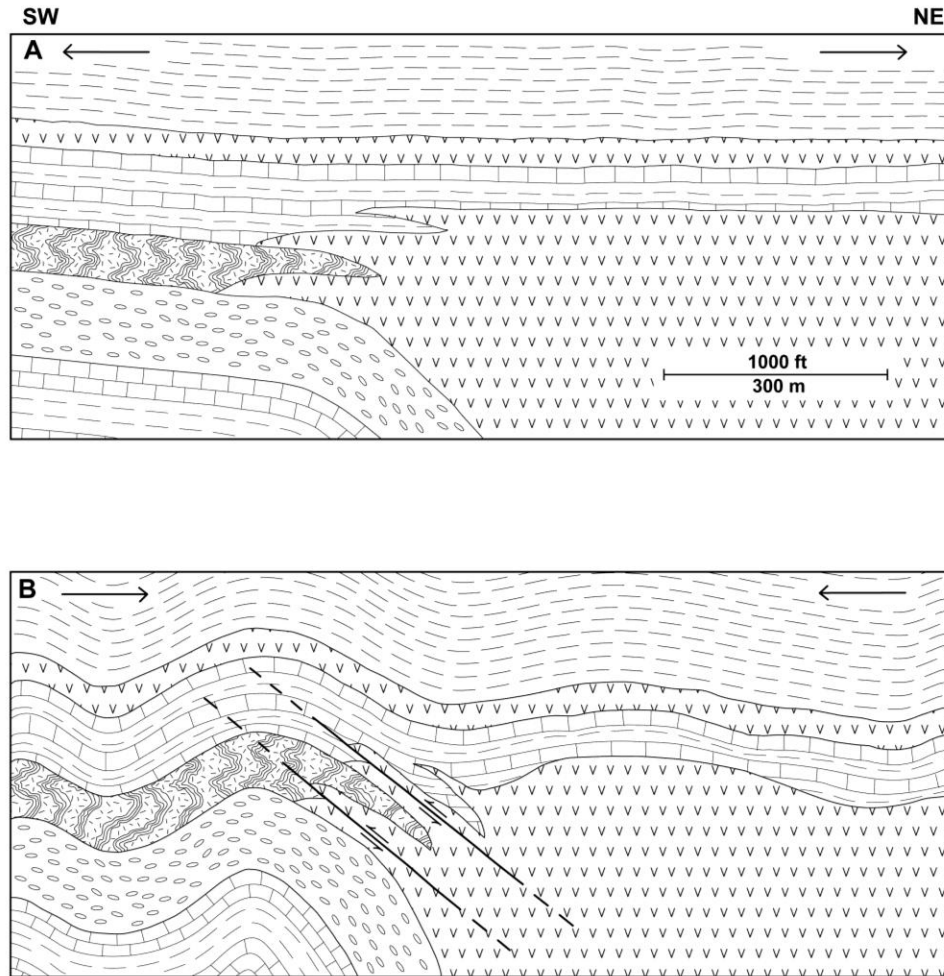


Figure 1.6. Schematic interpretation of the development and subsequent deformation of the Cambrian-Ordovician basin margin. A. Approximate interpreted geometry during Cambrian-Ordovician extension that resulted in formation of extensional monocline and eruption of northern pillow basalt. B. Compressive deformation focused on the margin of the basalt resulting in the folding of the less competent sedimentary rocks and thrusting of the more competent basalt.

Cretaceous dacite dikes intrude the Cambrian-Ordovician rocks in the cross-section in [Figure 1.3](#), and throughout Turquoise Ridge. A prominent dike transects the entire cross-section in [Figure 3](#) and varies between 4 and 11 meters in thickness. This “main dike” strikes sub-parallel to the Getchell fault, and its dip decreases significantly to the southwest. Zircons from the main dacite dike have given a U-Pb age of 115 ± 2.3 Ma (Ken Hickey, written communication, 2008), which is older than the Osgood stock, but similar in age to a dacite porphyry dike at Twin Creeks (Breit et al., 2005). The least altered samples of main dacite porphyry dike contain plagioclase phenocrysts (0.2-1.0 mm) and lesser biotite and hornblende phenocrysts (0.1-0.2 mm) set in a very fine-grained (<0.1 mm) groundmass of quartz, plagioclase, minor hornblende and biotite, and trace magnetite and zircon ([Fig. 1.4F](#)).

Abundant high-angle faults and fracture zones with variable orientations are located throughout the Turquoise Ridge deposit. The vast majority of the faults in the underground workings lack continuity along strike and down dip. The faults typically have apparent normal displacements of less than 5 meters and are very difficult to correlate between holes. Thus, none of these faults are shown in [Figure 1.3](#). Based on alteration and gold grade patterns discussed below, numerous steep, small-displacement antithetic faults occur on the west side of the cross-section in the hanging wall of the Getchell fault. Drill intersections of the Getchell fault in [Figure 1.3](#) show it to be an approximately 140 m thick zone composed of an elaborate fracture network represented by closely spaced, often overlapping, broken zones that show evidence for variable fault movement. The broken zones vary from gouge to rubble with locally

preserved slickenlines along graphite(?) -coated fracture surfaces. The drill intersections show similar-looking carbonaceous mudstone and limestone on both sides of the fault, which argues against large-scale net displacement along the Getchell fault.

ALTERATION AND GOLD MINERALIZATION

Currently-defined ore zones at Turquoise Ridge occur within a north-plunging mineralized zone roughly 1,000 meters (N-S) by 600 meters (E-W) (Chevillon et al, 2000). Gold mineralization follows a N30-40°W fabric that is sub-parallel to the Getchell fault. The ore zones within the Turquoise Ridge deposit occur along complex intersections between: 1) northeast- to northwest-trending, high-angle small-displacement faults and fracture zones, 2) the west-northwest-trending Paleozoic basin margin, 3) synforms and antiforms, and 4) calcareous lithologies (Muntean et al., 2009). The alteration and mineralization patterns at the north end of Turquoise Ridge, discussed in this paper, are based on the detailed underground cross-section in [Figure 1.3](#). Decalcification, argillization, and silicification are the alteration features most closely associated with gold mineralization at Turquoise Ridge and are the result of interaction of an acidic hydrothermal fluid with the host rocks. Decalcification occurred where acidic fluids reacted with calcareous lithologies, such as calcareous mudstone and recrystallized micritic limestone, as well as quartz+carbonate veins associated with the emplacement of the Osgood stock. Such decalcified veins commonly have vugs lined with pre-ore, terminated quartz crystals. Strong decalcification significantly enhanced porosity and permeability, leading to local collapse breccias and increased fluid-rock interaction. Argillic alteration is also the result of acidic fluids, but results from reaction with silicate

minerals such as feldspars, amphiboles, biotite, and muscovite to form clay minerals. It is best developed in the non-calcareous brown mudstones, basalts, and dacite dikes, forming primarily kaolinite±illite as discussed below. Unlike decalcification of carbonates, argillic alteration did not enhance porosity and permeability.

Strongly altered, decalcified limestones locally retain their original rock fabric despite dissolution of almost all the carbonate within the rock. [Figures 1.7A-B](#) show unaltered, finely interbedded, recrystallized micritic limestone and mudstone. The limestone layers are typically composed of fine-grained subhedral calcite grains (<0.01-0.1 mm) along with minor quartz-silt (<0.01 mm) and diagenetic pyrite (<0.1 mm). In strongly decalcified/silicified samples of similar interlayered limestone and mudstone ([Figures 1.7C-D](#)), hydrothermal quartz grains (<0.01mm) have completely replaced calcite grains, leaving a delicate sponge-like texture with about 20-40% pore space. Gold-bearing arsenian pyrite or marcasite occur along the boundaries of the hydrothermal quartz grains and are intergrown with kaolinite and/or illite as discussed in detail below. The contemporaneous association between Au-bearing arsenian pyrite/marcasite and hydrothermal quartz (jasperoid) indicates that these minerals formed during a single hydrothermal event. In addition, the hydrothermal quartz exhibits primarily a reticulate texture that has been interpreted to represent formation at temperatures greater than 180°C (Lovering, 1972; Dong et al, 1995). Such rock could very well scratch by fracturing the delicate sponge-like quartz framework, and most field geologists would log such alteration as decalcification, despite the abundance of quartz. Cline (2001) referred to such alteration at the Getchell deposit as jasperoid, which it

technically is. However, field geologists in Nevada typically log rocks as jasperoid only if it leaves steel upon scratching, that is, rocks are completely silicified and lack the

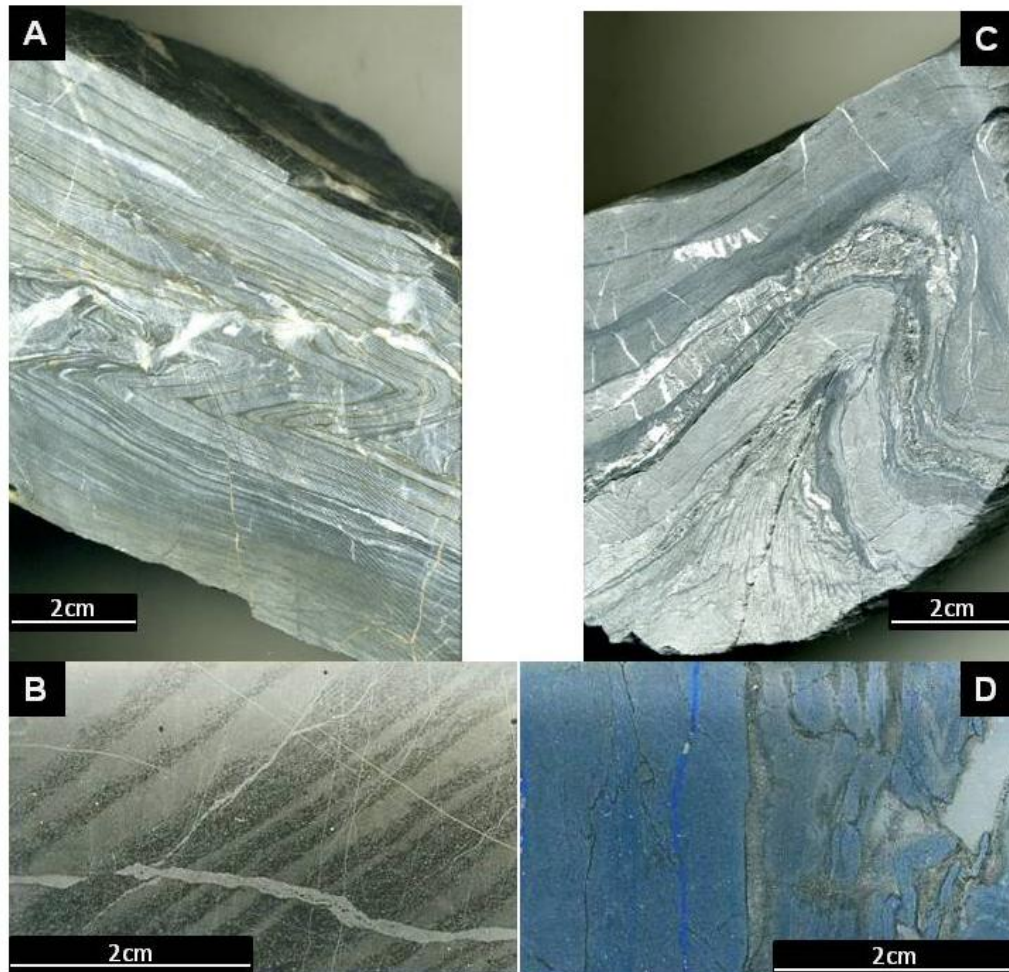


Figure 1.7. A. Unaltered, folded, finely laminated recrystallized micritic limestone (gray) and brown mudstone (hole TU01166). B. Thin section of unaltered finely laminated micritic limestone (light layers) and mudstone (dark layers) (hole TU01165). C. Strongly decalcified, laminated limestone and mudstone that is very similar to A (hole TU01165). Note the preservation of primary rock fabric despite the total dissolution of carbonate. D. Thin section of strongly decalcified, laminated limestone and mudstone that is very similar to C (hole TU01165). Note the increase in porosity in D relative to C, as represented by the abundant blue epoxy in D. The bluish layers in D were limestones in which the calcite has been completely dissolved. The limestone layers are now a delicate sponge-like framework of quartz and very fine-grained pyrite and marcasite.

sponge-like textures of incompletely silicified, decalcified rocks. Such dense jasperoid was only locally logged during this study.

Figure 1.8A shows the interpreted pattern of ore-stage hydrothermal alteration along the detailed cross-section. Because decalcification, silicification, and argillization resulted from interaction of acidic fluids with the country rocks, they were lumped together into the following categories: 1) moderate to strong alteration consisting of lithologies having rock textures that are commonly (but not always as demonstrated in Fig. 1.7) destroyed and have little to no reaction with 5% HCl and, 2) weak to moderate alteration consisting of wall rocks having moderate to strong bleaching, largely preserved rock texture, and weak to moderate reaction with 5% HCl. Outside the alteration zones shown in Figure 1.8A, rocks either show no visible, megascopic alteration or contain local, narrow alteration zones that were too sporadic and widespread to be contoured. Note that weak to moderate alteration does not form a halo around the moderate to strong alteration throughout most of the cross-section. Visually unaltered rock commonly occurs adjacent to moderately to strongly altered rock. The outer margins of the main dacite dike are almost everywhere argillized. Moderate to strong alteration occurs in the footwall and hanging wall of the dacite dike, extending into the folded sediments adjacent to the blunt edge of the NPB. In addition, weak to moderate alteration extends well into the hanging wall and footwall of the main dacite porphyry dike in the eastern portion of the cross-section. The Getchell Fault Zone in the lower, southwest corner of the section consists of a narrow central zone containing strong alteration that is surrounded by a broad zone of weak to moderate

alteration. Similarly, weak to moderate or moderate to strong alteration is interpreted to occur along the high-angle, west-dipping antithetic fault zones that extend upward from the Getchell fault zone. The largest alteration zone occurs where these antithetic structures intersect the footwall of the dacite dike within the sedimentary breccia unit. Although some of the antithetic fault zones can be traced across the dike, alteration appears to persist along only a few of them.

Late ore-stage realgar and orpiment mineralization, consistent with what Cline (2001) reported for the Getchell deposit, was logged. Realgar is slightly later paragenetically and is much more abundant than orpiment. The abundance of realgar progressively increases along the cross-section from northeast to southwest and primarily occurs in the footwall of the main dacite dike (Fig. 1.8B). Though spatially related to ore, its distribution does not form a consistent pattern with respect to ore, mainly because it is paragenetically later than the Au. Also, though logged in detail, the abundance of calcite veins shows no spatial pattern with respect to ore or alteration.

Gold assays of drill core intervals that were up to 1.5 meters in length were plotted using Target software, an add-on for ArcGIS developed by Geosoft and hand-contoured using the following intervals: 1) ≥ 0.34 ppm, 2) ≥ 3.4 ppm, and 3) ≥ 17 ppm (Fig. 1.8C). The Au grades commonly show abrupt variations, locally changing from ≥ 17 ppm to < 0.34 ppm within meters. The HGB is represented by the large zone of ≥ 3.4 ppm Au that occurs at the intersection of the main dacite dike and the steep antithetic faults that extend upward from the Getchell fault zone. The HGB extends over 60 meters into the footwall of the dacite dike within the lower member of the sedimentary breccia unit

and 105 meters into the hanging wall within the upper member of the sedimentary breccia unit and the folded brown mudstones and limestones adjacent to the blunt edge of the NPB. Gold grades ≥ 17 ppm extend up to 20 meters into the footwall of the dacite dike within the central portion of the HGB and extend up to 75 meters into the hanging wall of the dike. The high-grade zones in the hanging wall are commonly lenticular bodies that are discordant to bedding and occur along the thrust faults associated with the folded sediments adjacent to the NPB. Pervasive Au grades ≥ 3.4 ppm within the HGB extend up to 40 meters above and 55 meters below the zone of ≥ 17 ppm Au. Zones of ≥ 0.34 ppm Au extend up to 120 meters above and up to 150 meters below the HGB, occur within the Getchell fault, and occur along several steep, small-displacement, antithetic faults in the hanging wall of the Getchell fault. Attempts were made to contour Au grades of ≥ 0.10 ppm, ≥ 0.05 ppm, and ≥ 0.025 ppm in order to evaluate whether they form broader haloes to the 0.34 ppm Au contour. Gold assays of ≥ 0.05 ppm locally extend up to 15 meters beyond the 0.34 ppm Au contour; however, such low grades lack sufficient continuity to contour at the scale of the cross-section in [Figure 1.8C](#).

Gold grades of ≥ 0.34 ppm display a strong spatial correlation with moderate to strong alteration. Weak to moderate alteration extends locally up to tens of meters beyond the ≥ 0.34 ppm Au contour, such as in the Getchell Fault Zone, in the footwall of the dacite dike below the central part of the HGB, and in the folded brown mudstones and limestones adjacent to the NPB. The strong spatial correlation between gold grade

and alteration suggests wall rock alteration occurred contemporaneous with gold mineralization.

Because much of the gold and alteration appear to be associated with fault and fracture zones, values of rock quality designation (RQD) were plotted and contoured to determine the relationship between gold grade and rock fracture density (Fig. 1.8D). Zones of high fracture density could be reflecting zones of greater permeability and paleo-fluid flow. Very poor RQD values of less than 25% (>150 fractures per 3m interval) coincide with the Getchell fault zone. The RQD values also show a broad halo of fractured rock around the narrow visible alteration zones associated with the steep antithetic faults in the hanging wall of the Getchell fault. Similarly, low RQD values exist in the hanging wall and footwall of the main dacite dike and extend into the folded tuffaceous mudstones and limestones adjacent to the NPB. There are very few areas along the cross-section where anomalous Au-values (≥ 0.34 ppm Au) are present in rocks having RQD values greater than 50%. The RQD distribution supports our interpretation that ascending ore fluids exploited pre-existing fault and fracture zones rather than being bound to specific stratigraphic horizons. Also the association of low RQD values with ore and alteration could be the result of fracturing caused by collapse during carbonate dissolution associated with ore formation.

Figure 1.8.

A. Distribution of hydrothermal alteration related to ore formation.

B. Late-stage realgar mineralization. The density of the stipple pattern reflects abundance of realgar.

C. Au-grade contours showing high (≥ 17 ppm Au, magenta) moderate (≥ 3.4 ppm, red) and low (≥ 0.34 ppm, orange) Au grades in relation to alteration (yellow). Note the individual assays of drill interval represented by points along individual drill holes.

D. Distribution of RQD, which was determined by the sum of the lengths of core longer than 10 cm divided by the total length of core multiplied by 100 for a given interval of core. Points represent individual RQD determinations.

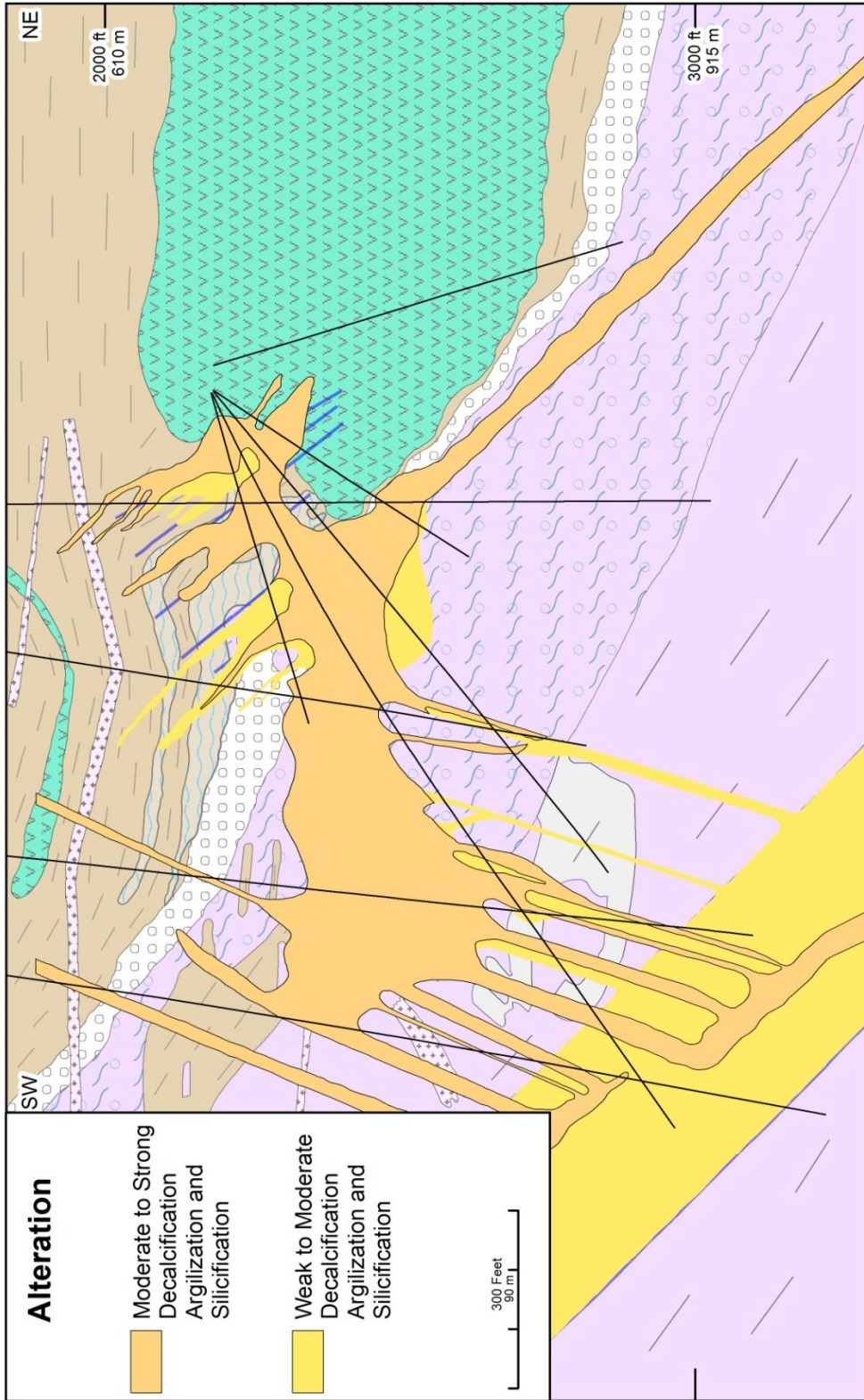


Figure 1.8A

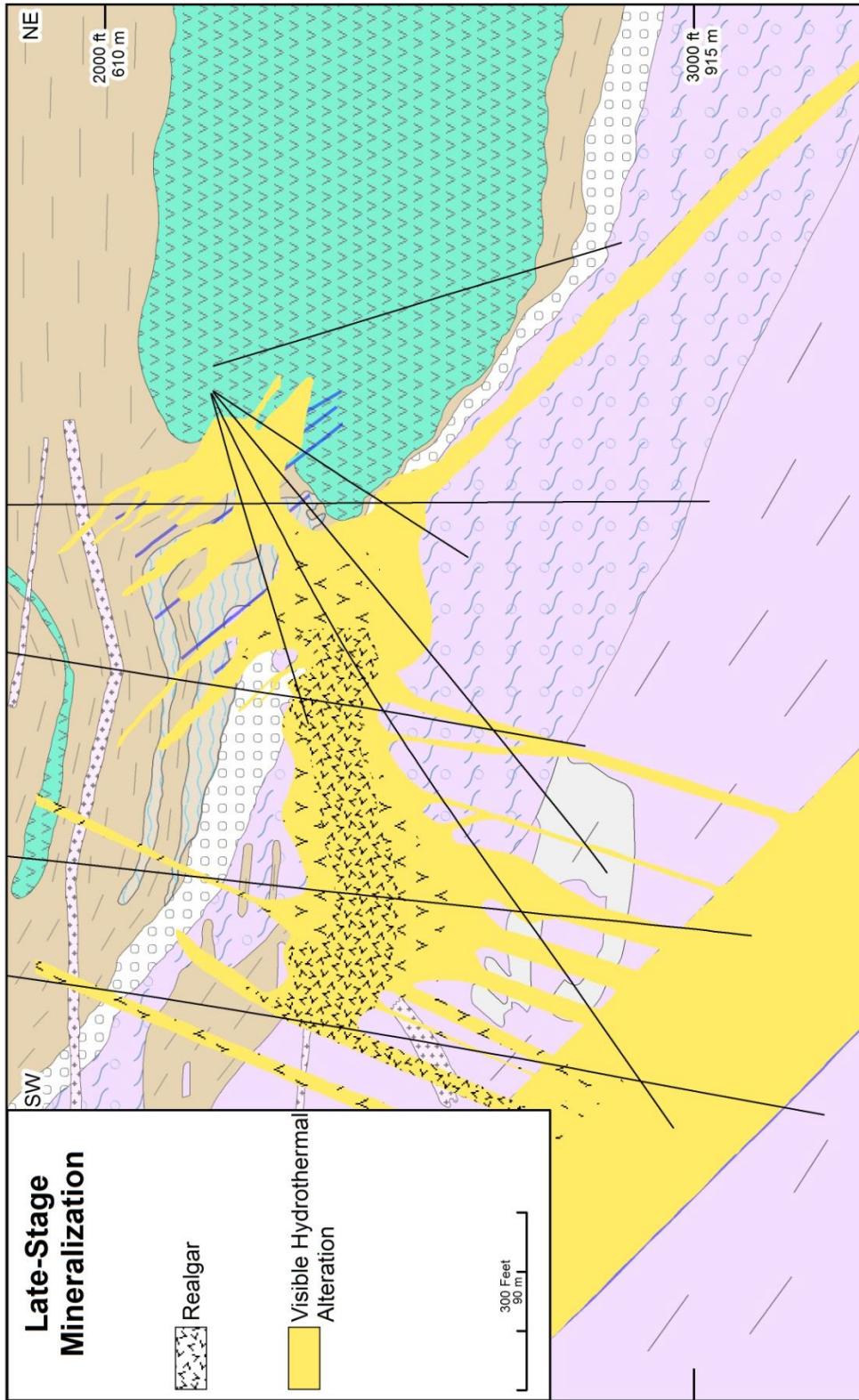


Figure 1.8B

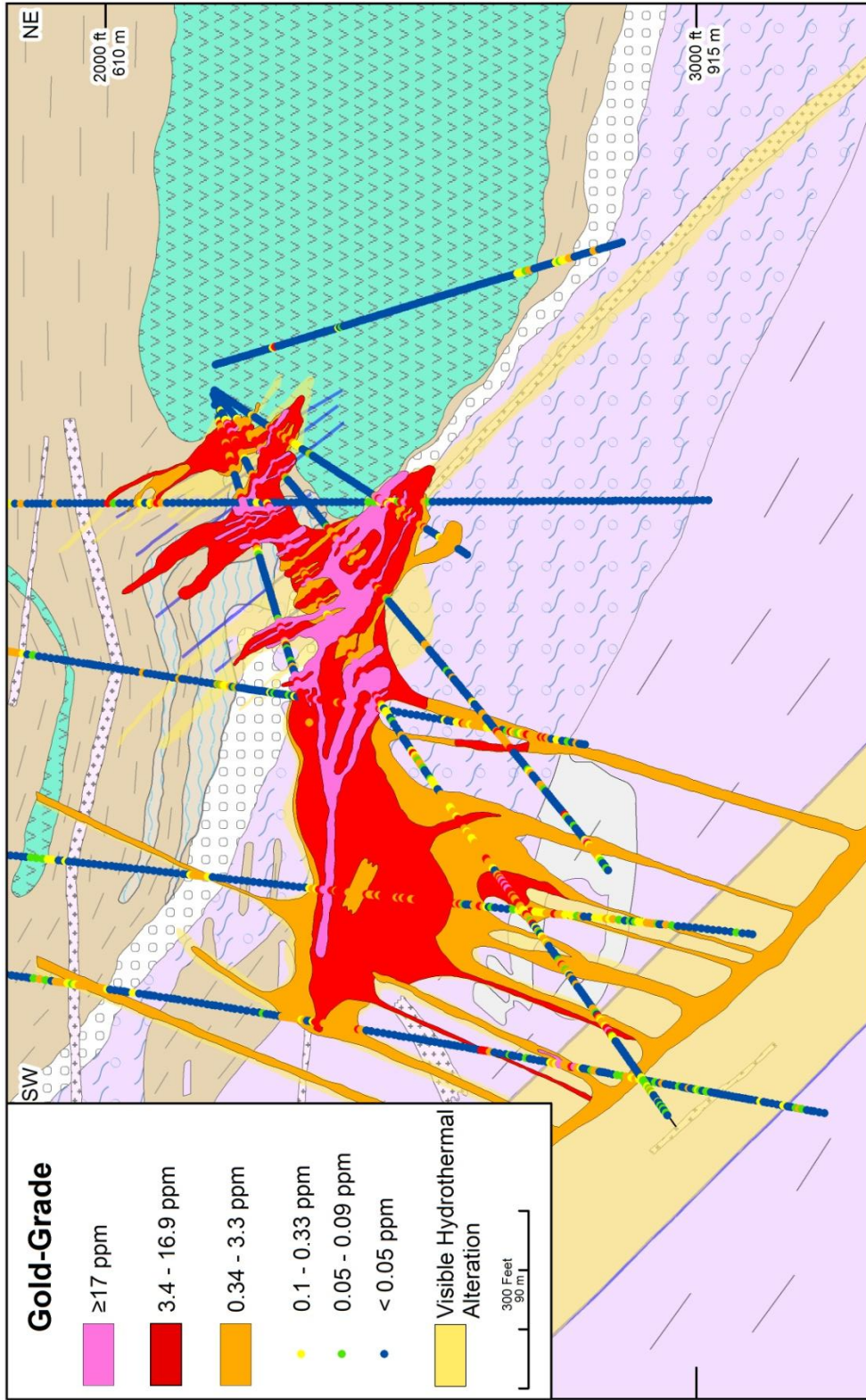


Figure 1.8C

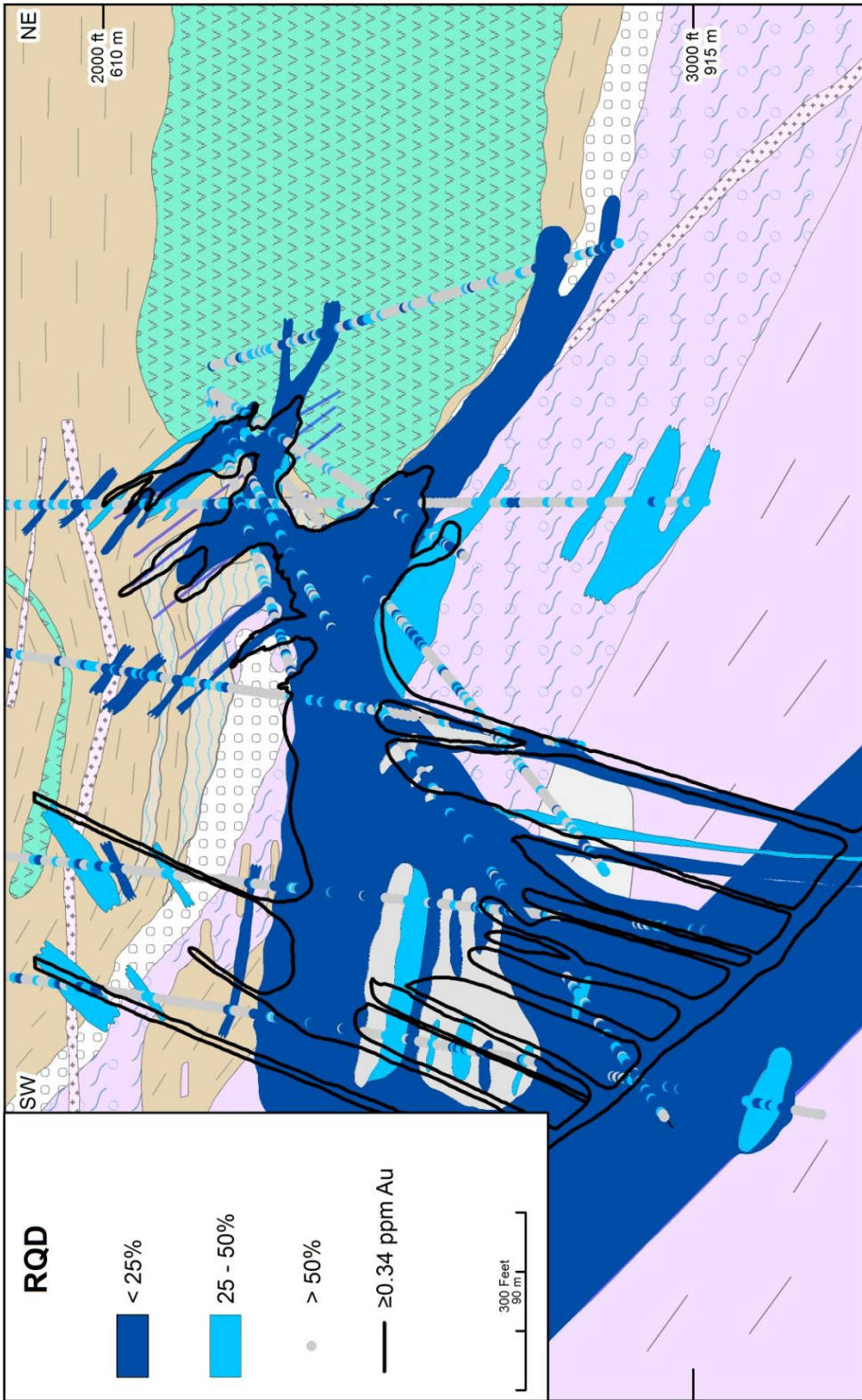


Figure 1.8D

MULTI-ELEMENT DATA

The statistics and distribution of downhole multi-element analyses, provided by Barrick, were evaluated along the detailed cross-section in order to assess dispersion haloes around the HGB ore zone. Barrick's downhole sampling of visually unaltered rock within the five underground drill holes was limited to 6 meters above and below visual alteration zones. Analyses of 50 elements were completed by ALS Chemex utilizing a nitric aqua regia digestion followed by analysis by ICP-MS-AES (ALS Minerals ME-MS41). Elements that are not completely digested by nitric aqua regia include Al, Ba, Be, Ca, Cr, Ga, K, La, Na, Sr, Ti, and W. The data were combined with the Au assays collected from the same drill interval. Multi-element data from surface holes analyzed by Placer Dome were composite samples from 3 m intervals. They are ICP-AES analyses that were completed by American Assay Laboratories using an aqua regia digestion. Analyses that contained values less than the detection limit for a given element were given a value of half the detection limit prior to statistical analysis and plotting. Statistical analyses, including descriptive statistics, Pearson correlation coefficients, Spearman rank correlation, and traditional R-mode factor analysis, were limited to analyses of the five underground drill holes. Statistical analyses were carried out using the software package SYSTAT 11. Trace element analyses from the four surface holes cover the entire length of the holes, but were excluded from the statistical analysis because of the differences between the older American Assay analytical package and the newer ALS Chemex package. Also, the detection limits were higher for several of the elements in the American Assay package.

Statistics

Pearson correlation coefficients were calculated to determine which trace elements correlate linearly with gold. Gold strongly correlates with Tl ($r=0.765$), Hg ($r=0.701$), and As ($r=0.611$) and more weakly with Te ($r=0.588$), Sn ($r=0.556$), and In ($r=0.502$). Spearman rank correlation coefficients were also calculated and are preferred because the method does not depend upon linear relationships and is less influenced by outliers. The Spearman rank correlation matrix for 18 of the elements, along with accompanying scatter plots, is presented in [Figure 1.9](#). Gold shows a strong positive correlation with Hg ($r=0.889$), As ($r=0.849$), W ($r=0.819$), S ($r=0.783$), Tl ($r=0.78$), and a weaker correlation with Sb ($r=0.671$), Te ($r=0.616$), In ($r=0.598$), and Sn ($r=0.575$). Gold displays a strong negative correlation with Mg ($r=-0.727$), Ca ($r=-0.677$), and Sr ($r=-0.69$).

Traditional R-mode factor analysis was conducted utilizing a varimax rotation and minimum eigen value of 1.00. Varimax rotation was utilized to maximize the variance that each factor symbolizes (Abdi, 2003). Because most of the elements showed log-normal distributions, the log values for each element were used for the factor analysis, because factor analysis is based on the assumption of normal populations. [Table 1.1](#) displays the six calculated factors and the associated factor loadings for the entire geochemical database. The six factors account for nearly 80% of the variance in the data set.

Factor 2, which explains nearly a quarter of the variance, is the factor most closely associated with gold mineralization. The highest loadings for Factor 2 are Au

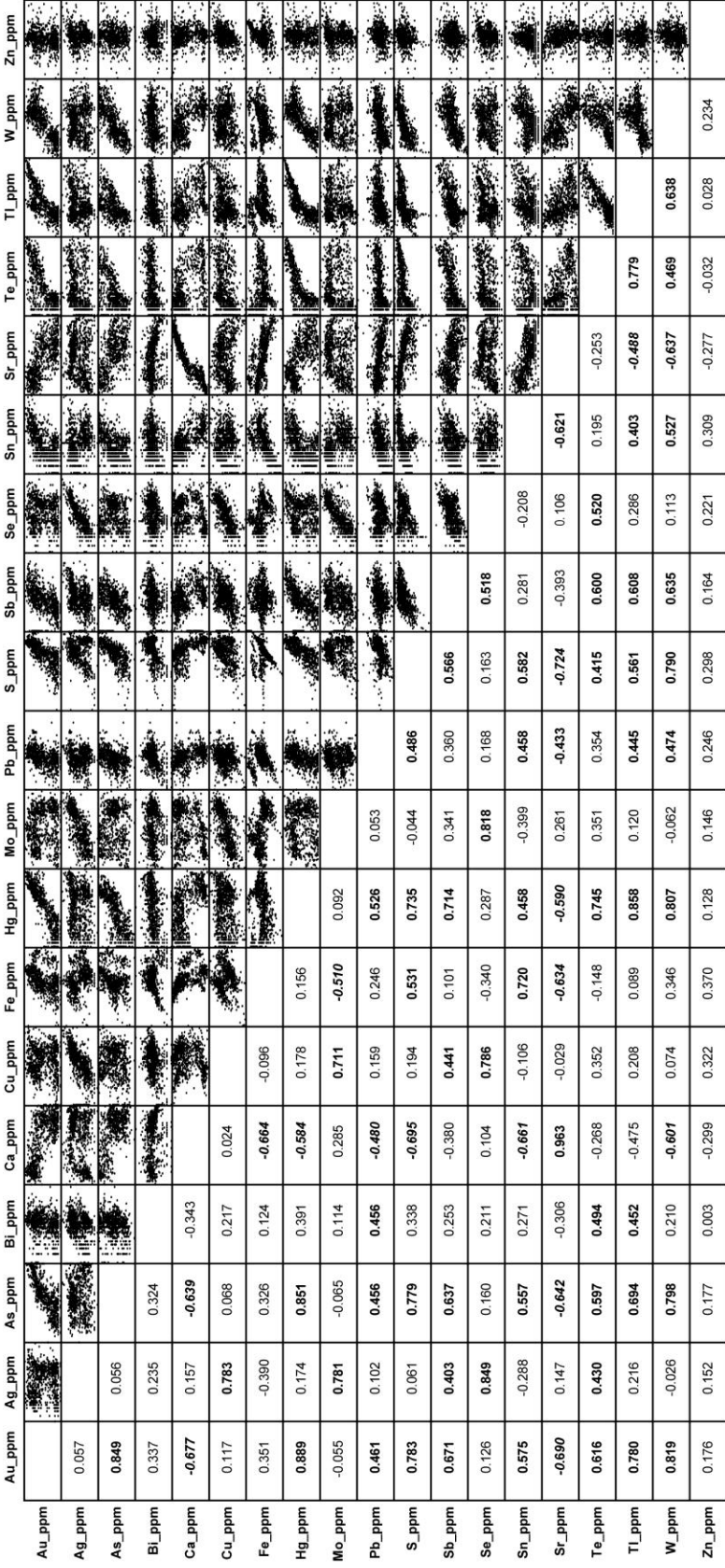


Figure 1.9. Correlation matrix of 18 selected trace elements based on analyses of ≤ 1.5 m drill hole intervals from the five underground drill holes. Shows Spearman rank correlation coefficients and accompanying scatter plots. Correlation coefficients that are >0.4 and <-0.4 are in bold and bold italics, respectively.

(0.922), Hg (0.906), As (0.879), W (0.864), S (0.813), Tl (0.734), Sb (0.712), Te (0.646), In (0.619), Sn (0.590), and Pb (0.507), an elemental suite similar to the one determined by the correlation coefficients. Conversely, negative loadings for Factor 2 include Mg (-0.844), Ca (-0.823), Sr (-0.796), and Mn (-0.791), again a suite similar to the one determined by the correlation coefficients. The five other factors all have very low loadings for Au. Factor 3 explains nearly 18% of the variance. The elements with high loadings in Factor 3 are Co, Fe, Ge, Ga, Sc, Y, Al, Ta, V, In, Ti, Li, Zn, Sn, Be, and Ni. These elements are interpreted to represent an igneous rock signature, including both the mafic Cambrian-Ordovician basalts and the felsic Cretaceous granitic intrusions. Elements with high loadings for Factor 4 include Re, P, Mo, Cu, Ag, Se, Cd, Hf, Zr, U, Nb, V, and Sb. This elemental association, which explains nearly 17% of the variance, is interpreted to represent a black shale or basinal fluid flow signature that formed prior to ore formation. A similar signature has been documented at Jerritt Canyon (Hofstra, 1994, Patterson, 2009) and other CTGDs (cf. Sha, 1993; Emsbo et al., 1999). Factor 1 explains 8% of the variance and elements and has significant loadings for K, Cs, Rb, Bi, Ba, Te, and Tl. This elemental association might be related to mineralization associated with the Osgood stock. The remaining Factors 5 and 6 do not contain high factor loadings for any of the elements and are considered to be geologically insignificant.

Table 1.1. Results of Factor Analysis showing Loadings for 6 Factors

	Factor 1	Factor 2	Factor 3	Factor 4	Factor 5	Factor 6
Ag	0.047	0.086	-0.227	0.848	0.148	-0.013
Al	0.326	-0.455	0.663	-0.280	-0.259	-0.188
As	0.106	0.879	-0.003	-0.040	-0.018	0.051
Au	0.095	0.922	-0.017	-0.026	0.034	0.068
B	0.331	0.066	-0.114	-0.252	-0.182	0.400
Ba	0.461	-0.669	-0.150	0.127	0.073	-0.092
Be	0.312	-0.113	0.477	-0.422	-0.478	0.168
Bi	0.556	0.296	-0.121	0.194	-0.279	0.059
Ca	-0.036	-0.823	-0.248	0.241	0.138	0.331
Cd	-0.020	-0.017	-0.390	0.819	0.051	0.142
Cd	0.052	0.195	0.035	-0.376	-0.807	-0.008
Co	0.050	0.206	0.904	-0.258	0.011	-0.005
Cr	0.349	-0.263	0.140	0.104	-0.605	0.012
Cs	0.750	0.098	0.307	-0.269	-0.154	0.149
Cu	0.034	0.194	0.128	0.865	0.098	0.026
Fe	0.059	0.355	0.863	-0.185	0.072	-0.032
Ga	0.242	-0.267	0.811	-0.270	-0.199	-0.209
Ge	0.032	0.152	0.853	-0.120	-0.100	-0.142
Hf	0.075	-0.178	0.085	0.676	-0.425	-0.339
Hg	0.098	0.906	-0.231	0.084	-0.018	0.157
In	0.226	0.619	0.610	-0.029	0.083	0.042
K	0.773	-0.208	0.002	-0.157	-0.478	-0.045
La	0.070	0.178	-0.097	-0.328	-0.834	0.014
Li	0.146	-0.388	0.557	-0.332	-0.466	-0.106
Mg	0.274	-0.844	0.243	-0.154	0.053	0.144
Mn	0.031	-0.791	0.003	0.141	0.341	0.291
Mo	-0.102	-0.015	-0.315	0.866	0.053	0.036
Na	0.392	-0.601	0.278	-0.121	0.091	-0.231
Nb	-0.037	-0.285	0.120	0.449	0.140	-0.292
Ni	0.184	0.346	0.410	0.258	-0.552	0.227
P	-0.203	-0.079	-0.074	0.866	0.126	-0.127
Pb	0.237	0.508	0.053	0.159	-0.481	0.111
Rb	0.738	-0.164	0.109	-0.164	-0.531	-0.053
Re	-0.151	0.046	-0.155	0.893	0.132	0.029
S	-0.129	0.813	0.165	0.187	-0.081	0.097
Sb	0.033	0.712	-0.077	0.404	0.254	0.111
Sc	-0.006	-0.274	0.756	-0.373	0.037	0.292
Se	0.019	0.200	-0.177	0.846	0.111	0.105
Sn	0.325	0.590	0.526	-0.149	-0.152	0.002
Sr	-0.001	-0.796	-0.332	0.151	0.101	0.308
Ta	-0.214	-0.047	0.651	-0.018	0.345	-0.146
Te	0.456	0.646	-0.345	0.242	0.152	0.085
Th	0.319	0.225	-0.325	-0.198	-0.786	0.078
Ti	0.223	-0.646	0.604	-0.117	0.124	-0.268
Tl	0.449	0.734	-0.237	0.149	0.085	-0.009
U	0.021	0.066	-0.587	0.539	-0.463	0.050
V	-0.106	-0.535	0.630	0.431	0.173	-0.048
W	-0.096	0.864	0.057	-0.021	0.001	0.181
Y	-0.339	-0.287	0.745	0.005	0.022	0.119
Zn	-0.055	0.218	0.537	0.361	-0.151	0.206
Zr	0.067	-0.042	-0.052	0.611	-0.553	-0.335
%Var	8.08	23.53	17.57	16.82	10.52	2.88

Loadings that are >0.4 are shown in bold typeface. Var=variance.

Distribution of Ore-Related Trace Elements

The Barrick and Placer Dome data sets were utilized to investigate the distribution of ore-related trace elements relative to Au assays and visible alteration. The study focused on Hg, Sb, As, Te, and Tl, which were the main elements related to gold deposition as determined by correlation coefficients and factor analyses (i.e., Factor 2) presented above. These five trace elements are commonly present in ore-stage, Au-bearing arsenian pyrites from the Getchell and Turquoise Ridge deposits, based on electron probe microanalyses (Cline, 2001; Longo et al., 2009) and, therefore, their distribution is interpreted to be the result of the Eocene Au-mineralization event. The values of these elements were plotted down the drill holes using Target and were compared to estimated background values (Table 1.2). Histograms of individual elements were used to locate breaks in the data distribution in order to classify the values for contouring. The values of Hg, Sb, and As, from the Placer Dome surface holes and the Barrick underground holes were hand-contoured (Fig. 1.10), whereas Te and Tl from only the underground holes were plotted (Fig. 1.11).

The spatial distribution of Hg is similar to that of Au (Fig. 1.10A). The 1 ppm Hg contour closely mimics the 0.34 ppm Au contour on the cross-section, and the 10 ppm Hg contour is very similar to the 3.4 ppm Au contour. Zones of >100 ppm Hg are almost entirely limited to within the 17 ppm Au contour. Overall Hg is concentrated in the zone of antithetic faults between the Getchell fault and the HGB ore zone. Within the Getchell Fault Zone, Hg values ≥ 1 ppm are limited to narrow intercepts that are 3-12 meters thick. Elevated Hg values above the inferred background average (>0.04 ppm,

Table 1.2) extend no more than 10 m beyond visibly altered wall rocks and the ≥ 0.34 ppm Au contour based on the underground holes. However, understanding of the overall pattern of < 1 ppm Hg, especially above the HGB, is hampered by a 1 ppm detection limit for the Hg analyses in the Placer Dome surface holes.

Antimony values are consistently above inferred background of 0.5 ppm (Table 1.2) in all of the holes (Fig. 10B). Antimony values ≥ 5 ppm commonly form haloes up to 12 m beyond the ≥ 0.34 ppm Au contour throughout the Getchell Fault Zone, the zone of antithetic faults zone below the HGB ore zone, and in the deformed brown mudstones and limestones adjacent to the NPB above the HGB. The 25 ppm Sb contour mimics fairly closely the 3.4 ppm Au contour. The largest zone of ≥ 25 ppm Sb occurs in the lower parts of the HGB in the footwall of the main dacite dike in the zone of antithetic faults.

Arsenic forms a slightly larger, more continuous halo around Au mineralization than Hg or Sb (Fig. 1.10C). Arsenic values of ≥ 100 ppm are broadly coincident with visibly altered rocks within the Getchell Fault Zone but extend beyond visible alteration and the 0.34 ppm Au contour in the antithetic fracture zone, forming a wide zone of ≥ 100 ppm As below the HGB. Persistent As values of ≥ 100 ppm extend up to 30 m beyond visible alteration and the 0.34 ppm Au contour along the thrust faults adjacent to the northern pillow basalt. The 1000 ppm As contour is broadly coincident with the 3.4 ppm Au contour.

The distribution of anomalous Tl, based on the five underground holes, is similar to Au (Fig. 1.11A). Tl values of > 5 ppm are mostly restricted to zones of ≥ 3.4 ppm

Table 1.2. Background Multi-Element Geochemistry

Sample ID	Easting SP_NV W	Northing SP_NV W	Au ppb	Ag ppm	As ppm	Bi ppm	Ca %	Cu ppm	Fe %	Hg ppm	Mo ppm	Pb ppm	S wt%	Sb ppm	Se ppm	Sn ppm	Sr ppm	Te ppm	Tl ppm	W ppm	Zn ppm
GETBGLS1	856455	2355218	2.5	0.07	2.5	0.02	33.2	14.7	0.12	0.01	0.34	2.8	0.03	0.2	3	0.1	1380	0.03	0.08	0.4	53
GETBGLS2	857155	2363985	2.5	0.03	2.5	0.04	28.0	3.1	0.8	0.01	0.11	6.7	0.01	0.37	4	0.6	1020	0.14	0.1	0.5	24
GETBGLS3	855334	2364633	2.5	0.11	7	0.01	33.4	10	0.21	0.1	0.39	13.9	0.01	0.66	4	0.1	239	0.05	0.11	0.2	20
00NM164_1355	862223	2368222	2.5	0.11	2.5	0.23	17.3	30.8	2.8	0.01	0.27	7.1	0.43	1.1	3	1.6	889	0.06	0.4	1.5	74
00MM202_1839	862019	2360294	2.5	0.59	5	5.75	15.8	85.3	2.93	0.07	6.49	20.6	1.32	0.7	4	4.7	201	0.27	0.03	7.9	1860
00NM138_3384	870149	2366474	2.5	0.04	23	0.17	20.0	14.9	1.94	0.01	0.34	9.4	0.08	0.74	3	1.3	863	0.05	0.27	1.7	50
00NM138_5016.5	870124	2366231	2.5	0.15	14	0.25	10.8	56.9	6.61	0.01	1.63	19	0.66	1.15	3	2.2	102	0.03	0.54	1.3	129
00NM162A_2664.5	861522	2363804	2.5	0.07	2.5	0.16	26.7	14.8	1.84	0.01	0.67	1.8	0.51	0.12	4	0.4	418	0.12	0.1	0.5	36
00MW153_2748.5	875720	2368837	2.5	0.15	10	0.02	25.3	6.4	0.9	0.07	1.27	4.9	0.46	0.58	3	0.1	373	0.1	0.08	0.1	22
00MW161A_3753	877477	2368150	2.5	0.03	2.5	0.09	25.6	3	0.26	0.03	0.31	2.2	0.22	0.19	3	0.1	953	0.12	0.01	0.2	7
00MW140_3407.5	878380	2363408	2.5	0.01	2.5	0.13	18.9	14.3	2.04	0.01	0.16	7.3	0.05	0.11	2	1.2	665	0.08	0.35	0.6	45
00MW161A_3838	877476	2368143	2.5	0.05	6	0.01	23.4	2.8	0.55	0.03	0.35	2	0.13	0.25	3	0.1	881	0.06	0.02	0.2	4
GB4	848557	2289650	2.5	0.1	21	0.04	25.0	11	0.41	0.17	2.08	3.1	0.05	0.73	1.1	0.1	682	0.04	0.04	3.8	30
GB5	828917	2269722	7	0.08	11.0	0.01	25.0	2.10	0.25	0.07	1.38	1.10	0.02	0.18	0.90	0.10	903	0.03	0.01	1.89	17
Average			2.8	0.11	8	0.50	23.45	19.29	1.55	0.04	1.13	7.3	0.28	0.51	3	0.9	684	0.08	0.15	1.5	169

Coordinates are Nevada State Plane West, NAD27. Analyses are from samples collected from 8 core holes and 5 surface sites located at least 600 m from known mineralization. All of the drill core samples came from intervals that assayed <10 ppb Au for several tens of meters below and above. Analyses that were less than the detection limit for a given element were converted to half the detection limit.

Au in the central core of the HGB ore zone. In the upper parts of the HGB, within the deformed mudstones and limestones adjacent to the NPB, Tl values are mainly <2 ppm even in zones of >3.4 ppm Au. Tl values of >0.5 ppm, which is greater than the inferred background of 0.15 ppm (Table 1.2), commonly extend up to about 10 m beyond visible alteration and the >0.34 ppm Au contour. The Tl values in the Getchell Fault Zone are mainly <0.5 ppm.

The distribution of anomalous Te, based on the five underground drill holes, is more restricted than Au (Fig. 1.11B). Tellurium values of >1 ppm are almost entirely confined to the central core of the HGB ore zone. In the upper parts of the HGB, Te values decrease to mostly <0.1 ppm, which is near the inferred background (0.08 ppm, Table 2), even in areas of ≥ 3.4 ppm Au. Te values are fairly consistently ≥ 0.1 ppm in the zone of antithetic fracture zones just below the HGB; however, the values are mainly <0.1 ppm in the Getchell Fault Zone.

Factor scores for Factor 2 (the Au factor discussed above, Table 1.1) were calculated for each sample from the underground data set by summing the products of the concentration and Factor 2 loading for each element. The scores for each sample were then plotted on the cross-section (Fig. 1.11C). Plotting gold factor scores on cross-sections or on maps enables one to seek out zones of high statistical association between Au-related trace elements, even in the absence of high Au values. For example, if As, Hg, Sb, Tl, and Te values are high in a given area where Au values are low, high Au factor scores may still be present. Figure 1.11C shows high Factor 2 scores (≥ 0.8) strongly correlate spatially with the ≥ 3.4 ppm Au contour. Unfortunately, the

factors scores outside the ≥ 3.4 ppm Au contour do not show a consistent pattern.

Likewise, Factor 2 scores of < 0.8 do not show any pattern in relation to either altered or unaltered rock.

Figure 1.10.

A. Spatial distribution of Hg in relation to the ≥ 0.34 ppm Au contour. Note the high detection limits for Hg (< 1 ppm Hg, plotted as 0.5 ppm) for the Placer Dome data in the surface holes, which limited understanding of the Hg halo above the HGB.

B. Spatial distribution of Sb in relation of the ≥ 0.34 ppm Au contour and visible alteration.

C. Spatial distribution of As in relation of the ≥ 0.34 ppm Au contour and visible alteration. Points represent individual analyses. Detailed discussion of patterns is in text.

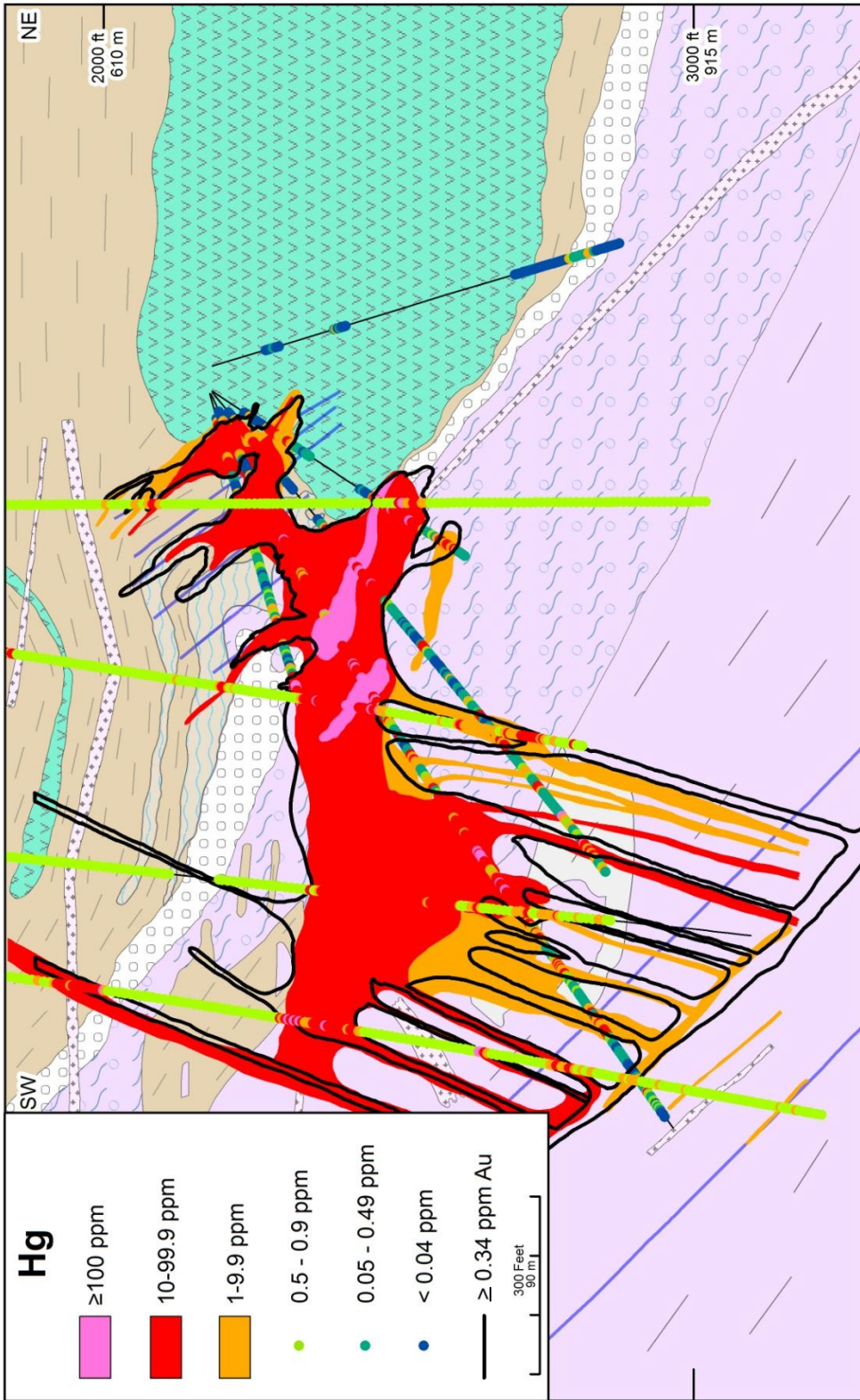


Figure 1.10A

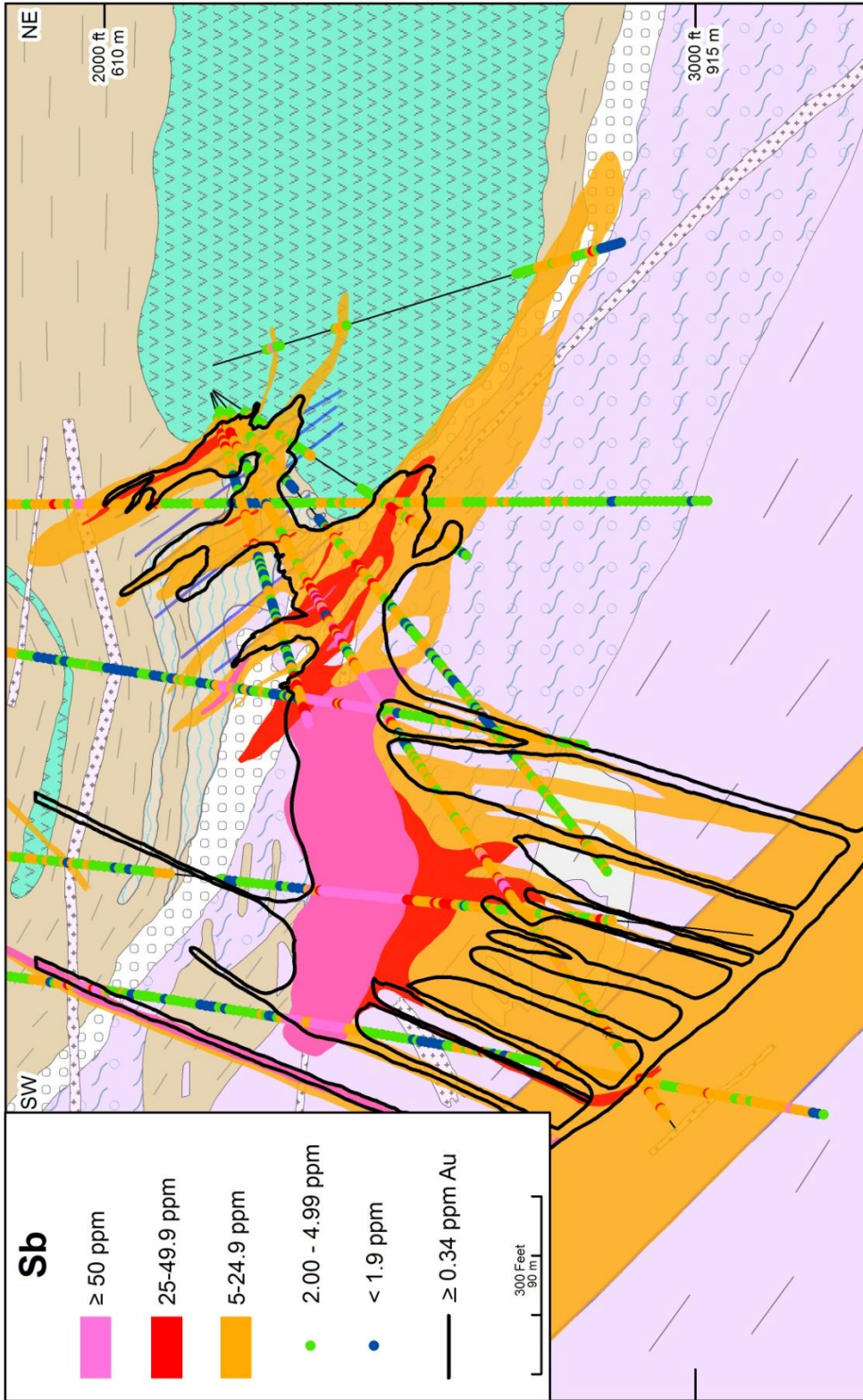


Figure 1.10B

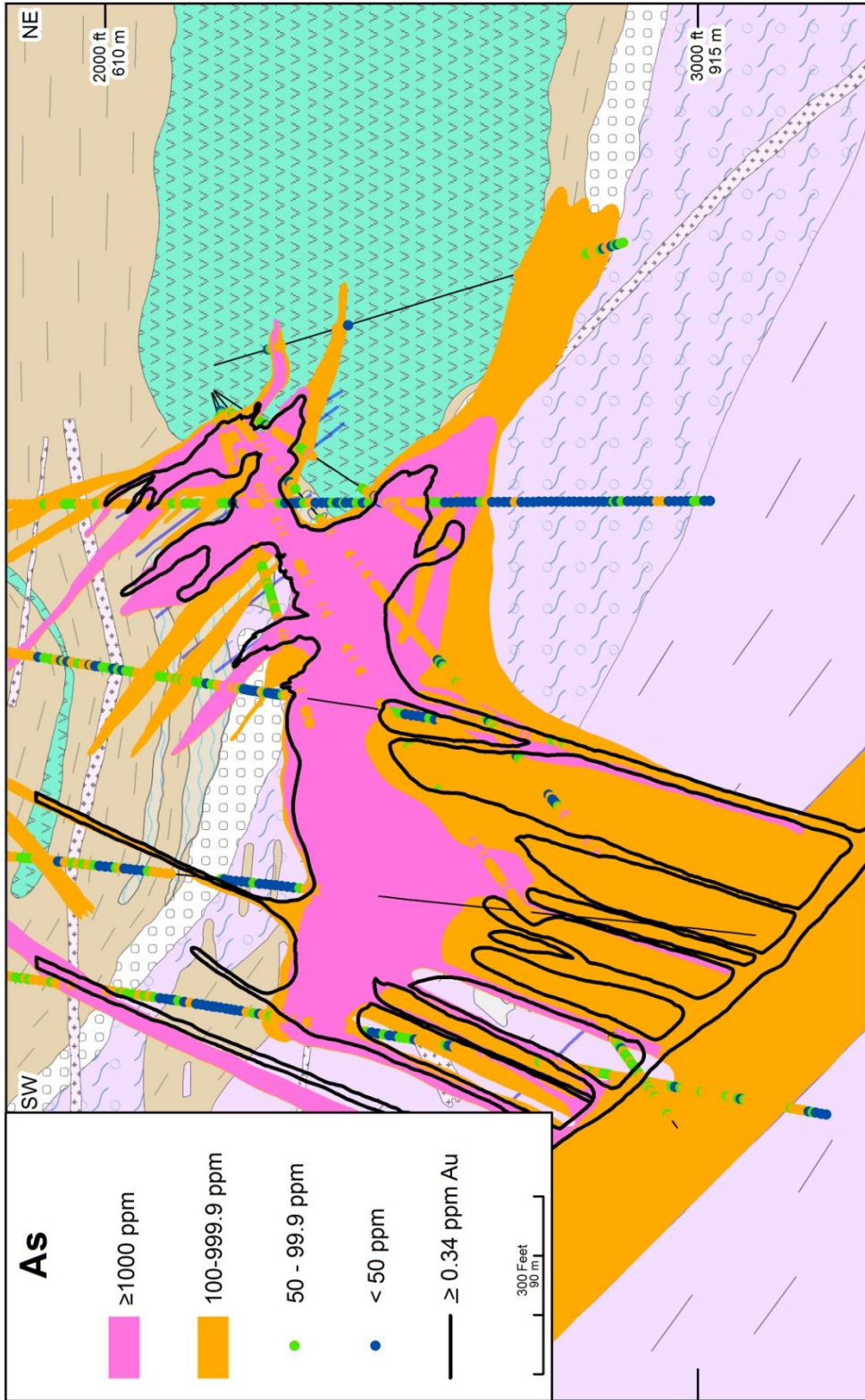


Figure 1.10C

Figure 1.11.

A. Spatial distribution of TI relative to visible alteration and the ≥ 0.34 ppm Au contour in the five underground holes. Points represent individual analyses. Detailed discussion of patterns is in text.

B. Spatial distribution of Te relative to visible alteration and the ≥ 0.34 ppm Au contour in the five underground holes. Points represent individual analyses. Detailed discussion of patterns is in text.

C. Spatial distribution of Au-factor scores relative to visible alteration and the ≥ 0.34 ppm Au contour in the five underground holes. Points represent individual analyses. Detailed discussion of patterns is in text.

D. Spatial distribution of DOS, relative to visible alteration and the ≥ 0.34 ppm Au contour in the five underground holes. Points represent individual analyses. Detailed discussion of patterns is in text.

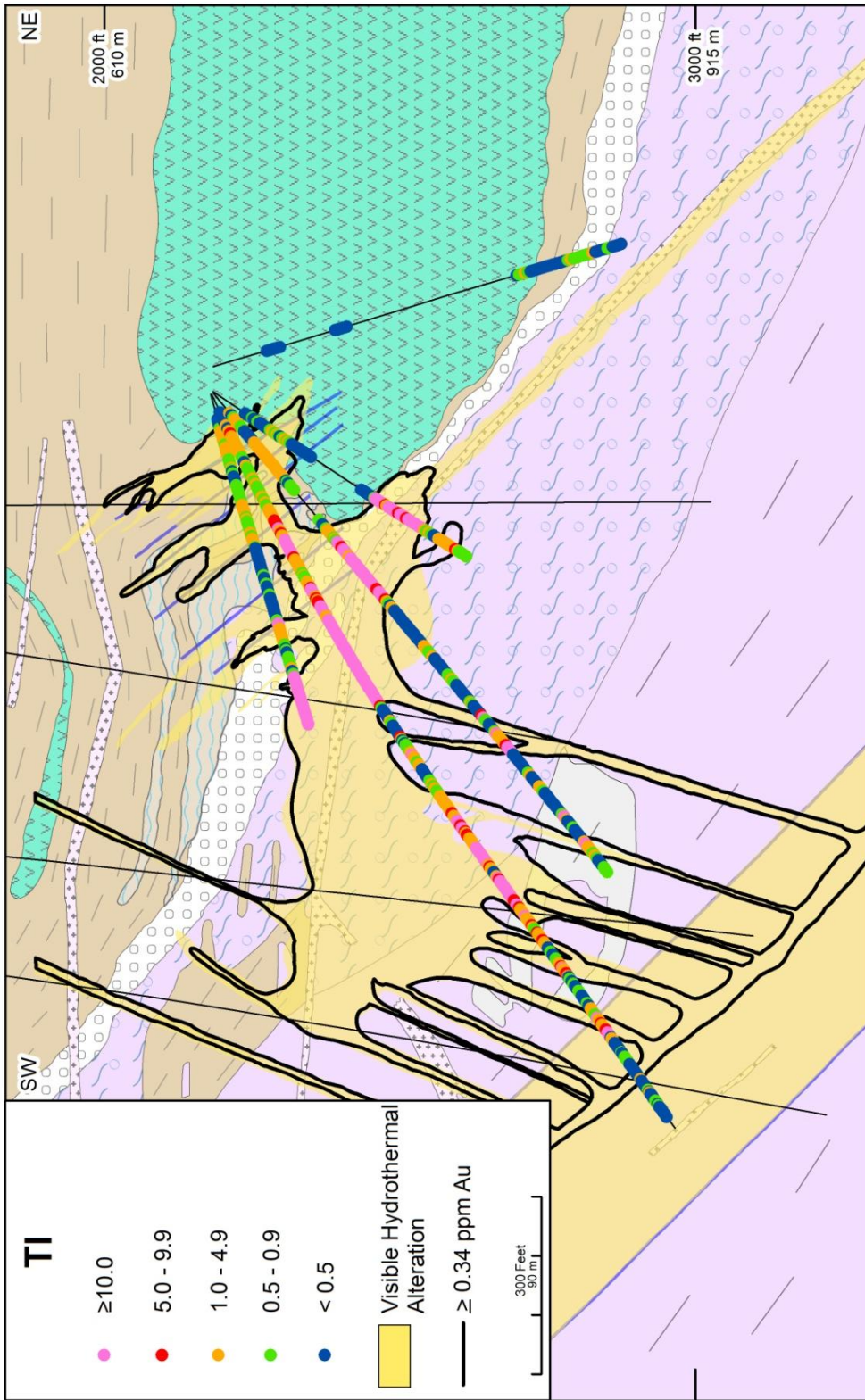


Figure 1.11A

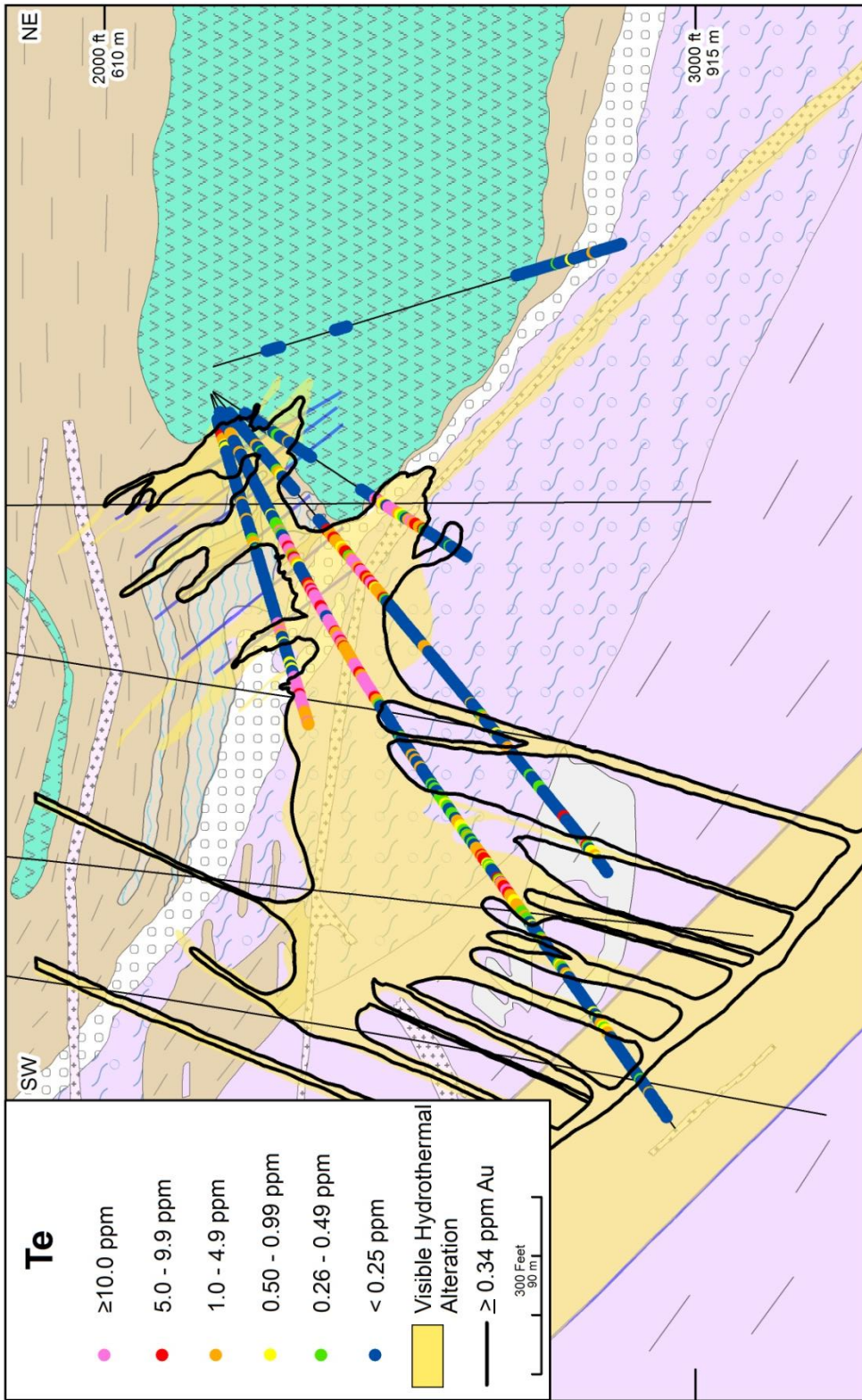


Figure 1.11B

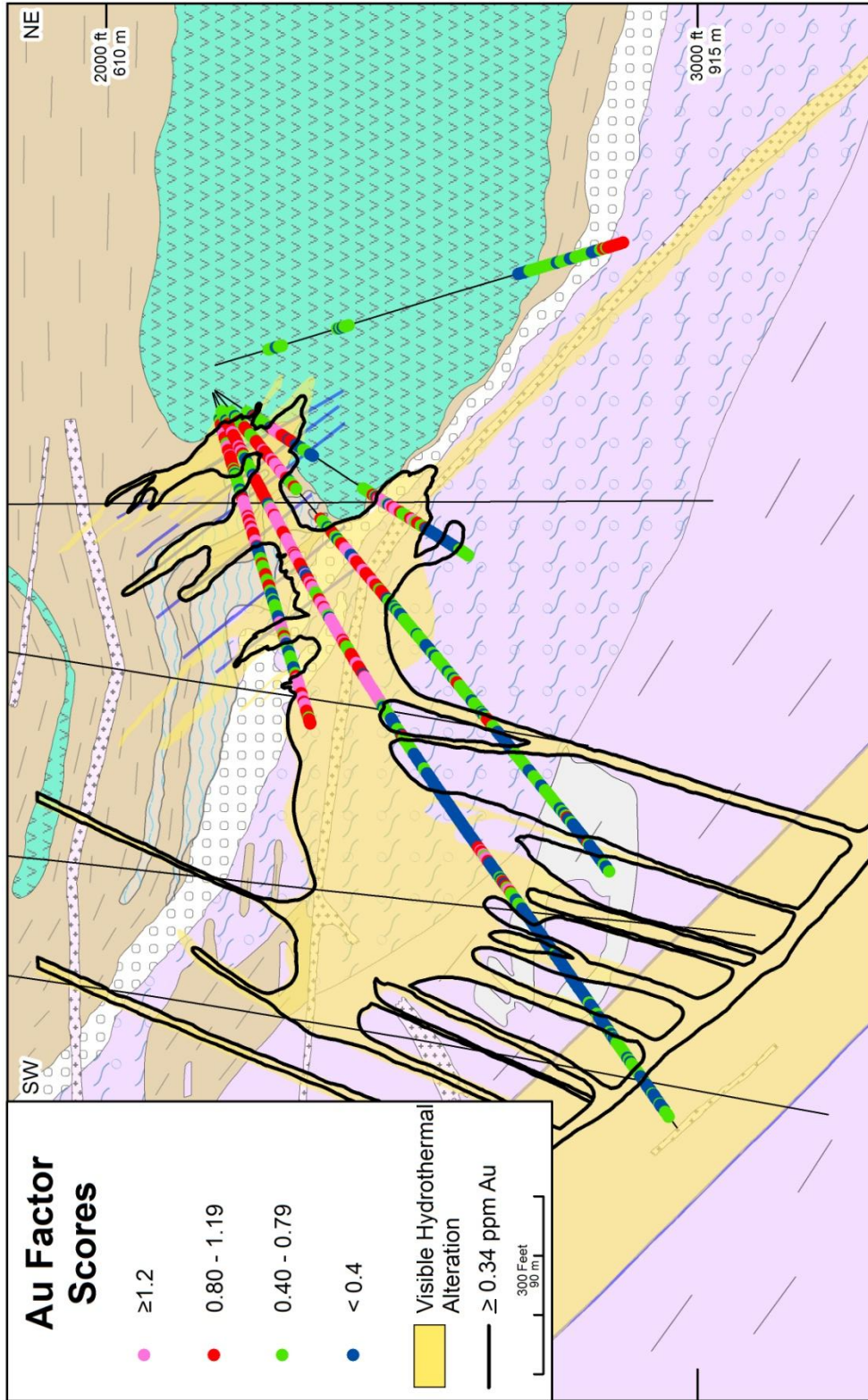


Figure 1.11C

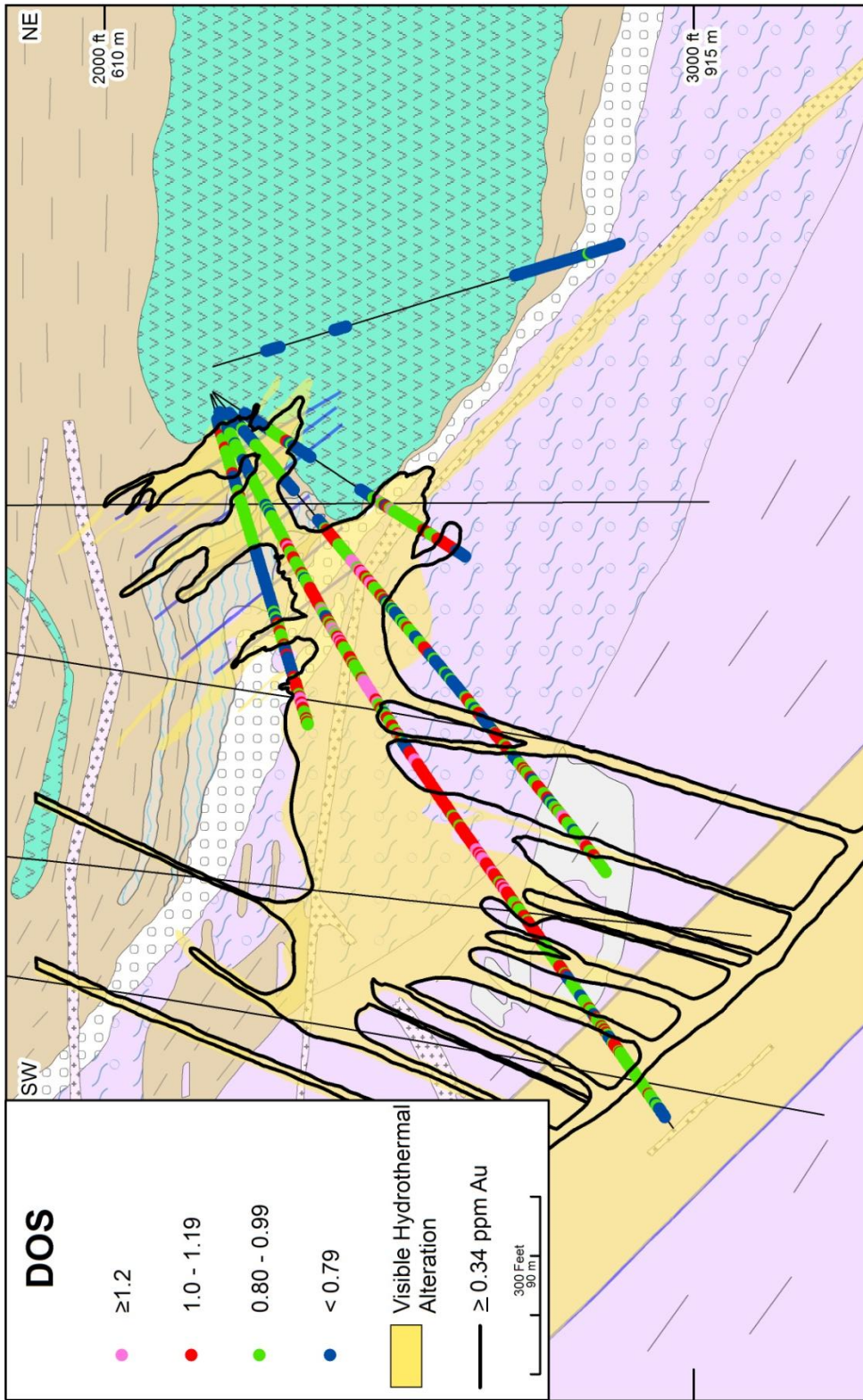


Figure 1.11D

Sulfidation

Gold primarily resides in trace element-rich arsenian pyrite, arsenian marcasite, or arsenopyrite in most CTGDs (cf. Hofstra and Cline, 2000). The gold-bearing pyrite at the Getchell and Turquoise Ridge deposits occurs as micron-sized, fuzzy, spheroidal grains or as micron-sized rims on trace element-poor, pre-ore pyrite (Cline, 2001; Longo et al., 2009). Based on electron microprobe analyses, the trace elements enriched in this ore-stage pyrite include Au, As, Hg, Sb, Tl \pm Te \pm Cu (Cline et al., 2005; Longo et al., 2009). Thus, the amount of this ore-stage pyrite is potentially the only direct, visible indicator of ore in CTGDs. When abundant, hand samples containing this ore-stage pyrite has a sooty appearance under a hand lens. However, if not abundant, the ore-stage pyrite can be very difficult to recognize and differentiate from pre-ore pyrite. Though attempted, the presence and abundance of ore-stage sooty pyrite could not be consistently logged during this study; therefore, its distribution around the HGB ore zone is not understood.

Sulfidation has been argued to be the primary Au-deposition process associated with CTGDs, based on litho-geochemical data indicating S, rather than S and Fe, is added to the rock (Hofstra et al., 1991; Stenger et al., 1998). Loss of S from the hydrothermal fluid would destabilize aqueous gold-sulfide complexes in the hydrothermal fluid, resulting in the gold deposition (Hofstra et al., 1991; Simon et al., 1999). Geochemical reaction path modeling has shown that sulfidation of host-rock iron can account for the gold content of pyrite and the ore grades observed in Carlin-type deposits (Hofstra et al., 1991). These geochemical models provide evidence that narrow high-grade ore

zones result from host rocks containing higher initial reactive Fe contents (e.g., Fe within the carbonate crystal lattice).

Given the importance of ore-stage pyrite, the difficulty in systematically mapping its distribution, and the likelihood that it is the result of sulfur addition to the host rocks, multi-element data from the five underground holes were used to calculate degree of sulfidation (DOS) to see whether it forms systematic patterns around the HGB.

$$(1) \quad \text{DOS} = \text{wt\% S} / [(1.15) (\text{wt\% Fe})]$$

The coefficient 1.15 is the Fe/S mass ratio in pyrite; thus, in the DOS notations, S contents are normalized to the amount of S necessary to convert all Fe in the rock to pyrite. Iron and S values from the five underground drill holes were analyzed utilizing a nitric aqua regia digestion followed by ICP-MS-AES. The ICP-MS-AES analyses were collected from 6m before and after visible hydrothermal alteration, whereas Leco total sulfur analyses were restricted to ore zones. Therefore, in order to verify the accuracy of the S analyses in both mineralized (≥ 0.1 ppm) and barren (< 0.01 ppm) samples, ICP-MS-AES samples were compared with Leco total sulfur analyses. [Figure 1.12](#) shows excellent correlation between the Leco and ICP-MS-AES sulfur analyses, lending confidence in the reliability of the ICP-MS-AES S values. It is important to note that sulfates are uncommon at Turquoise Ridge and, therefore, the S values are reflecting sulfides. Though realgar is locally abundant in the five underground holes, pyrite is the predominant sulfide.

Figure 1.11D shows the spatial distribution of DOS values relative to the 0.34 ppm Au contour and zones of visible alteration. DOS values ≥ 0.8 show little to no halo beyond the 0.34 ppm Au contour and visibly altered wall rock in the upper parts of the HGB. Rather, pervasive ≥ 0.8 DOS values extend below the HGB in the zone of antithetic faults, with little to no change between visibly altered and unaltered rocks. DOS values of ≥ 1.2 are almost entirely restricted to zones of ≥ 3.4 ppm Au.

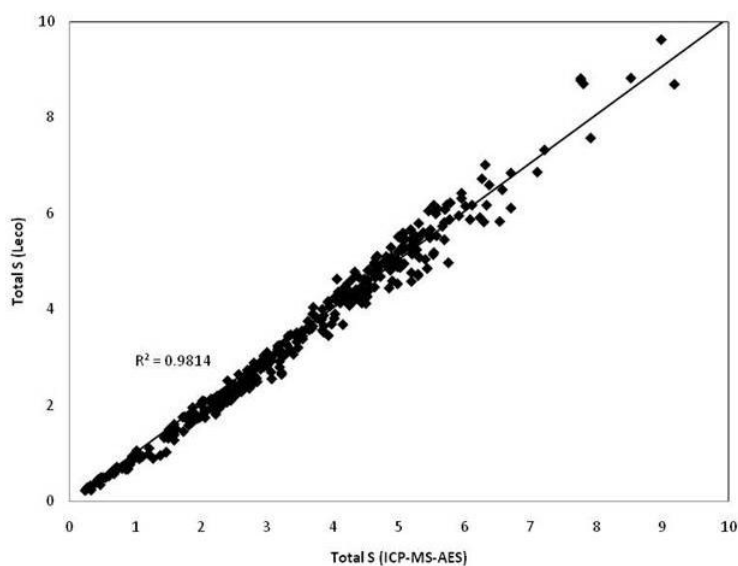


Figure 1.12. Plot of total wt% S determined by Leico versus wt% S determined by ICP-MS-AES. Note the strong positive correlation.

As was done by Stenger et al. (1998) for Twin Creeks, S values were plotted against the Fe values from the five underground holes to evaluate whether S and Fe or just S was introduced into the host rocks at Turquoise Ridge during mineralization (Fig. 1.13). The line in Figure 1.13 marks the relative concentrations of S and Fe in pyrite [$S = 1.15 * \text{wt\% Fe}$]. The black arrows in Figure 1.13 represent trends in the data that would

reflect either sulfidation or pyritization. Rocks undergoing sulfidation should show vertical trends toward the pyrite line. Complete sulfidation to form pyrite would occur at S contents along the pyrite line for each individual sample. Rocks undergoing pyritization should show trends with a positive slope, indicating addition of both Fe and S. Data along the pyrite line indicates all the Fe in a given sample is now in the form of pyrite. Excess S in the samples above the pyrite line in [Figure 1.13](#) is likely caused by other sulfides, such as orpiment and realgar.

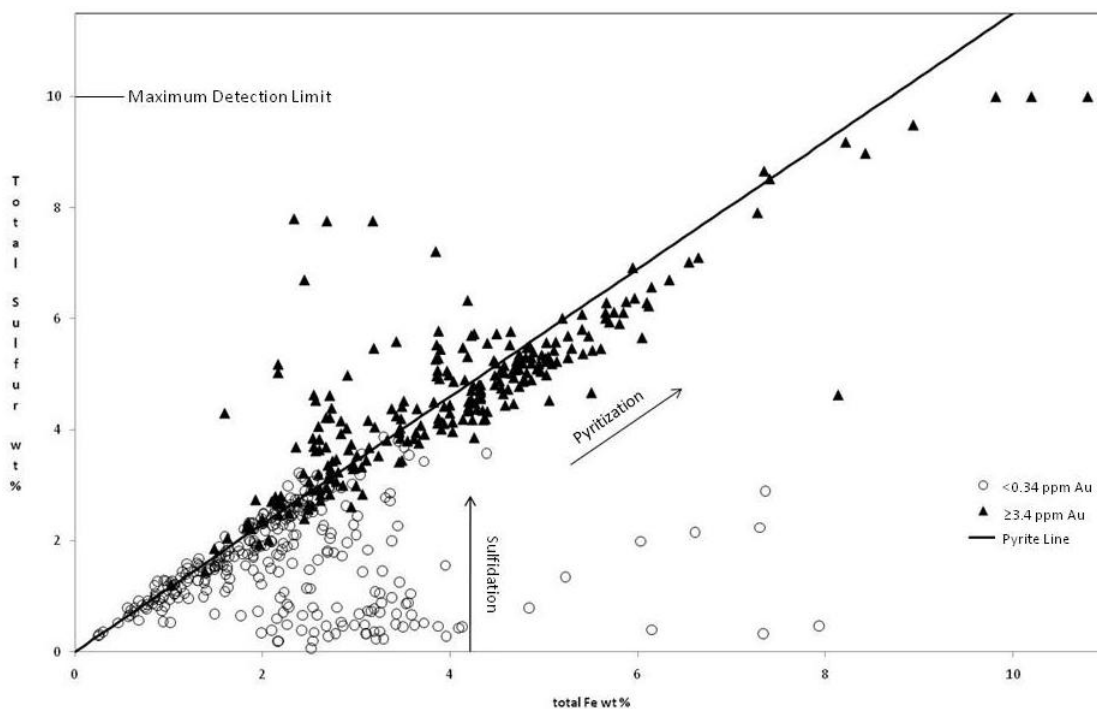


Figure 1.13. Plot of wt% S versus wt% Fe analyses from the five underground drill holes (derived from Stenger et al., 1998). Only drill intervals that contained limestone and had Au grades ≥ 3.4 ppm or < 0.34 ppm are plotted. The line represents the ratio of S and Fe in pyrite. Samples that plot below the line indicate not all of the Fe in those samples has been sulfidized to form pyrite. Note that samples with grades between 0.34 and 3.4 ppm Au, which are not shown, would plot primarily on the pyrite line and significantly overlap with the samples with ≥ 3.4 ppm Au. Arrows depict the direction of compositional change related to sulfidation (vertical arrow) and pyritization (diagonal arrow).

As seen in [Figure 1.13](#), samples with < 0.34 ppm Au contain lower S, but not necessarily lower Fe, than samples with ≥ 3.4 ppm Au. This suggests sulfidation; however, it remains

uncertain if the ≥ 3.4 ppm Au samples contained similar initial Fe and S values as the < 0.34 ppm Au samples. Therefore, we cannot definitively distinguish between pyritization and sulfidation. The few samples with ≥ 3.4 ppm Au that contain > 4 wt% S and > 8 wt% Fe suggest pyritization, because there are no corresponding < 0.34 ppm Au samples with similar high Fe values, but with lower S values.

Decalcification

Dissolution and silicification of carbonate, as described above, is the most common alteration feature at the Turquoise Ridge deposit. Carbonate-bearing host rocks throughout the deposit contain abundant calcite, while pre-ore dolomite is only locally present in minor amounts. The zones of alteration shown in [Figure 1.8A](#) are where visible alteration could be correlated between drill holes. Though rocks outside the alteration zones on [Figure 1.8A](#) are mostly visibly unaltered, there are zones of visible alteration that are too narrow to correlate between holes. As has been noted, the multi-element data show that Ca negatively correlates with Au, which is to be expected if decalcification is the major alteration type associated with gold mineralization. Therefore, mapping the distribution of Ca might show an increasing number of narrow alteration zones toward the larger zones of visible alteration shown in [Figure 1.8A](#). Hence, point maps were constructed from the five underground drill holes in order to compare the spatial distribution of Ca, Ca/Au, and Ca/Au factor score relative to visible alteration and the 0.34 ppm Au contour ([Figure 1.14A-C](#)).

Unfortunately, the distribution of Ca does not show an obvious halo of progressively decalcified rock beyond visible alteration and the > 0.34 ppm Au contour

(Fig. 1.14A). In general, Ca values <0.5% strongly correlate with ≥ 3.4 ppm Au throughout the HGB. Above the HGB zone, Ca values are commonly >10% within meters of visible alteration. The distribution of Ca values below the HGB within the zone of antithetic faults shows highly variable Ca concentrations, ranging from 15% to <1%, within meters of visible alteration and the 0.34 ppm Au contour. The distribution of Ca/Au ratios also shows no obvious halo and strongly mimics the Ca pattern (Fig. 1.14B). The Ca to Au factor score (Factor 2, Table 1) ratio also does not show any obvious halo (Fig. 1.14C).

Figure 1.14.

- A. Spatial distribution of wt% Ca in the five underground holes relative to visible alteration and the ≥ 0.34 ppm Au contour.
- B. Spatial distribution Ca/Au in the five underground holes relative to visible alteration and the ≥ 0.34 ppm Au contour.
- C. Spatial distribution Ca/Au-factor score (scores for Factor 2 in Table 1) in the five underground holes relative to visible alteration and the ≥ 0.34 ppm Au contour.

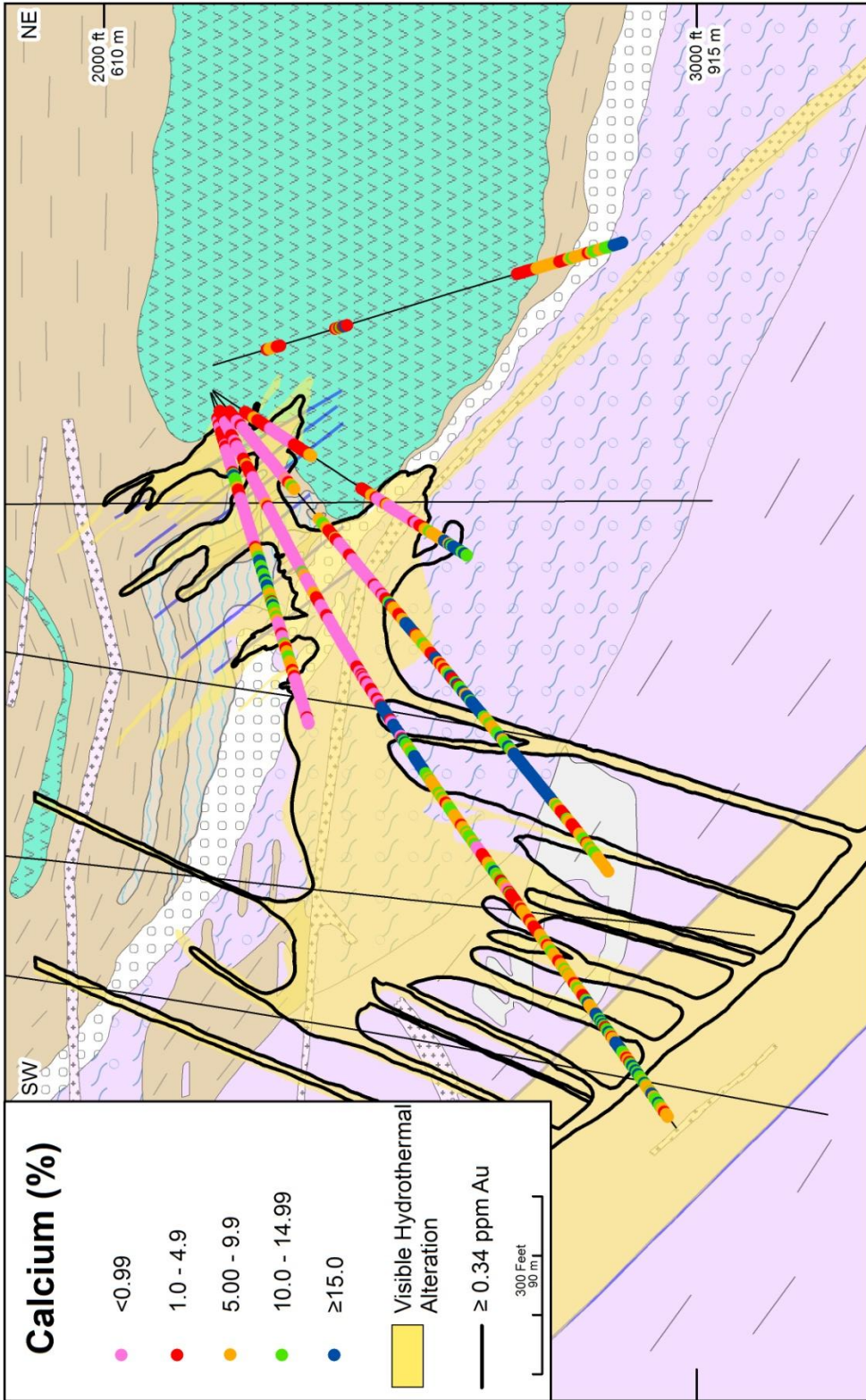


Figure 1.14A

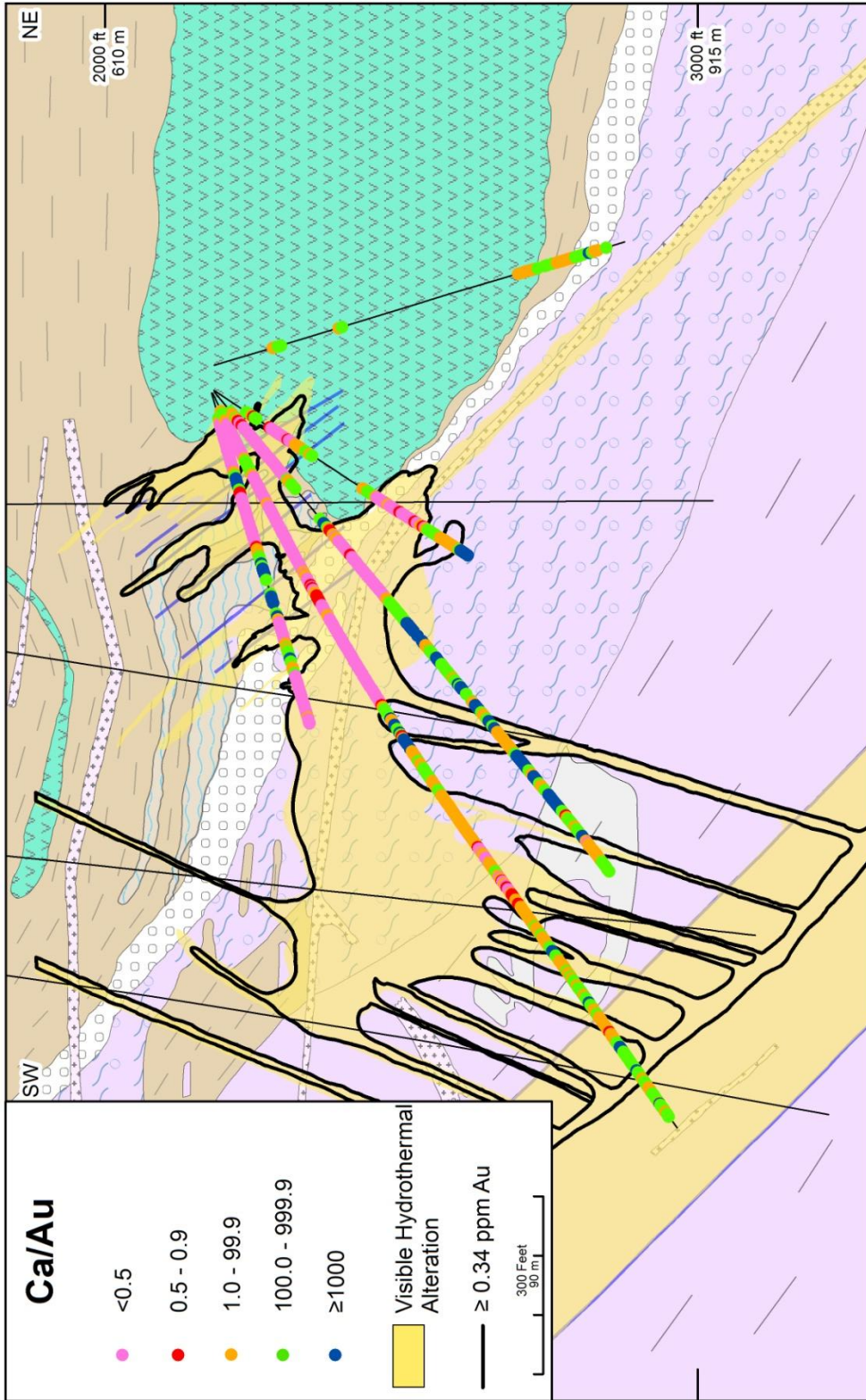


Figure 1.14B

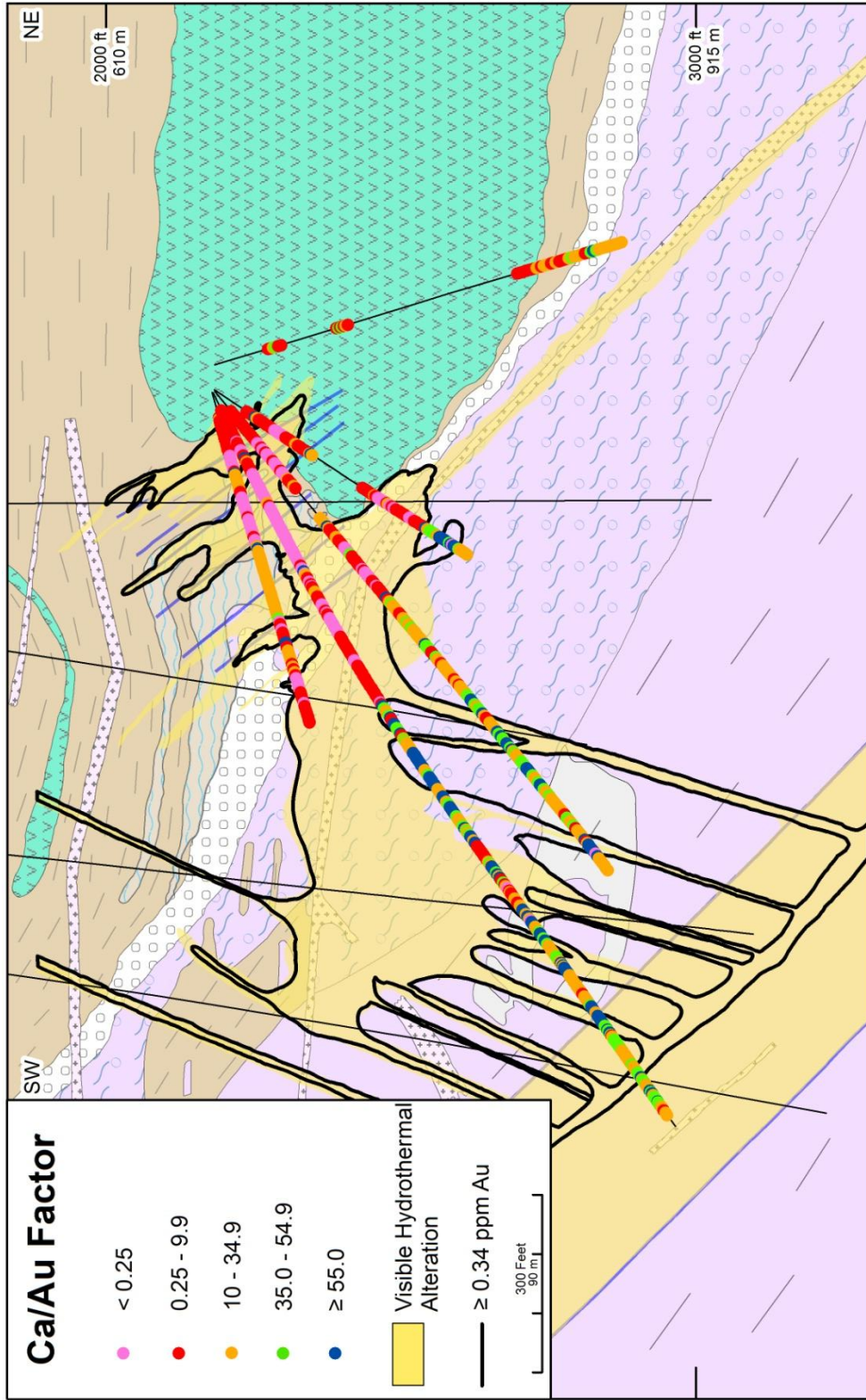


Figure 1.14C

SPECTRAL REFLECTANCE DATA

Spectral reflectance data were collected using an Advanced Spectral Device (ASD) TerraSpec portable reflectance spectrometer to determine whether there were any patterns in clay mineralogy around the HGB ore zone. Minerals with the following radicals, molecules and bonds can be identified with spectral reflectance: OH^- , Al-OH^- , H_2O , SO_4^{2-} , CO_3^{2-} , Fe-OH^- , Mg-OH^- , and NH_4^+ . Therefore, the technique is most widely used to identify clay, sulfate, and carbonate minerals. Portable reflectance spectrometers such as the older PIMA and the newer ASD, are widely used in porphyry and epithermal systems to identify patterns in clay mineralogy around ore (cf. Thompson et al., 1999). Their use in CTGDs has been more limited, mainly because of the commonly dark, carbonaceous nature of the rocks that host CTGDs. Dark rocks reflect very little light back into the spectrometer, resulting in spectra with low signal to noise ratios. Limited published spectral reflectance studies of CTGDs have reported ore associated with illite, kaolinite, and dickite (Hauff et al., 1991; Thompson et al., 1999)

1,065 spectra were collected from the five underground holes and three of the surface holes in the cross-section. Spectra were collected from visibly unaltered wall rocks, variably altered rocks in zones with variable Au grades, and clay-lined fracture surfaces that were present in both visibly altered and unaltered wall rocks. The sampling focused on determining the clay mineral patterns around the ≥ 0.34 ppm Au contour (Figs. 1.15 and 1.16). Spectra were individually interpreted by John Muntean by comparing unknown spectra with library spectra of known minerals using the software packages Specwin and Specmin, developed by Spectral International Inc. The minerals

identified in this study included kaolinite, illite, muscovite, chlorite, montmorillonite, nontronite, beidellite, tremolite/actinolite, biotite, epidote, calcite, and dolomite.

Samples containing spectra lacking interpretable mineralogical features or high background noise were excluded from the data set. Interpretable spectra were mainly limited to clay-lined fracture surfaces and light-colored lithologies that included the upper, less carbonaceous limestone and brown mudstone, basalt, and dacite dikes.

Very few interpretable spectra were collected from dark-colored rocks such as the lower carbonaceous mudstones and limestones and the sedimentary breccias. Therefore most of the interpretable data are in the upper parts of the cross-section (Fig. 1.15).

Ten representative samples from the dataset were analyzed by X-ray diffraction (XRD) to verify the ASD interpretations. The XRD results closely matched the ASD results.

Kaolinite was identified in 157 visibly altered wall rock samples and on 158 bleached fracture surfaces (Fig. 1.15A-B). Many of the altered wall rock samples were from intervals within the HGB that had Au grades >3.4 ppm. The intimate spatial association between hydrothermal alteration, Au mineralization and kaolinite is strong evidence that kaolinite was coeval with ore formation as documented below. Beyond the ≥ 0.34 ppm Au contour, kaolinite-bearing rock samples occur along local, narrow zones of weakly to moderately altered rocks. In addition, kaolinite-bearing fracture surfaces extend up 4 m beyond of visibly altered rock above the HGB, up to 20 m beyond visibly altered rock below the HGB, and for 15 m laterally beyond the extent of visible alteration associated with the zone of antithetic faults.

Illite was detected in 94 visibly altered rock samples and on 79 fracture surfaces (Fig. 1.15C, D). In visibly altered rock samples, illite displays a similar spatial distribution to kaolinite. Visibly altered rock samples containing illite primarily occur with Au grades >3.4 ppm within the HGB and rarely extend beyond the ≥ 0.34 ppm contour. Like kaolinite, illite-bearing fracture surfaces extend up to 4 m beyond visibly altered rocks above the HGB, up to 20 m below the HGB zone, and for 15 m laterally beyond the extent of visible alteration associated with the zone of antithetic faults. The sharpness of the illite features and the wavelength of its main absorption feature were also recorded, and are referred to here as the “2200 feature”. The wavelength of the 2200 feature in the illites ranged from 2198 nm to 2215 nm, with most between 2206 and 2208 nm. Illites with sharper features tended to have 2200 features with shorter wavelengths, mainly 2206 nm and below. However, neither the wavelength of the 2200 feature nor the sharpness of the illite features shows any systematic spatial relationship with respect to gold grade. In addition, no evidence for ammonium was seen in any of the illites.

Figure 1.15.

- A. Spatial distribution of wall rock kaolinite in relation to visible alteration and the ≥ 0.34 ppm Au contour.
- B. Spatial distribution of wall rock illite in relation to visible alteration and the ≥ 0.34 ppm Au contour.
- C. Spatial distribution of kaolinite-bearing fracture surfaces in relation to visible alteration and the ≥ 0.34 ppm Au contour.
- D. Spatial distribution of illite-bearing fractures in relation to visible alteration and the ≥ 0.34 ppm Au contour.

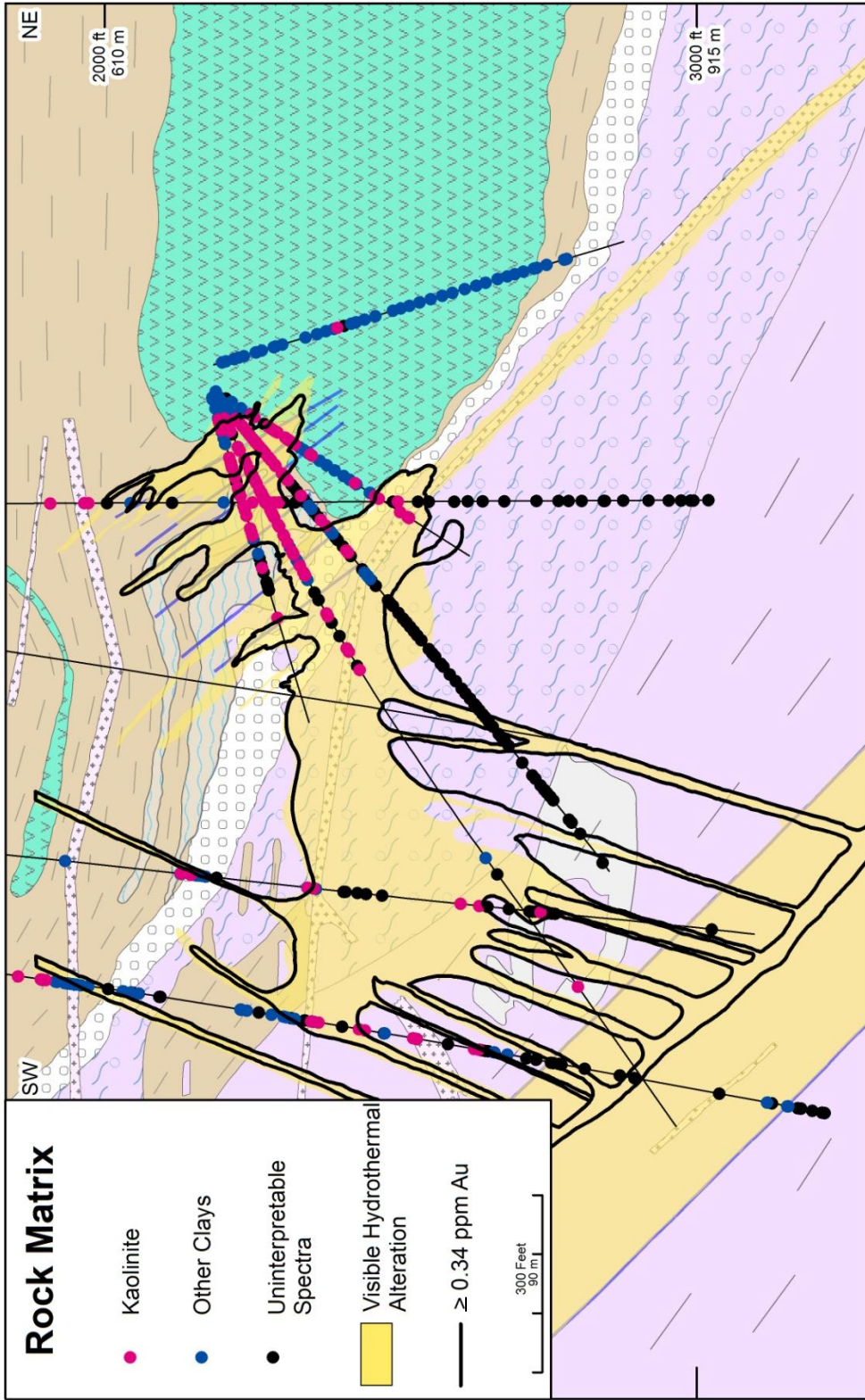


Figure 1.15A

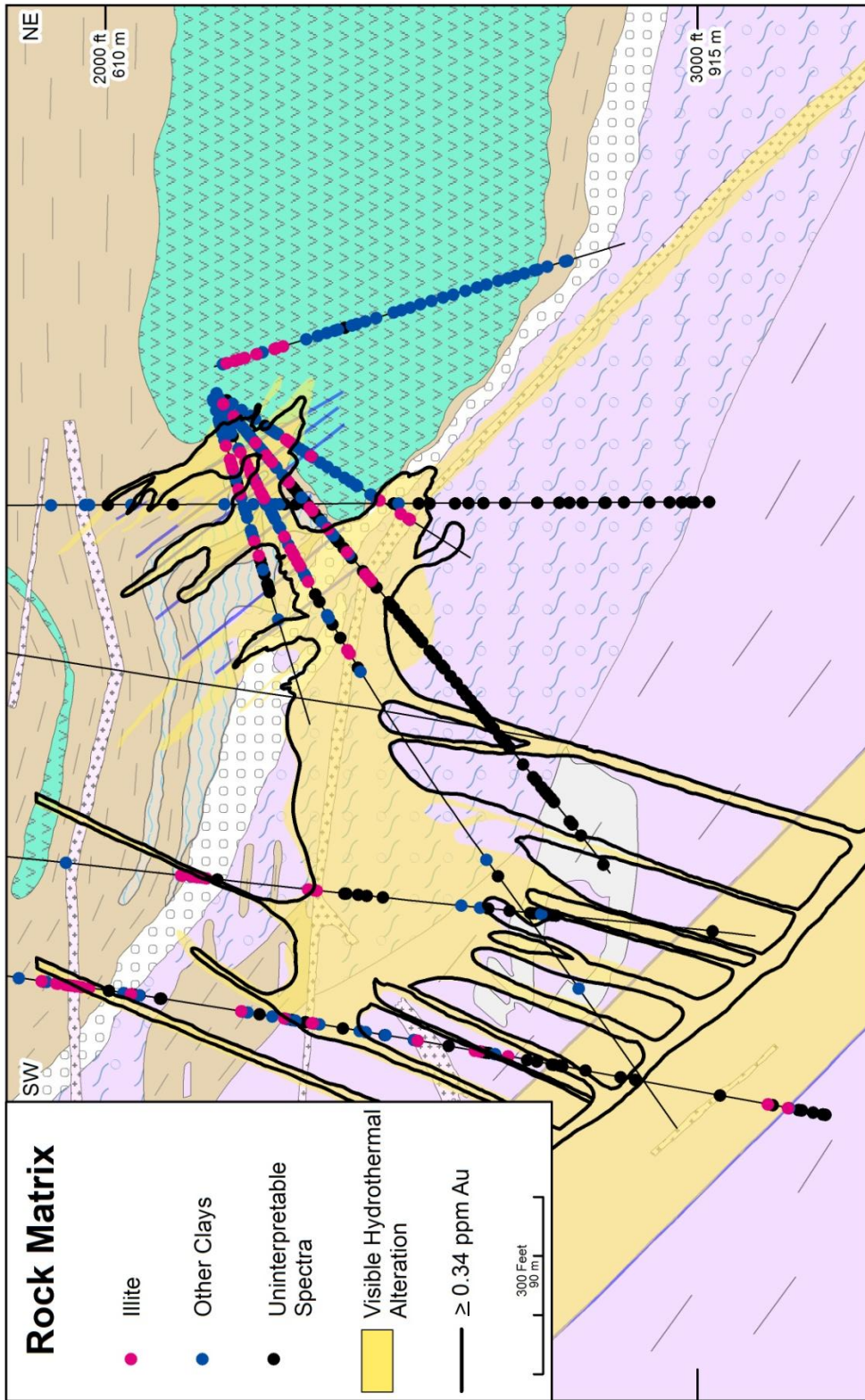


Figure 1.15B

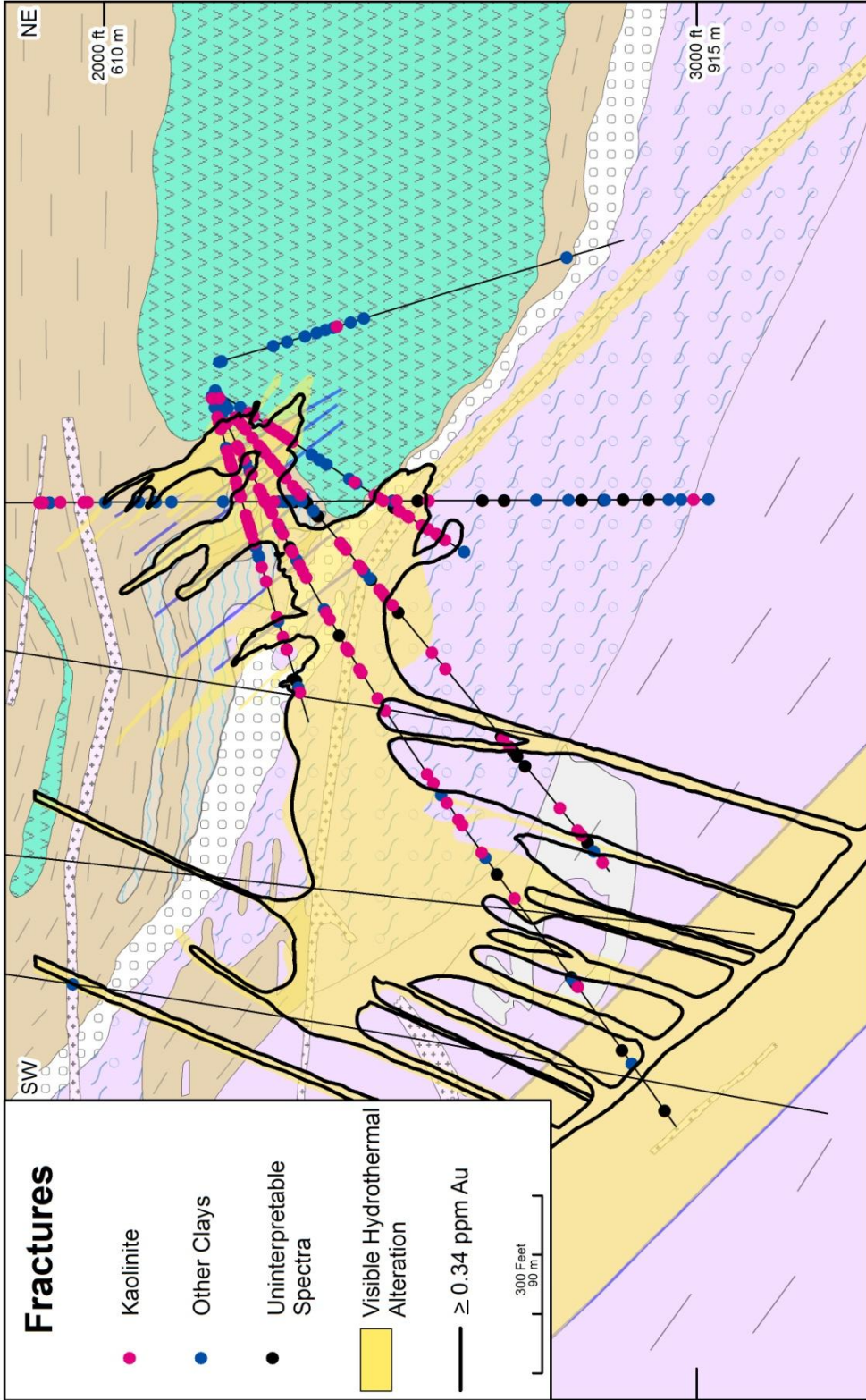


Figure 1.15C

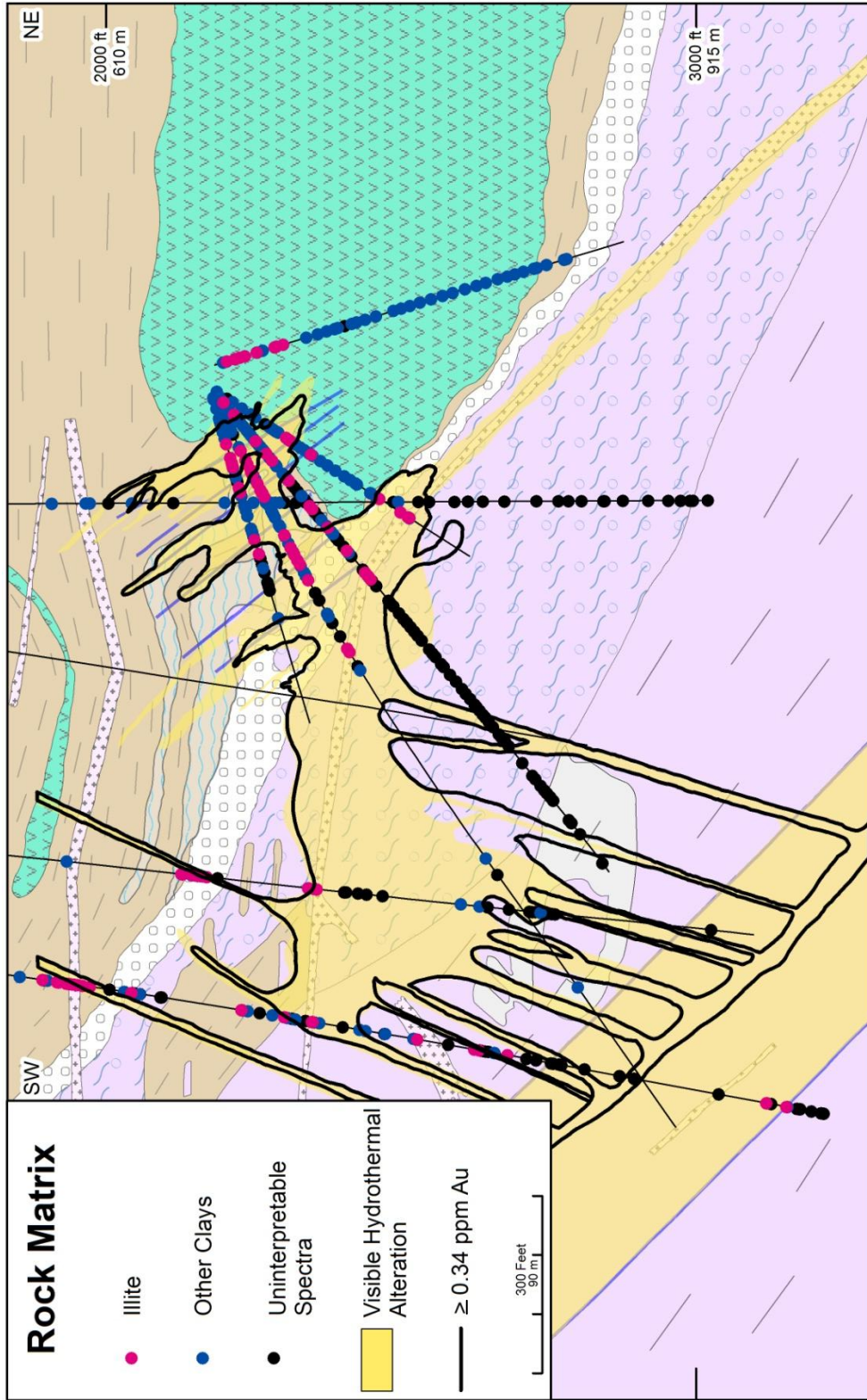


Figure 1.15D

Back scattered electron (BSE) imaging and energy dispersive spectroscopy (EDS) using a scanning electron microscope (SEM) were utilized to document the paragenetic relationships between ore minerals and kaolinite and illite. Kaolinite and/or illite were identified in multiple samples from zones containing >11 ppm Au. Kaolinite was identified with the SEM by high Al and Si peaks and a high Al/Si peak ratio using EDS. Illite was recognized by a significant K peak in addition to Al and Si peaks. Under the SEM several ore-stage pyrite textures were recognized that are very similar to pyrite textures from Turquoise Ridge that were described by Longo et al. (2009). Arsenic peaks and, in some samples, Hg peaks were observed in these ore-stage pyrites, in addition to Fe and S peaks. [Figure 1.17](#) shows examples of intimate intergrowths between ore-stage pyrite and either kaolinite or illite.

A Niton handheld XRF analyzer was used on a few visually unaltered samples with bleached, clay-lined fracture surfaces. The fracture surfaces and adjacent wall rock were analyzed. Calibration issues while conducting the XRF readings resulted in unreliable analyses for most elements, with the exception of As. The results from four samples are shown in [Table 1.3](#). In two samples, the As values are significantly higher from kaolinite-lined fracture surfaces than from the adjacent wall rock, which suggests the clay-lined fractures represent limited flow of ore fluids in otherwise visibly unaltered rocks.

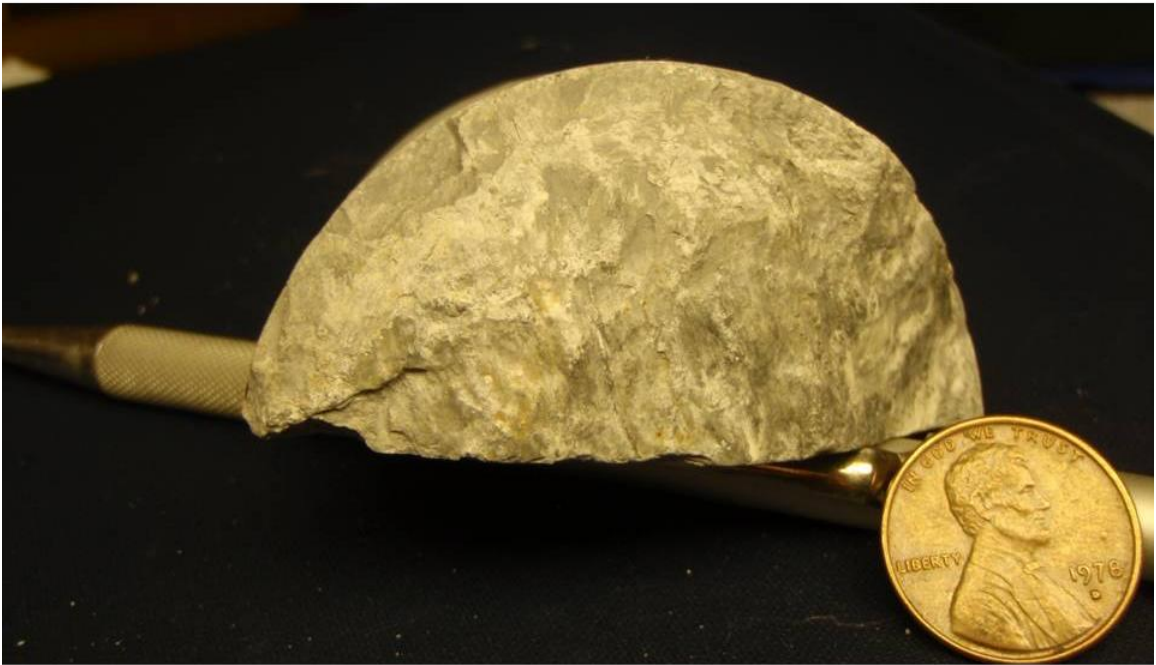


Figure 1.16. Typical clay-coated fracture surface cutting interbedded carbonaceous mudstone and limestone (hole 99NZ022).

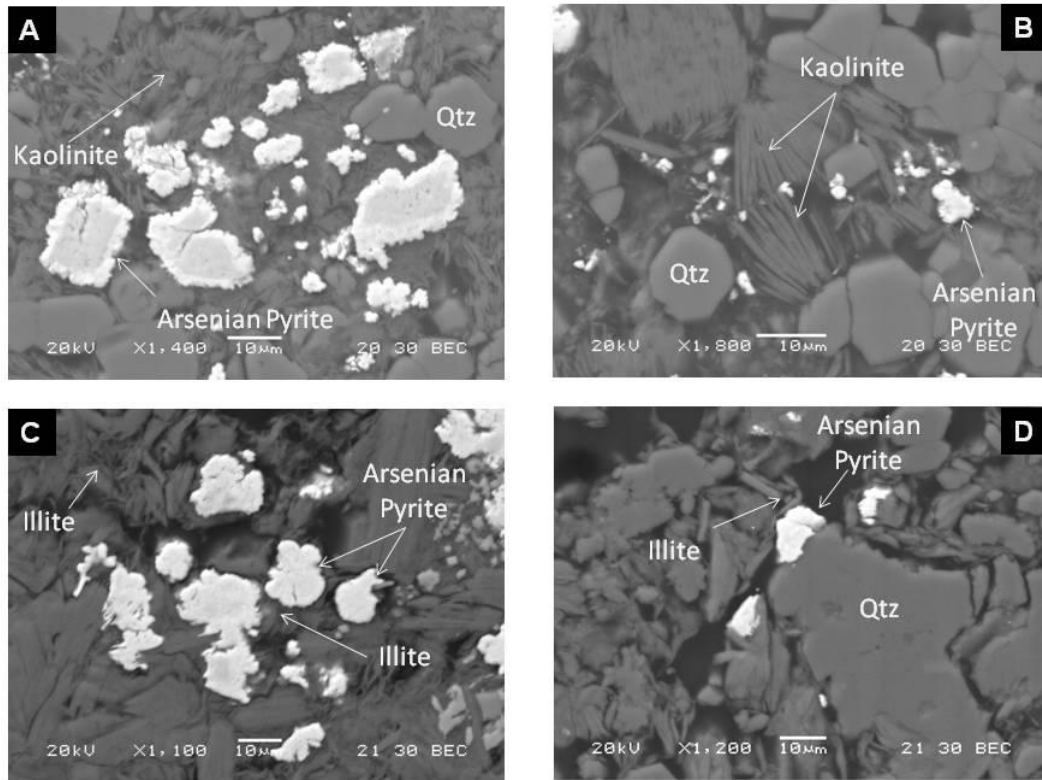


Figure 1.17. Back-scattered electron images of high-grade samples showing kaolinite and illite intergrown with ore-stage pyrite. A. Kaolinite intimately intergrown with ore-stage pyrite rimming a pre-ore pyrite grains in decalcified, silicified limestone. The rims contain As and Hg peaks using EDS, whereas the earlier pyrite cores showed no peaks with EDS other than Fe and S. B. Spheroidal pyrite containing ragged “fuzzy” edges with interstitial kaolinite and ore-stage quartz. C. Intimately intergrown ore-stage pyrite and illite. The large pyrite grain consists of a pre-ore pyrite core with no EDS peaks other than Fe and S. The edges of the core display dissolution textures and are rimmed by anhedral ore-stage pyrite. Also shown are spheroidal “fuzzy” pyrites. The illite occurs as radiating, sheet-like masses adjacent to the ore-stage pyrites. D. Intergrown illite and ore-stage pyrite adjacent to hydrothermal quartz in decalcified, silicified limestone.

Table 1.3. ASD and Niton XRF Results Conducted on Rock and Fracture Surfaces

Drill Hole	DH Footage	Context	Rock type	Alteration	Au ppm Drill Interval	As ppm Niton	Kaolinite	Illite	2200 feature
TU01164A	454	Fracture Surface	Carbonaceous Black Mudstone	Bleached	0.017	83	X		2207
TU01164A	454	Rock	Carbonaceous Black Mudstone	Unaltered	0.017	14	?	?	?
TU01166	613.5	Fracture Surface	Siliceous Black Mudstone	Bleached	0.01	1750	X	X	2207
TU01166	613.5	Rock	Siliceous Black Mudstone	Bleached	0.01	740	?	?	?
00NZ184	1828	Fracture Surface	Dacite	Unaltered	<0.01	< Detection	X	X	2206
00NZ184	1828	Rock	Dacite	Unaltered	<0.01	< Detection		X	2206
TU01164A	292	Fracture Surface	Tuffaceous Mudstone	Bleached	0.045	57		X	2199
TU01164A	292	Rock	Tuffaceous Mudstone	Unaltered	0.045	61	?	?	?

? – spectrum was too noisy to interpret or adjacent rock was not analyzed with the ASD

The remaining clay minerals identified with the ASD show no spatial association with Au, either within ore or as a halo to ore. Chlorite and nontronite occur in the NPB and adjacent tuffaceous mudstone in both the wall rock and along fracture surfaces. Montmorillonite is also commonly associated with the NPB and locally occurs in a few altered sedimentary rocks distal to the HGB, but shows no consistent pattern with respect to visible alteration or Au grades. Muscovite was identified in a few of the spectra and, based on thin section petrography, is most likely related to pre-ore metamorphism.

DISCUSSION

This study set out to define the nature and extent of the hydrothermal features around a high-grade ore zone in an underground Carlin-type deposit, with the goal of deriving practical tools that might aid in mine development and the discovery of future underground ore zones at Turquoise Ridge and other CTGDs. [Table 1.4](#) summarizes the data sets presented in this study, whether or not they formed haloes, and the size of the haloes. The most coherent haloes to the HGB ore zone at Turquoise Ridge are Au values ≥ 0.34 ppm and visible hydrothermal alteration in the form of decalcification, argillization and silicification. Similar to what was reported by Muntean et al. (2009), moderate to strong alteration closely correlates spatially with gold grades ≥ 0.34 ppm. Lower Au grades extend beyond the ≥ 0.34 ppm contour but are not sufficiently persistent to be contoured.

Table 1.4. Summary of the Extent of Haloes of Features at Turquoise Ridge

Feature	Occurs within >0.34 ppm Au contour and visible alteration	Forms halo to >0.34 ppm Au contour and visible alteration	Maximum extent of halo (meters)	Nature of Halo
As (≥100 ppm)	Yes	Yes	30	coherent halo
Sb (≥5 ppm)	Yes	Yes	12	coherent halo
Hg (≥1ppm)	Yes, coincident	No	-	-
Tl (≥5 ppm)	Yes, smaller	No	-	-
Te (≥1 ppm)	Yes, smaller	No	-	-
Au Factor Scores (≥0.8)	Yes, smaller	No		locally occurs outside of visible alteration but forms no pattern
DOS (≥0.8)	Yes, coincident	Yes	<5	local, discontinuous halo below HGB
Ca (<5 wt%)	Yes	No	-	rarely occurs outside of visible alteration-
Ca/Au (<100)	Yes, coincident	No	-	-
Ca/Au Factor Score (<10)	Yes	No	-	-
Kaolinite-coated fracture surfaces	Yes	Yes	20	discontinuous halo
Illite-coated fracture surfaces	Yes	Yes	20	discontinuous halo
RQD (<25%)	Yes	Yes	30	coherent halo

Statistical analysis of multi-element data in this study shows Au is associated mainly with Hg, As, W, S, Tl, Sb, and Te. With the exception of As, Sb, and possibly Hg, the spatial distribution of CTGD trace elements do not form large, coherent haloes to Au that would effectively serve exploration or development. Arsenic values of >100 ppm form a contourable halo, extending up to 30 meters beyond visible alteration and the ≥ 0.34 ppm Au contour. The greater dispersion of As relative to the other ore-related elements might be partly caused by the presence of arsenic sulfides. However, the 100 ppm As contour commonly extends into areas without visible realgar or orpiment. Other sulfides, such as cinnabar and stibnite are rare at Turquoise Ridge; therefore, most of the ore-related elements are likely in the ore-stage pyrite. The extent of anomalous Hg levels above the HGB, in the range of 0.04 to 1 ppm, is unknown because of the high detection limits for the analyses from the four surface holes. Given the lack of haloes in other ore-related trace elements, it should be no surprise that factor scores for the gold factor (Factor 2 in [Table 1.1](#)) did not show any consistent halo around visible alteration and the 0.34 ppm Au contour. Moreover, the lack of haloes in DOS values suggest the amount of ore-stage pyrite probably decreases away from ore in the same manner as does gold and the ore-related elements (except As and possibly Hg). This suggests there is not a large halo of ore-stage pyrite that is poor in trace elements surrounding the zones of visible alteration at Turquoise Ridge. Another possible explanation for the lack of a recognizable halo in DOS values could be variations in the amount of pre-ore pyrite and/or the amount of Fe in the various lithologies at Turquoise Ridge.

Gold negatively correlates with Mg, Ca, and Sr, which directly reflects the dissolution of carbonate during ore formation; therefore, it is tempting to map decalcification by plotting Ca values. However, when Ca, Ca/Au and Ca/Au factor scores were plotted, they displayed no obvious halo relative to visible alteration. The inability of Ca values to track very weak alteration or narrow zones of stronger alteration surrounding ore is probably because the variation in the Ca content of the various lithologies at Turquoise Ridge is greater than the variation in Ca caused by such weak or narrow zones of decalcification.

The ASD analyses and SEM work demonstrate kaolinite and illite are spatially and temporally associated with Au mineralization and the ore-stage pyrite. Kaolinite and illite are the dominant clay minerals found within moderate to strong alteration zones containing ≥ 3.4 ppm Au. Fractures surfaces containing kaolinite and/or illite extend up to 20 meters beyond the ≥ 0.34 ppm Au contour. Furthermore, the limited data collected with the Niton handheld XRF suggest these clay-lined fractures contain strongly anomalous As and possibly other trace elements.

Few maps and cross-sections depicting haloes of low-grade Au, alteration, and trace elements around CTGDs are available in the literature. [Table 1.5](#) is a non-exhaustive compilation of published data. Only those examples where two or three-dimensional data were reported are included, whereas publications that only had one-dimensional data (e.g. transects, individual drill holes) were not included. Examples of both high-grade underground deposits, similar to Turquoise Ridge, and lower-grade open pit deposits are listed. High-grade underground deposits, like the Deep Star

deposit in the northern Carlin trend, show abrupt patterns in gold grade similar to Turquoise Ridge. At Deep Star, Au values of >0.34 ppm extend only 0-30 m away from the ≥ 6.8 ppm Au contour (Heitt et al., 2003). The lower-grade underground deposits and especially the large open pit deposits have low gold grades that extend for much

Table 1.5. Characteristics of Hydrothermal Haloes Surrounding Ore in other CTGDs.

Deposit	Nature of haloes around ore	References
Twin Creeks (Megapit)	<ol style="list-style-type: none"> 1. The 0.34 ppm Au contour extends up to 150 m beyond the 1.7 ppm Au contour. 2. The 100 ppm As contour extends up to 90 m beyond the 1.7 ppm Au contour. 3. The 50 ppm Sb contour extends up to 70 m beyond the 1.7 ppm Au contour. 4. The 10 ppm Hg contour extends up to 90 m beyond the 1.7 ppm Au contour. 5. The As, Sb, and Hg contour mentioned above do not appear to form haloes around the 0.34 ppm Au contour. 6. The <5 wt% total carbonate contour extends up to 40 m beyond the 1.7 ppm Au contour. 	Stenger et al., 1998
Deep Star (underground)	<ol style="list-style-type: none"> 1. The 0.34 ppm Au contour extends 0-30 m beyond the 6.8 ppm Au contour. 2. Kaolinite-bearing wall rock alteration occurs within the 6.8 ppm Au contour. 3. The 100 ppm As contour extends at least 400 m above the 6.8 ppm Au contour. 	Heitt et al., 2003
Alligator Ridge (Vantage pit)	<ol style="list-style-type: none"> 1. Au grades commonly decrease from >3ppm to <0.1 ppm over distances of <5 m. 2. Zone of decarbonatization coincides with the ore-waste boundary. 3. Kaolinite-bearing veinlets extend 75 m beyond ore. 	Ilchik, 1990
Carlin	<ol style="list-style-type: none"> 1. Decalcification extends 25 m above and 75 m below the 1 ppm Au contour 	Kuehn and Rose, 1992
Ren	<ol style="list-style-type: none"> 1. Au values 0.02 ppm Au form a discontinuous halo 350 m above the 1 ppm Au contour, but form no halo below the 1 ppm Au contour. 2. The 25 ppm As contour extends up to 60 m from the 1 ppm Au contour. 3. The 2 ppm Sb contour extends up to 120 m from the 1 ppm Au contour. 4. The 0.5 ppm Hg contour extends up to 70 m above the 1 ppm Au contour, but only <10 m below the 1 ppm Au contour. 	Albino, 1994
Gold Bar	<ol style="list-style-type: none"> 1. The 0.034 ppm Au contour extends 50 m above ore, but not below ore. 2. Weak decalcification forms a zone that is slightly larger than the 0.068 ppm Au contour. 3. The 100 ppm As contour is mostly coincident with ore. 4. The 20 ppm Sb contour is mostly coincident with ore. 5. The 1 ppm Hg contour forms a halo to ore. 	Broili et al., 1988 Masinter, 1990
Turf	<ol style="list-style-type: none"> 1. Decalcification extends up to 100 m beyond the 6.8 ppm Au contour. 	Mohling, 2002
Leeville	<ol style="list-style-type: none"> 1. Decalcification extends up to 120 m beyond the 6.8 ppm Au contour. 	Jackson et al., 2002
Gold Quarry	<ol style="list-style-type: none"> 1. The 0.34 ppm Au contour extends up to 200 to 300 m from zones of ≥ 6.8 ppm Au. 2. The zone of fairly continuous alteration is roughly coincident to slightly smaller than the 0.34 ppm Au contour. 	Harlan et al., 2002

further distances beyond ore than they do at Turquoise Ridge. For example, the ≥ 0.34 ppm Au contour extends for 100-300 m beyond the ≥ 6.8 ppm Au contour at the Twin Creeks (Megapit), Gold Quarry, Leeville, and Turf deposits. However, like Turquoise Ridge, controllable alteration at Twin Creeks and Gold Quarry roughly coincides with the ≥ 0.34 ppm Au contour. The data from the underground Ren deposit suggests very low grades of Au (≥ 0.020 ppm) can form large, albeit discontinuous, haloes several hundred meters above ore, but not below ore. The open pits with low-grade ore that were mined at Turquoise Ridge prior to underground mine are likely an example of such a halo, although the patterns of gold grades between the open pit and the underlying individual ore zones, like the HGB, have not been established in detail. Though difficult to directly compare, the limited trace element data summarized in [Table 1.5](#) suggest patterns not that dissimilar to Turquoise Ridge.

Like Turquoise Ridge, kaolinite has been identified in a number of CTGDs, of which some also have dickite (e.g., Alligator Ridge, 1990, Ilchick; Vista ore-body at Twin Creeks, Osterberg and Guilbert, 1991; Carlin, Kuehn and Rose, 1992; Betze Post, Arehart et al., 1993b; Deep Star, Heitt et al., 2003). In most cases, like at Turquoise Ridge, the zone of kaolinite-bearing alteration is restricted to ore zones. For example, kaolinite-bearing alteration at Deep Star is restricted to Au grades of ≥ 6.8 ppm Au. Similar to Turquoise Ridge, kaolinite-bearing veinlets extend beyond ore for several tens of meters at the Alligator Ridge (Ilchik, 1990), Carlin (Kuehn and Rose, 1992), and Screamer (Ye et al., 2003) CTGDs.

The lack of wide, coherent haloes of various hydrothermal features surrounding ore at Turquoise Ridge is suggestive of a restrictive, fracture-controlled fluid flow network, rather than large-scale, pervasive, lithologic-controlled fluid flow. As pointed out by Muntean et al. (2009), ore fluids likely ascended along the pre-existing Getchell fault zone and into the steep, small-displacement, antithetic faults in the hanging wall as well as the main dacite porphyry dike before encountering highly-fractured, reactive carbonate lithologies, especially the sedimentary breccias and the deformed mudstones and limestones adjacent to edge of the NPB. Increased surface area in these fractured zones allowed more fluid:rock interaction, which resulted in more extensive carbonate dissolution, sulfidation and Au mineralization in the HGB. The exploitation of these pre-existing fracture networks by the hydrothermal fluids is supported by the large zone of RQD values that are <25%, which probably forms a better halo to visible alteration and ≥ 0.34 ppm Au than any of the hydrothermal features presented in this paper.

RECOMMENDATIONS

The results of this study demonstrate that the most reliable tools to use for vectoring into ore at Turquoise Ridge, and likely other high-grade ore zones in and around other CTGDs, is carefully hand-contouring gold grades and visible alteration on cross-sections. Carefully logged decalcification, dedolomitization, argillization, and possibly silicification should be lumped together when contouring alteration. The contouring needs to be done after geology is carefully logged, plotted and interpreted on cross-sections, ideally by the same geologist. The cross-section work should then be followed by three-dimensional modeling of various gold grade shells and surfaces of

visible alteration. Although cross-section work can be viewed as obsolete, given the complex three-dimensional geometry of CTGDs and the wide availability of sophisticated modeling software; however, until it can be demonstrated that detailed logging information (e.g., multiple lithologies, complex structures, etc.) can be effectively and routinely incorporated into the interpretation of three-dimensional surfaces of gold grades and alteration, detailed cross-section work should be included in the development of three-dimensional models for CTGDs.

With the exception of As and Sb, and possibly Hg, this study showed that other ore-related elements did not form coherent haloes around visible alteration associated with the HGB at Turquoise Ridge. The apparent tightly-confined nature of fluid flow throughout the Turquoise Ridge deposit appears to have prevented the development of large-scale pervasive dispersion haloes around the HGB. This is likely the case in many CTGDs. Although trace elements provide critical information in the early stages of exploration by helping to determine if mineralization has an elemental signature consistent with known CTGDs (e.g., Au-As-Hg-Tl-Sb with low Cu-Pb-Zn-Ag), they might not provide haloes that are any larger or more coherent than gold itself. When core holes are drilled, RQD values should be determined and contoured.

Besides simply contouring gold grades and visible alteration, another promising vectoring tool that might very well detect large, but likely discontinuous, haloes to contourable gold grades and visible alteration in otherwise unaltered rock is the analysis of fracture surfaces. This study demonstrated kaolinite- and illite-bearing fractures surfaces, as determined by reflectance spectroscopy, extended up to 20 meters beyond

contourable gold and alteration. Though these haloes are still somewhat narrow, such analyses should be done over a larger volume of rock at Turquoise Ridge and other CTGDs to see if haloes are larger and if the approach is indeed viable. More importantly, determination of the clay mineralogy along such fracture surfaces might be unnecessary, if such fracture surfaces are demonstrated to contain anomalous As-Hg-Tl-Sb by using a portable Niton XRF. Limited use of the Niton in this study suggested the kaolinite- and illite-bearing fractures surfaces might contain more As than adjacent unaltered wall rock. More mining and exploration companies are using such portable XRF units, but few to no data have been published. Comprehensive orientation studies of CTGDs, coupled with careful calibration of the units for precise As-Hg-Tl-Sb analysis, are warranted.

Chapter 2

Spatial Distribution of Ferroan Carbonates around a High-Grade Carlin-type Gold

Deposit: Getchell District, Nevada.

ABSTRACT

Carbonate staining was utilized to determine the spatial distribution of carbonate mineralogy relative to high-grade gold ore at the Turquoise Ridge Carlin-type gold deposit. Specifically, dilute hydrochloric acid containing both alizarin red S and potassium ferricyanide was utilized to differentiate between calcite, ferroan calcite, ferroan dolomite and dolomite in the Cambrian-Ordovician carbonate host rocks at Turquoise Ridge. Detailed carbonate staining was conducted on 31 drill holes throughout the north end of Turquoise Ridge. Results reveal a distinct spatial relationship between gold mineralization, ferroan calcite, and the southern margin of a thick basalt within the Cambrian-Ordovician stratigraphic package that is referred to as the northern pillow basalt (NPB). High-grade gold ore (≥ 17 ppm Au) within the HGB ore zone occurs exclusively within ferroan calcite-bearing host rocks. The transition from ferroan calcite to calcite with depth occurs at the base of the HGB ore zone. Non-ferroan calcite is distal to the NPB, both laterally and with depth.

A close spatial association between the distribution of ferroan calcite and the NPB suggests iron was likely liberated from the basalt during seawater alteration of the basalts, and/or the emplacement of the Cretaceous intrusions and was mobilized into adjacent limestones, forming ideal host rocks for subsequent gold mineralization.

Acidic, sulfur-rich, auriferous hydrothermal fluids dissolved ferroan carbonates, which liberated iron. Aqueous sulfide in the fluid reacted with the iron, which destabilized aqueous gold-sulfide complexes, resulting in the formation of auriferous pyrite and marcasite. The presence of interlayered basalts and ferroan carbonates could be important exploration criteria in the identification of future target areas in the Getchell District and throughout Nevada. Furthermore and most importantly, careful carbonate staining should be routinely employed, given that it provides inexpensive, real-time data.

INTRODUCTION

The discovery and subsequent classification of Carlin-type gold deposits (CTGDs) in the early 1960s has led to the identification of more than 100 CTGDs containing over 200 million ounces of gold within north-central Nevada. The resulting explosion in gold production has transformed Nevada into the fourth largest gold producer in the world. Production exceeded 5.5 Moz of gold in 2008, accounting for 76% of U.S. gold production and 8% of global production (NBMG, 2009). CTGDs are epigenetic, disseminated auriferous pyrite deposits characterized by carbonate dissolution, argillic alteration, and silicification, typically of Paleozoic calcareous sedimentary rocks (Hofstra and Cline, 2000; Cline et al., 2005). Gold occurs as solid solution in pyrite and less commonly as submicron native gold particles in pyrite (Well and Mullens, 1973; Arehart et al., 1993; Simon et al., 1999; Reich et al., 2005). Late ore-stage minerals commonly include orpiment, realgar, stibnite, and barite (Hofstra and Cline, 2000; Cline et al., 2005). CTGDs commonly occur in clusters along linear trends and formed mainly during the late Eocene (Hofstra et al., 1999; Arehart et al., 2003; Cline et al., 2005).

The geometry of CTGD ore bodies has historically been attributed to permeable features associated with high-angle faults, thrust faults, hinge zones of anticlines, lithologic contacts, reactive carbonate units, debris-flow deposits, facies changes, brecciated zones between rocks of different rheologies, and with the margins of contact metamorphic aureoles related to Mesozoic intrusions (Cline et al., 2005). In addition, numerous studies have identified sulfidation as a primary depositional mechanism in various CTGDs (Hofstra et al., 1991; Kuehn and Rose, 1992, 1995; Hofstra, 1994, Stenger

et al., 1998; Hofstra and Cline, 2000, Cail and Cline, 2001; Kesler et al., 2003; Fortuna et al., 2003; Patterson, 2009, Chapter 1). Past studies on several CTGDs have identified peripheral zones containing ferroan carbonate minerals that have been inferred to either represent relict components of the host rocks or hydrothermal minerals formed during gold mineralization (Jerritt Canyon, Hofstra 1994; Patterson, 2009; Deep Star, Clode et al., 1997; Heitt et al., 2003; Twin Creeks, Stenger et al., 1998). Despite our evolving knowledge of the role of sulfidation and gold mineralization, few published studies have documented the relationship between ferroan and non-ferroan carbonates and their potential control on high-grade gold mineralization. This report documents how carbonate staining can be utilized to identify potential exploration targets, based on the distribution of ferroan carbonates associated with CTGDs, specifically the Turquoise Ridge deposit within the Getchell District, Humboldt County, Nevada.

Sulfidation in CTGDs occurs when migrating hydrothermal sulfide-rich fluids come in contact and react with iron-rich wall rocks, resulting in the formation of pyrite and/or marcasite. The loss of reduced sulfur from the ore fluid causes the destabilization of dissolved gold bisulfide complexes, resulting in the deposition of auriferous sulfides. CTGDs are hosted primarily in Paleozoic miogeoclinal carbonates where ascending ore fluids exploited high-angle structures before intersecting more reactive strata. The extensive drill database at the Turquoise Ridge deposit provides the geologic control necessary to document the relationship between ferroan and non-ferroan carbonate host rocks, the High-Grade Bullion (HGB) ore zone, and interpreted

fluid conduits via staining of carbonates within a sequence of interlayered Cambrian-Ordovician sedimentary and igneous rocks.

DISTRICT GEOLOGY

The geology of the northern Osgood Mountains and the Getchell mine area has been discussed in detail in Chapter 1 as well as in many publications (Joralemon, 1951; Hotz and Willden, 1964; Chevillon et al., 2000; Crafford, 2000; McLachlan et al., 2000; Boskie, 2001; Breitt et al., 2005; Marlowe et al., 2007) and is briefly summarized here. The Turquoise Ridge deposit is located in the Getchell District on the northeastern flank of the Osgood Mountains approximately 72 km northeast of Winnemucca, Nevada (Figure 2.1). CTGDs within the Getchell District are primarily hosted within Cambrian-Ordovician carbonates and clastic rocks containing interlayered basaltic rocks that have historically been mapped as the Preble, Comus, and Valmy Formations (Hotz and Willden, 1964). The Cambrian-Ordovician sequence was complexly deformed prior to the deposition of the Pennsylvanian-Permian Etchart Formation, likely during the Antler Orogeny. The siliciclastic and basaltic rocks of the Mississippian-Permian Havallah Formation occur northwest of the Getchell mine area and were emplaced over the Etchart Formation along the Golconda Thrust during the late Permian to early Triassic Sonoma Orogeny. Broad, northeast-trending folds in the Etchart Formation are interpreted to have occurred during the Sonoma and/or subsequent Mesozoic orogenies. The Cretaceous Osgood stock and associated dikes intrude the Paleozoic section and appear to be part of a protracted magmatic-hydrothermal event ranging from 115-80 Ma based on $^{40}\text{Ar}/^{39}\text{Ar}$ dates and a U-Pb zircon date from Twin Creeks (Hall

et al., 2000; Breit et al., 2005) and $^{40}\text{Ar}/^{39}\text{Ar}$ dates on igneous biotite and hornblende and hydrothermal K-feldspar and sericite at Getchell (Groff et al., 2005). The primary ore-controlling structure in the district is the Getchell Fault Zone, which runs along the northeast flank of the stock and strikes NNW and dips 40-55°E. The Getchell Fault Zone has a long, complex tectonic history that shows evidence for normal, reverse, and strike-slip motion (Joralemon, 1951; Hotz and Wilden, 1964; Berger and Taylor, 1980; Crafford, 2000; Boskie, 2001; Muntean et al., 2007).

Ores within the Getchell District are largely devoid of supergene alteration with gold strongly correlating with fine-grained, gold-bearing arsenian pyrite. The main ore-stage mineralization is characterized by carbonate dissolution, argillization of silicates, sulfidation of Fe-bearing minerals, and silicification of limestones (Cline, 2001). Late-ore-stage minerals in order of deposition include drusy quartz, orpiment, fluorite, stibnite, realgar, and calcite (Cline, 2001). Mineralization occurred during the Eocene, based on a 39.0 ± 2.1 Ma Rb-Sr age on galkhaite, which is a late ore-stage mineral (Tretbar et al., 2000).

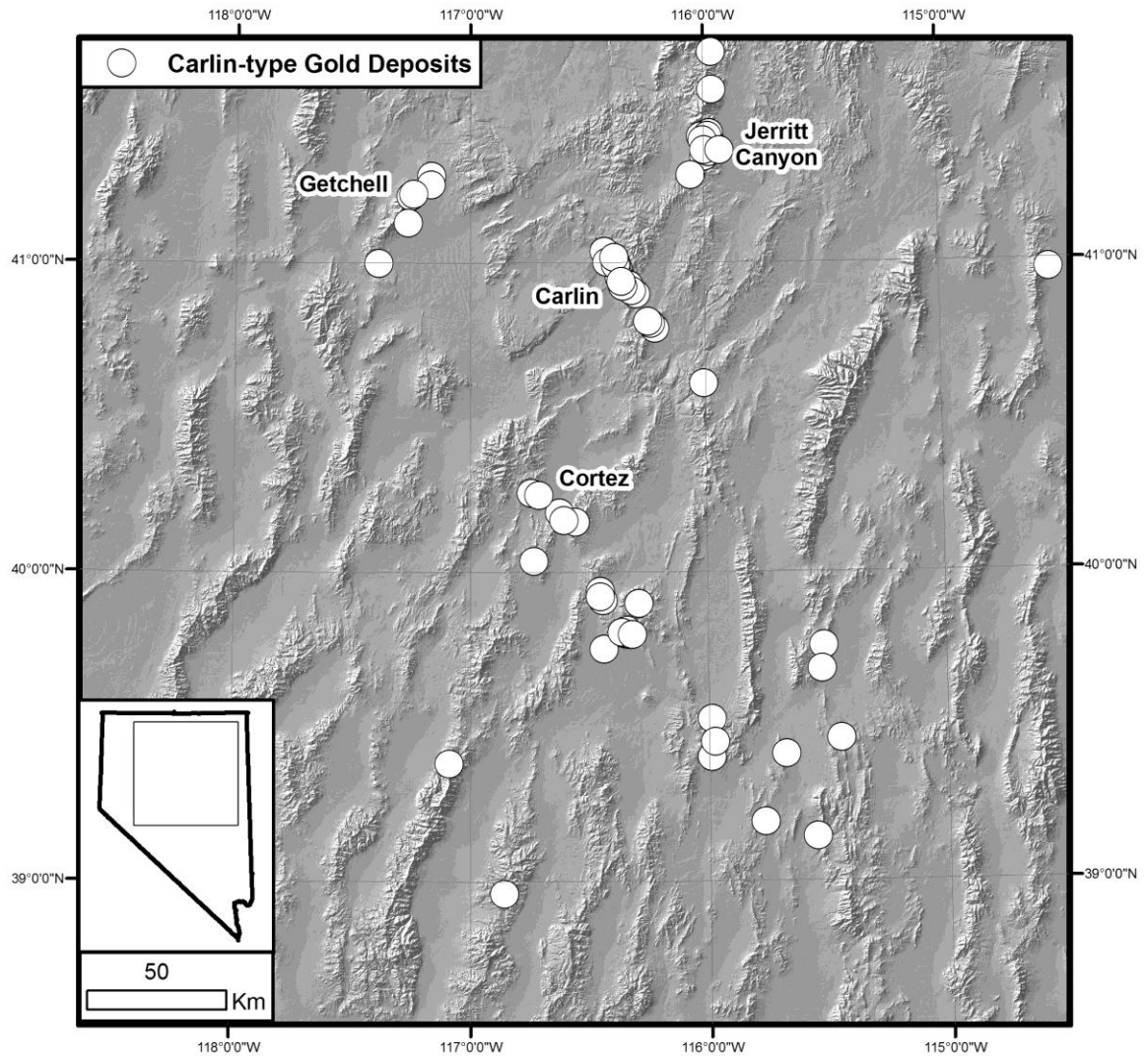


Figure 2.1. Digital elevation model of northern Nevada, showing locations of the Getchell Deposit relative to the locations of other prominent large Carlin-type gold deposits.

GEOLOGY OF THE TURQUOISE RIDGE DEPOSIT

The geologic framework presented here is based primarily on underground cross-sections that trend east-west and northeast that cut the north part of the Turquoise Ridge deposit through the HGB zone, the largest and highest grade ore zone in the Turquoise Ridge deposit (Figs. 2.2-2.4). The geology of the northeast cross-section was described in detail in Chapter 1. The geology of the north end of the Turquoise Ridge deposit is characterized by a Cambrian-Ordovician sedimentary-volcanic package that has undergone a complex depositional, tectonic, metamorphic, and hydrothermal history. The complex depositional history of the Cambrian-Ordovician sequence is compounded by rapid facies changes and the lack of marker units. Sedimentary rocks within the deposit record multiple compressive and extensional deformational features, including both syn-sedimentary and tectonic features. Pre-ore metamorphism related to the tectonic deformation and contact metamorphism and hydrothermal activity related to emplacement of the Cretaceous Osgood stock further hampers unraveling the geologic history. The lithologic units in Figures 2.3 and 2.4 represent a series of lithologic packages. Each of the individual lithologies described below can be seen in various proportions within each lithologic package. Unit designations at the deposit scale are assigned based on the most prominent rock types within a given unit.

The lowermost lithologic unit consists primarily of carbonaceous mudstones and limestones with interlayers of calcarenite turbidites (purple unit in Fig. 2.3 and the “carbonaceous mudstone and limestone” and “siliceous mudstone” units in Fig. 2.4).

The mudstones vary from siliceous and non-calcareous to argillaceous and variably calcareous and are overlain by a sedimentary breccia unit that pinches out to the south (black stippled unit in Fig. 2.3 and the lower and upper members of the sedimentary breccia unit in Fig. 2.4). Overlying the sedimentary breccia unit are slumped micritic

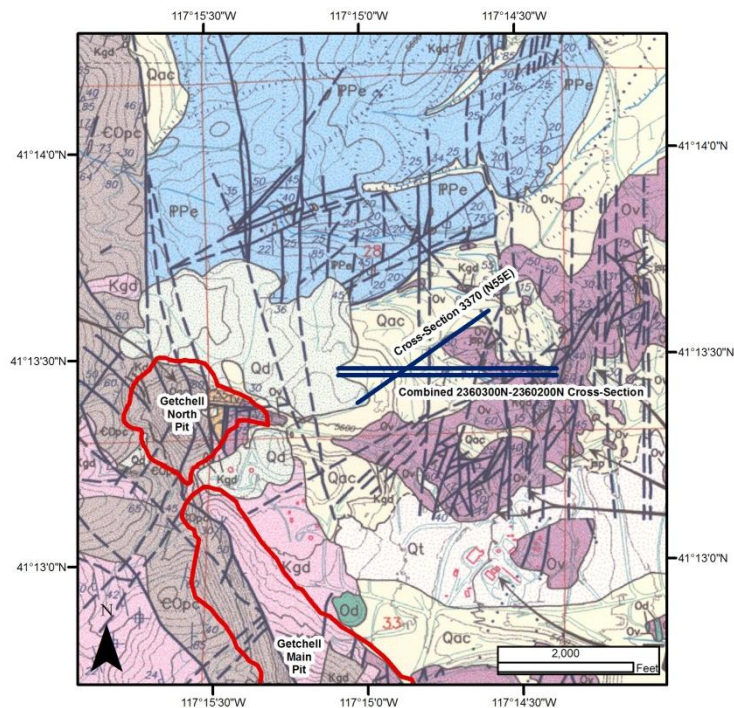


Figure 2.2. Simplified geologic map of the Getchell District (Unpublished map by Placer Dome Exploraton, based on Hotz and Willden, 1964 and unpublished Placer Dome mapping). The main units in the map are the Comus/Preble Formations (grey), Valmy Formation (purple), Etchart Formation (blue), Osgood granodiorite (pink), and alluvium (yellow). Map also shows the surface projections of the east-west cross-section and the northeast cross-section relative to the Getchell open pits (large red outlines), faults (black lines), and mine buildings (thin red lines in SE corner). The east-west cross-section is a combination of the 2360200N and 2360300N cross-sections and is composed of both surface diamond drill core and underground drill fans that were constructed at a 1:600 scale by John Muntean utilizing detailed core logs, core photos, and spot inspection of drill core and underground exposures. The northeast cross-section was constructed utilizing detailed core logging of four diamond drill holes spaced 60 m apart, and a fan of underground diamond drill holes. A color-coded logging scheme similar to that used by the Anaconda Company in the 1960s was employed, in which lithology, structure, alteration, vein types, and mineralization was graphically recorded at a scale of 1:120. The logging information was transferred by hand onto a 1:600 scale cross-section. Background is geologic map compiled by Placer Dome geologists.

limestones and brown mudstones (brown and blue unit in Fig. 2.3 and the “slumped brown mudstone and limestone” and the “interbedded limestone and brown mudstone” in Fig. 2.4). A pillow basalt, referred to as the northern pillow basalt (NPB), overlies the brown mudstones and limestones and also pinches out to the south forming a west-northwest-trending, blunt margin across the north end of the Turquoise Ridge deposit. Brown mudstones containing thin basalt flows and sills are present further up section. The Cambrian-Ordovician rocks are complexly deformed throughout the Turquoise Ridge deposit. Cretaceous dacite porphyry dikes intrude the Cambrian-Ordovician sequence, the most prominent being the “main dacite dike” that cuts across the entire north end of Turquoise Ridge. The dike strikes roughly sub-parallel to the Getchell Fault Zone, maintaining a slightly shallower easterly dip. The continuity of the dike throughout the cross-sections is interpreted to represent lack of displacement along normal faults during Tertiary extension. Abundant high-angle faults and fracture zones that strike mainly north-northwest and northeast, are located throughout the Turquoise Ridge deposit; however, the vast majority of the faults in the underground workings lack continuity along strike and down dip. The faults typically have apparent normal displacements of less than a few meters and are difficult to correlate between holes.

Fluid pathways at the Turquoise Ridge deposit were determined based on patterns of lithology, structure, hydrothermal alteration, and gold grade (Muntean et al., 2009; also refer to Chapters 1 and 3). Inspection of gold grades utilizing gold grade thickness maps, block models of gold grade, a three-dimensional geologic model of the

district utilizing GOCAD software, and detailed cross-sections indicate that gold mineralization occurs along complex intersections between: 1) north-northwest-striking high-angle fracture zones sub-parallel to the Getchell fault, 2) the west-northwest-trending southern margin of the sedimentary breccias unit and NPB (refer to Chapters 1 and 3) limbs of north-northeast-trending folds, 4) northeast-trending fracture zones, and 5) calcareous lithologies. Gold mineralization along the east-west and northeast cross-sections (Figs. 2.3 and 2.4) is confined along narrow zones including: 1) the Getchell fault; 2) high-angle, antithetic fracture zones in the hanging wall of the Getchell fault; 3) the main dacite dike; and 4) high-angle north-northwest- and north-northeast-trending fracture zones in the hanging wall of the main dike (148 zone, see Fig. 9). Moderate to strong alteration, which typically contains gold grades of >0.34 ppm, is most prominent in the western portions of the cross-sections where antithetic fracture zones in the hanging wall of Getchell fault intersect the footwall of the main dacite dike (HGB zone and BBT zone, see Fig. 5).

Hydrothermal solutions are interpreted to have migrated up the Getchell Fault Zone and then into the steeply west-dipping antithetic fracture zones in the hanging wall of the Getchell Fault Zone (Fig. 2.5). These fluids are believed to have fed the HGB ore zone which occurs along the west-northwest-trending basin margin as defined by the southward pinch-out of the sedimentary breccia unit and the NPB (Muntean et al., 2009). Fluid migration along the eastern portion of the section occurred along a northeast-trending fracture zone that tapped the Getchell fault at depth (Deep East Feeder). The ascending fluids either breached the main dacite dike and continued

flowing upward along steeply-dipping fracture zones (148 zone) or they traveled westward up-dip along the margins of the dike and escaped along exhaust zones in the hanging wall of the dike. Fluid flow in the exhaust zones was passive and opportunistic and took advantage of local fractures and lithologic contacts. Fluid flow throughout the Turquoise Ridge deposit was primarily discordant to bedding.

Figure 2.3. Geologic interpretation of the underground combined 2360200N-2360300N east-west cross-section. Interpreted and constructed by John Muntean (unpublished). The cross-section is composed of surface holes from the 2360200N cross-section (mostly on the west end of the section) and underground fans of core holes from the 2360300N cross-section (central and east end of the section). The section is an underground section looking north. The top of the section is approximately 1,500 feet below the surface; the bottom 3,000 feet. Purple unit consists of the lowermost planar carbonaceous mudstones and limestones containing local bedding disruptions and sporadic turbidite sequences consisting of coarse-grained calcarenite. Stippled unit represents the upper and lower member of the sedimentary debris flow breccia unit (see text for discussion). The upper brown mudstones (brown) and limestones (blue) represent non-calcareous brown mudstones containing variable amounts of micritic limestone. The interbedded Northern Pillow Basalt (NPB) is represented in green. The section is intruded by Cretaceous dacite porphyry dikes (e.g., main dacite dike within the center of the cross-section; eastern dacite dike within the Getchell Fault Zone). The Getchell fault (blue checkered pattern) is located the southeastern portion of the section. Note labeled drill holes represent the holes that were stained for this study.

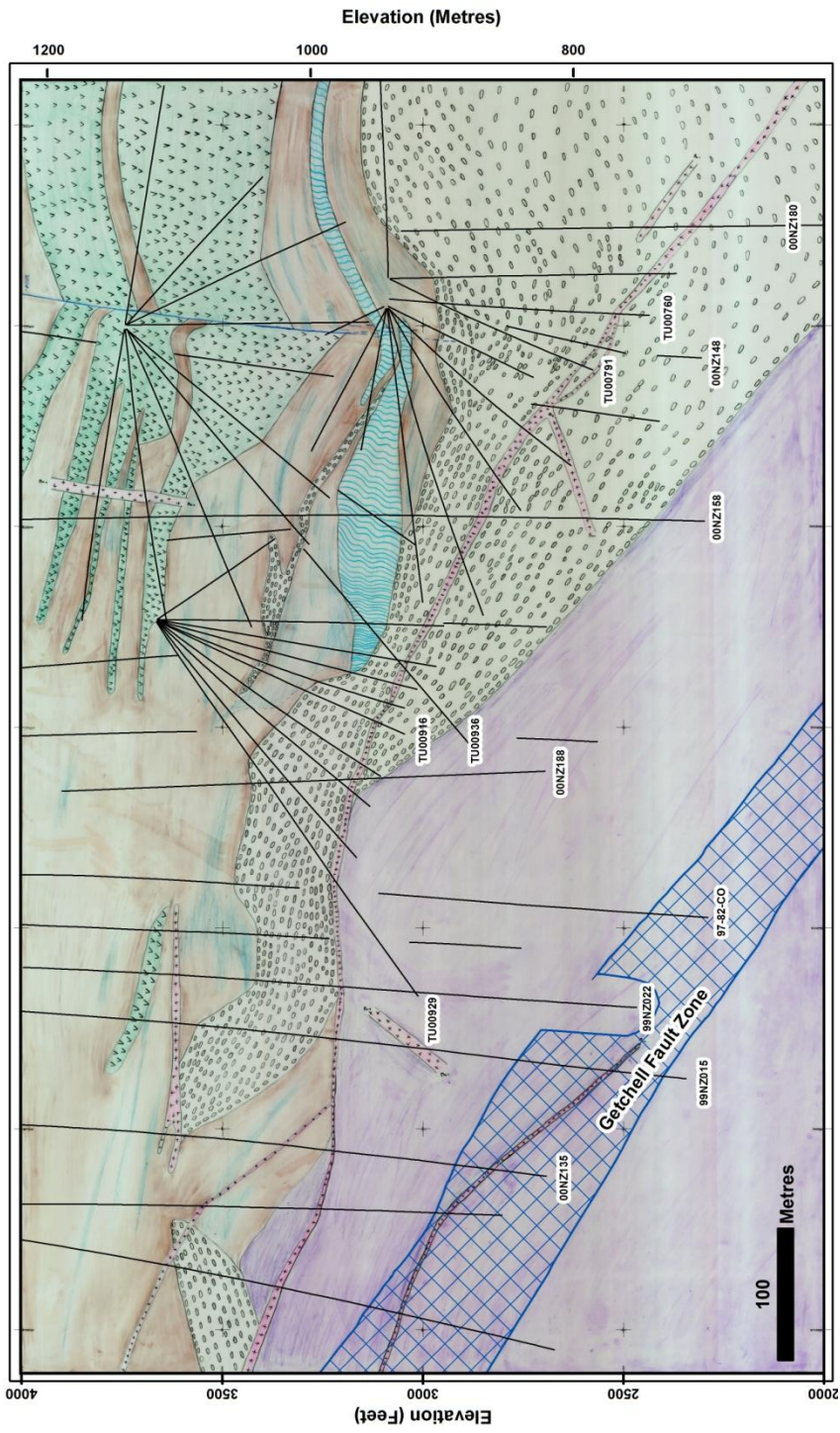


Figure 2.3

Figure 2.4. Interpreted geology of the northeast underground cross-section constructed from four surface diamond drill holes and a fan of five underground diamond drill holes through the Turquoise Ridge deposit oriented N55°E (section 3370, drill station 3) extending roughly 550 m to 975 m below the surface. The section's length extends roughly 720 m. Purple unit consists of the lowermost planar carbonaceous mudstones and limestones containing local bedding disruptions and sporadic turbidite sequences consisting of coarse-grained calcarenite. The variably siliceous mudstones within this lower carbonaceous planar mudstone and limestone unit is represented in solid grey. The sedimentary breccias unit is represented by the upper (white stippled) member and the lower (purple stippled) member (see text for discussion). The upper brown mudstones (brown) and limestones (blue) represent non-calcareous brown mudstones containing variable amounts of micritic limestone. The interbedded northern pillow basalt (NPB) is represented in green. The section is intruded by Cretaceous dacite porphyry dikes (e.g., upper dacite dike intruding the brown mudstone and limestone unit; main dacite dike within the center of the cross-section; eastern dacite dike within the Getchell Fault Zone). The Getchell fault (blue checkered pattern) is located the southeastern portion of the section. Note labeled drill holes represent the holes that were stained during the duration of this study.

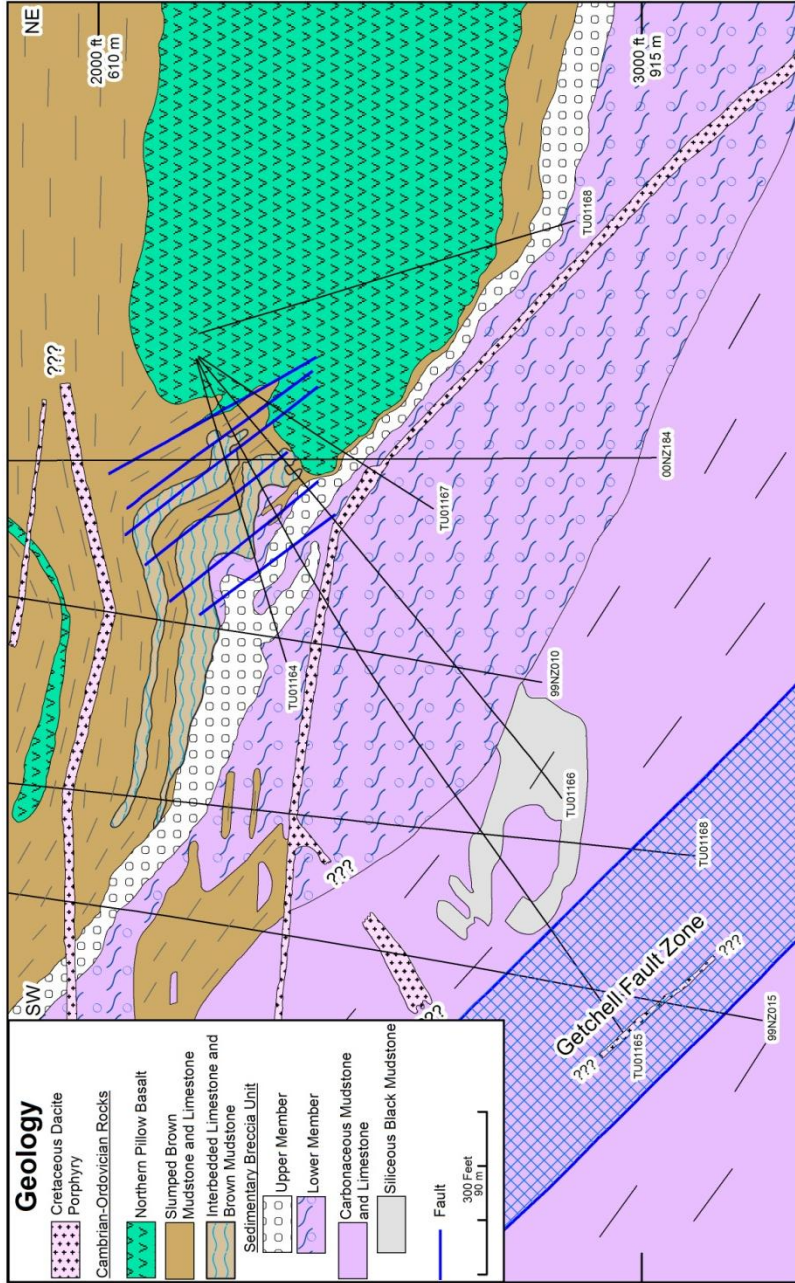


Figure 2.4

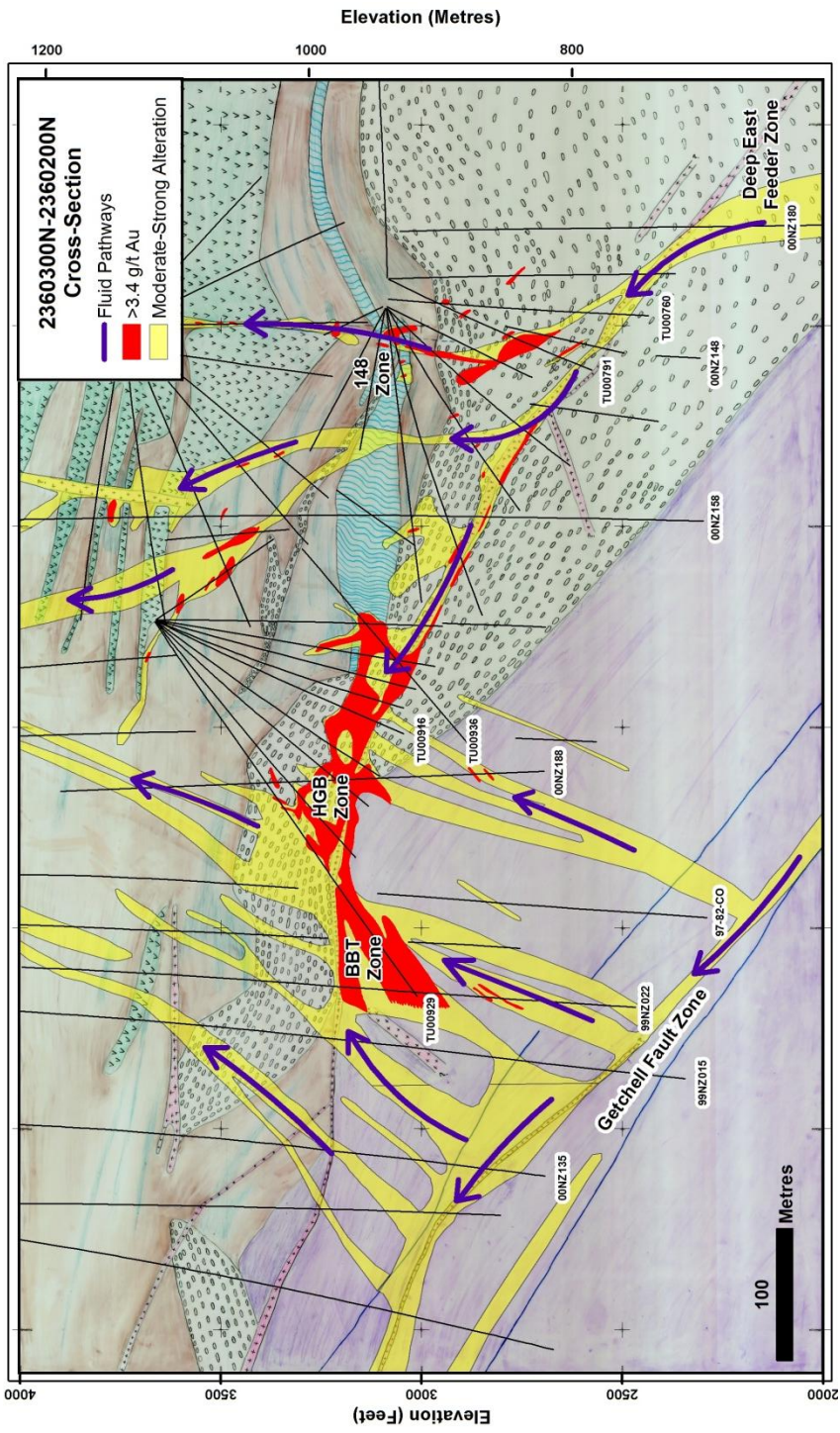


Figure 2.5. Combined 2360200N-2360300N east-west cross-section showing moderate to strong visible hydrothermal alteration (decalcification, argillization, and silicification) correlating with ≥ 0.34 ppm Au (yellow) and ≥ 3.4 ppm Au (red). Note purple arrows depicting interpreted fluid pathways. Refer to Figure 2.3 for descriptions of lithologic

CARBONATE STAINING TECHNIQUES

Stock Solutions

A variety of carbonate staining techniques has been described in the published literature (Freidman, 1959; Warne, 1962; Reid, 1969). The simplest and most effective technique, utilized in this study, is one derived by Dickson (1966), which consists of a dilute hydrochloric acid solution containing alizarin red S and potassium ferricyanide. An extensive review of carbonate staining techniques was published by Hitzman (1999) and is briefly reviewed here (Table 2.1). Alizarin red S reacts with calcite producing a pink stain, but does not react with dolomite, resulting in no stain. Potassium ferricyanide produces a precipitate of Turnbull's blue in the presence of ferrous iron (Dickson, 1966). Ferrous iron can readily substitute for calcium and magnesium within the trigonal carbonate crystal structure. The 50-50 mixture of alizarin red S and potassium ferricyanide reacts with carbonate minerals producing a variety of shades of red, pink, purple, and blue depending on the dominant cations within the carbonate crystal structure. Three working stock solutions should be prepared when conducting carbonate staining. The standard stock solutions consist of 250 ml of 2% HCl. This concentration can be produced by mixing 60 ml of 10% HCl with 190 ml of distilled H₂O. The potassium ferricyanide solution consists of 1.25 g of potassium ferricyanide dissolved into 250 ml of 2% HCl. The alizarin red S solution consists of 0.3 g of alizarin red-S dissolved into 250 ml of 2% HCl. These stock solutions can then be mixed together in a 50-50 concentration to create the 50-50 stock solution. Powdered crystals of both alizarin red S and potassium ferricyanide work best to ensure quicker and more uniform

mixing of the stock solutions. Stock solutions should be stored in tinted glass bottles to reduce exposure to light.

Table 2.1. Color of common carbonate minerals after staining

Carbonate Mineral	Alizarin Red S	Potassium Ferricyanide	Combined Reagents
Calcite (CaCO_3)	Pink to red	Unstained	Pink to red
Ferroan Calcite (Ca,FeCO_3)	Pink to Pale Pink	Pale to deep blue	Purple
Dolomite ($\text{CaMg}(\text{CO}_3)_2$)	Unstained	Unstained	Unstained
Ferroan Dolomite ($\text{Ca}(\text{Mg,Fe})\text{CO}_3)_2$)	Unstained	Pale to deep blue	Pale to deep blue

Application of Stains

Utilization of all the three stock solutions consisting of 1) alizarin red S solution 2) potassium ferricyanide solution and the 3) 50-50 solution is the most effective method for carbonate mineral identification. First, for optimal staining results, sawed pieces of drill core were first etched by applying a uniform coat of 2% HCl and waiting 1-2 minutes. The samples were then stained by applying a uniform coat of the 50-50 stock solution onto the etched surface. After staining, the samples were allowed to air dry or were lightly dried with a towel. The staining results were interpreted while the samples were still slightly damp. Color shades can change somewhat once the sample dries. A damp surface has more noticeable, vibrant shades of pink, purple, and blue that allows for more consistent interpretation. Painting the solutions on the sawed drill core with a brush and then wiping off excess solution results in subdued colors. Uncut drill core or uneven surfaces can be difficult to apply even coats of stain; therefore, it is best to apply small drops of solution onto uneven surfaces. If complete stain coverage

is desired on these uneven surfaces, painting of the solution can be done. If one paints on the solution with an applicator brush, multiple coats are recommended to ensure the proper reaction time between the sample and the stock solutions. Typically, multiple coats provide more vibrant colors that are easier to interpret.

Stain Interpretation

The 50-50 stain solution when applied to fresh carbonate surfaces will stain a variety of shades of pink, red, purple, and blue. When various color shades are not clearly distinguishable when stained using the 50-50 mixture, rocks should be stained with the individual solutions. For example, the individual solutions can be used to distinguish darker shades of pink and lighter shades of purple produced by staining with the 50-50 mixture. If a sample is composed of ferroan calcite, the potassium ferricyanide solution will react with iron resulting in a blue stain and the alizarin red S solution will stain the calcite pink to red.

Carbonate staining conducted on recrystallized micrite and calcarenite limestones revealed calcite and ferroan calcite to be the dominant carbonate species throughout the Turquoise Ridge deposit. [Figure 2.6](#) shows a typical example of non-ferroan calcite in calcarenite from the lower carbonaceous mudstone/limestone unit, displaying both a pink-staining rock matrix and pink-staining veins. [Figure 2.7](#) shows ferroan calcite (purple stain) in micritic limestone interbedded with brown mudstone. Note the upper left hand corner where the potassium ferricyanide, the alizarin red S, and 50-50 mixture were utilized to accurately determine the staining characteristics of the sample. [Figure 2.8](#) shows a sample that was collected within the calc-silicate

contact aureole associated with the Osgood stock. It shows the replacement of calcite (pink) by ferroan dolomite (blue) in the wall rock, which is cross-cut by late calcite (pink) veins.

In order to ensure that the staining results were reliable, 12 samples were analyzed using the electron microprobe at the University of Nevada Las Vegas. They were analyzed using energy-dispersive spectrometry (EDS) to determine whether or not there was detectable iron in samples. Neither the pink- nor the purple-staining carbonates displayed iron peaks when analyzed using EDS. Initially, this cast doubt on the reliability of the staining results. Subsequently, samples were analyzed by wavelength-dispersive spectrometry (WDS) using the electron microprobe at the University of Michigan (John Muntean, unpublished data). The WDS analyses showed that potassium ferricyanide will stain carbonates with iron concentrations as low as approximately 0.15 weight percent. The majority of the pink-staining calcite samples had iron concentrations below 0.10 weight percent, while most purple-staining ferroan calcites and blue-staining ferroan dolomites had Fe-concentrations greater than 0.15 weight percent.

Precautions

One needs to be aware that the potassium ferricyanide solution is highly unstable and tends to break down after one to two weeks. Exposure to sunlight will increase rate of the degeneration of the solution. The solutions should be kept in dark brown bottles and away from direct sunlight whenever possible to ensure a longer shelf life. The degeneration of the potassium ferricyanide solution causes false staining colors

to develop. Old, degenerated solution will begin to stain all carbonates purple.

Advanced degenerative states of this solution will develop purple particulates at the base of the container that will be distributed throughout the entire solution during mixing. The alizarin red S solution is much more stable and can be effectively used for up to a month or more if it has not been mixed with potassium ferricyanide.



Figure 2.6. Example of carbonate staining from the east-west cross-section (hole 00NZ158 2237.5 ft). Lower carbonaceous mudstone/limestone unit showing pink stain, indicating calcite, both in the veins and the calcarenite wall rock.

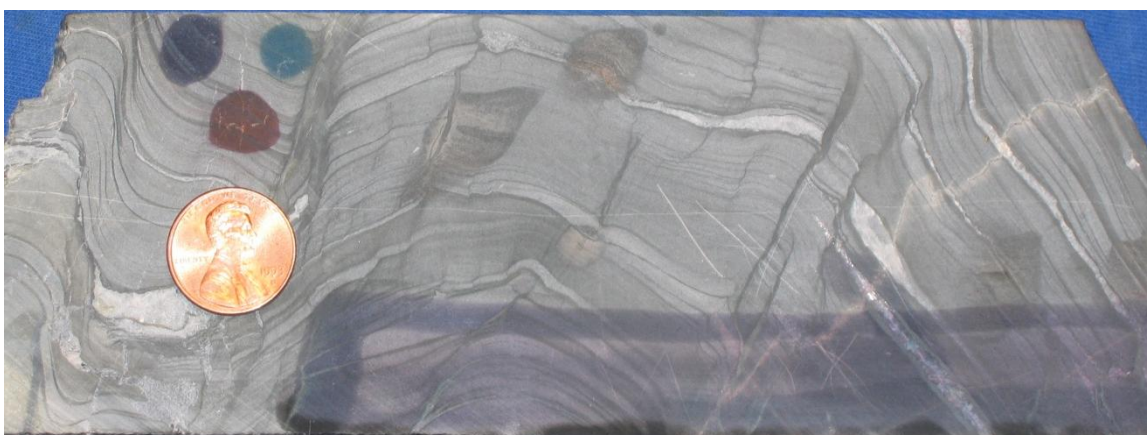


Figure 2.7. Example of carbonate staining from the east-west cross-section (hole 00NZ158 2237.5 ft). Upper thin bedded limestone/mudstone showing purple stain, indicating ferroan calcite, both in the veins and the calcarenite wall rock. Note upper left corner displaying the staining characteristics of the three separate stock solutions.



Figure 2.8. Example of carbonate staining collected from background samples within the contact aureole (green dashed line in Figure 2.8). Near total replacement of calcite (pink “speckles” within the blue stain) by ferroan dolomite (blue stain) containing crosscutting calcite (pink stain) veins (hole 00MW161A 3847.5 ft).

Due to the instability of the potassium ferricyanide solution, the utilization of smaller stock solutions, ideally 125 ml, is highly recommended. Although making smaller stock solutions is more time-consuming, this method ensures that all reagents will be utilized without having to dispose of any unused material due to chemical breakdown. This precautionary step ensures more accurate staining results, saves chemical supplies, and is more cost effective.

Samples containing non-carbonate, iron-bearing minerals can cause “iron-bleeding” to occur. This iron-bleeding can cause misinterpretation of the staining results. Iron-bleeding is particularly evident during casual staining of core (e.g., with a brush) where misleading results are likely to arise. Particular attention is warranted by the researcher doing the staining to try to avoid staining iron-bearing silicates (e.g., clays or micas) and iron sulfides. Application of the three stock solutions as individual drops in areas away from sulfides and mudstones can allow for more accurate determination

of individual carbonate species. Most of the samples stained for this study were examined with a binocular microscope during staining to check for such complications.

Table 2.2 summarizes precautionary measures that should be adopted in any carbonate-staining program.

The removal of the stain from the surface of carbonates can be accomplished by applying 10% HCl to the carbonate surface and wiping clean. Calcite and ferroan calcite stains are effectively removed with this method. Ferroan dolomite stains and staining of iron-bearing non-carbonate minerals can be difficult to remove. If stains do not come off with acid, the stain can be ground off with a flat-surface grinding wheel.

Table 2.2. Carbonate Staining Recommendations

- 1) Work with three separate stock solutions as necessary to differentiate darker shades of pink from lighter shades of purple.
- 2) Use powdered crystals of both reagents (alizarin red S and potassium ferricyanide) to ensure complete mixing of stock solutions.
- 3) Store stock solutions in tinted glass and limit exposure to prolonged sunlight. Do not store solutions in metal containers
- 4) To ensure consistent, accurate staining results, replace stock solutions (particularly potassium ferricyanide) within days to no more than 2 weeks, depending on amount of sunlight exposure.
- 5) Apply uniform coat of stock solution with acid dropper. On uncut drill core and uneven, broken surfaces, apply small drops of stock solution to ensure an even coat of stain.
- 6) Allow 1-2 minutes for accurate stain color to develop.
- 7) If utilizing brush to paint sawed drill core, apply multiple coats to ensure vibrant stain colors develop.
- 8) Avoid staining Fe-bearing silicates and Fe-sulfides during casual staining of core. "Fe-bleeding" may cause inaccurate stain interpretations
- 9) Utilize binocular microscope while staining if staining characteristics remain unclear.

RESULTS OF CARBONATE STAINING AT TURQUOISE RIDGE

Carbonate staining was done on samples collected from core holes along the east-west cross-section (Fig. 2.3). In addition, carbonate staining was done while logging core holes along the northeast cross-section. However, in order to establish the local background staining characteristics of the Cambrian-Ordovician carbonates in the Getchell District, staining was first conducted on 48 samples collected from eight core holes from intervals that assayed <5 pbb gold. The goal of the background staining program was to determine the regional carbonate zonation patterns distal to gold mineralization. The holes were located at least 600 m from known ore zones. In addition, samples were stained from five surface localities on the west side of the Osgood stock, 2.5 km from the gold deposits at Getchell. These samples selected for background did not contain visible Carlin-type alteration or mineralization (e.g., decalcification, argillization, silicification, or fine-grained pyrite). The staining characteristics of these background samples were variable and showed no recognizable pattern in relation to the gold deposits at Getchell or to the Osgood stock (Figure 2.9).

Eleven of the 13 background localities contain non-ferroan calcite. Ferroan calcite is present in five localities and dolomite is present in three localities. Many background samples consist of multiple carbonate species with some drill holes containing all four carbonate species (calcite, ferroan calcite, dolomite, and ferroan dolomite). The majority of the light grey recrystallized limestone beds adjacent to zones replaced by calc-silicates are composed of calcite. Dolomite often replaces calcite within the calc-silicate contact aureole. Locally, recrystallized limestones in drill holes

containing calc-silicate alteration contain ferroan calcite and/or calcite that have been overprinted by patchy ferroan dolomite (e.g. [Fig. 2.8](#)).

The spatial distribution of ferroan versus non-ferroan carbonate in carbonate-bearing lithologies along the east-west cross-section reveals a distinct zoning from calcite at depth on the west side of the cross-section to ferroan calcite to the east and at higher elevations ([Figure 2.10](#)). Non-ferroan dolomite was recognized in only a few samples. Carbonate veins show a very similar pattern to the carbonate in the rocks ([Figure 2.11](#)). Non-ferroan calcite in rocks and veins are concentrated along the interpreted Gatchell Fault Zone and in the footwall of the HGB ore zone below the main dacite porphyry dike. Ferroan calcite in rocks and veins is widespread above the main dacite porphyry dike, but is commonly present below the dike on the east side of the east-west cross-section and locally on the very west side of the east-west cross-section. The northeast cross-section shows a very similar zonation ([Figure 2.12](#)). The transition between calcite and ferroan calcite in both cross-sections occurs approximately at the base of the HGB ore zone. Gold grades greater than 3.4 ppm in both cross-sections mainly occur in rocks containing ferroan calcite, but straddle the boundary between calcite and ferroan calcite. High-grade ore (>17 ppm Au) is entirely within zones of ferroan calcite in the northeast cross-section. Close examination of the distribution of ferroan calcite along both cross-sections indicates that the carbonate staining pattern is not stratabound. For example, ferroan calcite extends throughout the upper brown mudstones and limestones, the debris flow breccias, and the lower planar carbonaceous

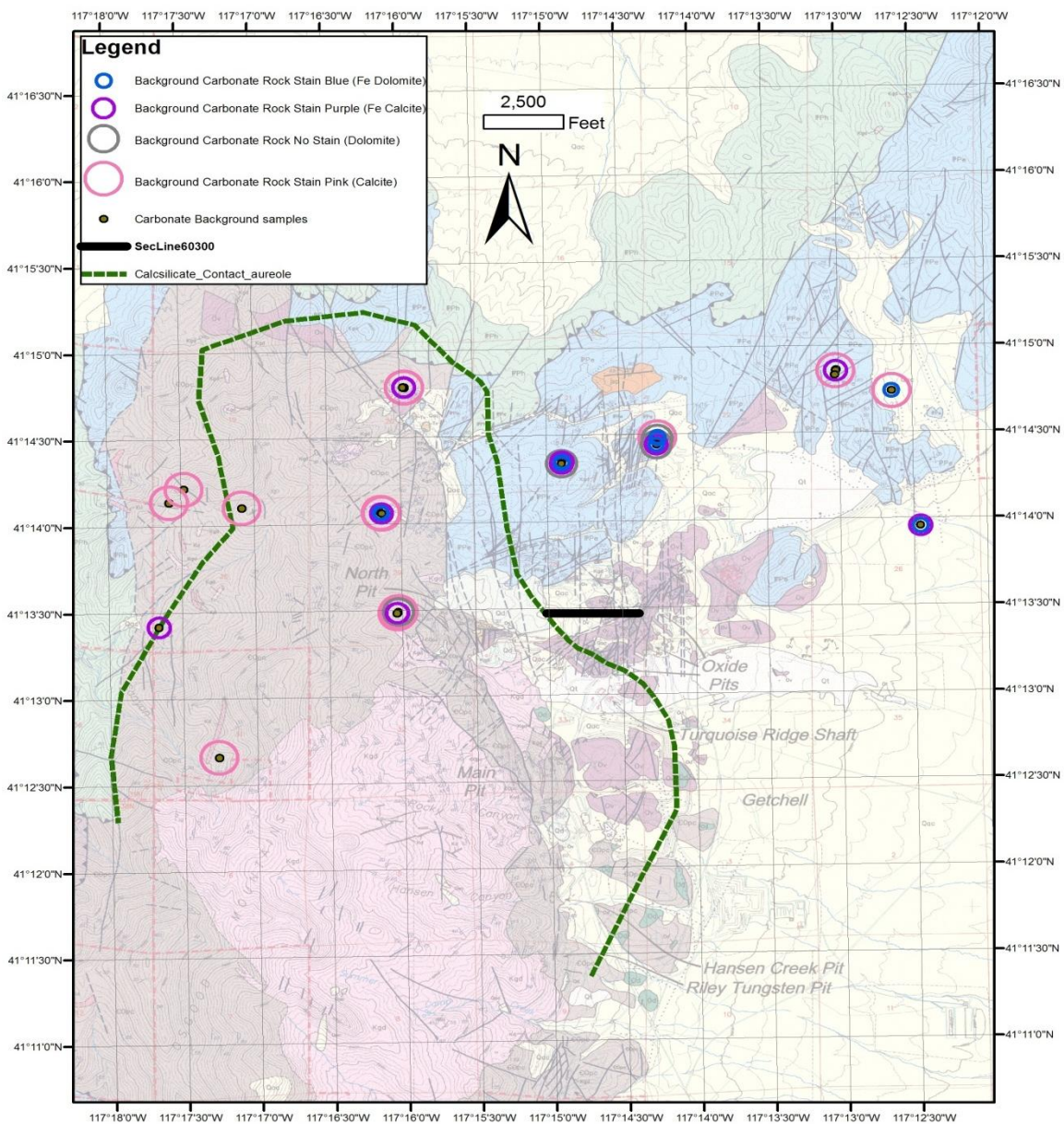


Figure 2.9. Map view of Getchell District showing staining characteristics of carbonate wall rocks, distal to CTGDs. The green dashed line represents the contact aureole of the Osgood stock, determined by the presence of calc-silicates on the surface or in drill holes. Black line represents the combined east-west 2060200N-2060300N cross-section. Background is geologic map compiled by Placer Dome geologists (See Figure 2 for unit descriptions). Note five western most localities are from surface samples, whereas remaining localities are core holes.

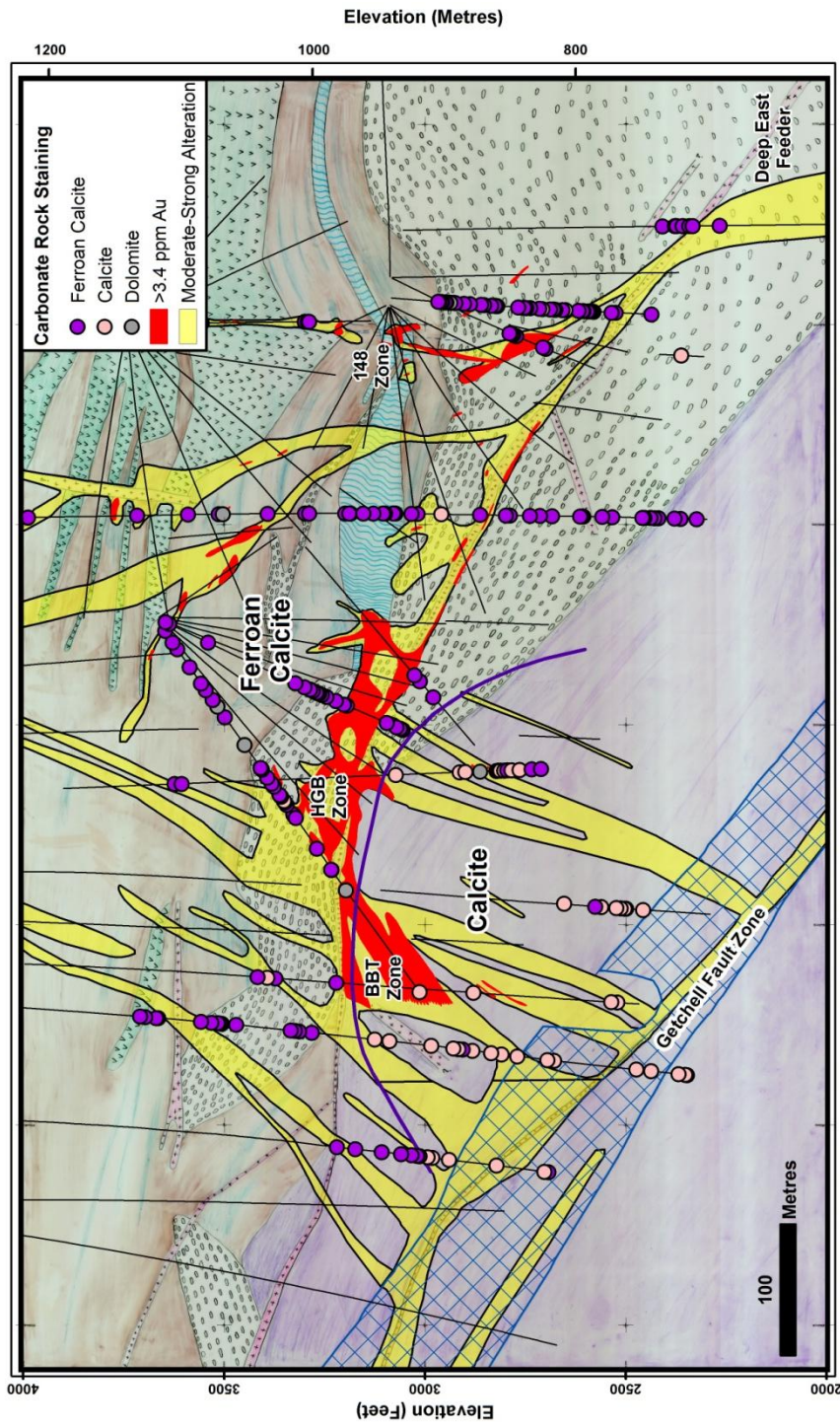


Figure 2.10. Underground east-west cross-section showing results of staining of carbonate wall rock relative to gold grades and visible decalcification, argillization, and silicification related to gold mineralization. Point data represents the different carbonate mineralogy of samples that were stained. Note most of the gold grades ≥ 3.4 ppm Au occurs within rocks that contain ferroan calcite (purple dots). Refer to Figure 3 for descriptions of underlying geologic units.

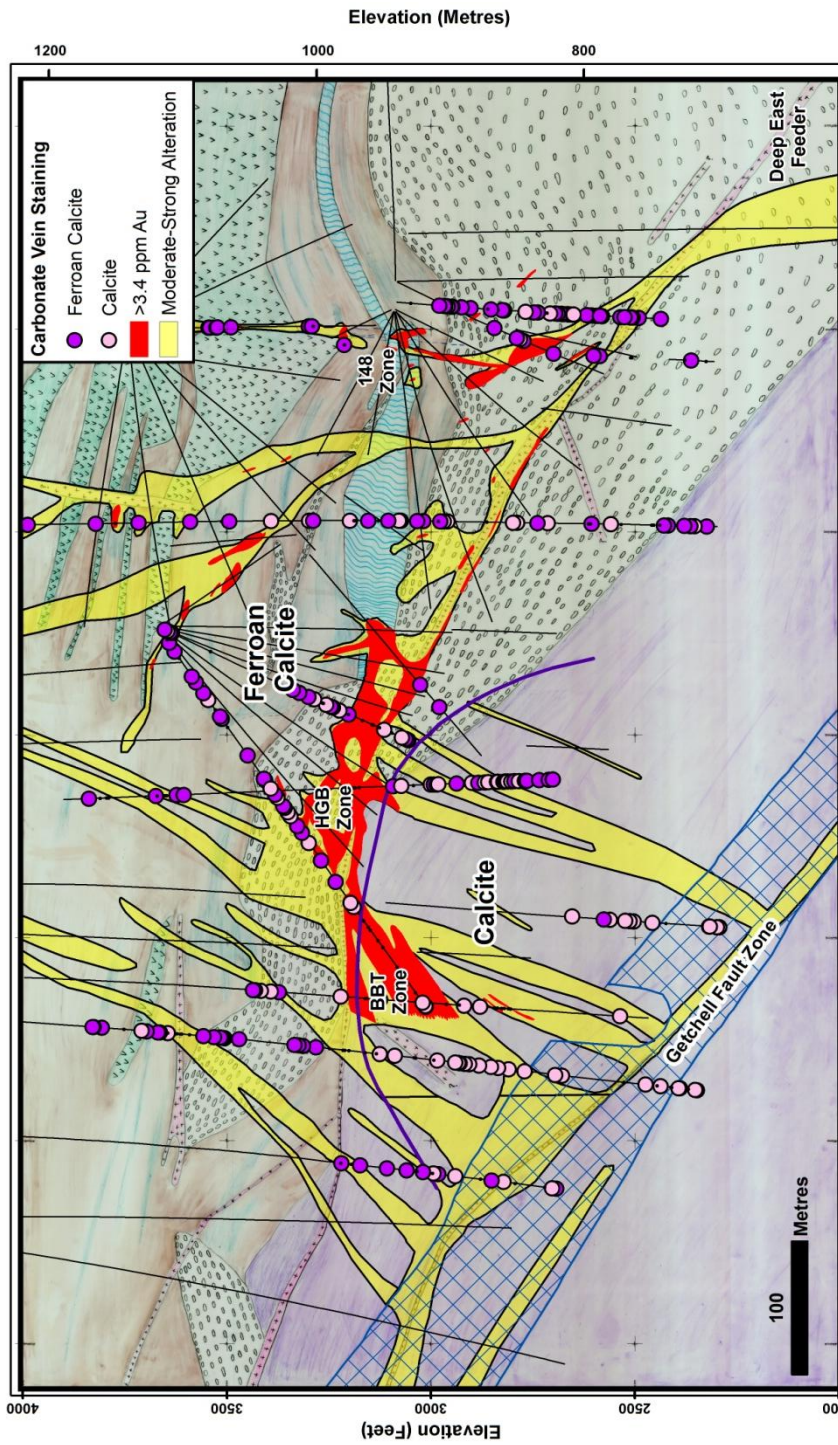


Figure 2.11. Underground combined 2360200N-2360300N east-west cross-section showing results of staining of carbonate veins relative to gold grades and visible decalcification, argillization, and silicification related to gold mineralization. Point data represents the different carbonate mineralogy of samples that were stained. Purple line represents the transition from ferroan calcite to calcite with depth.

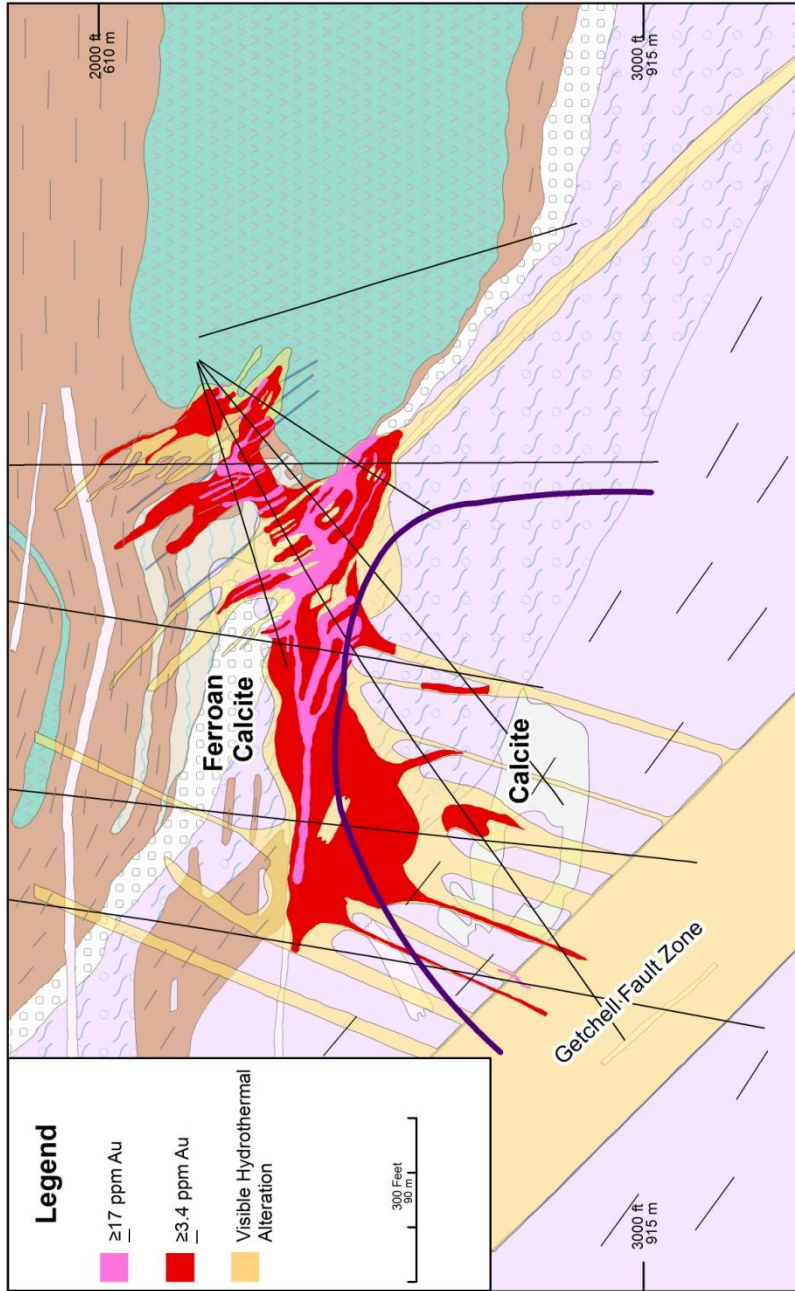


Figure 2.12. Underground northeast cross-section showing distribution of visible hydrothermal alteration and Au-grade relative to calcite and ferroan calcite determined by continuous downhole staining of rocks and veins that was conducted during core logging. The purple line represents the boundary between calcite and overlying ferroan calcite in both the wall rock and in veins. Refer to Figure 4 for detailed description of geologic units.

mudstones and limestones in the eastern portions of the east-west and northeast cross-sections.

Due to the close spatial association between ferroan calcite and the HGB ore zone, carbonate staining was conducted on an additional eleven core holes (31 total, including cross-sections) in the Turquoise Ridge deposit, up to 1,650 m north and 1,200 m south of the east-west and northeast cross-sections. Carbonate staining was conducted in order to test whether the pattern of deep calcite to the west extended beyond the east-west and northeast cross-sections. The expanded carbonate staining found that individual drill holes transitioned from ferroan calcite to calcite with depth, contained ferroan calcite throughout the length of the drill hole, or displayed no systematic staining pattern. The holes lacking systematic patterns were located within the metamorphic contact aureole marked by significant development of calc-silicate minerals. [Figure 2.13](#) shows elevation contours that mark the boundary between calcite and overlying ferroan calcites, relative to the east-west and northeast cross-sections, the southern margin of the NPB, the calc-silicate contact aureole, and gold at Turquoise Ridge. The boundary between calcite and overlying ferroan calcite dips northeast underneath the NPB. The ferroan calcite occurs in close proximity both laterally and vertically to the NPB. The shape of the calcite-ferroan calcite contact closely mimics the spatial distribution of the NPB, with ferroan calcite extending directly below and extending laterally away from the NPB. All of the stained core holes that were drilled through the NPB (excluding drill hole 99NZ073 which intersected the Getchell Fault Zone) contain ferroan calcite to the bottom of each drill hole (e.g. < symbols in [Figure](#)

2.13). The spatial distribution of ferroan carbonate within the calc-silicate contact aureole is not systematic. Carbonate staining within the Turquoise Ridge deposit outside of the calc-silicate contact aureole reveals an apparent systematic spatial association between ferroan calcite, the NPB, and possibly gold mineralization. In order to further test the association between ferroan calcite and gold mineralization at the scale of the entire Turquoise Ridge deposit, a three-dimensional surface of the calcite-ferroan calcite needs to be constructed and compared with ore shells using three-dimensional computer software such as Vulcan or GOCAD.

Potential Causes for Ferroan Calcite Distribution

The apparent close spatial association between ferroan calcite, gold mineralization, and the NPB brings into question the timing of ferroan calcite formation relative to gold mineralization. This spatial association suggests that iron may have been remobilized out of the basalt and into the underlying carbonates during diagenesis, seawater alteration, the emplacement of the Osgood stock, or during Eocene gold mineralization (syn-ore). The formation of diagenetic ferroan carbonate typically occurs when seawater sulfate is reduced to react with iron in sediment resulting in the formation of pyrite. This formation of pyrite can be limited in sulfate-poor diagenetic environments which leads to an increase of iron in diagenetic carbonate minerals (Canfield, 1989, 1991; Raiswell and Canfield, 1998). Therefore, if the carbonate mineralogy at Turquoise Ridge was derived from diagenesis, the distribution of ferroan and non ferroan calcite should be stratabound. This relationship is not seen at Turquoise Ridge where ferroan carbonate and non ferroan carbonate are present in

similar stratigraphic units (e.g. planar carbonaceous mudstones and limestones; sedimentary breccia unit). The spatial association between the ferroan calcite and the propylitically-altered northern pillow basalt suggests iron may have been remobilized out of the basalt for a distance into the underlying carbonates during seawater alteration of the basalt during the Cambrian-Ordovician. The NPB at Turquoise Ridge

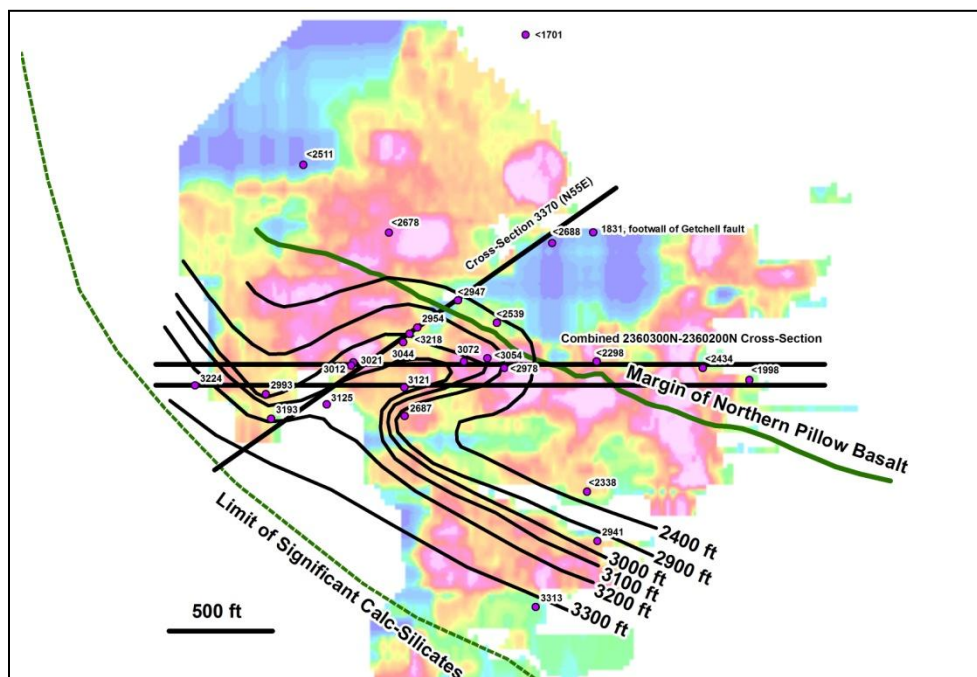


Figure 2.13. Expanded carbonate staining conducted along the Turquoise Ridge corridor. Map shows block model of gold grades that was constructed by Placer Dome in 2003 by vertically summing of blocks. Red represents higher gold grades; the blue represents lower grades. The colors are the limits of the model. The solid green line depicts the blunt southern margin of the west-northwest striking northern pillow basalt (NPB). The dotted green line represents the limit of significant calc-silicates associated with the Osgood stock. The east-west (combined 2360200N-2360300N) cross-section and the northeast (3370 N55°E) cross-section are shown by thick black lines. The purple dots indicate drill holes, in which staining was conducted. The labels next to the purple dots are the lowest elevations that ferroan calcite occurred within each drill hole (contact between ferroan calcite surface and calcite surface). The labels with the less than symbols indicate ferroan calcite was present to the bottom of the hole. The contour lines are elevations of the interpreted boundary between ferroan calcite and underlying calcite. Note that the calcite body dips northeast underneath the NPB. See text for further discussion.

has undergone propylitic alteration where primary mafic minerals have been replaced by chlorite, and plagioclase has been variably altered to albite and K-feldspar, likely during low-temperature seawater alteration. Alternatively, iron may be remobilized into adjacent carbonate strata during contact metamorphism and hydrothermal activity associated with the emplacement of the Osgood stock as discussed in detail below.

Ferroan carbonate minerals are commonly associated with igneous or contact metamorphic host rocks at various CTGDs originally containing primary iron oxide and iron silicate minerals (Hofstra and Cline, 2000).

Alternatively, the ferroan calcite could have formed during ore formation. The presence of hydrothermal ferroan carbonate adjacent or distal to ore zones in CTGDs has been speculated to represent evidence of CO₂ metasomatism of iron-bearing minerals resulting from decalcification during formation of CTGDs (Hofstra et al., 1991; Hofstra and Cline 2000). High fluxes of acidic sulfide-rich fluids along the Getchell Fault Zone and in fluid pathways in its hanging wall below the HGB would have prevented formation of iron carbonate, however, sulfide-depleted fluids rich in CO₂ derived from dissolution of carbonates could have formed above the HGB by carbonation of iron-bearing minerals in the rock. However, much of the ferroan calcite occurs in clean micrite and shows no evidence of replacement of any precursor iron minerals, arguing against carbonation of iron-bearing minerals.

Fortuna et al. (2003) proposed that iron within the Paleozoic sedimentary rocks at the nearby Twin Creeks deposit was sourced from interbedded basalts. The basalts at Twin Creeks were shown to be enriched in iron and potassium relative to average

basaltic compositions. The basalts were proposed to have provided an abundant iron reservoir, from which iron was ultimately remobilized into the adjacent sedimentary strata. This argument was substantiated by the documentation of two stages of hydrothermal alteration associated with the basalts at Twin Creeks. The first stage of alteration consists of the replacement of primary mafic minerals by iron-rich chlorite, replacement of Fe-Ti oxide minerals by rutile and iron-rich chlorite, and alteration of plagioclase feldspars to albite and K-feldspar, which Fortuna et al. (2003) interpreted to be the result of low-temperature seawater alteration. Analogous chlorite-rich alteration assemblages have been documented at modern midocean ridges (Alt et al., 1985, 1998). The first alteration event was followed by replacement of the iron-rich chlorite by illite or sericite, possibly associated with the emplacement of Cretaceous intrusions. Ar-Ar dating by Hall et al. (2000) of illite within altered intrusive and volcanic rock in the Twin Creeks Megapit indicated the illite formed at about 109-103 Ma. This age is similar to an altered and gold mineralized porphyritic dacite dike within the Vista pit (Twin Creeks) dated at 114 ± 2 Ma (Breit et al., 2005), but is significantly older than the 92-90 Ma Osgood stock (Groff et al., 1997). These widespread age dates suggest that this second state of alteration was likely derived from a protracted Cretaceous igneous-hydrothermal event that took place between 109-83 Ma (Hall et al., 2000). Furthermore, Ar-Ar dating conducted on adularia associated with CTGD ore-stage mineralization at Twin Creeks indicates adularia formed around 42 Ma (Eocene). Therefore, Fortuna et al., (2003) concluded that the formation of ferroan dolomite at Twin Creeks was derived from the liberation of iron during sericitization of propylitized

basalt during a Cretaceous hydrothermal event, resulting in the formation of illite along the basalt margins. They interpreted iron was remobilized out of the margins of the basalt and into the adjacent sedimentary rocks during this Cretaceous event, forming ferroan dolomite. Subsequent interaction of reduced sulfur-rich auriferous fluids and reactive ferroan dolomite resulted in sulfidation and the deposition of auriferous pyrite in the Eocene.

In contrast to Twin Creeks, there is no evidence for widespread sericitization along the margins of the NPB at Turquoise Ridge. Rather, iron appears to have been liberated from the NPB by 1) seawater alteration and/or, 2) pervasive/widespread metasomatism derived from the emplacement of the Osgood stock and/or associated hydrothermal activity related to the protracted Cretaceous magmatic events from 103 to 82 Ma. Metasomatic skarn associated with the stock is expressed mainly by tungsten mineralization associated with andraditic garnet and iron-rich diopside and retrograde tremolite/actinolite-epidote-quartz-scheelite-sulfides (Taylor and O'Neill, 1977). Later and/or more distal metasomatic mineralization is expressed by quartz veins that contain variable amounts of carbonate, pyrite, pyrrhotite, arsenopyrite, and base metal sulfides (Cline, 2001). Iron remobilization associated with the emplacement of the Osgood stock is evident in the erratic spatial distribution of iron in carbonates within the calc-silicate-bearing contact aureole. Calcite, ferroan calcite, dolomite, ferroan dolomite all occur within the calc-silicate-bearing contact aureole. Carbonate staining relationships between ferroan and non-ferroan carbonates within the contact aureole suggest that calcite was locally replaced by ferroan dolomite during metasomatism related to the

emplacement of the Osgood stock (see [Fig. 8](#)), but such replacement was not observed outside the calc-silicate-bearing contact aureole. Calcareous strata outboard of the calc-silicate-bearing contact aureole are composed primarily of recrystallized micritic limestones containing calcite or ferroan calcite. Therefore, the widespread metasomatism related to the protracted Cretaceous magmatic events that are responsible for the skarn mineralization throughout the Osgood Mountains is likely responsible for the regional recrystallization of limestone and remobilization of iron from the NPB into the adjacent limestone-dominated sedimentary calcareous strata beyond the calc-silicate contact aureole boundary.

Comparison to other CTGDs

The results of this study are similar to relationships between iron within host rocks and gold mineralization observed in other CTGDs ([Table 2.3](#)). The relationship between gold, iron, and sulfur as sulfide within the Twin Creeks gold deposit indicates that mineralization is concentrated in rocks that had gained sulfur and not iron during the formation of gold-bearing arsenian pyrite (Stenger et al., 1998). As discussed above, the formation of ferroan dolomite adjacent to sericitized basalt margins is interpreted to have been derived from a multi-stage alteration process where iron was liberated from Comus igneous rocks into adjacent sedimentary rocks during a protracted Cretaceous magmatic event, prior to Eocene gold mineralization (Fortuna et al., 2003).

High-grade gold values at the Meikle CTGD dramatically decrease outboard of ferroan dolomite zones (Evans, 2000), indicating the formation of ferroan dolomite was a critical rock-preparation event that controlled gold mineralization. Evans (2000)

describes five separate breccia events within the Bootstrap limestone of the Silurian-Devonian Roberts Mountains Formation at the Meikle deposit. The first event resulted in formation of breccias during Paleozoic karsting along the shelf margin during sea water regression. Evans (2000) laid out evidence that these Paleozoic karsts were then subsequently overprinted by a late Paleozoic (?) Mississippi Valley type (MVT) hydrothermal event that resulted in the replacement of massive limestone by ferroan dolomite. Gold-related hydrothermal alteration in the Eocene resulted in ore-stage hydrothermal dissolution, collapse, and intense replacement of the permeable ferroan dolomite body along primary structures, resulting in the deposition of fine-grained auriferous pyrite and/or hydrothermal quartz. Later breccias mark the collapse of the hydrothermal system. In contrast, Emsbo et al., (2003) interpreted ferroan dolomite and base metal mineralization at the adjacent Rodeo deposits in the northern Carlin Trend to be the result of syngenetic sedimentary exhalative (SEDEX) processes during the Devonian. Regardless of the process and timing of the formation of the ferroan dolomite, the emplacement of this reactive ferroan dolomite prior to the migration of Eocene CTGD hydrothermal fluids provided the favorable host rocks responsible for subsequent sulfidation and deposition of auriferous pyrite at the Meikle deposit.

The Storm CTGD occurs at structural intersections and at favorable contacts of the Paleozoic Popovich Formation, the Rodeo Creek unit, and the Bootstrap limestone in the northern Carlin trend. Dobak et al. (2002) described ferroan dolomite breccias in close proximity to ore that have been overprinted by ore-stage silica-sulfide breccias at the Storm deposit. The ferroan dolomite breccias consist of crackle breccias and locally

exhibit “zebra dolomite” textures. Dobak et al. (2002) interpreted the ferroan dolomite breccias to be younger than Jurassic intrusions, based on 162 Ma lamprophyre dike fragments within the ferroan dolomite breccia body. Although there is no sign of a base metal event or Mesozoic dikes at Storm, the ferroan dolomite breccias were interpreted by Trotman (2009) to have been derived from a similar Paleozoic base-metal event proposed by Evans (2000) at the Meikle deposit. High-grade gold mineralization at Storm occurs as cross-cutting and replacement-type silica-sulfide breccias containing 37.57 ± 0.34 Ma basalt dike fragments (Ressel, 2000) that cross-cut ferroan dolomite crackle breccias.

High-grade gold mineralization at the Deep Star deposit is primarily hosted within the calc-silicate contact aureole of the Goldstrike stock. Alteration zonation at Deep Star consists of quartz-sericite-pyrite that is overprinted by quartz-dolomite alteration which is cross-cut by ore-stage quartz-kaolinite mineralization. Clode et al. (2002) interpreted the quartz-dolomite (no mention of ferroan vs. non ferroan dolomite) assemblage to be part of the hydrothermal event associated with Carlin-type mineralization, but do not provide supporting evidence. More detailed paragenetic studies of the Deep Star deposit conducted by Heitt et al., (2003) documented five stages of hydrothermal alteration. Stages 1 and 2 are interpreted to derive from the emplacement of the Jurassic Goldstrike stock and associated metamorphism, metasomatism, and possible retrograde alteration. Stage 3 consists of pre-ore quartz-dolomite alteration that is zoned both vertically and laterally from proximal kutnahorite ($\text{Ca}(\text{Mn}, \text{Mg}, \text{Ca})(\text{CO}_3)_2$) – ankerite ($\text{Ca}(\text{Fe}, \text{Mg}, \text{Mn})(\text{CO}_3)_2$) – ankerite-dolomite – dolomite

distal to ore. Stage 3 alteration is most strongly developed in calc-silicate-bearing rocks. Stage 4 consists of quartz-kaolinite alteration and associated gold mineralization that is hosted in As-rich rims on marcasite and pyrite. Locally, stage 4 quartz is intergrown with dolomite. Stage 4 mineralization is cross-cut by the 38 Ma Deep Star rhyolite. Post ore stage 5 alteration consists of calcite, siderite and barite. Thus, Heitt et al. (2003) argue for formation of ferroan carbonate prior to ore formation but suggest it formed during the Eocene, rather than during emplacement of the Goldstrike stock or by Paleozoic hydrothermal activity.

In the Jerritt Canyon district, Hofstra (1994) reported carbonates zoned from dolomite – dolomite±ankerite – calcite progressively distal from ore at the West Generator CTGD. Recent carbonate staining along the lowermost Roberts Mountain Formation throughout the Jerritt Canyon district by Patterson (2009) showed ferroan dolomite forms the largest, most consistent haloes to CTGDs in the district. The ferroan dolomite halo extends up of 500 feet beyond the 50 ppb Au contour along the base of the Roberts Mountains Formation. Unlike Getchell and the northern Carlin trend, there is no evidence of Mesozoic magmatism and hydrothermal activity in the Jerritt Canyon District. Similar to Evans' (2000) interpretation for Meikle, Patterson (2009) concluded that the formation of non-ferroan dolomite occurred during a Paleozoic base metal event.

Table 2.3. Characteristics of Ferroan Carbonates Surrounding Ore in other CTGDs.

Deposit	Nature of haloes around ore	References
Turquoise Ridge	<ol style="list-style-type: none"> 1. Distinct zonation between Fe-calcite vs. calcite within both the 2360200N-2360300N and 3370 cross-sections. 2. Spatial association between NPB and Fe-calcite. 3. High-grade Au mineralization (≥ 17 ppm) occurs exclusively within Fe-calcite. 4. Most ≥ 3.4 ppm Au mineralization occurs within Fe-calcite 5. Sporadic distribution of ferroan calcite, ferroan dolomite, calcite, and dolomite within calc-silicate contact aureole associated with emplacement of the Cretaceous Osgood stock. 6. Fe-calcite likely derived from NPB and leached into adjacent carbonates as a result of wide-spread metasomatism related to the protracted Cretaceous magmatic event 103-82 Ma. 	This Study
Twin Creeks	<ol style="list-style-type: none"> 1. Basalts within the Comus Formation contain elevated Fe relative to average basalt Fe compositions. 2. Formation of albite and Fe-rich chlorite during sea water alteration. 3. Destruction of Fe-rich chlorite by illite or sericite which released iron to form ferroan dolomite into adjacent sedimentary rocks. 4. Eocene auriferous ore fluids overprint reactive ferroan dolomite strata along seritized basalt margins resulting in Au mineralization. 	Fortuna et al., 2003
Meikle	<ol style="list-style-type: none"> 1. Replacement of massive limestone by ferroan dolomite during Paleozoic (?) MVT hydrothermal alteration (Evans, 1999). 2. Replacement of massive limestone by ferroan dolomite during syngenetic SEDEX processes during the Devonian (Evans, 2000). 3. Hydrothermal dissolution and replacement of ferroan dolomite along primary structures resulting in deposition of fine grained auriferous pyrite. 	Emsbo, et al., 1999 Evans, 2000
Storm	<ol style="list-style-type: none"> 1. Ferroan dolomite breccias host ore stage silica-sulfide breccias. 	Dobak et al., 2002
Deep Star	<ol style="list-style-type: none"> 1. Identification of quartz-dolomite assemblage prior to CTGD mineralization. 2. Formation of zoned (vertically and horizontally) quartz-dolomite from kutnahorite – ankerite – ankerite-dolomite – dolomite. 3. Quartz-kaolinite alteration associated with Au mineralization hosted in As-rich rims on marcasite and pyrite spatially associated with quartz-dolomite alteration 	Clode et al., 2002 Heitt et al., 2003
Jerritt Canyon	<ol style="list-style-type: none"> 1. Ferroan dolomite forms halo to 50 ppb Au contour along the Saval discontinuity. 2. No evidence for replacement of Fe-bearing minerals in sedimentary rocks associated with Eocene CTGD mineralization. 3. Paleozoic brines deposited Fe, resulting in the formation of ferroan dolomite prior to Eocene CTGD mineralization. 	Patterson, 2009

CONCLUSIONS

This study shows that carbonate staining can be effectively utilized to map out the spatial distribution of ferroan and non-ferroan carbonate minerals relative to gold mineralization in CTGDs. The distribution of ferroan calcite in carbonate host rocks has a clear spatial association with high-grade ore (≥ 17 ppm) at the Turquoise Ridge deposit. The close proximity of ferroan calcite to iron-rich basalts in the Cambrian-Ordovician sequence at Turquoise Ridge suggests iron was likely liberated from the NPB during the emplacement of the Cretaceous Osgood stock and associated dikes and mobilized into adjacent sedimentary strata. Infiltration of reduced, auriferous, sulfur-rich acidic hydrothermal fluids during the Eocene resulted in the dissolution of reactive ferroan carbonates. Consequent interaction between iron liberated from dissolved calcite and sulfur from the hydrothermal fluid resulted in sulfidation and the formation of auriferous pyrite and marcasite, because loss of reduced sulfur from the ore fluid destabilized gold-sulfide complexes. The enrichment of iron in carbonates adjacent to the NPB, resulting from the emplacement of Cretaceous magmatism, produced ideal reactive host rocks at the Turquoise Ridge deposit.

This study also points out the importance of interlayered carbonates and basalts in identifying future targets in the Getchell district and throughout Nevada. Furthermore and most importantly, careful carbonate staining should be routinely employed in order to identify favorable strata containing ferroan calcite and/or ferroan dolomite. Carbonate staining provides cheap, real time data that can be critical in

exploration programs targeting CTGDs and high-grade zones within and around known CTGDs.

Chapter 3

Oxygen and Carbonate Isotope Characteristics associated with Carlin-type gold deposits at the Turquoise Ridge Gold Deposit, Getchell District, Nevada

ABSTRACT

This study was conducted to determine the spatial distribution of “cryptic” alteration haloes, specifically $\delta^{18}\text{O}$ and $\delta^{13}\text{C}$ values of carbonate rocks, in relation to visible decalcification, argillization, and silicification associated with high-grade gold mineralization at the Turquoise Ridge Carlin-type gold deposit. The Turquoise Ridge deposit is hosted within a complexly deformed package of Cambrian-Ordovician sedimentary and volcanic rocks that is characterized by rapid facies changes and soft-sediment deformation. Gold grades commonly display abrupt variations that locally change from ≥ 17 ppm to < 0.34 ppm within a few meters. Visible alteration, consisting of decalcification, argillization, and silicification, strongly correlates with Au grades of > 0.34 ppm.

Analyses of carbonates from both visibly altered and unaltered rocks at Turquoise Ridge yielded $\delta^{18}\text{O}$ values from 13.5‰ to 21.6‰ and $\delta^{13}\text{C}$ values from -8.2‰ to 1.2‰. Most of the $\delta^{18}\text{O}$ values associated with visibly unaltered recrystallized micrite are between 17.6‰ and 19.0‰, well below typical $\delta^{18}\text{O}$ values associated with unaltered Paleozoic carbonates (22‰ to 28‰). The spatial distribution of $\delta^{18}\text{O}$ values along an east-west cross-section through the northern portion of the Turquoise Ridge deposit reveal the lowest $\delta^{18}\text{O}$ and $\delta^{13}\text{C}$ values occur within visibly altered wall rocks

associated with ore zones and defined fluid pathways. Stable isotopic alteration haloes are limited to visible alteration and do not extend beyond hydrothermal alteration into adjacent unaltered wallrocks. Similarly, elevated trace element concentrations (e.g., Au, As, Hg, Te, Sb, and Tl) are largely limited to visibly altered wall rocks, with elevated concentrations associated with bleached clay/calcite-lined fractures extending beyond continuous hydrothermal alteration in otherwise visibly unaltered wall rocks.

The lack of wide, coherent haloes of various hydrothermal features surrounding ore at Turquoise Ridge is suggestive of a restrictive, fracture-controlled fluid flow network, rather than large-scale, pervasive, lithologic-controlled fluid flow. The results of this study suggest that the confined nature of fluid flow associated with the Turquoise Ridge deposit and possibly other high-grade underground Carlin-type gold deposits does not result in large cryptic alteration haloes.

INTRODUCTION

Carlin-type gold deposits continue to provide the majority of gold production from Nevada that in 2008 was valued at \$5 billion and accounted for 76% of US production and 8% global gold production (NBMG, 2009). Traditional exploration techniques utilized to identify the geochemical and alteration signature for Carlin-type gold deposits (CTGDs) have included anomalous gold assays, elevated trace elements, namely arsenic, mercury, antimony, and thallium, as well as favorable alteration, primarily jasperoids distal to identified ore bodies. Conventional exploration techniques also focus on numerous structural features that include high-angle faults, thrust faults, and hinge zones of anticlines that intersect favorable calcareous stratigraphic horizons. Increasingly, exploration for CTGDs is being focused on underground targets that require high grades to be mined. Grades in known underground deposits can vary from >5-20 ppm gold to <0.5 ppm within meters (e.g., Deep Star, Heitt et al., 2003; Turquoise Ridge, Cassinerio and Muntean, 2010), making exploration, development, and mining very difficult. As discussed in Chapter 1, the most coherent hydrothermal halo associated with high grade gold mineralization (>17 ppm) at the Turquoise Ridge deposit consists of spatially correlated low-grade (>0.34 ppm) gold and visible hydrothermal alteration (e.g., decalcification, argillization, and silicification). Although coherent, the visible alteration haloes are tightly confined along preexisting fractures therefore producing limited alteration haloes beyond high grade gold mineralization. This chapter focuses on the nature and spatial distribution of non-visible paleothermal anomalies, or “cryptic” alteration haloes associated with wall rocks having undergone hydrothermal

alteration. Specifically, the zonation of oxygen and carbon isotopes relative to trace element distributions distal to high grade gold mineralization in order to further understand the relationship between visible and cryptic alteration features. These analyses provide insights as to the nature and extent of fluid flow around high grade ore zones within the Turquoise Ridge deposit, Humboldt County, Nevada.

Stable isotope studies of ore deposits have been utilized to provide information concerning: 1) temperature of mineral deposition, 2) sources of hydrothermal fluids, and 3) degree of water-rock interaction. Isotopic studies concerning the amount of water-rock interaction, specifically documenting the spatial distribution of $\delta^{18}\text{O}$ values relative to visible alteration, gold-grade, and trace elements in carbonate hosted CTGDs at the deposit scale have historically lagged behind studies conducted on volcanic-hosted epithermal systems (e.g., Engel et al., 1958; Taylor, 1971, 1973, 1974; O'Neil et al., 1973; Criss and Taylor, 1983; Criss et al., 1985, 2000; Larson and Zimmerman, 1991). Hydrothermally-altered volcanic rocks have progressively lower $\delta^{18}\text{O}$ values with increased proximity to ore zones and associated intrusive centers. Most of these studies have shown lower $\delta^{18}\text{O}$ values present within propylitically altered rocks (e.g., Tonopah, Goldfield, and Comstock Lode, Taylor, 1973). In some cases, low $\delta^{18}\text{O}$ values extend up to 2 km beyond the metamorphic contact aureole of the intrusive center and 800 m beyond propylitic alteration (e.g., Bohemia Mining District, Taylor, 1971). The lowering of $\delta^{18}\text{O}$ values occurs when hydrothermal fluids containing low initial $\delta^{18}\text{O}$ values come in contact with wall rocks having higher initial $\delta^{18}\text{O}$ values. The result of isotopic exchange between the fluid and the wall rock causes the ore fluid to become

higher in $\delta^{18}\text{O}$ while the wall rock becomes progressively lower in $\delta^{18}\text{O}$. Similar $\delta^{18}\text{O}$ isotopic studies on carbonate-hosted base metal-silver manto deposits (Kesler et al., 1996; Vazquez et al., 1998; Frieauf and Pareja, 1998) and CTGD's (Radtke et al., 1980; Rye, 1985; Kuehn and Rose, 1995; Stenger et al., 1998; Hofstra and Cline, 2000; and Schmauder et al., 2005; Arehart and Donelick, 2006; Patterson, 2009) have suggested $\delta^{18}\text{O}$ depletion haloes around ore.

The objective of this study was to document the existence, magnitude, pattern, extent, and consistency of isotopic values around the high-grade ore zones and comparison to visible alteration at the Turquoise Ridge deposit. Identification of the spatial extent of cryptic alteration haloes surrounding visible alteration and gold mineralization provides key insights into the nature and extent of ore fluid migration. Stable isotope analyses of visibly unaltered recrystallized carbonate host rocks would test whether unaltered rocks interacted with fluids during gold mineralization or whether they remained "high and dry" during mineralization, with migrating hydrothermal fluids restricted to fractures, bedding planes, and veinlets. In addition, this research seeks to assess the utility of stable isotope analyses as a potential vectoring tool for future CTGD exploration programs.

DISTRICT GEOLOGY

The Turquoise Ridge deposit is located within the Getchell District on the northeastern flank of the Osgood Mountains approximately 72 km northeast of Winnemucca, Nevada (Figure 3.1). The geology of the northern Osgood Mountains and the Getchell mine area has been discussed in detail in Chapter 1, as well as in many

publications (Joralemon, 1951; Hotz and Willden, 1964; Chevillon et al., 2000; Crafford, 2000; McLachlan et al., 2000; Boskie, 2001; Breitt et al., 2005; Marlowe et al., 2007, Cassinerio and Muntean, 2010) and will be briefly summarized here. CTGDs within the Getchell District are primarily hosted within Cambrian-Ordovician carbonates and clastic rocks containing interlayered basaltic rocks that have historically been mapped as the Preble, Comus, and Valmy Formations. The Cambrian-Ordovician sequence was complexly deformed, likely during the Antler Orogeny, prior to the deposition of the Pennsylvanian-Permian Etchart Formation. The siliciclastic and basaltic rocks of the Mississippian-Permian Havallah Formation occur northwest of the Getchell mine area and were emplaced over Etchart Formation along the Golconda thrust during the late Permian to early Triassic Sonoma Orogeny. Broad, northeast-trending folds in the Etchart Formation are interpreted to have occurred during the Sonoma and/or subsequent Mesozoic orogenies. The Cretaceous Osgood stock and associated dikes intrude the Paleozoic section and appear to be part of a protracted magmatic-hydrothermal event ranging from 115-80 Ma based on $^{40}\text{Ar}/^{39}\text{Ar}$ dates and a U-Pb zircon date from Twin Creeks (Hall et al., 2000; Breit et al., 2005) and $^{40}\text{Ar}/^{39}\text{Ar}$ dates on igneous biotite and hornblende and hydrothermal K-feldspar and sericite at Getchell (Groff et al., 2005). The primary ore-controlling structure in the district is the Getchell Fault Zone, which runs along the northeast flank of the stock and strikes NNW and dips 40-55°E. The Getchell Fault Zone has a long, complex tectonic history that shows evidence for normal, reverse, and strike-slip motion (Joralemon, 1951; Hotz and Willden, 1964; Berger and Taylor, 1980; Crafford, 2000; Boskie, 2001; Muntean et al., 2007).

The Getchell District hosts several CTGDs, which are epigenetic, disseminated auriferous pyrite deposits characterized by carbonate dissolution, argillic alteration and silicification of typically Paleozoic calcareous sedimentary rocks (Hofstra and Cline, 2000). The ores within the Getchell District are largely devoid of supergene alteration with gold occurring primarily in very fine-grained gold-bearing arsenian pyrite. Late-ore-stage minerals in order of deposition include drusy quartz, orpiment, fluorite, stibnite, realgar, and calcite (Cline, 2001). Mineralization occurred during the Eocene, based on a 39.0 ± 2.1 Ma Rb-Sr age on galkhaite, which is a late ore-stage mineral (Tretbar et al., 2000).

GEOLOGY, MINERALIZATION, AND ALTERATION OF THE TURQUOISE RIDGE DEPOSIT

The geologic framework presented here is based primarily on underground cross-sections that trend East-West and N55°E and cut the north part of the Turquoise Ridge deposit through the HGB, the largest and highest-grade ore zone in the Turquoise Ridge deposit (Figure 3.2) (Muntean et. al, 2009; Chapter 1). The 1:600 scale combined east-west cross-section (Figure 3.3) was constructed by John Muntean utilizing detailed core logs and core photos, as well as inspection of drill core and underground exposures. The geology of the north end of the Turquoise Ridge deposit is characterized by a Cambrian-Ordovician sedimentary-volcanic package that has undergone a complex depositional, tectonic, metamorphic, and hydrothermal history. The complexity of the depositional history at Turquoise Ridge is compounded by rapid facies and tectonic overprints. Pre-ore metamorphism related to the tectonic deformation and contact metamorphism, along with hydrothermal activity related to emplacement of the

Osgood stock further hampers unraveling the geologic history. The lithologic units in [Figure 3.3](#) represent a series of lithologic packages. Each of the individual lithologies described below can be seen in various proportions within each lithologic package.

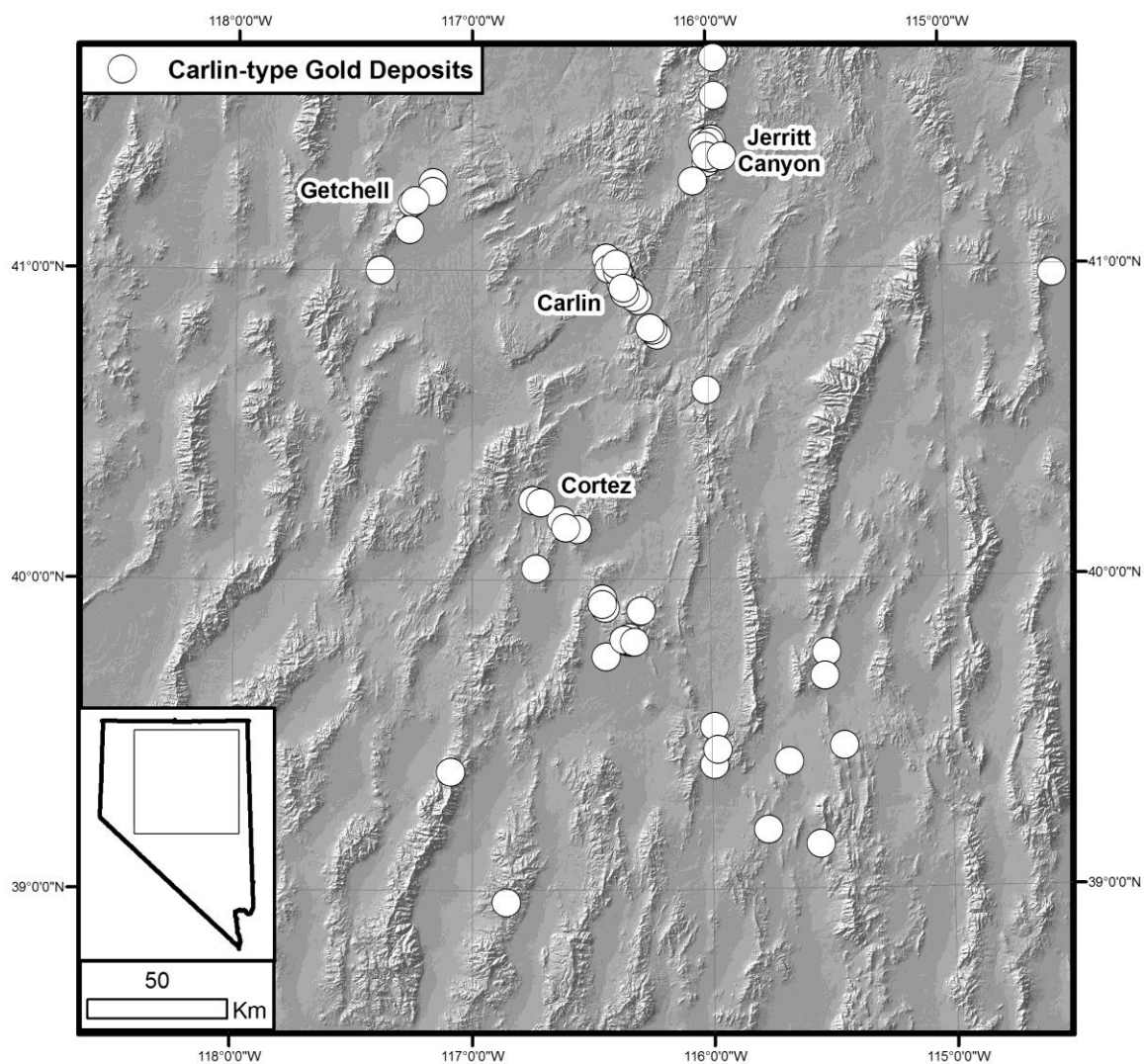


Figure 3.1. Digital elevation model of northern Nevada, showing locations of the Getchell deposit relative to the locations of other prominent large CTGDs.

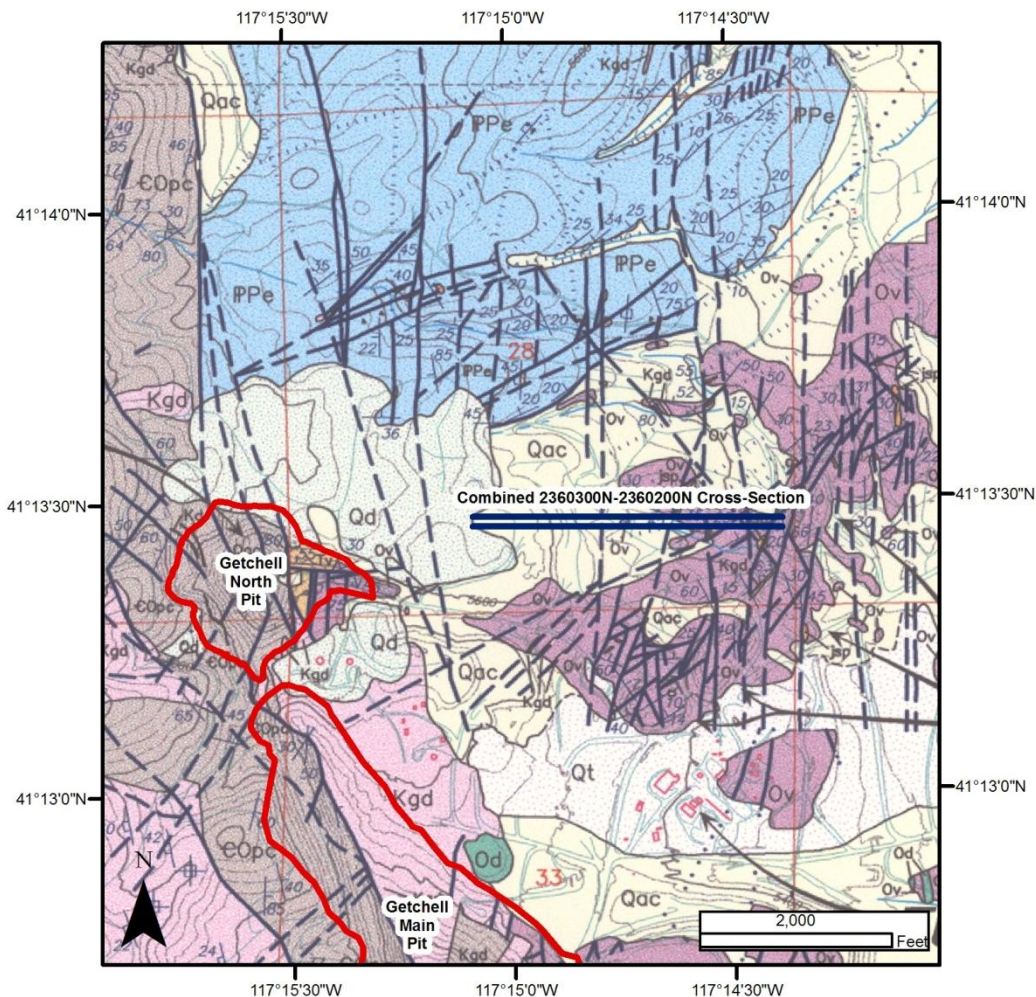


Figure 3.2. Simplified geologic map of the Getchell District (Unpublished map by Placer Dome Exploration, based on Hotz and Willden, 1964 and unpublished Placer Dome mapping). The main units in the map are the Comus/Preble Formations (grey), Valmy Formation (purple), Etchart Formation (blue), Osgood granodiorite (pink), and alluvium (yellow). Map also shows the surface projections of the East-West cross-section and the Northeast cross-section (Chapters 1 and 2) relative to the Getchell open pits (large red outlines), faults (black lines), and mine buildings (thin red lines in SE corner). The East-West cross-section is a combination of the 2360200N and 2360300N cross-sections and is composed of both surface diamond drill core and underground drill fans that were constructed at a 1:600 scale by John Muntean utilizing detailed core logs and core photos, as well as inspection of drill core and underground exposures.

The lowermost unit consists primarily of carbonaceous mudstones and limestones with interlayers of calcarenite turbidites (purple unit). The mudstones vary from siliceous and non-calcareous to argillaceous and variably calcareous and are overlain by a series of limestone debris flow breccias that pinch out to the south (black stippled unit).

Above this unit are slumped micritic limestones and brown mudstones (brown and blue unit). A pillow basalt, referred to as the northern pillow basalt (NPB), overlies the brown mudstones and limestones and also pinches out to the south forming a west-northwest-trending, blunt margin across the north end of the Turquoise Ridge deposit. Brown mudstones containing thin basalt flows and sills are present further up section. The Cambrian-Ordovician rocks are complexly deformed throughout the Turquoise Ridge deposit. Cretaceous dacite porphyry dikes intrude the Cambrian-Ordovician sequence, the most prominent being the "main dacite dike" that cuts across the entire north end of Turquoise Ridge. The dike strikes roughly sub-parallel to the Getchell Fault Zone, maintaining a slightly shallower easterly dip. The continuity of the dike throughout the cross-sections is interpreted to represent lack of displacement along normal faults during Tertiary extension. Abundant high-angle faults and fracture zones that strike mainly north-northwest and northeast, are located throughout the Turquoise Ridge deposit; however, the vast majority of the faults in the underground workings lack continuity along strike and down dip. The faults typically have apparent normal displacements of less than a few meters and are difficult to correlate between holes.

Figure 3.3. Geologic cross-section of the underground combined 2360200N-2360300N east-west cross-section, interpreted and constructed by John Muntean (unpublished). The cross-section is composed of surface holes from the 2360200N cross-section (mostly on the west end of the section) and underground fans of core holes from the 2360300N cross-section (central and east end of the section). The section is an underground section looking north. The top of the section is approximately 1,500 feet below the surface; the bottom 3,000 feet. Purple unit consists of the lowermost planar carbonaceous mudstones and limestones containing local bedding disruptions and sporadic turbidite sequences consisting of coarse-grained calcarenite. Stippled unit represents the upper and lower member of the sedimentary debris flow breccia unit (see text for discussion). The upper brown mudstones (brown) and limestones (blue) represent non-calcareous brown mudstones containing variable amounts of micritic limestone. The interbedded Northern Pillow Basalt (NPB) is represented in green. The section is intruded by Cretaceous dacite porphyry dikes (e.g., main dacite dike within the center of the cross-section; eastern dacite dike within the Getchell Fault Zone). The Getchell fault (blue checkered pattern) is located the southeastern portion of the section.

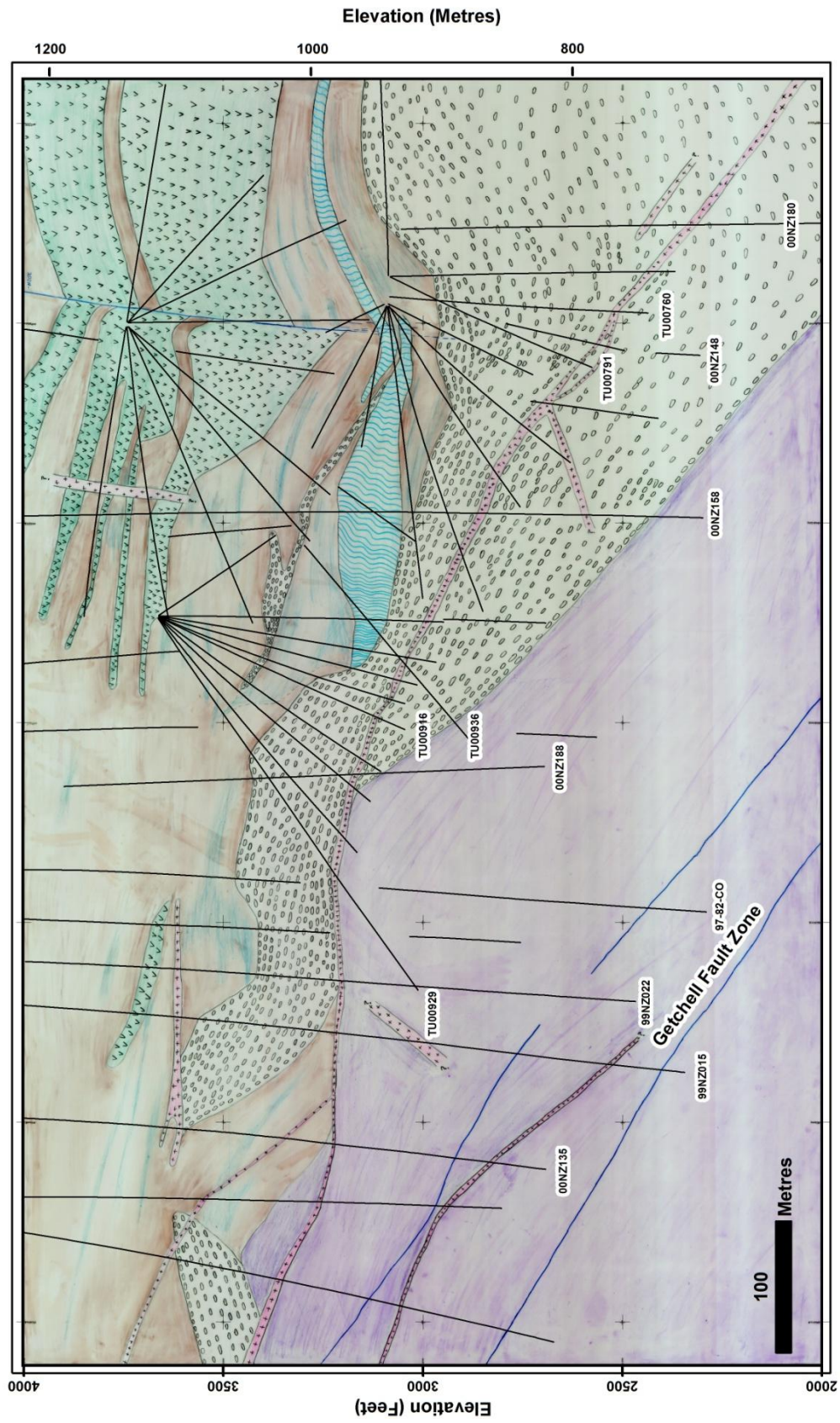


Figure 3.3

Fluid pathways at the Turquoise Ridge deposit were determined by Muntean et al. (2009), based on patterns of lithology, structure, hydrothermal alteration, gold grade, carbonate oxygen isotopes, and trace elements. Inspection of gold grades utilizing gold grade thickness maps, block models of gold grade, a three-dimensional geologic model of the district utilizing GOCAD software, and detailed cross-sections indicate that gold mineralization occurs along complex intersection between: 1) north-northwest-striking high-angle fracture zones sub-parallel to the Getchell fault, 2) west-northwest-trending margin of the sedimentary breccias unit and basalt, 3) margins of north-northeast-trending folds, 4) northeast-trending fracture zones, and 5) calcareous lithologies. Gold mineralization along the east-west cross-section (Fig. 3.4) is confined along narrow zones consisting of: 1) the Getchell Fault Zone, 2) high-angle, antithetic fracture zones in the hanging wall of the Getchell fault, 3) the main dacite dike, and 4) high-angle north-northwest- and north-northeast- trending fracture zones in the hanging wall of the dike (148 zone). Moderate to strong alteration which typically contain gold grades of >0.34 ppm is most prominent in the western portion of the cross-section where antithetic fracture zones in the hanging wall of the Getchell fault intersect the footwall of the main dacite dike (HGB zone and BBT zone).

Hydrothermal fluids were interpreted by Muntean et al. (2009) to have migrated up the Getchell Fault Zone and into steeply west-dipping antithetic fracture zones in the hanging wall (Fig. 3.4). These fluids are believed to have fed the large HGB zone, which happens to occur along the west-northwest-trending basin margin. Fluid migration along the eastern portion of the section occurred along a

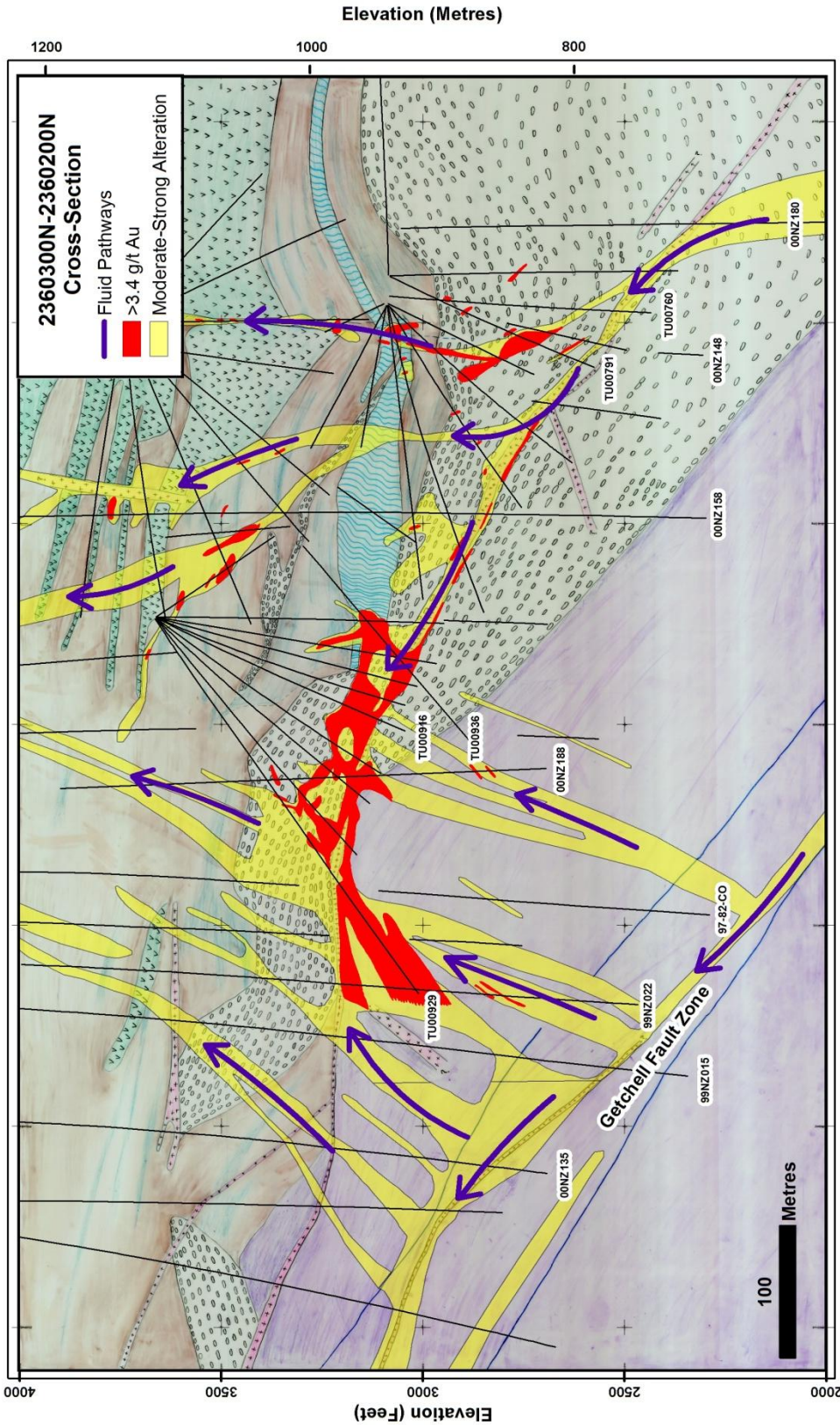


Figure 3.4. Combined 2360200N-2360300N East-West cross-section showing moderate to strong visible hydrothermal alteration (decalcification, argillization, and silicification) correlating with ≥ 0.34 ppm Au (yellow) and ≥ 3.4 ppm Au (red). Note purple arrows depicting interpreted fluid pathways. Refer to Figure 3 for descriptions of lithologic units.

northeast-trending fracture zone that tapped fluids from the Getchell fault at depth (Deep East Feeder). The ascending fluids either broke through the dacite dike and continued flowing upward along steeply dipping fracture zones (148 zone) or they traveled westward up-dip along the margins of the dike and escaped along fracture zones. Fluid flow in the exhaust zones was passive and opportunistic and took advantage of local fractures and lithologic contacts. Fluid flow throughout the Turquoise Ridge deposit was primarily discordant to bedding.

OXYGEN AND CARBON ISOTOPE WHOLE-ROCK DATA

Sampling and analytical methods

Oxygen and carbon isotope analyses were conducted on 180 samples of carbonate lithologies within the Cambrian-Ordovician Sequence within, adjacent, and distal to the Turquoise Ridge deposit (Table 3.1). The majority of the samples were collected from diamond drill core. Most of the samples were collected along transects across visually altered, gold-bearing zones along the east-west cross-section through the HGB ore zone in the northern portion of the Turquoise Ridge deposit (Figure 3.4). The closely spaced underground diamond drill fans and the surface core holes (50 m spacing) along the east-west cross-section provide excellent geologic control that allows interpretation of the isotopic distribution relative to visible hydrothermal alteration, prominent structural zones, and host rock lithologies throughout the Turquoise Ridge deposit. The strong geologic control provided by the 1:600 scale east-west cross-section enables a more detailed stable isotope study within an underground high-grade CTGD that was not possible with past stable isotope research conducted on low-grade high

ton CTGDs with limited geologic control due to more widely spaced surface holes (e.g., Twin Creeks, Stenger et al., 1998; Pipeline, Arehart and Donelick, 2006). Each transect in this study utilized multiple drill holes to establish greater sampling control above, within, and below ore zones, both distal and proximal to mineralized zones. Sampling focused on four zones, 1) the High Grade Bullion (HGB) ore zone, 2) the Getchell fault and the north-south trending feeder zones in its hanging wall, 3) the 148 zone on the east side of the cross-section, down-dip of the High Grade Bullion and 4) the deep east feeder zone down-dip of the HGB along the main dacite dike that intercepts the Getchell fault at depth (not on section). Also, samples were collected across a transect of the deep Getchell fault intercept below the interpreted combined East-West cross-section (e.g. drill hole 99NZ073). Calcite samples were hand-drilled (3-4 representative holes) from carbonate lithologies in a given sample of drill core. Only rock carbonate was sampled; veins were avoided. In addition, a representative piece of the core (~5 cm long that, in many cases, included carbonate veins and other lithologies), from which carbonate was separated for isotopic analyses, was submitted to ALS Chemex for multi-element analyses by ICP-MS, using a four-acid near-total digestion (50 elements, ME-MS41 or ME-MS61) as well as a fire assay for gold, and a cold vapor atomic absorption analysis for mercury. The degree of visible hydrothermal alteration was recorded for each of the analyzed samples. Only alteration interpreted as resulting from Carlin-type gold mineralization, which includes decalcification, argillization, bleaching, and/or silicification, was recorded. The sample locations, degree of alteration, $\delta^{18}\text{O}$ and $\delta^{13}\text{C}$ values, and values of gold, mercury, arsenic and antimony are shown in [Table 3.1](#); background samples are listed last and

include “BG” in their sample number. Twenty-two samples in [Table 3.1](#), mainly from strongly altered, high-grade ore zones, did not have sufficient carbonate contents, due to decalcification, to yield isotopic analyses.

Isotopic compositions of Cambrian-Ordovician carbonates

Isotopic samples containing orthophosphoric acid-soluble fractions within the Cambrian-Ordovician carbonates have $\delta^{18}\text{O}$ values that range from 13.5 to 21.6‰, with the majority of the data clustered between 17.6 and 19.0‰ ([Figure 3.5](#)). Similar isotopic studies conducted on CTGDs included the following $\delta^{18}\text{O}$ values; Stenger et al., (1998) 12.0 to 24.0‰ (Twin Creeks), Arehart and Donelick (2006) -1.7 to 21.9‰ (Pipeline), and Patterson (2009) 7.2 to 25.4‰ (Jerritt Canyon).

The 14 background samples yield $\delta^{18}\text{O}$ values that range from 15.1 to 20.3‰. These background samples, shown in [Figure 3.6](#) display a crude pattern where $\delta^{18}\text{O}$ values decrease with increasing proximity to the Osgood stock and associated contact aureole. The $\delta^{13}\text{C}$ values range from -8.2 to 1.2‰ and show no distinct zoning patterns ([Figure 3.7](#)) but are depleted relative to unaltered Ordovician marine carbonates, which typically have $\delta^{13}\text{C}$ values near 0‰ (Arehart, 2006). The $\delta^{18}\text{O}$ values of the background samples are significantly lower than unaltered Paleozoic carbonates in northern Nevada, which typically range from 22.0 to 28.0‰ (Hofstra and Cline, 2000), and are also lower than values of Ordovician marine limestones throughout the world, which typically range from 22.0 to 29.0‰ (Veizer and Hoefs, 1976; Veizer et al., 1977).

Isotopic analyses of tungsten skarn deposits associated with the Osgood stock by Taylor and O’Neil (1977) provide insight to the pre-Eocene $\delta^{18}\text{O}$ and $\delta^{13}\text{C}$ values of

carbonates in the Getchell District (Figure 3.8). Their data indicate that fine-grained marbles, likely similar to the recrystallized limestones at Turquoise Ridge, have $\delta^{18}\text{O}$ values ranging from 16.6 to 20.7‰, with all but one datum above 17.6‰, similar to the cluster of 17.6 to 19.0‰ associated with the Turquoise Ridge deposit. Figure 3.9 shows that there is a very weak positive correlation between $\delta^{18}\text{O}$ and $\delta^{13}\text{C}$ in the Cambrian-Ordovician carbonate samples at Turquoise Ridge. The highest $\delta^{18}\text{O}$ and $\delta^{13}\text{C}$ values within the visually unaltered samples are significantly lower relative to unaltered Paleozoic carbonates within northern Nevada. The lowest background sample collected during this study, 15.1‰ (00WM202_1839 BG CS), was from calcite intergrown with calc-silicate minerals. This value is similar to the $\delta^{18}\text{O}$ values in calcite in calc-silicate hornfels reported by Taylor and O'Neil (1977). Thus, a reasonable assumption is that local background along the east-west cross-section, prior to Carlin-type gold mineralization in the Eocene, was between 17.6 and 19.0‰. The $\delta^{13}\text{C}$ data collected by Taylor and O'Neil (1977) range from -0.7 to -6.6‰ and are analogous to the samples from Turquoise Ridge collected within this study.

Table 3.1 Oxygen and carbon isotope and trace element compositions of carbonate-bearing Cambrian-Ordovician samples

Sample_ID	Eastings SP_NvW	Northing SP_NvW	Elevation	Alteration	d18O VSMOW, ‰	d13C VPDB, ‰	Au ppb	Hg ppb	As ppm	Sb ppm	Te ppm	Tl ppm
2360300N-2360200N Cross-Section												
TU00760_197.5	869051	2360297	2887	1	18.7	-1.7	<5	<10	38	0.64	0.08	0.31
TU00760_231	869048	2360295	2853	1	18.6	-3.0	<5	<10	2.5	0.25	<0.05	0.34
TU00760_263	869046	2360294	2820	1	17.7	-3.6	<5	220	159	12.55	0.14	0.17
TU00760_331.5	869042	2360292	2752	1	18.5	-2.8	<5	10	15	1.16	0.08	0.58
TU00760_402.5-405.5	869037	2360290	2680	1	18.1	-1.7	<5	20	307	4.32	0.05	0.06
TU00760_433.5	869036	2360289	2650	1	18.1	-3.6	21	30	91	1.56	0.09	0.13
TU00760_476	869033	2360287	2608	1	18.0	-1.3	<5	90	47	1.05	0.15	0.05
TU00760_481	869033	2360287	2605	1	17.7	-1.7	<5	1950	340	3.74	0.1	1.23
TU00760_488	869033	2360287	2595	1	17.3	-2.5	14	1730	281	4.97	0.09	0.74
TU00760_491	869033	2360287	2595	1	16.1	-1.7	31	1110	371	9.87	0.21	0.71
TU00760_501	869032	2360287	2585	1	13.5	-5.0	226	3260	479	5.78	<0.05	1.44
TU00760_551	869030	2360285	2535	2	16.3	-3.4	<5	1450	201	4.67	0.11	0.36
TU00760_577.5	869028	2360284	2508	3	15.9	-2.5	21	3820	245	14.05	0.16	0.65
TU00760_648	869025	2360282	2435	1	18.2	-2.6	<5	320	56	3.24	0.11	0.27
TU00791_331.5	868975	2360298	2782	2	15.5	-4.8	<5	110	132	1.26	0.09	0.35
TU00791_419.5	868940	2360299	2699	1	15.6	-1.7	<5	200	330	1.37	0.09	0.04
TU00916_136.5	868205	2360308	3540	1	16.0	-3.2	<5	<10	2.5	0.59	0.05	0.11
TU00916_400.5	868094	2360319	3299	1	18.0	-2.0	<5	<10	65	2.09	<0.05	0.49
TU00916_449	868075	2360321	3256	1	18.0	-1.5	<5	<10	107	0.83	<0.05	0.51
TU00916_485.5	868060	2360323	3222	1	18.1	-5.2	<5	20	20.7	3.75	0.06	0.8
TU00916_507.5	868051	2360324	3201	2	15.4	-5.7	<5	50	79	5.65	0.06	0.39
TU00916_509.5	868051	2360324	3201	5	insuf. carb.	insuf. carb.	24309	21300	3130	36.4	9.41	27.9
TU00916_515.5	868048	2360324	3194	4	18.0	-4.3	147	3190	823	2.43	0.07	0.76
TU00916_546.5	868036	2360325	3167	5	insuf. carb.	insuf. carb.	11863	27700	1795	32.9	9.42	12.8
TU00916_573.1	868025	2360327	3142	5	insuf. carb.	insuf. carb.	87086	100000	10000	47.7	27.3	64.6

Sample_ID	Eastings SP_NW	Northing SP_NW	Elevation	Alteration	d18O VSMOW, ‰	d13C VPDB, ‰	Au ppb	Hg ppb	As ppm	Sb ppm	Te ppm	Tl ppm
TU00916_666	867988	2360330	3057	1	18.5	-1.4	41	70	227	3.57	0.21	0.53
TU00929_32	868234	2360303	3646	2	17.2	-5.6	41	1390	653	8.4	0.08	1.26
TU00929_65	868206	2360303	3628	1	17.6	-3.1	<5	20	7	0.63	0.07	0.67
TU00929_87	868189	2360303	3617	1	17.8	-1.8	<5	20	8	0.75	<0.05	0.5
TU00929_142	868144	2360303	3585	1	17.8	-2.4	<5	10	30	0.79	0.13	0.36
TU00929_212.5	868086	2360303	3545	1	17.8	-2.4	<5	10	118	2.45	0.05	0.29
TU00929_294	868019	2360302	3498	1	17.6	-1.8	<5	<10	14	0.34	0.34	0.11
TU00929_477.5	867868	2360301	3392	1	17.9	-4.3	<5	<10	465	1.54	0.13	0.48
TU00929_531.5	867825	2360301	3361	1	17.8	-2.8	7	130	161.5	1.74	0.06	0.74
TU00929_536.5	867821	2360301	3358	1	18.6	-2.9	360	2410	441	5.14	<0.05	0.46
TU00929_546.2	867813	2360301	3353	5	insuf. carb.	insuf. carb.	13783	39300	4280	36.9	7.01	3.86
TU00929_549	867810	2360301	3351	1	19.8	-3.3	<5	10	106	3.25	<0.05	0.4
TU00929_553	867806	2360301	3348	1	18.4	-3.0	<5	<10	112	7.14	0.1	0.58
TU00929_560.9	867800	2360300	3344	2	18.3	-3.7	82	6600	487	14.4	0.13	0.86
TU00929_591.5	867776	2360300	3327	1	18.3	-4.7	<5	280	162	11.55	0.15	0.46
TU00929_609	867761	2360300	3317	5	insuf. carb.	insuf. carb.	2146	6120	624	37.4	0.66	1.6
TU00929_694.3	867761	2360300	3317	1	18.2	-3.4	<5	240	142	7.17	0.18	0.48
TU00936_943.5	868226	2360273	3113	5	insuf. carb.	insuf. carb.	N/A	N/A	N/A	N/A	N/A	N/A
TU00936_959.3	868214	2360274	3102	5	insuf. carb.	insuf. carb.	N/A	N/A	N/A	N/A	N/A	N/A
TU00936_971	868206	2360274	3095	5	insuf. carb.	insuf. carb.	N/A	N/A	N/A	N/A	N/A	N/A
TU00936_1065	868133	2360279	3034	5	insuf. carb.	insuf. carb.	N/A	N/A	N/A	N/A	N/A	N/A
TU00936_1079	868124	2360279	3026	1	18.1	-6.0	96	130	304	1.56	0.1	0.75
TU00936_1149	868069	2360283	2978	1	18.2	-1.5	34	60	14	2.94	0.1	0.54
00NZ135_2542	866933	2360168	3108	1	18.3	-3.5	<5	10	13	0.68	<0.05	0.71
00NZ135_2589	866928	2360164	3059	1	18.4	-0.3	<5	<10	11	0.46	0.08	0.6
00NZ135_2669.5	866919	2360156	2981	1	18.5	-7.8	<5	30	57.4	2.88	0.31	0.82
00NZ135_2710.5	866913	2360152	2939	1	insuf. carb.	insuf. carb.	<5	50	82.4	3.64	0.16	0.85

Sample_ID	Eastings SP_NW	Northing SP_NW	Elevation	Alteration	d18O VSMOW, ‰	d13C VPDB, ‰	Au ppb	Hg ppb	As ppm	Sb ppm	Te ppm	Tl ppm
00NZ135_2840	866898	2360139	2812	3	18.3	-2.9	10	270	137	10.6	<0.05	0.33
00NZ135_2857	866895	2360137	2793	4	insuf. carb.	insuf. carb.	199	3070	282	11.35	0.17	2.04
00NZ135_2934	866886	2360129	2721	4	insuf. carb.	insuf. carb.	1262	1120	1375	27.3	0.08	0.99
00NZ135_2951.5	866884	2360128	2702	1	17.0	-5.9	51	240	259	12.05	0.18	0.9
00NZ135_2960	866882	2360127	2692	2	17.7	-7.8	34	220	95.9	20.6	<0.05	0.91
00NZ148_2812	868934	2360173	2601	1	17.9	-2.1	<5	20	78	6.69	0.07	0.71
00NZ148_3054	868923	2360165	2362	1	18.0	-5.1	<5	10	61	1.44	0.08	0.02
00NZ148_3087.5	868921	2360164	2325	1	18.0	-7.9	<5	260	563	14	0.12	0.42
00NZ158_2237.5	868528	2360323	3185	1	17.7	-1.6	<5	<10	29	0.91	0.1	0.4
00NZ158_2322.5	868528	2360324	3099	1	17.7	-2.3	<5	10	86	2.57	0.08	0.46
00NZ158_2348.3	868528	2360325	3073	1	18.3	-1.4	<5	<10	39	0.54	0.05	0.45
00NZ158_2389	868527	2360325	3033	1	18.1	-1.0	<5	100	189	4.37	0.07	0.12
00NZ158_2462.9	868526	2360325	2959	2	18.0	-5.3	21	620	194	2.57	0.09	0.22
00NZ158_2558.5	868524	2360324	2862	2	16.5	-7.2	7	1460	7040	4.65	0.09	1.87
00NZ158_2624	868523	2360324	2798	1	18.1	-1.4	<5	20	160	1.59	0.05	0.34
00NZ158_2680	868522	2360323	2738	1	18.1	-0.9	<5	<10	122	0.68	0.05	0.3
00NZ158_2709	868522	2360323	2714	1	18.3	-1.7	<5	10	151.5	2.71	0.07	0.39
00NZ158_2737.5	868521	2360323	2683	1	18.4	-0.8	<5	10	23	0.95	<0.05	0.35
00NZ158_2809	868520	2360322	2613	1	18.0	-0.6	<5	10	24	0.81	<0.05	0.36
00NZ158_2889.5	868519	2360321	2533	1	18.7	-1.4	<5	10	277	2.08	<0.05	0.42
00NZ158_2993	868516	2360318	2428	1	18.9	-1.0	<5	10	61	1.3	0.05	0.49
00NZ158_3098.5	868514	2360315	2323	1	18.2	-4.2	<5	200	19	1.38	0.07	0.02
00NZ180_2994.5	869245	2360238	2408	1	17.5	-1.3	<5	10	7	0.81	<0.05	0.44
00NZ180_3027	869246	2360237	2376	1	17.4	-2.3	<5	<10	60	0.62	<0.05	0.51
00NZ180_3045.5	869246	2360236	2358	1	17.5	-3.0	10	<10	23	0.73	<0.05	0.66
00NZ180_3061	869246	2360236	2342	1	17.2	-3.2	7	1360	793	1.4	<0.05	0.88
00NZ180_3108	869246	2360234	2295	3	13.5	-5.7	3	10	62	1.52	<0.05	0.54

Sample_ID	Eastings SP_NW	Northing SP_NW	Elevation	Alteration	d18O VSMOW, ‰	d13C VPDB, ‰	Au ppb	Hg ppb	As ppm	Sb ppm	Te ppm	Tl ppm
00NZ180_3137	869247	2360233	2266	4	insuf. carb.	insuf. carb.	178	15100	4220	43.4	8.02	5.57
00NZ180_3173-3174	869247	2360232	2230	4	insuf. carb.	insuf. carb.	21	880	345	3.36	0.08	0.82
00NZ188_2724.5	867888	2360284	2764	1	18.8	-4.3	10	200	112.5	1.93	0.1	0.49
00NZ188_2749	867889	2360281	2734	1	19.0	-1.6	7	30	10	0.4	0.06	0.55
00NZ188_2752.5	867889	2360281	2734	1	18.9	0.0	<5	20	15	0.79	0.07	0.71
00NZ188_2753.3	867889	2360281	2734	1	18.7	0.2	14	30	7.9	0.84	0.05	0.58
00NZ188_2774	867890	2360278	2710	1	17.7	-4.1	<5	20	437	1.59	0.05	0.78
99NZ022_2641	867691	2360299	3269	1	18.9	-6.7	31	100	107.5	3.74	<0.05	0.78
99NZ022_2985.5	867307	2360271	2536	1	19.1	-4.1	7	120	105	8.15	0.17	0.7
99NZ022_3004.5	867306	2360270	2521	1	18.9	-7.9	17	40	58.4	14.85	0.14	1.1
99NZ015_1854.3	867270	2360184	3696	1	16.5	-1.9	<5	10	34	1.03	0.3	0.28
99NZ015_1881	867268	2360180	3668	3	13.8	-5.1	998	3800	4130	73.5	0.49	0.97
99NZ015_1882.8	867268	2360180	3668	1	17.0	-2.2	3	30	86	6.9	0.2	0.7
99NZ015_1889	867267	2360180	3663	2	16.9	-4.0	7	30	79	1.98	<0.05	0.95
99NZ015_1908	867266	2360177	3644	5	insuf. carb.	insuf. carb.	4937	21000	7860	7.61	2.9	0.9
99NZ015_1921.5	867265	2360175	3630	5	insuf. carb.	insuf. carb.	N/A	36800	8890	16.6	6.24	1.38
99NZ015_2021.4	867256	2360163	3531	1	16.4	-8.1	21	180	152	0.84	0.41	0.11
99NZ015_2083	867250	2360155	3470	1	18.0	-2.1	<5	10	18	1.63	0.12	0.41
99NZ015_2222	867237	2360137	3334	1	17.9	-6.3	<5	10	44.2	1.59	0.15	0.78
99NZ015_2434.8	867214	2360109	3125	1	17.8	-6.5	<5	<10	20	0.26	<0.05	0.05
99NZ015_2468	867210	2360104	3088	1	18.2	-6.9	<5	10	113	2.33	0.2	0.44
99NZ015_2576.7	867198	2360089	2984	1	18.0	-1.9	24	20	69	5.25	0.07	0.44
99NZ015_2656	867189	2360078	2905	1	18.0	-1.4	<5	10	98	1.16	0.12	0.72
99NZ015_2727.5	867180	2360068	2835	1	18.7	-6.4	<5	10	64	1.32	<0.05	0.31
99NZ015_2793.5	867172	2360059	2770	2	15.7	-2.8	1683	4300	255	8.08	0.2	3.48
99NZ015_2811	867170	2360057	2752	4	16.3	-3.4	38	710	154	9.5	<0.05	0.53
99NZ015_2887.5	867161	2360045	2678	1	18.0	-4.4	21	110	39	2.85	<0.05	0.09

Sample_ID	Eastings SP_NW	Northing SP_NW	Elevation	Alteration	d18O VSMOW, ‰	d13C VPDB, ‰	Au ppb	Hg ppb	As ppm	Sb ppm	Te ppm	Tl ppm
99NZ015_2898	867160	2360044	2668	4	14.8	-6.5	1392	3260	1185	20.9	0.95	2.05
99NZ015_3042.5	867144	2360020	2526	5	insuf. carb.	insuf. carb.	45	600	242	18.3	0.19	1.27
99NZ015_3097.5	867139	2360011	2473	2	18.0	-4.8	7	30	107	3.09	0.05	0.14
99NZ015_3125	867136	2360006	2445	4	insuf. carb.	insuf. carb.	27	820	884	51.4	0.17	1.71
99NZ015_3133	867135	2360005	2437	1	19.4	-6.7	<5	220	638	28.6	0.08	1.55
99NZ015_3219	867126	2359990	2352	1	18.4	-6.5	<5	60	10	6.17	<0.05	1.39
99NZ015_3222.7	867126	2359990	2352	1	18.6	-2.6	<5	<10	7	0.61	<0.05	0.35
97-082-CO_2826	867553	2360151	2653	1	17.9	-4.0	<5	10	23	1	0.14	0.07
97-082-CO_2938	867545	2360139	2572	4	16.7	-5.3	645	620	2660	22.7	0.06	1.52
97-082-CO_2998.5	867541	2360132	2512	1	18.9	-5.3	<5	10	50	3.11	0.27	0.27
97-082-CO_3008.5	867541	2360131	2502	1	18.9	-3.9	14	90	47	14.75	0.24	0.93
97-082-CO_3055	867538	2360126	2456	1	18.2	1.2	10	60	15	5.45	<0.05	0.13
97-082-CO_3220	867526	2360106	2293	4	13.5	-5.2	936	5500	706	18.05	3.18	1.08
Getchell Fault Transect												
99NZ073_3224.5	868501	2360981	2213	1	17.9	-0.9	<5	30	6	1.28	<0.05	0.32
99NZ073_3357	868500	2360965	2082	1	17.8	-1.1	<5	20	5	0.64	<0.05	0.31
99NZ073_3411.5	868500	2360959	2028	1	17.8	-2.4	7	20	6	1.72	<0.05	0.55
99NZ073_3419	868499	2360957	2018	1	18.1	-3.0	<5	20	5	0.57	<0.05	0.75
99NZ073_3590	868497	2360937	1850	3	insuf. carb.	insuf. carb.	10	1230	154	6.1	0.04	0.36
99NZ073_3595	868497	2360936	1845	3	insuf. carb.	insuf. carb.	N/A	N/A	N/A	N/A	N/A	N/A
99NZ073_3598-3608	868497	2360935	1834	4	insuf. carb.	insuf. carb.	3	380	92.1	2.31	<0.05	0.43
99NZ073_3615	868497	2360934	1826	1	21.6	-3.0	1255	3740	257	14.95	1.08	1.56
99NZ073_3656.3	868496	2360929	1785	1	20.8	-1.5	10	220	63.8	3.39	0.05	0.66
99NZ073_3731	868494	2360920	1760	1	20.0	-1.9	813	1960	298	31.3	0.48	2.17
N55° E Cross-Section												
TU01165_1049-1051.5	67351	60228	2841	2	15.8	-5.9	106	1500	215	4.59	0.06	0.93
TU01165_1084-1087.5	67328	60210	2820	4	13.8	-6.2	274	2050	276	5.03	0.13	1.01

Sample_ID	Eastings SP_NW	Northing SP_NW	Elevation	Alteration	d18O VSMOW, ‰	d13C VPDB, ‰	Au ppb	Hg ppb	As ppm	Sb ppm	Te ppm	Tl ppm
TU01166_325.5	67863	60630	3170	2	21.0	-3.9	1848	19800	2760	8.28	5.98	0.7
Fracture Transects												
TU00929_142_MT1	868144	2360303	3585	1	18.6	-2.7	<5	20	48	0.49	<0.05	0.39
TU00929_142_MT2	868144	2360303	3585	1	18.6	-2.5	<5	20	48	0.49	<0.05	0.39
TU00929_142_MT3	868144	2360303	3585	1	17.8	-2.7	<5	20	48	0.49	<0.05	0.39
TU00929_142_MT4	868144	2360303	3585	1	18.1	-3.5	<5	20	48	0.49	<0.05	0.39
TU00929_142_MT5	868144	2360303	3585	1	18.1	-3.2	<5	20	48	0.49	<0.05	0.39
TU00929_142_MT6	868144	2360303	3585	1	18.2	-2.7	<5	20	48	0.49	<0.05	0.39
TU00929_536.5_MT1	867821	2360301	3358	2	18.7	-2.7	<5	100	239	7.33	0.12	0.8
TU00929_536.5_MT2	867821	2360301	3358	2	18.8	-2.3	<5	100	239	7.33	0.12	0.8
TU00929_536.5_MT3	867821	2360301	3358	2	18.6	-2.3	<5	100	239	7.33	0.12	0.8
TU00929_536.5_MT4	867821	2360301	3358	2	17.9	-0.9	<5	100	239	7.33	0.12	0.8
00NZ158_2032.5_MT1	868527	2360322	3391	1	17.7	-1.1	<5	10	2.5	2.33	0.1	0.57
00NZ158_2032.5_MT2	868527	2360322	3391	1	17.8	-1.0	<5	10	3	2.33	0.1	0.57
00NZ158_2032.5_MT3	868527	2360322	3391	1	17.8	-1.0	<5	10	3.5	2.33	0.1	0.57
00NZ158_2032.5_MT4	868527	2360322	3391	1	17.8	-1.0	<5	10	4	2.33	0.1	0.57
00NZ158_2032.5_MT5	868527	2360322	3391	1	17.8	-1.0	<5	10	4.5	2.33	0.1	0.57
00NZ158_2631_MT1	868523	2360324	2788	2	16.8	-3.1	<5	10	180	0.94	0.05	0.28
00NZ158_2631_MT2	868523	2360324	2788	1	17.8	-1.0	<5	10	180	0.94	0.05	0.28
00NZ158_2631_MT3	868523	2360324	2788	1	17.8	-1.2	<5	10	180	0.94	0.05	0.28
00NZ158_2631_MT4	868523	2360324	2788	1	insuf. carb.	insuf. carb.	<5	10	180	0.94	0.05	0.28
00NZ158_2631_MT5	868523	2360324	2788	1	18.0	-1.6	<5	10	180	0.94	0.05	0.28
00NZ158_2631_MT6	868523	2360324	2788	1	18.0	-2.2	<5	10	180	0.94	0.05	0.28
99NZ015_2242_MT1	867234	2360134	3313	1	17.7	-3.8	<5	10	35.7	2.5	0.11	1.01
99NZ015_2242_MT2	867234	2360134	3313	1	17.9	-5.2	<5	10	35.7	2.5	0.11	1.01
99NZ015_2242_MT3	867234	2360134	3313	1	17.6	-5.9	<5	10	35.7	2.5	0.11	1.01
99NZ015_2242_MT4	867234	2360134	3313	1	17.8	-5.9	<5	10	35.7	2.5	0.11	1.01

Sample_ID	Eastings SP_NW	Northing SP_NW	Elevation	Alteration	d18O VSMOW, ‰	d13C VPDB, ‰	Au ppb	Hg ppb	As ppm	Sb ppm	Te ppm	Tl ppm
99NZ073_3441_MT1	868499	2360955	1998	1	16.5	-7.0	7	10	2.4	3.92	0.05	0.31
99NZ073_3441_MT2	868499	2360955	1998	1	18.1	-6.4	7	10	2.4	3.92	0.05	0.31
99NZ073_3441_MT3	868499	2360955	1998	1	18.1	-6.3	7	10	2.4	3.92	0.05	0.31
99NZ073_3441_MT4	868499	2360955	1998	1	18.3	-6.6	7	10	2.4	3.92	0.05	0.31
99NZ073_3441_MT5	868499	2360955	1998	1	18.2	-6.7	7	10	2.4	3.92	0.05	0.31
Background												
BG_GETBGLS1	856455	2355218		1	18.2	-1.2	<5	<10	2.5	0.2	<0.05	0.08
BG_GETBGLS2	857155	2363985		1	15.8	-3.8	<5	<10	2.5	0.37	0.14	0.1
BG_GETBGLS3	855334	2364633		1	18.9	-2.1	<5	100	7	0.66	0.05	0.11
BG_GB4	473027	4542282	4399	1	18.3	0.8	<5	170	21	0.73	0.04	0.04
BG_GB5	466934	4536320	4347	1	19.9	-0.1	7	70	11	0.18	<0.05	<0.02
BG_00MW161A_3753	877477	2368150	1421	1	19.8	0.4	<5	30	2.5	0.19	0.12	<0.02
BG_00MW161A_3838	877476	2368143	1336	1	20.3	-0.1	<5	30	6	0.25	0.06	0.02
BG_00MW153_2748.5	875720	2368837	2528	1	18.1	-5.4	<5	70	10	0.58	0.1	0.08
BG_00MW140_3407.5	878380	2363408	1567	1	18.1	0.0	<5	10	2.5	0.11	0.08	0.35
BG_00NM164_1355	862223	2368222	4275	1	17.3	-2.9	<5	10	2.5	1.1	0.06	0.4
BG_00NM162A_2664.5	861522	2363804	3329	1	16.8	-2.2	<5	<10	2.5	0.12	0.12	0.1
BG_00NM138_3384	870149	2366474	1885	1	17.1	-0.6	<5	10	23	0.74	0.05	0.27
BG_00NM138_5016.5	870124	2366231	271	1	17.6	-5.0	<5	10	14	1.15	<0.05	0.54
BG_00WM202_1839	862019	2360294	4489	1	15.1	-5.9	<5	70	5	0.7	0.27	0.03

Coordinates: NAD27, Nevada State Plane West

Alteration: 1=Visually unaltered; 2=Very Weak - weak bleaching, strong reaction with 5% HCl

3=Weak - Moderate to strong bleaching, strong reaction with 5% HCl, very weak decalcification

4=Moderate - Weak to moderate decalcification, degraded textures, weak to moderate reaction with 5% HCl,

5=Strong - moderate to strong decalcification, textures destroyed, very weak reaction with 5% HCl

N/A = No analysis

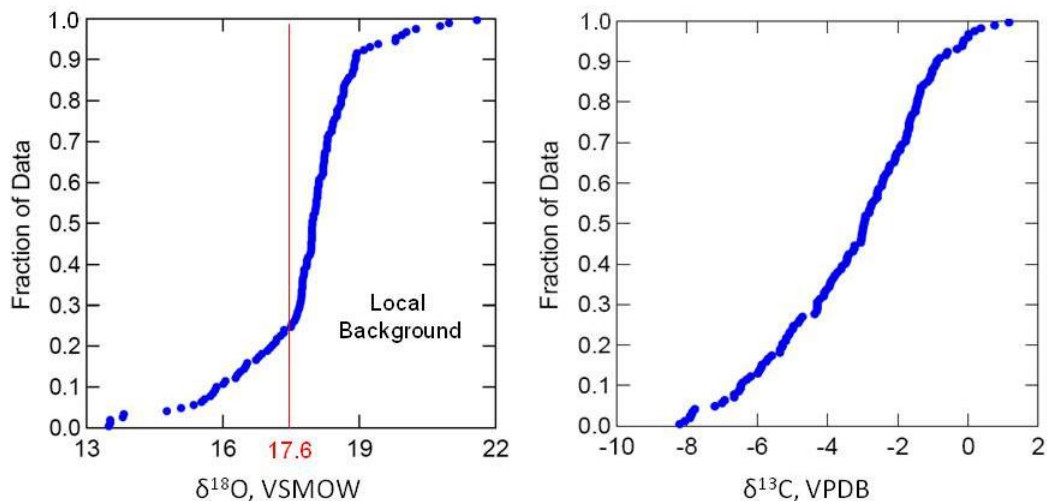


Figure 3.5. A. Cumulative distribution curve for the $\delta^{18}\text{O}$ data from sampled carbonates. B. Cumulative distribution curve for the $\delta^{13}\text{C}$ data from sampled carbonates. Red line represents the significant break in population that occurs at $\delta^{18}\text{O} = 17.6\text{‰}$. See text for discussion regarding local background

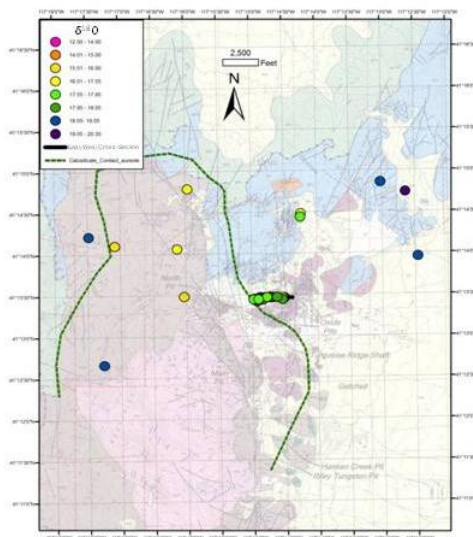


Figure 3.6. District map showing distribution of $\delta^{18}\text{O}$ values of calcite from both background samples and the surface projection of the underground East-West cross-section samples. The underlay is an unpublished geologic map compiled by Placer Dome in 2001 based mainly on mapping completed by Placer Dome geologists. The main units in the map are the Comus/Preble Formations (grey), Valmy Formation (purple), Etchart Formation (blue), Havallah Formation (green) Osgood granodiorite (pink), and alluvium (yellow). The green dashed line represents the contact aureole of the Osgood stock, determined by the presence of calc-silicates on the surface or in drill holes.

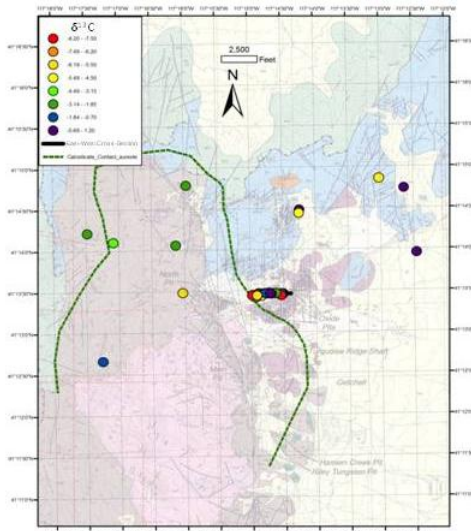


Figure 3.7. District map showing distribution of $\delta^{13}\text{C}$ values of calcite from both background samples and the surface projection of the underground East-West cross-section samples. The underlay is an unpublished geologic map compiled by Placer Dome in 2000 based mainly on mapping completed by Placer Dome geologists. The main units in the map are the Comus/Preble Formations (grey), Valmy Formation (purple), Etchart Formation (blue), Havallah Formation (green) Osgood granodiorite (pink), and alluvium (yellow). The green dashed line represents the contact aureole of the Osgood stock, determined by the presence of calc-silicates on the surface or in drill holes.

Carbon and oxygen isotopic analyses were plotted along the east-west cross-section in relation to visible alteration and gold mineralization (Figures 3.10-11). Although, low $\delta^{13}\text{C}$ values locally occur within or proximal to primary fluid pathways (e.g., the Getchell Fault Zone, HGB ore zone, and northeast 148 feeder zone), in most places, they do not display any recognizable pattern in relation to gold mineralization. Carbon values, on average, are lower in the footwall of the main dacite dike, within the carbonaceous mudstones and limestones, relative to the brown mudstones and limestones, which predominate above the HGB. These low carbon values could reflect increased fluid flux during gold mineralization along the plume upwelling along the antithetic fractures zones in the hanging wall of the Getchell fault. As discussed by Arehart and Donelick (2006), the inclusion of organic carbon in wall rock within the

system can decrease the carbon isotope signature of the resultant carbonate, since organic carbon typically has a very low carbon isotope signature (e.g., Ohmoto, 1986). Therefore the erratic nature of the shift in the $\delta^{13}\text{C}$ values may represent a function of the amount of organic carbon within the system. Thus, the irregular nature of the distribution of $\delta^{13}\text{C}$ is likely the result of a combination of the interaction between organic carbon and carbonate carbon within the wall rocks and multiple hydrothermal processes (e.g., Cretaceous intrusion, Eocene gold mineralization).

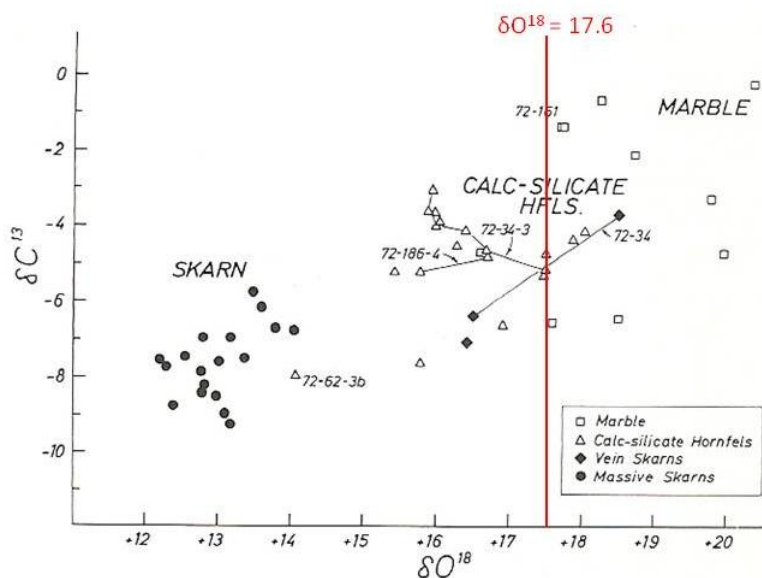


Figure 3.8. Graph of Taylor and O'Neil's (1977) data, showing $\delta^{13}\text{C}$ versus $\delta^{18}\text{O}$ values from carbonate in skarn, calc-silicate-bearing hornfels and marble. Samples are from tungsten skarn deposits adjacent to the Osgood stock. Taken directly from Taylor and O'Neil (1977). Note how all of Taylor and O'Neil's marbles plot at values above 17.6‰, above which is considered the pre-Eocene background $\delta^{18}\text{O}$ for the data on recrystallized unaltered limestones presented in this study as discussed in the text.

The spatial distribution of $\delta^{18}\text{O}$ values shows a distinct pattern relative to interpreted fluid pathways marked by visual CTGD-related alteration and gold mineralization. Lower $\delta^{18}\text{O}$ values are primarily associated with the Getchell Fault Zone,

the deep east feeder zone on the east side of the section down-dip of the HGB, and within the HGB orebody. Most fluid pathways containing visible alteration and gold mineralization contain lower $\delta^{18}\text{O}$ values. Samples containing low $\delta^{18}\text{O}$ values in visibly unaltered wall rock typically extend no more than 10 meters from visibly altered rock (e.g., Getchell fault hanging wall, 148 zone). Although $\delta^{18}\text{O}$ values generally decrease with increased proximity both adjacent to and within inferred fluid conduits, the results of the individual transects in relation to gold and alteration are inconsistent. For example, several visually altered samples contain $\delta^{18}\text{O}$ values greater than 18.0‰ within the Getchell Fault Zone and HGB orebody.

Isotope analyses conducted across the deep Getchell fault intercept in drill hole 99NZ073 do not show a progressive decrease in $\delta^{18}\text{O}$ values with increased proximity to the fault. In general, the $\delta^{18}\text{O}$ values are lower in the hanging wall of the fault (17.8 to 18.1‰) relative to the footwall samples (20.0 to 21.6‰). Although lower $\delta^{18}\text{O}$ values are present in the hanging wall, the values fall within the background data cluster of data from 17.6 to 19.0‰ (Figure 3.5). The three moderate to strongly hydrothermally altered samples within the Getchell Fault Zone in hole 99NZ073 did not contain sufficient amounts of carbonate to yield isotope values. The $\delta^{13}\text{C}$ values in the hanging wall and foot wall of the fault show a progressive decrease in $\delta^{13}\text{C}$ values with proximity to the Getchell fault. For example, $\delta^{13}\text{C}$ values progressively decrease from -0.9 to -3.0‰ with proximity to visible hydrothermal alteration.

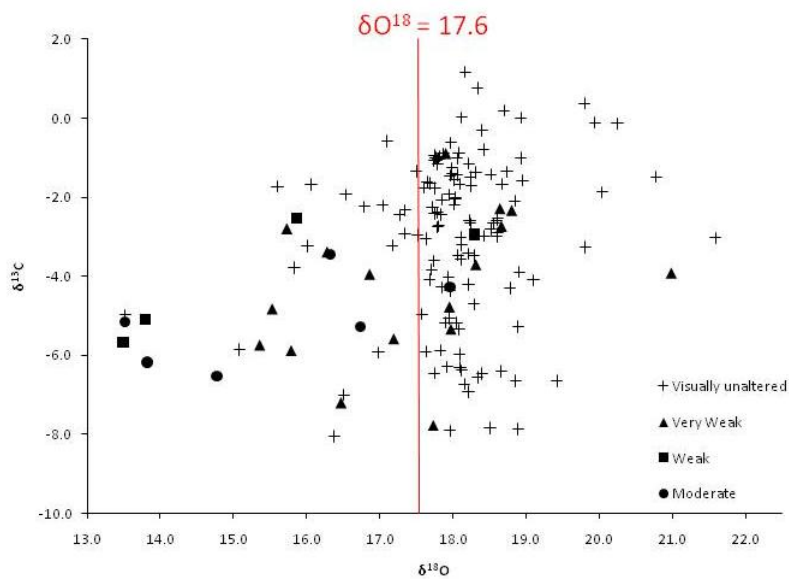


Figure 3.9. ($\delta^{13}\text{C}$ vs $\delta^{18}\text{O}$ for this study) Plot of $\delta^{13}\text{C}$ versus $\delta^{18}\text{O}$ for calcite from recrystallized limestones collected for this study. Data points are symbolized based on degree of alteration associated with Carlin-type gold mineralization. See Table 1 for explanation of alteration. Note how most but not all of the altered samples plot at values below 17.6‰. See text for discussion.

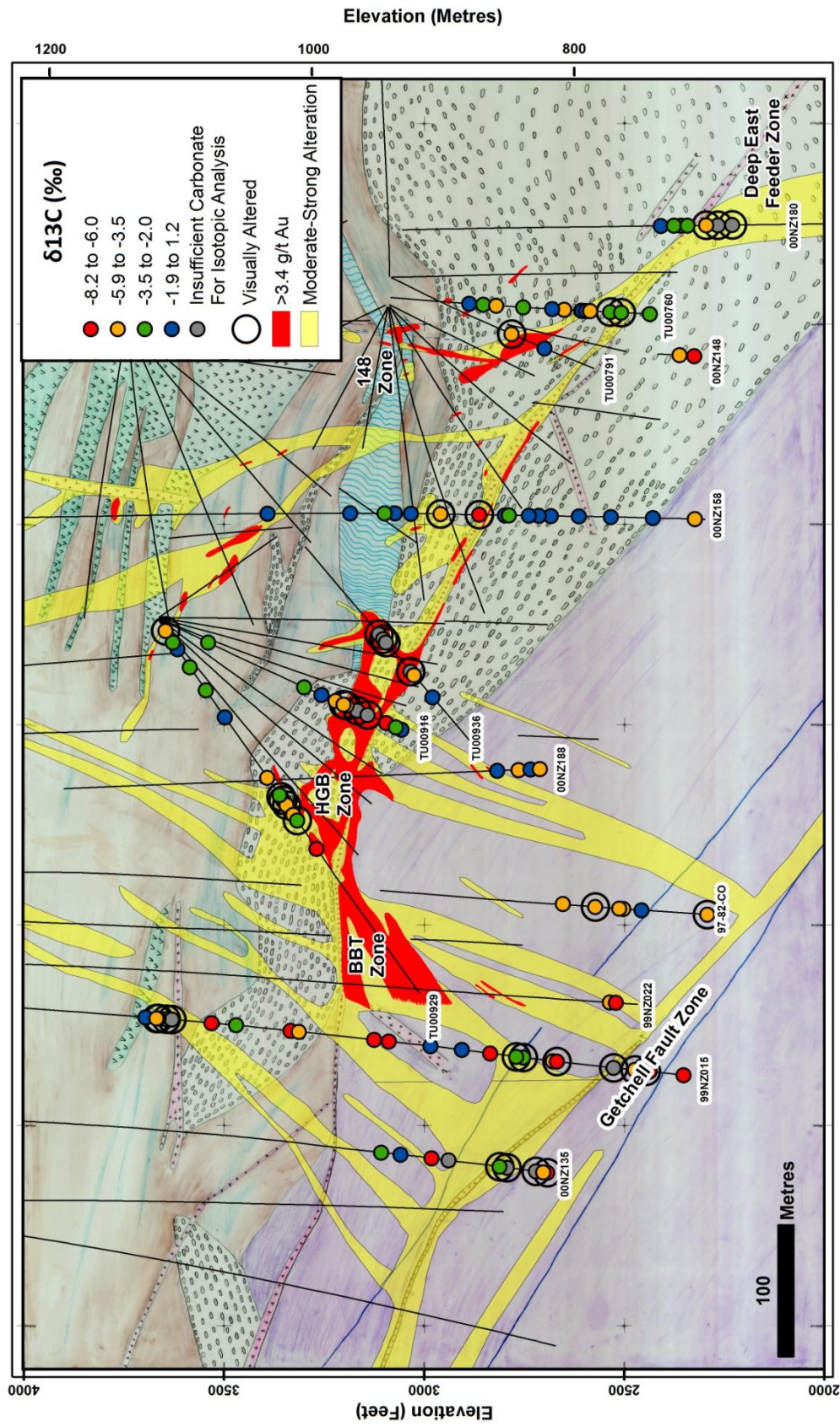


Figure 3.10. Combined cross-section 2360300N-2360200N showing spatial distribution of $\delta^{13}\text{C}$ values of calcite from carbonate rocks. Black rings indicate visually altered samples (e.g., bleaching, decalcification, argillization, silicification).

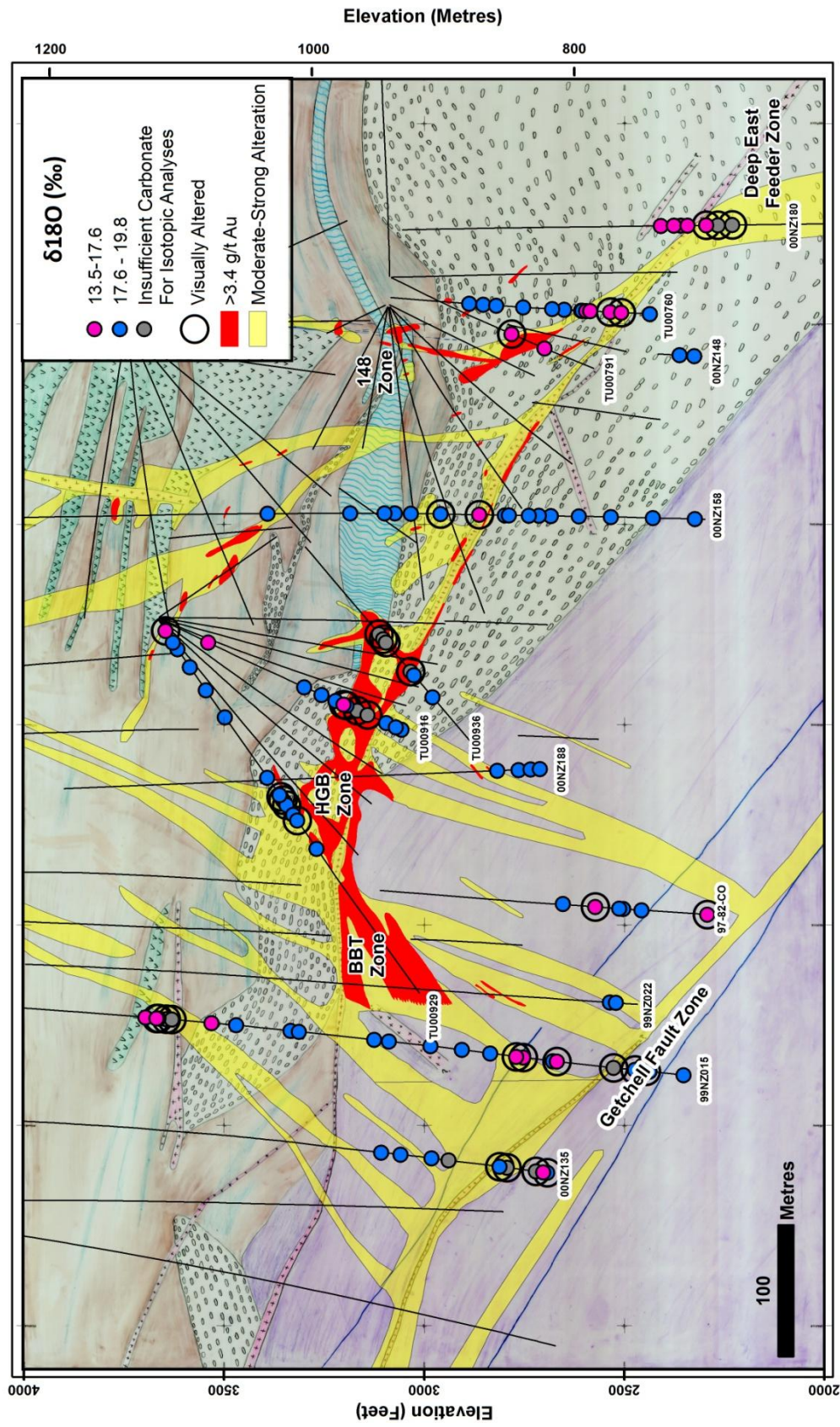


Figure 3.11. Combined cross-section 2360300N-2360200N showing spatial distribution of $\delta^{18}\text{O}$ values of calcite from carbonate rocks. Black rings indicate visually altered samples (e.g., bleaching, decalcification, argillization, silicification)

FLUID FLOW DYNAMICS RELATIVE TO WHOLE-ROCK ISOTOPE COMPOSITION OF CARBONATE ROCKS

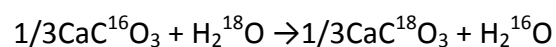
Close examination of the distribution of $\delta^{18}\text{O}$ values in [Figure 3.11](#) reveals that 11 of the 25 samples that are visually unaltered (e.g., no decalcification, argillization, silicification, or bleaching) contain $\delta^{18}\text{O}$ values less than 17.6‰. Similarly, five background samples consisting of recrystallized micrite (no calc-silicate alteration) display $\delta^{18}\text{O}$ values below 17.6‰ but are visually unaltered. These apparent discrepancies bring into question whether the visibly unaltered samples containing low $\delta^{18}\text{O}$ values (<17.6‰) experienced isotopic exchange during the CTGD mineralization or during hydrothermal activity associated with emplacement of the Cretaceous Osgood stock. Furthermore, five samples containing visibly altered CTGD alteration contain $\delta^{18}\text{O}$ values >17.6‰. These discrepancies might be the result of the lack of contrast between the $\delta^{18}\text{O}$ values of the gold-bearing hydrothermal fluids and the pre-Eocene $\delta^{18}\text{O}$ values of the recrystallized Cambrian-Ordovician carbonates (17.6 to 21.3‰). Therefore, in some places hydrothermal fluid may have circulated through visibly unaltered limestones at very low water:rock during the Eocene, thereby only slightly lowering the $\delta^{18}\text{O}$ values of the carbonates. Alternatively, the Eocene hydrothermal fluid may have been close in isotopic equilibrium with carbonate rocks that had previously experienced isotopic exchange during fluid flow associated with the emplacement of the Cretaceous Osgood stock.

At the Turquoise Ridge deposit, two primary factors may have influenced the limited extent of isotope haloes relative to CTGD mineralization. First, the variation in

$\delta^{18}\text{O}$ values of the gold-bearing hydrothermal fluids may have been near equilibrium with the recrystallized limestones. Second, low water:rock ratios may have prevented a significant decrease in $\delta^{18}\text{O}$ values in wall rock experiencing low flux. In order to assess these possibilities, isotopic exchange between fluid and rock was modeled.

Isotopic fractionation occurs during the partitioning of isotopes of a given element, in this case exchange of carbon and oxygen between carbonate minerals and water. The primary question at Turquoise Ridge centers on how much fluid from the Eocene gold mineralization event would need to come in contact with adjacent wall rocks to cause a recognizable isotopic shift, or depletion in $\delta^{18}\text{O}$ whole-rock values. The amount of isotopic shift is dependent upon the initial $\delta^{18}\text{O}$ value of the host rock, the initial $\delta^{18}\text{O}$ value of the hydrothermal fluid, the temperature of the hydrothermal fluid, and the water:rock mass ratio (Criss and Taylor, 1986). For oxygen in calcite, the isotopic exchange reaction with water is described by:

(1)



The isotopic fractionation described in equation 1 can be quantified by its fractionation factor (α), where $\alpha_{\text{calcite-water}}$ is the ratio of the ^{18}O to ^{16}O in calcite divided by the ratio of ^{18}O to ^{16}O in water (Faure, 1986). The fractionation factor is dependent upon temperature.

Experimentally-derived water-rock fractionation factors and estimated $\delta^{18}\text{O}$ values of the hydrothermal fluid can be utilized to calculate the $\delta^{18}\text{O}$ of the rock as a function of temperature and water:rock. The water:rock values in this study were

calculated assuming equilibrium within a closed system, as defined by Taylor (1979).

The closed system represents the minimum water:rock that may have occurred during isotopic exchange (Ohmoto, 1985). In natural systems where a continuous water supply is likely present, such as Turquoise Ridge, the water:rock were, therefore, likely higher than the estimates calculated in this study. The composition of a closed system model is represented by the equation:

(2)

$$w\delta_{H_2O}^i + r\delta_{rock}^i = w\delta_{H_2O}^f + r\delta_{rock}^f$$

where i is the initial isotopic value, f is the final isotopic value after exchange, w is the atom percent of meteoric water oxygen in the total system, and r is the atom percent of exchangeable rock oxygen in the bulk system. If we assume that $\delta_{H_2O}^f$ is determined by isotopic equilibrium with the rocks at the temperature of hydrothermal alteration, then the water:rock (w:r) can be described by the following equation:

(3)

$$\frac{w}{r} = \frac{\delta_{rock}^f - \delta_{rock}^i}{\delta_{H_2O}^i - (\delta_{rock}^f - \Delta)}$$

where $\Delta = \delta_{rock}^f - \delta_{H_2O}^f$. Therefore, if the fluid temperature remains constant, the final rock composition is controlled by the water:rock. For calcite the isotopic equilibrium fractionation factor for calcite and water is best represented the equation derived by O'Neil (1969) where:

(4)

$$\Delta \approx 1000 \ln \alpha = 2.78(10^6 T^{-2}) - 3.39$$

Therefore if the water:rock remains constant, the final rock composition is determined by Δ which is a function of temperature.

The most important factors governing calculations based on equation 3 include the initial isotopic composition of the ore fluid, the initial isotopic composition of calcareous lithologies prior to Eocene gold mineralization, and the temperature of the fluid and rock during isotopic exchange. Hydrogen and oxygen isotope analyses of fluid inclusions in orpiment and realgar as well as hydrogen isotope analyses of fluid inclusions in quartz and calcite coupled with oxygen analyses of quartz and calcite by Cline and Hofstra (2000) suggest that ore-forming fluids at the Getchell deposit (Getchell Main Pit in Fig. 2) had a $\delta^{18}\text{O}$ signature of 0 to 12‰. They interpreted the oxygen and hydrogen data as representing mixtures of meteoric water and magmatic or metamorphic water. In addition, ore stage jasperoids at the nearby Getchell deposit contain aqueous fluid inclusions trapped mainly between 180 to 220°C (Cline and Hofstra, 2000). The initial pre-Eocene isotopic $\delta^{18}\text{O}$ value of the unaltered, recrystallized Cambrian-Ordovician carbonates was estimated to be 18.3‰, which is the mean of the cluster of $\delta^{18}\text{O}$ values between 17.6 and 19.0‰.

These parameters were utilized to evaluate the degree at which $\delta^{18}\text{O}$ may have been lowered given variable water:rock ratios, temperatures, and initial $\delta^{18}\text{O}$ rock and $\delta^{18}\text{O}$ fluid values. [Figure 3.12](#) represents a series of calculated curves showing how the $\delta^{18}\text{O}$ of calcite in the carbonate rock varies as a function of water:rock ratio for different initial $\delta^{18}\text{O}$ values (0‰, 3‰, and 6‰) of the fluid and for different temperatures (180, 200, 220°C). Note how the $\delta^{18}\text{O}$ of the unaltered Cambrian-Ordovician carbonates

significantly shifts to lower values with increasing water:rock ratios as low as 1:1 to 5:1, then remain relatively constant at ratios above 10:1. [Figure 3.12](#) shows that an initial ore fluid having a $\delta^{18}\text{O}$ of 6‰ (red lines) would not be capable of producing $\delta^{18}\text{O}$ values near 13.5‰, the lowest rock carbonate $\delta^{18}\text{O}$ value obtained in this study. Therefore, it is unlikely that the ascending ore fluid at Turquoise Ridge was equal to or greater than 6‰. Similarly, an initial fluid composition of 0‰ (blue line) effectively lowers the $\delta^{18}\text{O}$ values of carbonates to 10 to 12‰ with a relatively low water:rock ratio, though $\delta^{18}\text{O}$ values less than 13.5‰ were not encountered during this study. An initial $\delta^{18}\text{O}$ fluid composition of 3‰ (yellow line) is capable of producing the range of depleted isotopic values found in this study with water:rock ratios varying from 1 to 10. This initial ore fluid composition is well within the 0 to 12‰ range of $\delta^{18}\text{O}$ values of ore-forming fluids estimated by Cline and Hofstra (2000).

The spatial distribution of rock carbonate $\delta^{18}\text{O}$ values relative to inferred fluid pathways and water:rock calculations suggest that isotopic depletion throughout the Turquoise Ridge deposit is almost entirely limited to fluid conduits that experienced high flux. As discussed in Chapter 1, many of the unaltered limestones at Turquoise Ridge that did not display visible alteration contain bleached fracture surfaces consisting of variable amounts of clay and calcite coatings. To further understand the nature of fluid flow in visually unaltered rocks surrounding zones of visible alteration and gold mineralization, isotopic transects were conducted on individual drill core samples that contain visually unaltered limestone adjacent to a bleached fracture surface. In order to test whether such fracture surfaces served as significant fluid conduits, individual

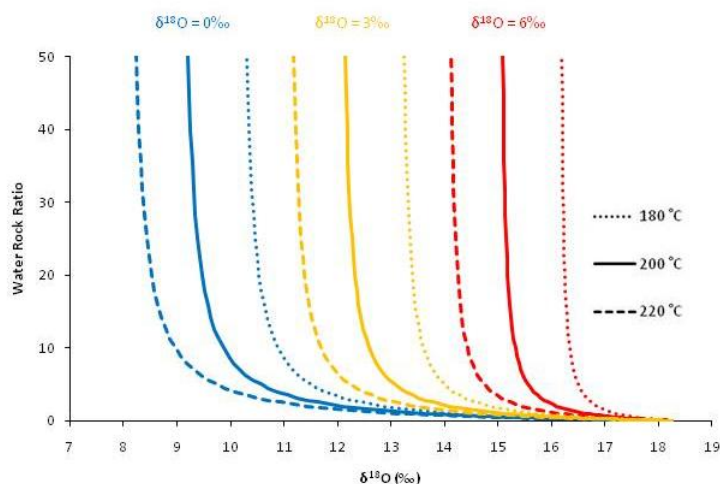


Figure 3.12. Calculated change in isotopic compositions of calcite (whole rock $\delta_{\text{rock}}^i = 18.3\text{‰}$) in equilibrium with ore fluid compositions of 0, 3, and 6‰ at various water to rock ratios and temperatures (180°, 200°, and 220°). Lines represent the change in δ_{rock}^f at various water:rock.

limestone beds were sampled at 1 cm intervals progressively away from bleached fractures to determine if isotopic values varied with distance from the fracture (Figure 3.13). A total of six core samples were collected and analyzed with the results displayed in Table 3.2. In two of the six samples the actual bleached fracture surface was sampled in order to document any shift to lower $\delta^{18}\text{O}$ values along the fracture surface.

Two of the six transect samples within this pilot study displayed significant isotopic depletion along the bleached fractures relative to the adjacent, visually unaltered limestone beds. Sample 99NZ073_3441 contains $\delta^{18}\text{O}$ values consistently greater 18.0‰ within the unaltered limestone bed regardless of the distance from the fracture surface, which had a lower O isotopic composition of 16.5‰. Similarly, sample 00NZ158_2032.5 contained a bleached fracture coating with a $\delta^{18}\text{O}$ value of 16.8‰, whereas the adjacent unaltered limestone contained a $\delta^{18}\text{O}$ values ranging from 17.7 to 17.8‰ away from the bleached fracture surface. Sample 00NZ158_2631 was not

sampled along the bleached fracture surface and contained $\delta^{18}\text{O}$ values of 17.8 to 18.0‰ in the visibly unaltered limestone. In contrast, the other three mini-transects did not show a consistent pattern relative to bleached fractures. However, the actual fracture surfaces were not sampled in these three transects. Furthermore, the limestone bed in the two of the three transects contained hairline fractures and veinlets of calcite (e.g., TU00929_142 and TU00929_142). In the third sample, fragments of limestone in a carbonate debris flow breccia were sampled away from a fracture, rather than a limestone bed (99NZ015_2242). Isotopic depletion along bleached fracture surfaces relative to adjacent unaltered limestone was not limited to $\delta^{18}\text{O}$. The $\delta^{13}\text{C}$ isotopic signatures in samples 99NZ073_3441 and 00NZ158_2032.5 also have lower $\delta^{13}\text{C}$ values along visibly altered fractures relative to the adjacent unaltered limestone.

The results of the isotopic transect sampling indicates that when sampled properly (e.g., bleached fracture surfaces and adjacent unfractured/unveined limestone beds that are perpendicular to the fractures), the limestone beds display a progressive decrease in isotopic values with decreasing distance to the fracture. $\delta^{18}\text{O}$ values vary up to 1.8‰ and $\delta^{13}\text{C}$ values vary of up to 2.0‰ along fractures relative to adjacent, unaltered limestone that were within centimeters of the fractures. Although this study contains limited data, the findings suggest that the bleached, clay±calcite-lined fractures experienced high flux relative to the adjacent unaltered rock, which experienced very low to no water:rock interaction, as indicated by the lack of both visible alteration and low $\delta^{18}\text{O}$ values.



Figure 3.13. Photo of a typical mini-transect along an individual limestone bed away from a bleached fracture surface. Samples 00NZ158_2032.5 MT1-5.

Table 3.2 - Fracture Transects

Sample_ID	$\delta^{18}\text{O}$ VSMOW, ‰	$\delta^{13}\text{C}$ VPDB, ‰
99NZ073_3441_MT1*	16.5	-7.0
99NZ073_3441_MT2	18.1	-6.4
99NZ073_3441_MT3	18.1	-6.3
99NZ073_3441_MT4	18.3	-6.6
99NZ073_3441_MT5	18.2	-6.7
00NZ158_2032.5_MT1*	16.8	-3.1
00NZ158_2032.5_MT2	17.7	-1.1
00NZ158_2032.5_MT3	17.8	-1.0
00NZ158_2032.5_MT4	17.8	-1.0
00NZ158_2032.5_MT5	17.8	-1.0
00NZ158_2032.5_MT6	17.8	-1.0
00NZ158_2631_MT1	17.8	-1.0
00NZ158_2631_MT2	17.8	-1.2
00NZ158_2631_MT3	insuf. carb.	insuf.carb.
00NZ158_2631_MT4	18.0	-1.6
00NZ158_2631_MT5	18.0	-2.2
TU00929_142_MT1	18.6	-2.7
TU00929_142_MT2	18.6	-2.5
TU00929_142_MT3	17.8	-2.7
TU00929_142_MT4	18.1	-3.5
TU00929_142_MT5	18.1	-3.2
TU00929_142_MT6	18.2	-2.7
TU00929_536.5_MT1	18.7	-2.7
TU00929_536.5_MT2	18.8	-2.3
TU00929_536.5_MT3	18.6	-2.3
TU00929_536.5_MT4	17.9	-0.9
99NZ015_2242_MT1	17.7	-3.8
99NZ015_2242_MT2	17.9	-5.2
99NZ015_2242_MT3	17.6	-5.9
99NZ015_2242_MT4	17.8	-5.9

Table 2 – Fracture Transects. Note lower number indicates closer proximity to fracture. * indicates sample taken on the fracture surface.

CATHODOLUMINESCENCE

Cathodoluminescence (CL) was utilized to assess whether there were multiple calcite generations within the recrystallized Cambrian-Ordovician carbonates (both whole rock and veins) at the Turquoise Ridge deposit. Multiple calcite generations within carbonates surrounding massive copper sulfide replacement ores in the Superior district in Arizona were shown to have distinct contrasting isotopic values between hydrothermal veins and carbonate matrix (Frieauff and Pareja, 1998). Isotopic differences were the result of direct precipitation of carbonate rather than from diffusional equilibration between sedimentary carbonates and the hydrothermal fluid. In order to differentiate the potential multiple sources of isotopic variation at Turquoise Ridge, cathodoluminescence was utilized to determine the presence or absence of multiple generations of calcite precipitation. If the $\delta^{18}\text{O}$ analyses of carbonates are to provide a reliable vectoring tool for exploration, a basic understanding of the sedimentary diagenetic and isotopic history of the unaltered strata is critical.

The basic principle of CL involves the excitation and luminescence that are present during electronic transitions between energy levels and ions. CL occurs when a given mineral, in this case calcite, is bombarded with an electron beam under vacuum. Photons are emitted when the given element returns to ground state. The photon that is emitted is a function of the energy imparted to the atom by the electron beam, and is therefore representative of the element itself. CL is responsible for elemental reactions in carbonates caused by electron bombardment that can be classified as activators, sensitizers, and quenchers. For the purposes of this study, we closely monitored the CL

of 12 representative carbonates collected from both background samples and from the east-west cross-section.

Activators represent elements that emit photons when bombarded by an electron beam. Common activators in calcite include: Mn^{2+} , Mg^{2+} , Sm^{3+} , Tb^{3+} , Dy^{3+} , Eu^{2+} , Eu^{3+} , Pb^{2+} (Machel et al., 1991; Machel, 2000). Visually detectable luminescence ranging in color from yellow to orange red occurs with Mn^{2+} concentrations as low as 10-20 ppm Mn^{2+} , provided that Fe contents are below 150 ppm (Machel et al., 1991; Neuser et al., 1996). Quenchers absorb a percentage of the photon emissions from activators. Given that Mn^{2+} is the most common activator in Ca, all quenchers in carbonates are referred to as quenchers of Mn^{2+} . Common quenchers include Fe^{2+} , Co^{2+} , Ni^{2+} , and Fe^{3+} . Samples containing minimal concentrations of quenchers (30-50 ppm) have reported interpretable effects on calcite in photoluminescence studies (Gies, 1976). Sensitizers are responsible for increasing the intensity and range of the colors produced by activators. Pb^{2+} and Ce^{3+} are important sensitizers of Mn^{2+} -activated luminescence and appear effective at concentrations as low as 10 ppm (Gies, 1976).

Analysis of the recrystallized micrite and calcarenite limestones containing associated calcite veinlets display relatively homogenous CL. A suite of carbonate samples that included both ferroan and non ferroan calcite (see Ch. 2) maintained similar orange to orange red luminescence (Figure 3.14). The luminescence is interpreted to be the result of homogenous recrystallization resulting from the Cretaceous intrusive activity. Such homogenization of CL properties within the Cambrian-Ordovician carbonates during Cretaceous magmatism is consistent with the

homogenous lowering of $\delta^{18}\text{O}$ values from the higher, expected values that are typically associated with unaltered lower Paleozoic carbonates, as discussed above. Therefore, the depleted background signature of isotopic values present in visually unaltered recrystallized carbonates throughout the Getchell district is likely the result of emplacement of the Cretaceous Osgood stock. The strong correlation of regionally-low background isotopic values and homogenous distribution of CL supports the hypothesis that the regional isotopic background was significantly lowered relative to unaltered Paleozoic carbonates in Nevada during the protracted Cretaceous magmatic event and was overprinted by water-rock interaction associated with Eocene gold mineralization.

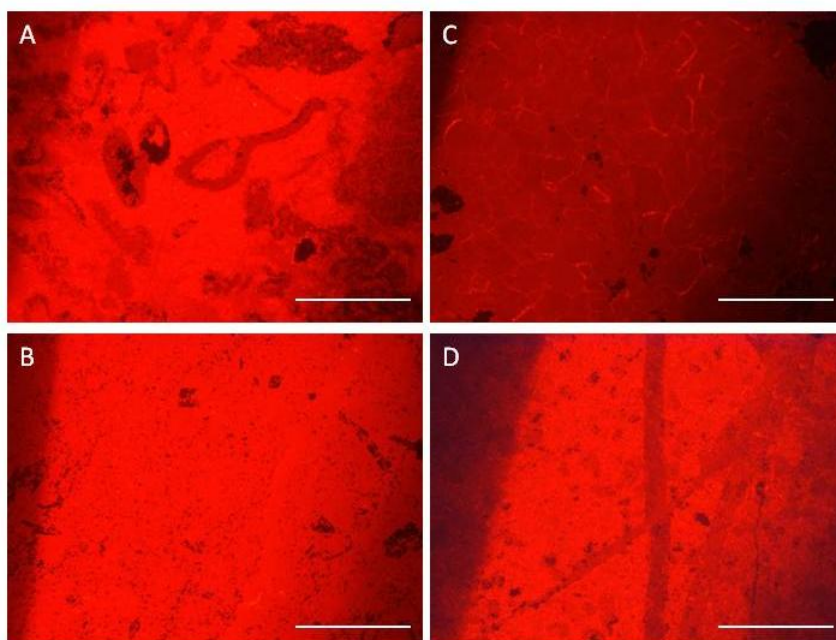


Figure 3.14. Typical cathodoluminescence samples. Scale bars represent 1 cm. A. TU00760_433.5 fossiliferous recrystallized micrite. B. 99NZ022_2985.5 recrystallized micrite. C. 99NZ015_3222.2 recrystallized micrite D. GETBGS3 crosscutting calcite veinlets within recrystallized micrite.

TRACE ELEMENT DISTRIBUTION

As demonstrated in Chapter 1, trace element haloes comprising elevated Au (≥ 0.34 ppm), As (≥ 100 ppm), Hg (≥ 1 ppm), and Sb (≥ 5 ppm) extend from meters to tens

of meters beyond visible alteration (decalcification, argillization, and silicification). In order to determine the spatial distribution of trace elements relative to the oxygen and carbon isotope distributions at the scale of the combined east-west cross-section, a representative piece of core from which the isotope sample was collected (~5 cm long that, in many cases, included carbonate veins and other lithologies) and submitted to ALS Chemex, where 50 element analyses utilizing a near-total 4-acid digestion followed by ICP-MS-AES (ALS Chemex package ME-MS61) were conducted. In addition, a fire assay for Au was completed, as well as a cold vapor atomic absorption analysis for Hg. R values ≥ 0.4 were considered significant for this study. Pearson correlation coefficients were calculated to determine which trace elements correlate linearly with Au. Gold is positively correlated with Tl ($r=0.925$), Hg ($r=0.896$), Te ($r=0.880$), As ($r=0.572$), Sn ($r=0.452$), and Sb ($r=0.411$). Spearman rank correlation coefficients were also calculated and are preferred because the method does not depend upon linear relationships and is less influenced by outliers. Gold shows a positive correlation with Hg ($r=0.634$), Sb ($r=0.610$), W ($r=0.539$), As ($r=0.523$), S ($r=0.519$), Ag ($r=0.444$), Tl ($r=0.471$). The Spearman rank correlation matrix for 18 of the elements, along with accompanying scatter plots, is presented in [Figure 3.15](#).

In addition, traditional R-mode factor analysis was conducted utilizing a varimax rotation and minimum eigen value of 1.00. Varimax rotation was utilized to maximize the variance that each factor symbolizes (Abdi, 2003). Because most of the elements showed lognormal distributions, the log values for each element were used for the factor analysis, because factor analysis is based on the assumption of normal

populations. [Table 3.3](#) displays the seven calculated factors and the associated factor loadings for the entire geochemical database. The seven factors account for just over 83% of the variance in the data set and are listed from highest to lowest percent variance. Factor loadings ≥ 0.4 were considered significant for this study.

Factor 2 is the factor most closely associated with gold mineralization, explaining 13.9% of the variance. The highest positive factor loadings include Hg (0.889), W (0.850), As (0.849), Sb (0.778), Au (0.767), S (0.687), Te (0.604), and Tl (0.575). Conversely, negative loadings associated with Factor 2 include Mg (-0.629), Sr (-0.604), Na (-0.564), Ca (-0.499), and Ba (-0.463) which reflects decalcification and argillization associated with gold mineralization, as discussed in Chapter 1. Factor 1 contains elevated factor loadings (≥ 0.4) of Ga, Co, Sc, Fe, Al, Sn, Cs, Th, Be, In, Rb, Li, Ni, C, K, La, Cr, Ge, Zn, Pb, Ti, Bi, Y, Tl, Na, V, Hf, and Mg, representing nearly 35% of the variance. This factor appears to be reflecting a combination of igneous rocks (both Cambrian-Ordovician mafic rocks and Cretaceous felsic rocks) and base metal sulfide-quartz-carbonate veins associated with emplacement of the Osgood stock. Factor 4 represents 11.5% of the variance and contains high factor loadings of the following elements: Ta, Nb, Zr, Hf, Ti, Ba, and U. It appears to be reflecting felsic rocks. Factor 3, representing 13.4% of the variance within the dataset, is composed of Cd, Mo, P, Re, Ag, Cu, U, V, Se, Zn, S, and Sb. This elemental association is interpreted to represent a black shale or basinal fluid flow signature that formed prior to ore formation. Similar trace element signatures have been documented at Jerritt Canyon (Hofstra, 1994; Patterson, 2009) and other CTGDs (cf. Sha, 1993; Emsbo et al., 1999), as discussed in Chapter 1. The

remaining factors represent only 9.2% of the variance and their elemental associations do not appear to have any geologic significance.

Spatial distribution of Trace Elements relative to $\delta^{18}\text{O}$ values

Weak negative correlations can be observed in [Figure 3.16](#) between Au, As, Hg, Sb, Te, and Tl and low $\delta^{18}\text{O}$ values. Also, as expected, increased trace element concentrations are associated with increased alteration in most samples; however, there are a significant number of weakly altered to visibly unaltered samples containing elevated trace elements. The highest trace element concentrations in visually unaltered samples include 1255 ppb Au, 3740 ppb Hg, 638 ppm As, 31.3 ppm Sb, 1.08 ppm Te, and 2.17 ppm Tl. Several of these samples with high trace element values have $\delta^{18}\text{O}$ values greater than 17.6‰. The presence of elevated trace element concentrations relative to both visually and isotopically altered and visually and isotopically unaltered samples led to the examination of the spatial distribution of trace elements relative to isotopic values, alteration, and gold grades.

In general, the spatial distribution of trace elements along the East-West cross-section appear to be more coherent and systematic than the oxygen and carbon isotope patterns ([Figures 3.10, 3.11, and 3.17A-F](#)). Elevated Au is almost exclusively associated with moderate to strong visible alteration throughout the east-west cross-section, extending no further than 3 meters beyond visible hydrothermal alteration. The zone of anomalous Au is wider in the footwall of the ore zones than in the hanging wall, at least ppb Au, interpreted to reflect an increase in fluid flux. Mercury displays a similar narrow

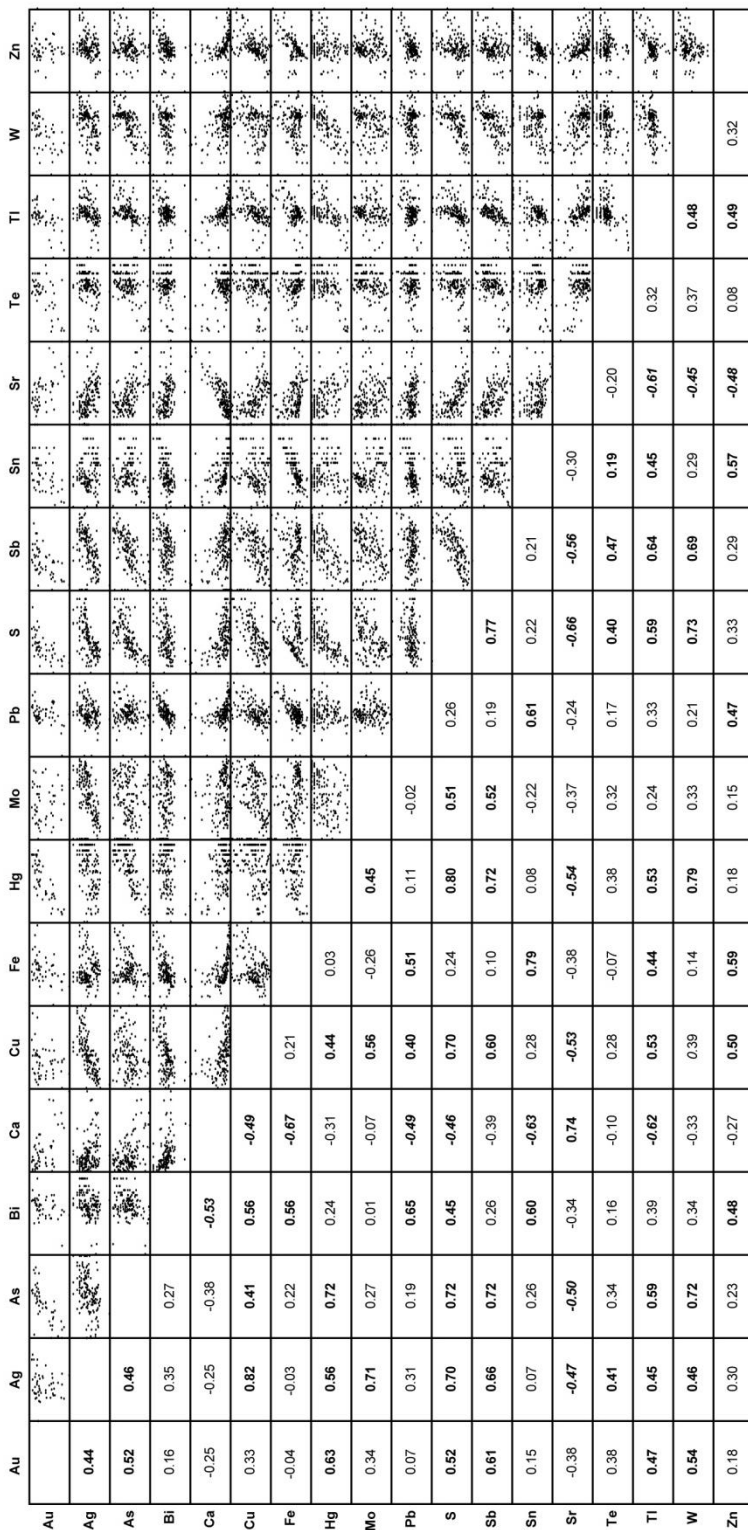


Figure 3.15. (Spearman Correlation Matrixes) Correlation matrix and associated scatter plots of 18 selected trace elements based on analyses of ~5 cm long representative drill hole intervals correlating to where isotopic analyses were conducted. Correlation coefficients considered significant (either >0.4 or <-0.4) are shown in bold.

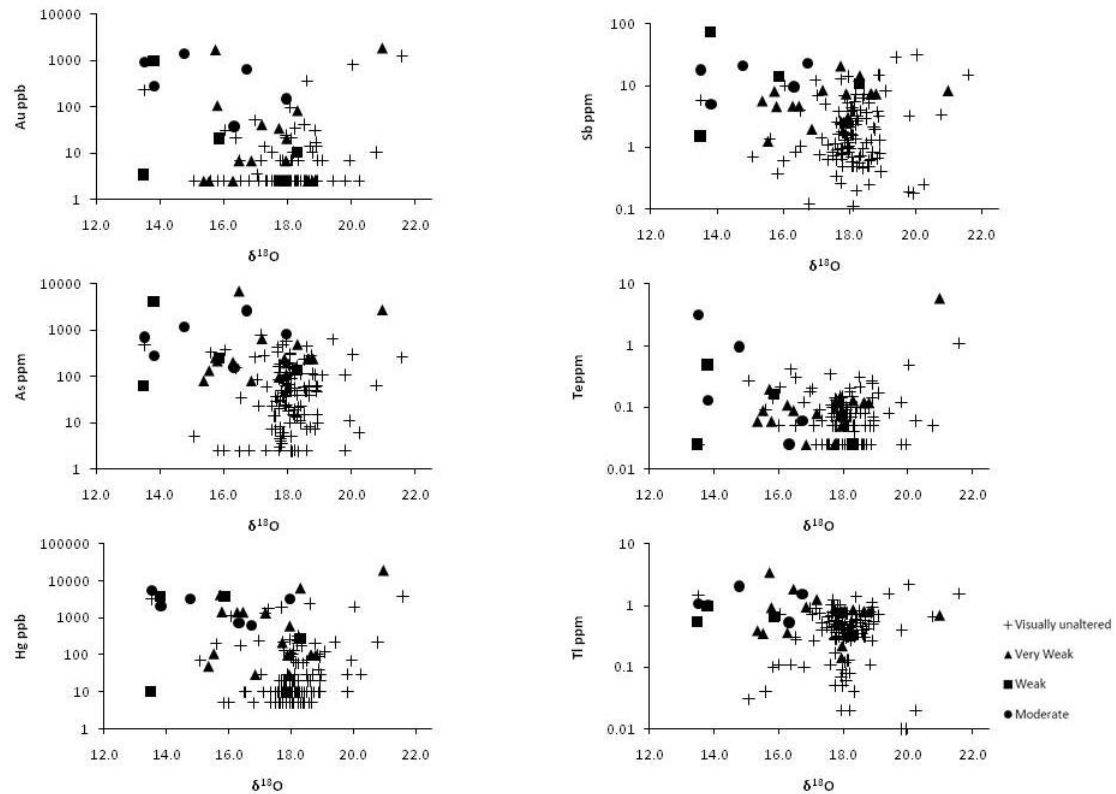


Figure 16. Cross-plots of trace elements (Au, As, Hg, Sb, Te, and Tl) vs. $\delta^{18}\text{O}$ at Turquoise Ridge. Data from Table 1.

halo to visible alteration, with concentrations of ≥ 175 ppb Hg extending no more than 8 m beyond visible hydrothermal alteration. The highest Hg concentrations throughout the cross-section are associated with visible alteration along the main dacite dike and the Getchell Fault Zone. Similar to Hg, Tl values ≥ 0.5 ppm extend no more than 8 meters outboard of visibly-altered wall rocks and are intimately associated with high flux zones that include the main dacite dike and Getchell Fault Zone. Likewise, elevated Sb (≥ 2.5 ppm) extends up to 15 m beyond visible alteration. Elevated Sb is primarily associated with the Getchell Fault Zone, antithetic fractures in the hanging wall of the Getchell Fault, and the HGB zone. Arsenic (≥ 100 ppm) displays the largest geochemical halo to Au, extending 22 m into visually-unaltered hanging wall and foot-wall of

interpreted fluid pathways. Arsenic concentrations appear to systematically increase with increased proximity to visually-altered gold bearing zones. Conversely, elevated Te (≥ 0.5 ppm) is limited to within visibly-altered wall rock and displays no halo to gold mineralization.

Niton Results

The spatial distribution of CTGD trace element concentrations relative to oxygen and carbon isotope patterns along the east-west cross-section suggests that elevated trace elements related to gold mineralization commonly occur in what appear to be otherwise unaltered wall rocks. A possible explanation for this is elevated trace metal concentrations along the bleached clay/calcite-lined fracture surfaces. If the trace element concentrations along the fracture surfaces are very high, the fracture surfaces would produce anomalous metal concentrations in the whole-rock geochemical analyses in otherwise unaltered rocks. To test this hypothesis, a Niton portable XRF was utilized to analyze the As contents of visually unaltered wall rocks and associated bleached clay-lined fractures and carbonaceous fracture coatings, in order to test whether the fractures contained significantly higher As concentrations than the adjacent wall rock. Unfortunately, calibration problems led to As values being the only accurate trace element values obtained while conducting the Niton analyses. [Table 3.4](#) shows the whole-rock Au and As values for the drill hole interval from which the Niton sample was collected (assays supplied by Barrick), the Niton As analyses of the unaltered wall rock, the corresponding As analyses of the fracture surfaces and the whole rock $\delta^{13}\text{C}$ and $\delta^{18}\text{O}$ values, on samples where isotope analyses had been conducted.

Nineteen of the 48 bleached, clay-lined fracture surfaces analyzed within this study display significantly elevated As relative to otherwise visually unaltered rock samples (Figure 3.18A-B). For example, sample 00NZ184_157 had 24 ppm As in unaltered diabase versus 993 ppm As on a bleached, clay-lined fracture surface. Sample TU00916_668 had <10 ppm As in unaltered carbonaceous mudstone but had 1537 ppm As in a bleached, clay-lined fracture surface), and sample TU00929_591 had 111 ppm As in an unaltered debris flow breccia versus 1070 ppm As in a bleached, clay-lined fracture surface. Elevated As levels are also pronounced along carbonaceous fracture coatings throughout the east-west cross-section. These carbonaceous fracture coatings typically have As concentrations that are several times greater than the adjacent unaltered host rocks. For example, sample TU01166_684 had 169 ppm As in unaltered micrite versus 1335 ppm As along a carbonaceous fracture surface, and sample TU01166_843 had 79 ppm As in unaltered micrite compared to 1813 ppm As in an adjacent carbonaceous fracture coating. The Niton analyses conducted within this study provide further support for tightly-confined, fracture-controlled hydrothermal fluid flow in wall rocks surrounding the HGB ore zone within the Turquoise Ridge deposit. The distribution of elevated trace elements along bleached and carbonaceous fracture surfaces indicate potential for haloes extending a significant distance beyond ore zones and pervasive hydrothermal alteration.

Table 3.3 Results of Factor Analysis showing Loadings for 7 Factors.

	Factor 1	Factor 2	Factor 3	Factor 4	Factor 5	Factor 6	Factor 7
Au	0.009	0.767	0.055	0.108	0.328	0.082	0.062
Ag	-0.009	0.355	0.792	0.029	0.125	0.167	0.026
Al	0.902	-0.091	-0.120	0.330	0.011	-0.067	0.098
As	0.184	0.849	0.105	-0.061	0.056	-0.064	0.074
Ba	0.236	-0.463	0.133	0.509	0.227	-0.157	0.386
Be	0.880	-0.041	-0.041	0.292	0.042	0.069	0.107
Bi	0.603	0.163	0.201	-0.133	0.108	0.559	-0.042
Ca	-0.397	-0.499	-0.051	0.162	-0.669	0.033	0.116
Cd	-0.118	0.097	0.837	0.020	-0.101	0.187	-0.050
Ce	0.815	0.114	-0.098	0.296	0.094	0.100	-0.217
Co	0.940	0.144	-0.056	-0.048	0.071	-0.021	-0.053
Cr	0.742	-0.003	0.212	0.303	0.069	-0.025	0.272
Cs	0.891	0.147	-0.073	0.070	-0.016	-0.075	0.176
Cu	0.315	0.259	0.736	-0.051	0.183	0.152	0.001
Fe	0.903	0.151	-0.041	-0.107	0.062	-0.029	-0.045
Ga	0.941	-0.040	-0.092	0.246	0.038	-0.089	0.068
Ge	0.734	-0.126	0.006	0.185	0.156	-0.112	-0.245
Hf	0.441	-0.010	0.134	0.863	-0.006	0.026	-0.012
Hg	-0.036	0.889	0.196	-0.192	0.099	0.132	-0.023
In	0.863	0.102	-0.035	-0.071	-0.013	0.136	-0.192
K	0.798	-0.184	-0.101	0.333	0.057	-0.056	0.373
La	0.770	0.087	-0.090	0.349	0.072	0.129	-0.202
Li	0.853	-0.038	-0.144	0.204	-0.059	-0.089	0.000
Mg	0.428	-0.629	-0.178	0.169	-0.165	-0.029	0.295
Mn	-0.026	-0.263	-0.097	0.009	-0.844	-0.086	-0.095
Mo	-0.231	0.259	0.829	-0.047	-0.048	-0.071	0.065
Na	0.532	-0.564	-0.205	0.251	0.065	0.090	0.157
Nb	0.224	-0.084	0.129	0.935	-0.086	-0.033	-0.007
Ni	0.824	0.168	0.319	-0.027	0.098	0.056	0.142
P	-0.178	0.100	0.805	-0.006	0.130	-0.130	-0.142
Pb	0.689	0.110	0.211	0.016	0.109	0.446	-0.050
Rb	0.861	-0.138	-0.132	0.256	0.034	-0.052	0.286
Re	-0.173	0.283	0.803	0.197	-0.077	-0.140	-0.029
S	0.153	0.687	0.450	-0.126	0.076	0.031	-0.121
Sb	0.140	0.778	0.414	0.047	0.018	-0.081	0.157
Sc	0.917	0.083	-0.154	0.109	-0.041	-0.053	-0.107
Se	-0.259	0.094	0.665	0.348	0.045	0.098	-0.013
Sn	0.895	0.219	-0.038	0.170	0.041	0.120	-0.032
Sr	-0.287	-0.604	-0.242	0.285	-0.391	0.150	0.145
Ta	0.213	-0.053	0.090	0.945	-0.043	0.008	-0.016
Te	-0.022	0.604	0.129	0.293	0.066	0.477	0.180
Th	0.891	0.040	-0.104	0.215	0.027	0.163	0.124
Ti	0.612	-0.248	0.020	0.592	-0.003	-0.241	0.114
Tl	0.534	0.575	0.168	-0.003	0.155	-0.031	0.354
U	0.018	0.021	0.723	0.507	-0.045	0.147	0.127
V	0.452	0.022	0.698	0.189	0.185	-0.325	0.113
W	0.162	0.850	0.126	0.086	-0.091	0.087	-0.171
Y	0.575	0.088	0.319	0.283	-0.090	-0.204	-0.467
Zn	0.708	0.053	0.455	-0.059	0.026	0.118	-0.086
Zr	0.393	0.016	0.172	0.876	-0.020	0.058	-0.035
% Var	34.83	13.92	13.41	11.46	3.60	2.75	2.86

Loadings that are >0.4 are shown in bold typeface. Var=variance.

Table 3.4: Niton fracture surface analyses

Sample	Description	Au DHI ppb	As Niton ppm	As DHI ppm	$\delta^{13}\text{C}$ VPDB, ‰	$\delta^{18}\text{O}$ VSMOW, ‰
99NZ022_2084R	weakly bleached tuffaceous mudstone	3	101	N/A		
99NZ022_2084F	patchy calcite clay-lined fracture	3	103	N/A		
99NZ022_2101R	tuffaceous limestone and mudstone with realgar and orpiment fractures	374	2160	N/A		
99NZ022_2102F	orpiment-lined fracture surface	374	12958	N/A		
99NZ022_2605R	unaltered siliceous black mudstone	22	119	N/A		
99NZ022_2605F	bleached clay-lined fracture	22	441	N/A		
99NZ015_2274.5R	unaltered chaotic breccia	7	67	170		
99NZ015_2274.5F	patchy calcite-lined fracture	7	368	170		
99NZ015_2523.8R	weakly argillized dacite	14	15	194		
99NZ015_2523.8F	bleached clay-lined fracture	14	344	194		
99NZ015_2629.5R	calcareous/carbonaceous black mudstone	7	184	267		
99NZ015_2629.5F	clay-lined fracture	7	116	267		
99NZ015_2645.7R	fractured black carbonaceous limestone	1490	92	255		
99NZ015_2645.7F	carbonaceous fracture surface	1490	417	255		
TU01164A_152R						
TU01164A_152F	unaltered tuffaceous mudstone and limestone	10	86	478		
TU01164A_292R	bleached clay-lined fracture	10	152	478		
TU01164A_292F	unaltered tuffaceous mudstone	45	61	116		
TU01164A_374R	bleached clay/calcite-lined fracture	45	57	116		
TU01164A_374F	unaltered tuffaceous limestone and mudstone/ realgar and orpiment fractures	0	22	120		
TU01164A_397R	calcite-lined fracture	0	25	120		
TU01164A_397F	weakly argillized tuffaceous mudstone	58	62	694		
TU01164A_397F	green clay-lined fracture	58	120	694		
TU01164A_397F	calcite-lined fracture	58	12	694		

Sample	Description	Au DHI ppb	As Niton ppm	As DHI ppm	$\delta^{13}\text{C VPDB}$, ‰	$\delta^{18}\text{O}$ VSMOW, ‰
TU01164A_454R	unaltered carbonaceous mudstone	17	14	270		
TU01164A_454F	green-blue clay-lined fracture	17	83	270		
TU01165_626R	unaltered micritic limestone	21	432	717		
TU01165_626S	stylolite	21	371	717		
TU01165_626F	calcite vein	21	97	717		
TU01165_626F	carbonaceous fracture surface	21	3698	717		
TU01165_711R	unaltered calcarenite limestone	79	192	591		
TU01165_711F	carbonaceous fracture surface	79	1981	591		
TU01165_723R	debris flow breccia	998	680	820		
TU01165_723F	carbonaceous fracture surface	998	3425	820		
TU01165_868R	carbonaceous micrite	833	259	687		
TU01165_868F	carbonaceous fracture surface	833	1998	687		
TU01165_1072.5R	weakly decalcified micritic limestone	34	84	204		
TU01165_1072.5F	carbonaceous fracture surface	34	127	204		
TU01165_1282R	propylitized dacite dike	86	62	45		
TU01165_1282F	bleached fracture surface	86	101	45		
TU01165_1303R	calcarenite debris flow	14	32	60		
TU01165_1303F	calcite-lined fracture	14	15	60		
TU01165_1325R	unaltered siliceous black mudstone	21	40	77		
TU01165_1325F	patchy calcite-lined fracture	21	24	77		
TU01166_275.5R	limestone clast supported breccia	0	32	69		
TU01166_275.5F	calcite-lined fracture	0	9	69		
TU01166_414.7R	weak-moderate argillized dacite	3857	651	8860		
TU01166_414.7F	bleached clay/realgar-lined fracture	3857	88800	8860		
TU01166_453R	bleached carbonaceous mudstone	2506	792	1070		
TU01166_453F	bleached clay-lined fracture	2506	1731	1070		
TU01166_543R	carbonaceous mudstone	0	456	1220		

Sample	Description	Au DHI ppb	As Niton ppm	As DHI ppm	$\delta^{13}\text{C VPDB}$, ‰	$\delta^{18}\text{O}$ VSMOW, ‰
TU01166_543F	green clay-lined fracture	0	4107	1220		
TU01166_612R	unaltered siliceous black mudstone	10	739	1114		
TU01166_612F	green clay-lined fracture	10	1750	1114		
TU01166_681R	crackle breccia	507	1328	1315		
TU01166_6681F	carbonaceous fracture surface	507	6249	1315		
TU01166_684R	recrystallized micritic limestone	278	169	398		
TU01166_684F	carbonaceous fracture surface	278	1335	398		
TU01166_707R	weakly argillized carbonaceous mudstone	2808	1263	1190		
TU01166_707F	carbonaceous fracture surface	2808	3998	1190		
TU01166_843R	recrystallized micritic limestone	14	79	462		
TU01166_843F	carbonaceous fracture surface	14	1813	462		
TU01167_286R	propylitized basalt	0	<LOD	N/A		
TU01167_286F	tan clay-lined fracture surface	0	50	N/A		
TU01167_484R	recrystallized micritic limestone	552	122	1430		
TU01167_484F	carbonaceous fracture surface	552	2155	1430		
00NZ184_1275R	calcarenite debri flow	25	21	230		
00NZ184_1275F	bleached clay/calcite-lined fracture	25	29	230		
00NZ184_1318R	unaltered tufaceous mudstone	10	29	623		
00NZ184_1318F	calcite-lined fracture	10	245	623		
00NZ184_1571R	unaltered diabase	188	24	792		
00NZ184_1571F	calcite/clay-lined fracture	188	993	792		
TU00760_263R	recrystallized micritic limestone	34	114	N/A	-3.6	17.7
TU00760_263F	carbonaceous/clay-lined fracture	34	182	N/A	-3.6	17.7
TU00760_481R	recrystallized micritic limestone/carbonaceous mudstone	480	102	N/A	-1.7	17.7
TU00760_481F	weakly bleached fracture surface	480	191	N/A	-1.7	17.7
TU00760_488R	recrystallized micritic limestone	137	67	N/A	-2.5	17.3

Sample	Description	Au DHI ppb	As Niton ppm	As DHI ppm	$\delta^{13}\text{C VPDB}$, ‰	$\delta^{18}\text{O}$ VSMOW, ‰
TU00760_488F	carbonaceous fracture surface	137	624	N/A	-2.5	17.3
TU00760_491R	weakly decalcified micritic limestone	754	194	N/A	-1.7	16.1
TU00760_491F	carbonaceous fracture surface	754	193	N/A	-1.7	16.1
00NZ158_2032.5R	unaltered tuffaceous mudstone and limestone	8	<LOD	6		
00NZ158_2032.5F	patchy calcite-lined fracture	8	17	6		
00NZ158_2462.9R	weakly decalcified micritic limestone	901	13	493		
00NZ158_2462.9S	stylolite	901	61	493	-5.3	18.0
00NZ158_2462.9F	carbonaceous fracture surface	901	427	493	-5.3	18.0
00NZ158_2624R	recrystallized micritic limestone	3	50	67	-1.4	18.1
00NZ158_2624F	bleached calcite/clay-lined fracture	3	144	67	-1.4	18.1
00NZ158_2709R	unaltered carbonaceous mudstone	5	14	2066	-1.7	18.3
00NZ158_2709F	patchy calcite/clay-lined fracture	5	75	2066	-1.7	18.3
00NZ188_2752.5R	recrystallized calcarenite limestone and noncalcareous mudstone	3	9	47	0.0	18.9
00NZ188_2753.3F	bleached clay-lined fracture	3	17	47	0.2	18.7
TU00916_668R	unaltered carbonaceous mudstone	34	<LOD	N/A		
TU00916_668F	patchy bleached calcite-lined fracture	34	1537	N/A		
TU00927_142R	unaltered recrystallized limestone and mudstone	4	17	N/A		
TU00927_142F	bleached calcite/clay-lined fracture	4	14	N/A		
TU00929_609R	unaltered recrystallized limestone and mudstone	1920	169	N/A		
TU00929_609F	bleached clay-lined fracture	1920	1588	N/A		
TU00929_591.5R	debris flow breccia	34	111	N/A	-4.7	18.3
TU00929_591.5F	grey-blue clay-lined fracture	34	1070	N/A	-4.7	18.3

R = Niton Analysis on rock surface
F = Niton analysis on fracture surface
Au DHI = Gold drill hole interval assay
As Niton = Arsenic value from portable Niton XRF
As DHI = Arsenic drill hole interval assay
 $\delta^{13}\text{C}$ VPDB, ‰ = Delta 13-carbon value relative to Vienna Pee Dee Belemnite standard
 $\delta^{18}\text{O}$ VSMOW, ‰ = Delta 18-oxygen value relative to Vienna Standard Mean Ocean Water standard
<LOD = Less than detection
N/A = Not analyzed

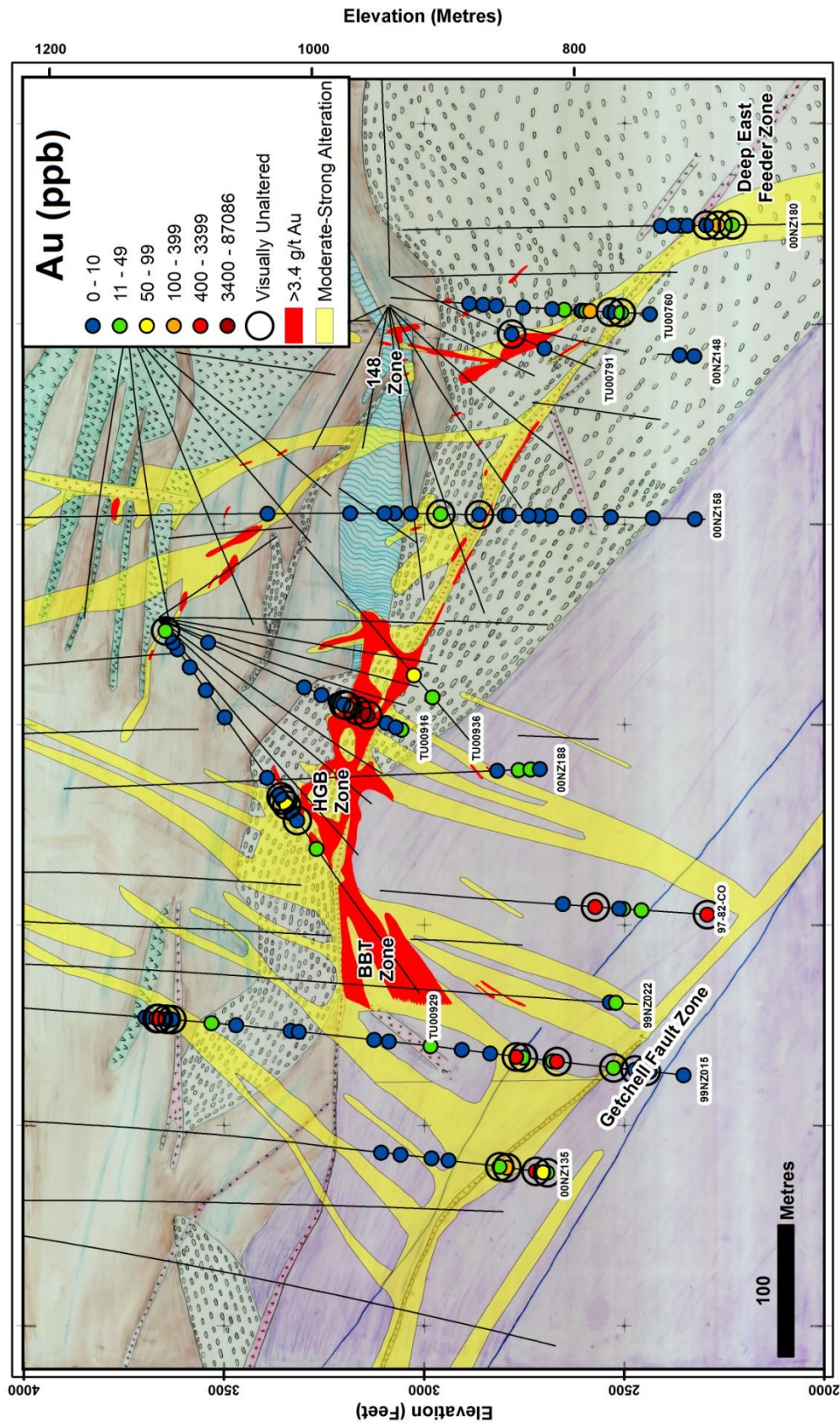


Figure 3.17A. Spatial distribution of Au along combined 2360300N-23600200N east-west cross-section. See text for discussion.

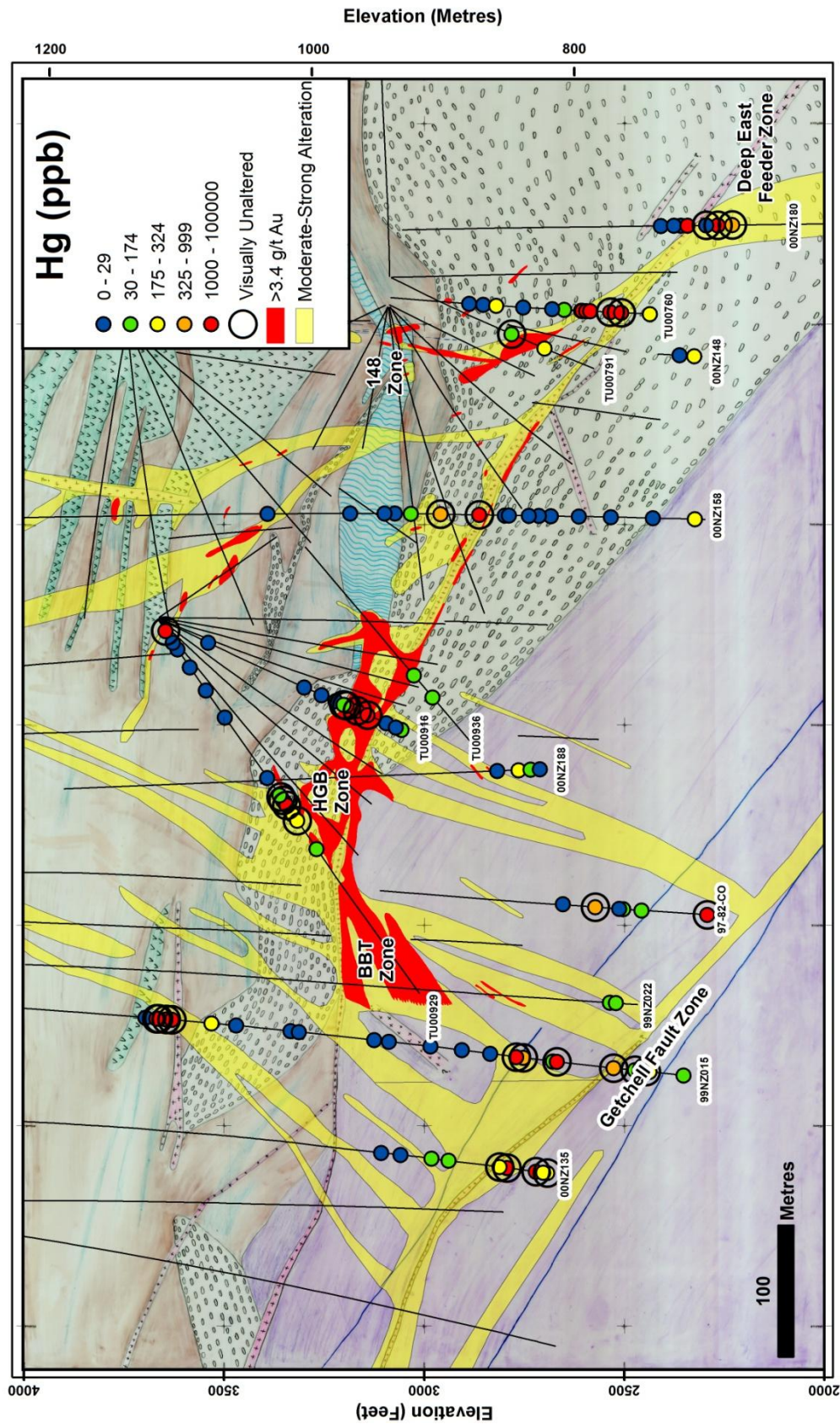


Figure 3.17B. Spatial distribution of Hg along combined 2360300N-23600200N east-west cross-section. See text for discussion.

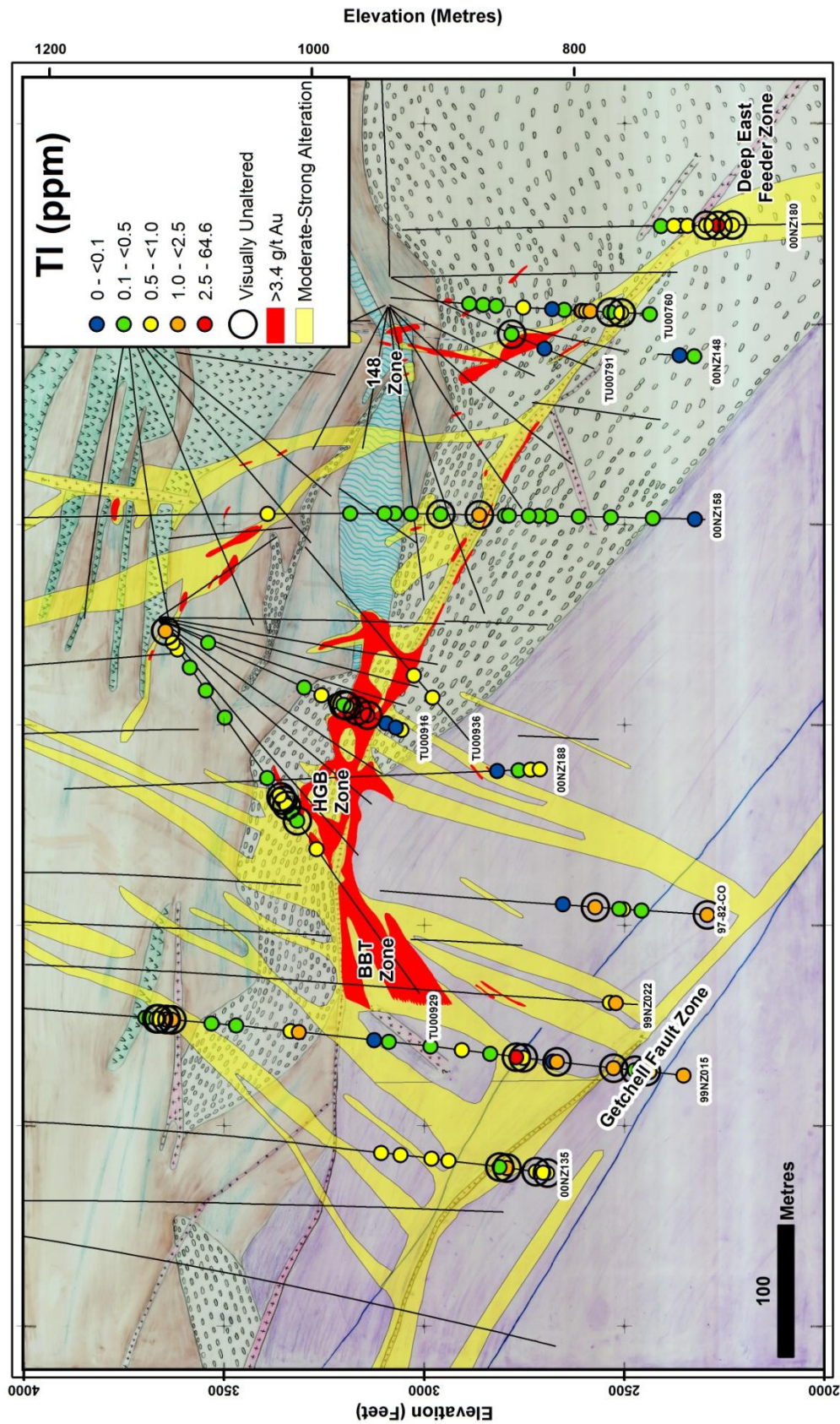


Figure 3.17C. Spatial distribution of Tl along combined 2360300N-23600200N east-west cross-section. See text for discussion.

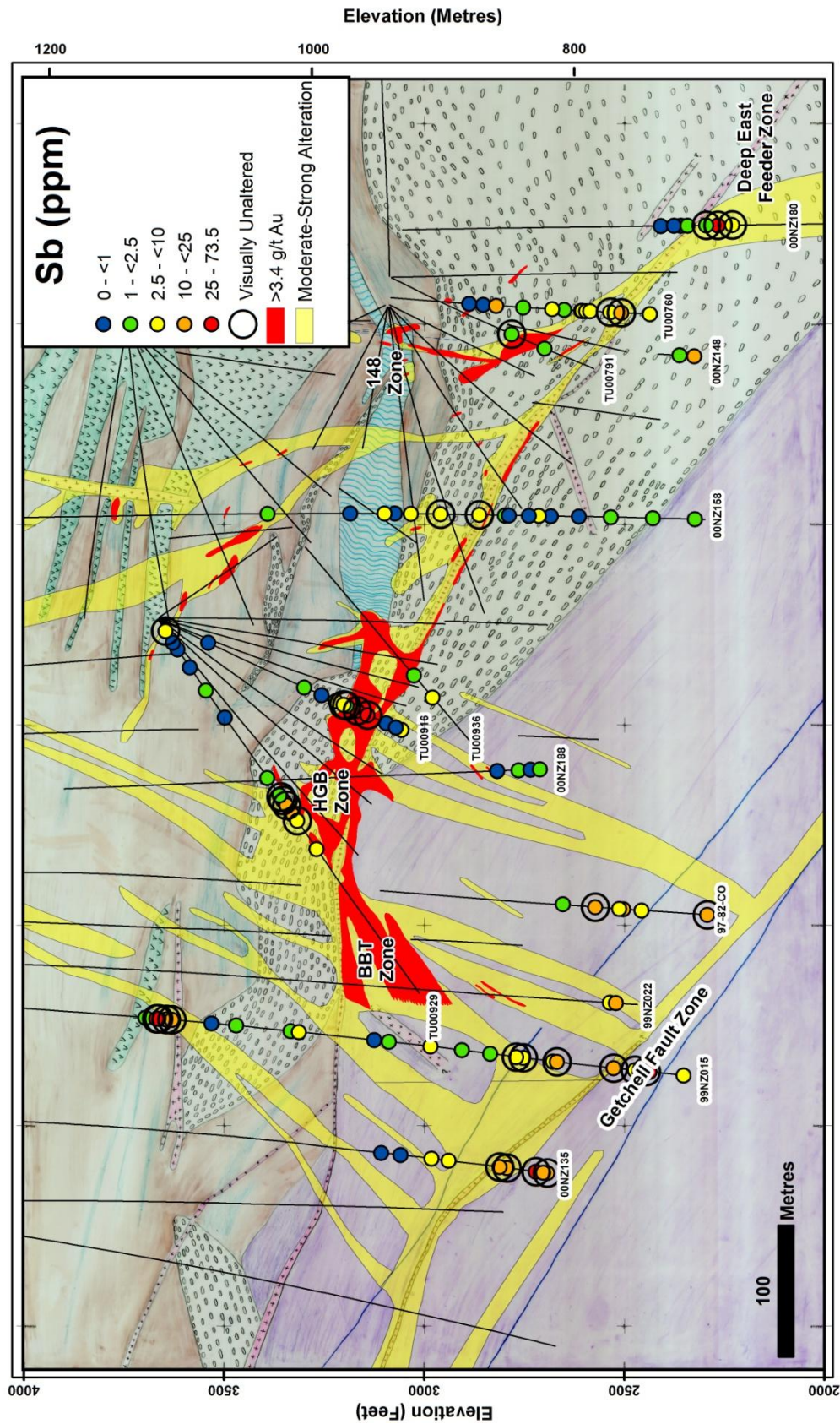


Figure 3.17D. Spatial distribution of Sb along combined 2360300N-23600200N east-west cross-section. See text for discussion.

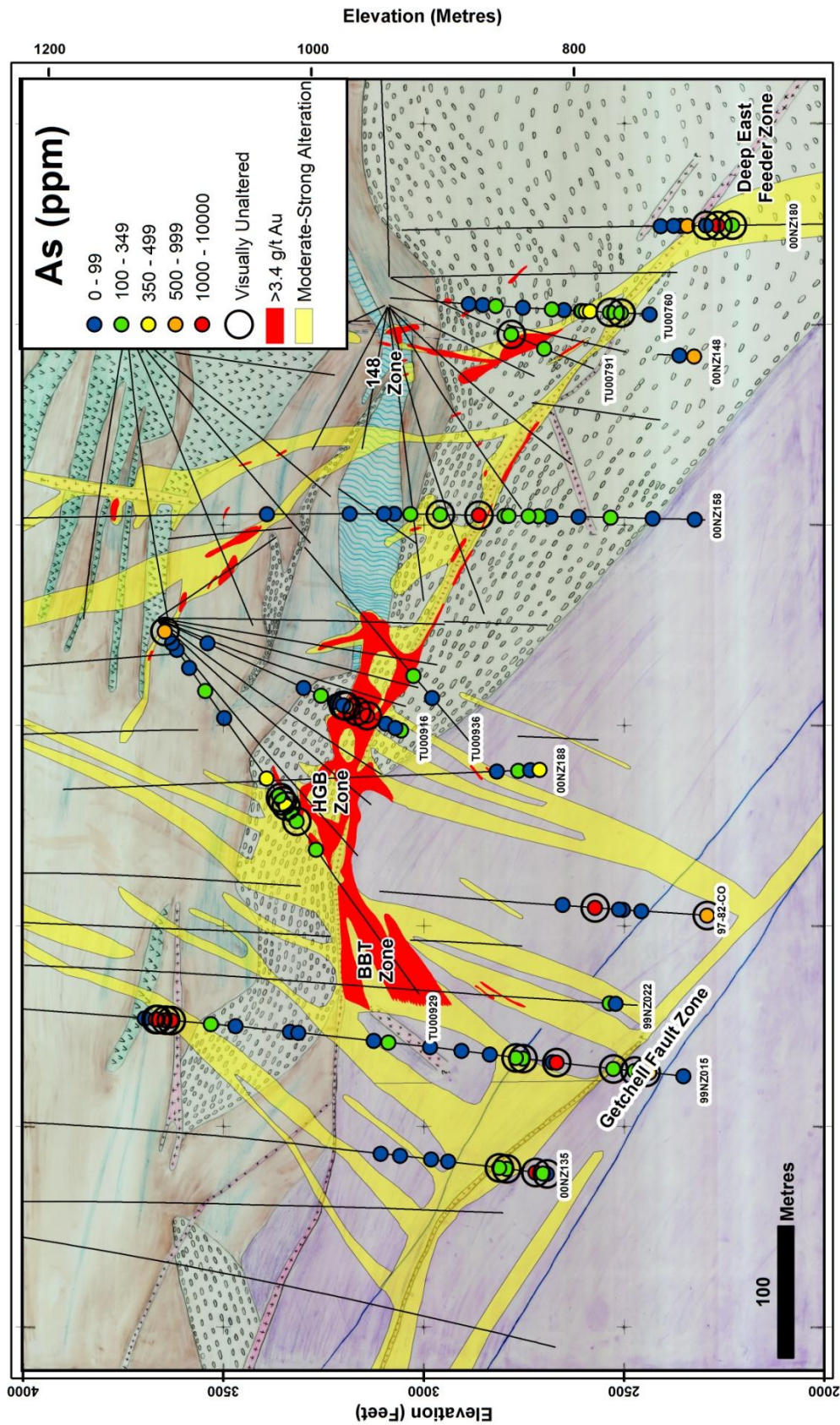


Figure 3.17E. Spatial distribution of Ar along combined 2360300N-23600200N east-west cross-section. See text for discussion.

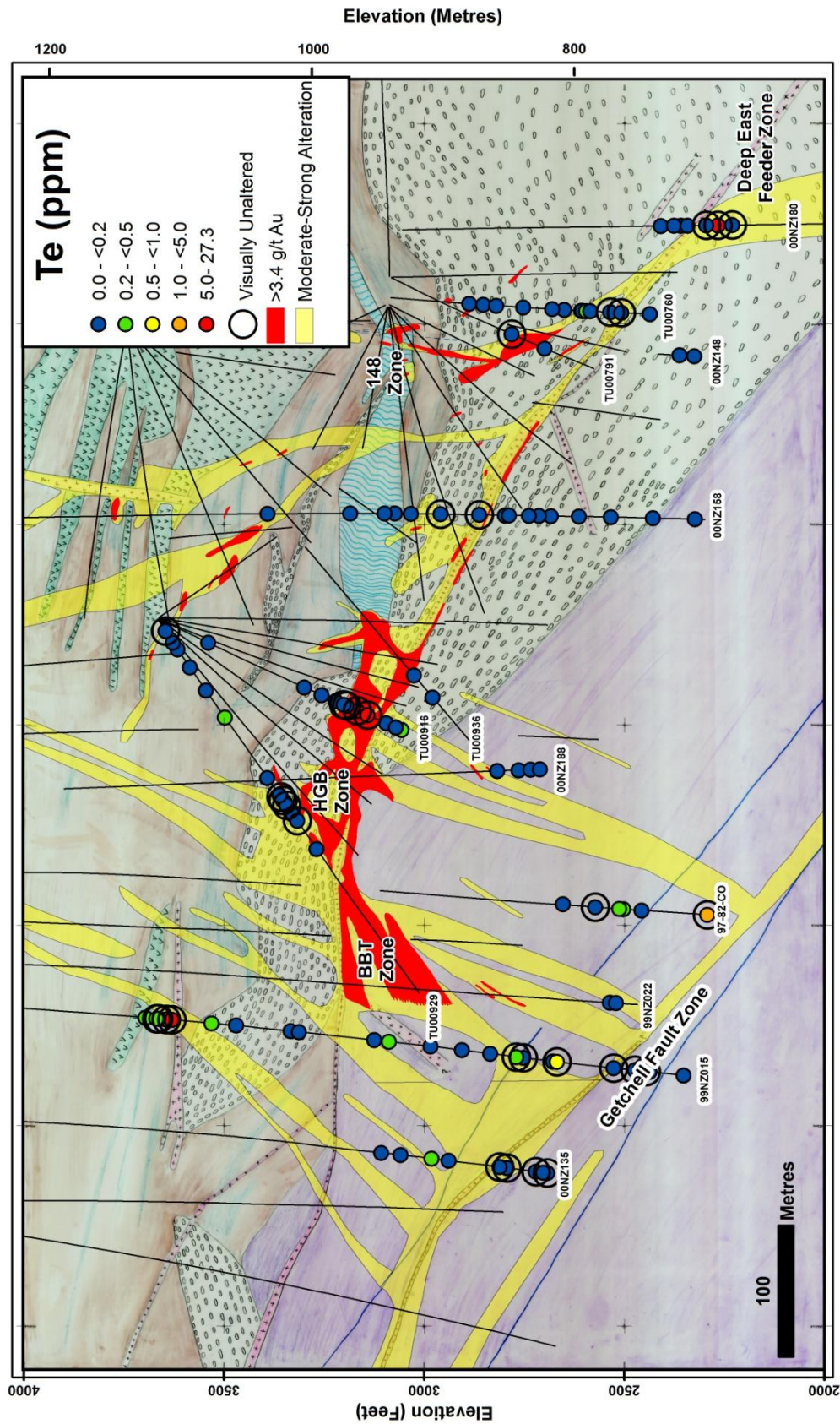
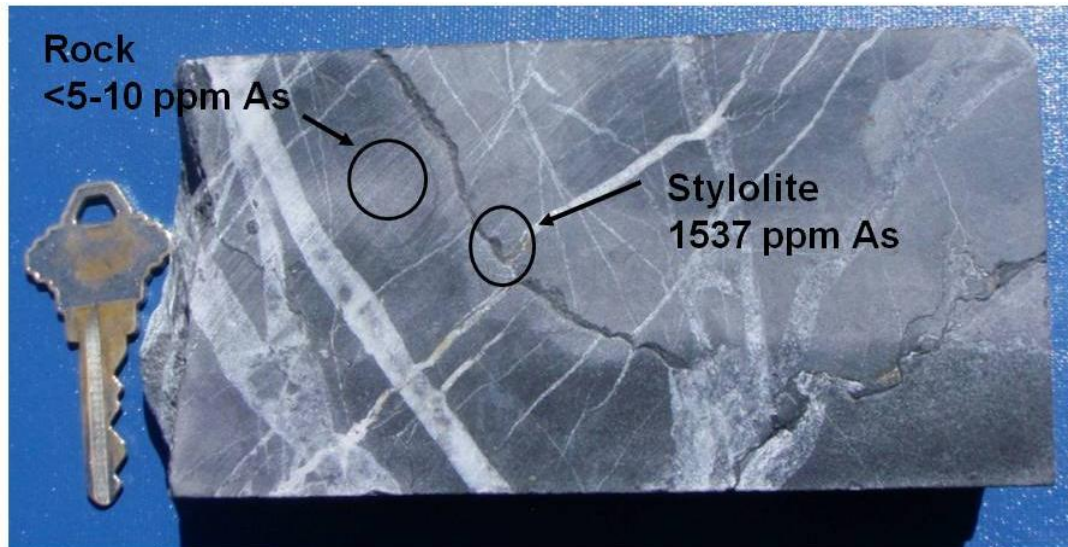
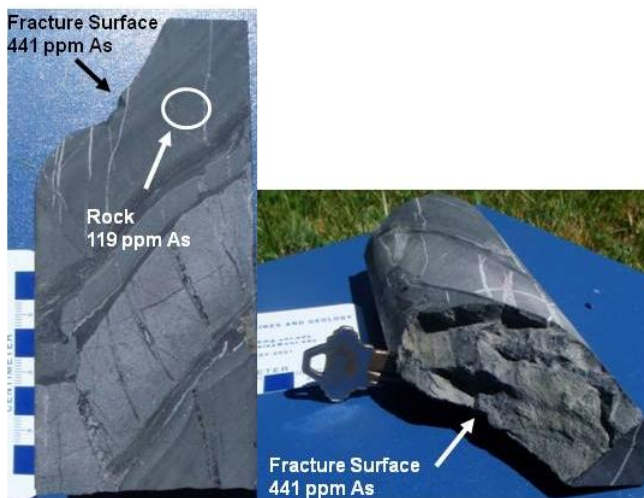


Figure 3.17F. Spatial distribution of Au along combined 2360300N-23600200N east-west cross-section. See text for discussion.



A



B

Figure 3.18. Typical drilled core rock matrix versus fracture surfaces. A. Niton analysis comparing As concentrations within a recrystallized micritic limestone. Note concentration of As in the rock matrix (<5ppm) versus As concentration of stylolite (1537 ppm) in sample TU00916 688 ft. B. Niton analysis comparing As concentrations within a siliceous black mudstone. Note elevated As concentration of bleached fracture surface (>441 ppm) relative to rock matrix (115 ppm) in sample 99NZ022_2605 ft. Note circles represent area where niton analyses were conducted.

DISCUSSION

This study was conducted to determine the nature and extent of cryptic alteration haloes, mainly looking for patterns of $\delta^{18}\text{O}$ in visibly-unaltered rock carbonate surrounding visible alteration and high-grade ore zones in the Turquoise Ridge CTGD. A potential practical outcome of this study would have been the identification of large haloes of low $\delta^{18}\text{O}$ values distal to visible hydrothermal alteration that could help future mine development and the discovery of future underground ore zones at Turquoise Ridge and other CTGDs by enlarging the target and providing additional vectors to ore. Although rock carbonate $\delta^{18}\text{O}$ values commonly decrease toward visible alteration and ore, the haloes are narrow and the patterns are too inconsistent to serve as a reliable exploration tool at Turquoise Ridge, at least at the scale of this study.

The high density of isotopic sampling conducted along individual isotopic transects utilizing multiple closely-spaced underground and surface drill holes above, within, and below visible hydrothermal alteration associated with interpreted fluid pathways along the east-west cross-section represents the most comprehensive isotopic study conducted to date at the deposit scale of a CTGD. Significant depletion distal to visible hydrothermal alteration is limited to bleached, clay-lined fractures in otherwise unaltered limestone having local background $\delta^{18}\text{O}$ values $>17.5\%$. The lack of wide, coherent haloes of various hydrothermal features surrounding ore suggests that hydrothermal fluid flow at the Turquoise Ridge deposit was limited to a restricted fracture-controlled fluid flow network, rather than large-scale, pervasive, lithologic-

controlled fluid flow. Although no systematic isotope halo was documented distal to visible hydrothermal alteration at the Turquoise Ridge deposit, this research expands upon similar isotopic studies conducted on carbonate hosted CTGD's.

Table 3.5 summarizes these stable isotope studies that have been conducted on individual CTGD deposits and/or districts. Stable isotope analyses of rock carbonate on lower-grade open pit deposits, such as the nearby Twin Creeks CTGD, display variable isotopic results (Stenger et al., 1998). The Cambrian-Ordovician sequence calcareous shales that host ore at the Mega Pit at Twin Creeks have low $\delta^{18}\text{O}$ values (<18.0‰) surrounding ore, which resulted from reaction with hydrothermal fluids. On the other hand, the pattern of lower $\delta^{18}\text{O}$ values in carbonates of the Etchart Formation relative to ore at the Vista Pit at Twin Creeks is ambiguous, and interpreted to be the result of variable pre-ore wallrock isotopic compositions or post-mineral isotopic changes.

Stenger et al. (1998) demonstrate decreased $\delta^{18}\text{O}$ values associated with ore in the Twin Creeks Mega Pit. However, limited sampling of the Cambrian-Ordovician calcareous shales within the Megapit (40 samples along two cross-sections) and wide spacing of the drill holes severely hampers the understanding and interpretation of the pattern of $\delta^{18}\text{O}$ values. Unfortunately, the spatial distribution of visible alteration relative to gold mineralization and isotopic values was not discussed by Stenger et al., (1998). Whether these $\delta^{18}\text{O}$ values form a coherent halo around ore that could be practically applied in exploration remains speculative. The Pipeline deposit displays local, low $\delta^{18}\text{O}$ values (<19.5‰) extending several kms beyond known gold mineralization, although limited geologic control (200 m drill-spacing within Pipeline pit) and widely spaced regional

sampling (500-1000m between samples) has hampered the interpretation of the discontinuous isotopic halo (Arehart and Donelick, 2006). Again, no individual comparison between the isotopic compositions of visibly altered vs. unaltered samples (e.g., alteration intensity criteria among individual samples) was reported in this study.

Unveined dolomite and calcite samples collected within the Roberts Mountains Formation at the Generator Hill deposit within the Jerritt Canyon district by Hofstra (1994) demonstrated that samples containing the strongest hydrothermal alteration contained the lowest $\delta^{18}\text{O}$ values. (e.g., dolomite $\delta^{18}\text{O} = 11.0$ to 16.0‰ , $\delta^{13}\text{C} = 0.0$ to 2.0‰ ; calcite $\delta^{18}\text{O} = 9.0$ to 12.0 , $\delta^{13}\text{C} = -6.0$ to 2.0) relative to unaltered carbonates (e.g., dolomite $\delta^{18}\text{O} = 27.0\text{‰}$, $\delta^{13}\text{C} = 2.5\text{‰}$; calcite $\delta^{18}\text{O} = 23.0\text{‰}$, $\delta^{13}\text{C} = 1.5\text{‰}$). Further isotopic analyses of unveined calcite and dolomite collected throughout the Jerritt Canyon District by Patterson (2009) reveals a strong spatial relationship between $\delta^{18}\text{O}$ values $<22.0\text{‰}$ and anomalous Au (300 ppm) at the base of the Roberts Mountains Formation. Detailed analysis of the data reveals that the lowest $\delta^{18}\text{O}$ values occur within rocks containing visible hydrothermal alteration.

Isotopic transects along an inferred feeder fault associated with the Carlin deposit (Radtke et al., 1980) documented progressive decrease in $\delta^{18}\text{O}$ and $\delta^{13}\text{C}$ in calcite with decreasing distance to the fault. However, little isotopic variation in $\delta^{18}\text{O}$ or $\delta^{13}\text{C}$ was observed in dolomite, regardless of degree of alteration or proximity to fluid conduits. Additional isotopic analyses conducted at both the Carlin and Cortez deposits (Rye, 1985) found that low $\delta^{18}\text{O}$ and $\delta^{13}\text{C}$ values are more pronounced in calcite relative to dolomite since calcite is more readily recrystallized than dolomite under most low-

temperature hydrothermal conditions (Pinckney and Rye, 1972; Radtke et al., 1980; Rye, 1985).

Additional insight into the spatial distribution of stable isotopes relative to carbonate-hosted CTGDs can be found in isotopic studies conducted on chimney manto Pb-Zn-Cu-Ag deposits. Carbonate rock matrix isotopic values in the limestone-hosted El Mochito deposit range from 16.0 to 24.0‰, extending from 3-7.5 km from ore (Kesler et al., 1996; Vazquez et al., 1998). Larger isotopic haloes associated with chimney manto deposits are hosted in limestone rather than dolomite and form from higher temperature hydrothermal systems. The isotopic haloes within these documented chimney manto deposits appear to be more regionally extensive than the documented CTGD studies. In order for large $\delta^{18}\text{O}$ haloes to extend a significant distance from ore, a significant amount fluid flow is needed. Therefore high secondary porosity and permeability is necessary due to the low primary porosity and permeability associated with most limestones (Brown, 1947; Ohle, 1951). An increase in secondary porosity can result from heating and recrystallization (Garrels and Dyer, 1952) or structural deformation. Matrix carbonate from high-temperature dolostone-hosted ore deposits in the Superior District, Arizona has been shown to have original sedimentary variation in $\delta^{18}\text{O}$ values up to 8.0‰ in nonmineralized wall-rock within each stratigraphic unit (Frieauf and Pareja, 1998). This large isotopic variation within individual stratigraphic units was shown to mask the hydrothermal $\delta^{18}\text{O}$ signature, with hydrothermal depletion typically only extending up to 1 meter away from ore. As proposed by Nabelek (1991) diffusional exchange is not an effective mechanism for changing the composition of

carbonate rocks. Rather, the predominant isotopic shift is derived from direct precipitation of hydrothermal carbonate in open spaces, dissolution-precipitation, or neomorphism (Gregg and Shelton, 1990).

Table 3.5. Characteristics of Isotopic Haloes in Carbonates Surrounding Ore in CTGDs.

Deposit	Nature of haloes around ore	References
Turquoise Ridge	<ol style="list-style-type: none"> 1. 180 rock carbonate isotope samples collected from the Turquoise Ridge deposit primarily along the 1:600 scale 2360200N-2360300N cross-section. Sampling focused on isotopic transects above, within, and below visible hydrothermal alteration (interpreted fluid conduits and feeder zones) and orezones (>3.4ppm Au). 2. Sampling transects were conducted at approximately 10 m intervals between samples from surface holes having 50m drill spacing and underground drill fans having 20 m drill spacing. 3. $\delta^{18}\text{O}$: 12.5 to 21.6‰, $\delta^{13}\text{C}$: 8.2 to 1.2‰, Cambrian-Ordovician carbonates 4. Depleted $\delta^{18}\text{O}$ values mainly limited to visually altered carbonates. A few depleted, visibly unaltered samples (<17.6‰) occur within meters of visible alteration and elevated (>0.01ppm) Au grades. 5. Significant depletion distal to interpreted fluid pathways and ore bodies appears to be limited to bleached clay-lined fractures in otherwise unaltered limestone having local background $\delta^{18}\text{O}$ values (>17.5‰). 6. District-scale depletion in $\delta^{18}\text{O}$ values (17.5-21.3‰), relative to typical Paleozoic carbonates extends several kms away from known CTGDS. Caused by contact metamorphism and recrystallization of carbonates during emplacement of the Osgood Stock. 	1. This Study
Twin Creeks (Megapit) (Vista pit)	<ol style="list-style-type: none"> 1. 108 whole rock samples collected from 3 cross-sections with average drill hole spacing from 50 to 150 m. Two cross sections from the Megapit containing 26 and 14 samples respectively. One cross-section containing 49 samples from the Vista pit. 2. $\delta^{18}\text{O}$ 12.0‰ to 24.0‰, $\delta^{13}\text{C}$ 0.0‰ to -10.0‰, Cambrian-Ordovician calcareous shales; $\delta^{18}\text{O}$ 5.0‰ to 25.0‰, $\delta^{13}\text{C}$ -10.0‰ to 4.0‰, Pennsylvanian-Permian limestone. 3. Limited sampling in the Cambrian-Ordovician rocks within the Megapit resulted in erratic distribution difficult to accurately interpret. 4. Depleted $\delta^{18}\text{O}$ values (<18.0‰) roughly correlate with high gold grades (>0.05 opt) within the Megapit. 5. No systematic spatial variation in $\delta^{18}\text{O}$ values in the Pennsylvanian-Permian limestones relative to gold mineralization (>0.05 opt) at the Vista Pit. 6. Do not mention/compare isotopic values between visibly 	Stenger et al., 1998

	unaltered vs. altered samples within the study.	
Carlin	<ol style="list-style-type: none"> 24 rotary drill core and bench samples (Carlin pit) conducted on calcite and dolomite rock samples within the Roberts Mountains Formation through the East ore zone and an interpreted feeder structure within Carlin pit. Rock samples consisted of arenaceous dolomite or limy mud (type 1) and laminated arenaceous, peloid wackestone (type 2). Progressive depletion of $\delta^{18}\text{O}$ (12.7 to 16.3‰, calcite; 24.3 to 25.2‰, dolomite) and $\delta^{13}\text{C}$ (-1.7 to 0.8‰, calcite; -0.5 to -0.4‰, dolomite) from 0 to 30m within the hanging wall of the East ore zone. Progressive depletion of $\delta^{18}\text{O}$ (13.9 to 18.0‰, calcite; 19.4 to 24.5‰, dolomite) and $\delta^{13}\text{C}$ (-1.3 to -0.2‰, calcite; -0.1 to 1.1, dolomite) within visually altered rocks from 0 to 30 m distal to interpreted feeder structure along 6300 bench. Isotopic analyses and petrographic study of altered samples from the Carlin deposit confirmed that calcite was more readily dissolved and recrystallized relative to dolomite during hydrothermal alteration. 	Radtko et al., 1980
Pipeline	<ol style="list-style-type: none"> 133 drill core hand drilled limestone (rock) samples and 60 calcite vein samples were collected from drill core containing an average drill spacing of 200 m within the Pipeline pit. Additionally sampling was conducted on surface exposures and drill core up to 4 km beyond the outline of the Pipeline pit (roughly 200-500 m spacings). Isotopic compositions of drill rock samples from the study ranged from $\delta^{18}\text{O}$ -1.7‰ to 21.9‰, $\delta^{13}\text{C}$ -5.5‰ to 0.4‰. Lowest $\delta^{18}\text{O}$ values occur within the Pipeline pit. Depleted drilled rock isotopic samples (<19.5‰) extend roughly 50m (?) beyond increased Au mineralization (assays not provided) and up to 3 km beyond the outline of the Pipeline pit. Isotopic depletion extending roughly 200 m beyond plotted silicified zones (note elevated gold values also occur in zones outboard of these silicified zones). No individual comparison between the isotopic compositions between visibly altered vs. unaltered samples (e.g. alteration intensity criteria among individual samples). No discernable spatial relationship between the Pipeline deposit and $\delta^{13}\text{C}$ values (both regionally and within the Pipeline pit). No recognizable correlation between $\delta^{18}\text{O}$ and $\delta^{13}\text{C}$ of calcite veins and Au mineralization. 	Arehark and Donelick, 2006
Jerritt Canyon	<ol style="list-style-type: none"> 46 unveined rock samples containing unaltered and visually altered calcite and dolomite hand samples collected from the 7880 Level grid in the Generator Hill deposit (Hofstra, 1994). Unaltered dolomite composition ($\delta^{18}\text{O}$ = 27.0‰; $\delta^{13}\text{C}$ = 2.5‰), unaltered calcite compositions ($\delta^{18}\text{O}$ = 23.0‰; $\delta^{13}\text{C}$ = 1.5‰) 	Hofstra, 1994 Patterson, 2009

	<ol style="list-style-type: none"> 3. Samples containing strongest visible hydrothermal alteration containing dolomite ($\delta^{18}\text{O} = 11.0$ to 16.0‰; $\delta^{13}\text{C} = 0.0$ to 2.0‰) and calcite ($\delta^{18}\text{O} = 9.0$ to 12.0‰; $\delta^{13}\text{C} = -6.0$ to 2.0‰) 4. No discussion/interpretation of spatial distribution or isotopic haloes associated with ore (Hofstra, 1994). 5. 150 isotopic samples collected from the bottommost 1.5 m of the Roberts Mountains Formation of hand drill dolomite and calcite rock samples where veins were avoided District wide sampling from 67 drill holes having 30-100m drill spacing (Patterson, 2009). 6. Isotopic compositions of normalized dolomite and calcite values ranged $\delta^{18}\text{O} = 7.2$ to 25.4‰ and $\delta^{13}\text{C} = -6.9\text{‰}$ to 4.5‰. 7. Patchy, inconsistent halo of depleted $\delta^{18}\text{O}$ values ($<22\text{‰}$) extending up to 2,000ft beyond the 300 ppb Au contour in the SSX-Smith area occurs in both visibly altered and unaltered rock. 8. Patchy, inconsistent halo of depleted $\delta^{18}\text{O}$ values ($<22\text{‰}$) extending up to 800ft beyond the 300 ppb Au contour in the (Murray-Winters Creek area occurs in both visibly altered and unaltered rock.) 9. No association between $\delta^{13}\text{C}$ values, visible alteration, and gold mineralization. 	
--	--	--

CONCLUSIONS

Statistical analysis of multi-element data in this study shows that gold is mainly associated with Hg, As, Sb, W, Te, and Tl. Arsenic, Sb, and Hg form larger, more coherent haloes to visible alteration and ore zones than $\delta^{18}\text{O}$ or $\delta^{13}\text{C}$ values. Niton analyses reveal that most of these trace element anomalies in visibly unaltered rocks are likely related to bleached or carbonaceous, clay-lined fractures. Limited isotopic analyses of these fracture surfaces show they have lower $\delta^{18}\text{O}$ and $\delta^{13}\text{C}$ values relative to visibly unaltered limestones, consistent with their elevated As contents, indicating fluid flow was largely confined to narrow fractures in otherwise visibly unaltered rock. Fluid flow associated with gold mineralization at the Turquoise Ridge deposit was limited to a few confined, high-flux, fluid pathways (e.g., Getchell Fault Zone, main

dacite dike, 148 zone) before ore fluids encountered more reactive host rock (e.g., sedimentary breccias) where acid auriferous fluids reacted with rocks in the HGB zone. The acidic fluids subsequently reacted with these favorable lithologies resulting in carbonate dissolution, and increased pore space for fluid migration before ultimately exploiting pre-existing exhaust structures in less reactive overlying strata (e.g., tuffaceous mudstones and limestones). The passive and opportunistic fluid flow along confined fluid pathways resulted in narrow visual and cryptic hydrothermal alteration signatures along both the feeding structures in the footwall of the HGB and exhaust zones in the hanging wall of the HGB. These feeder and exhaust structures typically consist of narrow alteration zones and bleached, clay-lined fractures along narrow broken zones or fracture planes that extend outward into otherwise visually unaltered rocks in the footwall and hanging wall of the Turquoise Ridge ore zones.

The most promising vectoring tool derived in the studies reported in this Chapter is analysis of fracture surfaces for their trace elements. Bleached, clay-lined fractures and carbonaceous fracture surfaces along exhaust structures should contain elevated trace elements related to CTGD mineralization, such as As, Hg, Sb, Te, and/or Tl. Some of those elements, such as As, can be easily and quickly identified utilizing a portable XRF. Limited use of the Niton in this study indicated elevated As concentrations in the fractures relative to the adjacent unaltered wall rock. More mining and exploration companies are using such portable XRF units, but few to no data have been published. Comprehensive orientation studies of CTGDs are warranted.

References

- Abdi, H., 2003, Factor Rotations in Factor Analyses, *in* Lewis-Beck M., Bryman, A., and Futing, T. eds. Encyclopedia of Social Sciences Research Methods, Thousand Oaks, CA: Sage, p. 1-8.
- Albino, G.V., 1994, Geology and lithogeochemistry of the Ren gold prospect, Elko County, Nevada: the role of rock sampling in exploration for deep Carlin-type deposits: *Journal of Geochemical Exploration*, v. 51 p. 37-58.
- Alt, J.C., Laverne, C., and Muelenbachs, K., 1985, Alteration of the upper oceanic crust: Mineralogy and processes in DSDP hole 504B, leg 83: Deep Sea Drilling Project Initial Reports, v. 83, p. 217-247.
- Alt, J.C., Teagle, D.A.H., Brewer, T., Shanks, W.C., III, and Holliday, A., 1998, Alteration and mineralization of an oceanic forearc and the ophiolite-ocean crust analogy: *Journal of Geophysical Research*, v. 103, p. B12,365-12,380.
- Arehart, G.B., and Donelick, R.A., 2006, Thermal and isotopic profiling of the Pipeline hydrothermal system: Application to exploration for Carlin-type gold deposits: *Journal of Geochemical Exploration*, v. 91, p. 27-40.
- Arehart, G.B., Chryssoulis, S.L., and Kesler, S.E., 1993a, Gold and arsenic in iron sulfides from sediment-hosted disseminated gold deposits: Implications for depositional processes: *Economic Geology*, v. 88, p. 171-185.
- Arehart, G.B., Foland, K.A., Naeser, C.W., and Kesler, S.E., 1993b, $^{40}\text{Ar}/^{39}\text{Ar}$, K/Ar, and fission track geochronology of sediment-hosted disseminated gold deposits at Post-Betze, Carlin trend, northeastern Nevada: *Economic Geology*, v. 88, p. 622-646.
- Arehart, G.B., Chakurian, A.M., Tretbar, D.R., Christensen, J.N., McInnes, B.A., and Donelick, R.A., 2003, Evaluation of radioisotope dating of Carlin-type deposits in the Great Basin, North America, and implication for deposit genesis: *Economic Geology*, v. 98, p.235-248.
- Bakken, B.M., and Einaudi, M.T., 1986, Spatial and temporal relations between wall rock alteration and gold mineralization, main pit, Carlin gold mine, Nevada, USA, *in* Proceedings, Gold '86; an international symposium on the geology of gold deposits, Toronto, ON, Canada, p. 388-403.
- Berger, B.R., and Taylor, B.E., 1980, Pre-Cenozoic normal faulting in the Osgood Mountains, Humboldt County, Nevada: *Geology*, v. 8, p. 594-598.

- Boskie, R.M., 2001, Detailed structure and stratigraphy of the lower Paleozoic rocks of the Getchell trend, Osgood Mountains, Humboldt County, Nevada: unpublished MS thesis, University of Nevada Reno, 171 p.
- Breit, F.J., Ressel, M.W., Muirhead, E.M.M., 2005, Geology and Gold Deposits of the Twin Creeks Mine, Humboldt County, Nevada, *in* Geological Society of Nevada Symposium 2005, Field Trip Guidebook 4, p. 77-102.
- Broili, C., French, G.M., Shadrack, D.R., Weaver, R.R., 1988, Geology and gold mineralization of the Gold Bar deposit, Eureka County, Nevada, *in* proceedings, Schaefer, R.W., Cooper, J.J., and Vikre, P.G., Bulk mineable precious metal deposits of the Western United States: Geological Society of Nevada, p. 57-72.
- Brown, J.S., 1947, Porosity and ore deposition at Edwards and Balmat, New York: Geological Society of America Bulletin, v. 58, p. 532-533.
- Buchanan, L.J., 1981, Precious metal deposits associated with volcanic environments in the southwest: Arizona Geological Society Digest, v. 14, p. 237-262.
- Chevillon, V., Berentsen, E., Gingrich, M., Howald, B., Zbinden, E., 2000, Geologic overview of the Getchell gold mine geology, exploration, and ore deposits, Humboldt County, Nevada: Part II, Geology and gold deposits of the Getchell region, Crafford: Guidebook Series Society of Economic Geologists, v. 32, p. 195-201.
- Cail, T.L., and Cline, J.S., 2001, Alteration associated with gold deposition at the Getchell Carlin-type gold deposit, north-central Nevada: Economic Geology, v. 96, p. 1343-1359.
- Canfield, D.E., 1989, Reactive iron in marine sediments: *Geochimica et Cosmochimica Acta*, v. 53, p. 2483-2490
- Canfield, D.E., 1991, Sulfate reduction in deep-sea marine sediments: *American Journal of Science*, v. 291, p. 177-188.
- Cline, J.S., 2001, Timing of gold and arsenic sulfide mineral deposition at the Getchell Carlin-type gold deposit, North-central Nevada: *Economic Geology*, v. 96, p. 75-90.
- Cline, J.S., Hofstra, A.H., 2000, Ore-fluid evolution at the Getchell carlin-type gold deposit, Nevada, USA: *European Journal of Mineralogy*, v.12, p.195-212.

- Cline, J.S., Hofstra, A.H., Muntean, J.L., Tosdal, R.M., and Hickey, K.A., 2005, Carlin-type gold deposits in Nevada: Critical geologic characteristics and viable Models, *in* Hedenquist, J. W., Thompson, J. F. H., Goldfarb, R. J., and Richards, J. P., eds., 100th Anniversary Volume: Society of Economic Geologists, Littleton, CO, p. 451-484.
- Cline, J.S., Muntean, J. L., Longo, A.A., and Cassinero, M.D., 2008, Collaborative research on fluid pathway and metal transport in Carlin-type gold deposits: Insights from the Getchell deposit. Final Report for the U.S. Geological Survey 2006 Mineral Resources External Research Program (MRERP), 128 p.
- Clode, C.H., Grusing, S.R., Heitt, D.G., and Johnson, I.M., 1997, The relationship of structure, alteration, and stratigraphy to formation of the Deep Star gold deposit, Eureka county, Nevada: Society of Economic Geologists Guidebook Series, v. 28, p. 239-258.
- Cook, H.E., and Taylor, M.E., 1977, Comparison of continental slope and shelf environments in the Upper Cambrian and lowest Ordovician of Nevada: *in* Cook, H. E. and Enos, P., eds. Deep-water carbonate environments: SEPM Special Publication 25, p. 51-81.
- Crafford, E.J., 2000, Overview of regional geology and tectonic setting of the Osgood Mountains region, Humboldt County, Nevada: Part II, Geology and gold deposits of the Getchell region, Crafford: Guidebook Series Society of Economic Geologists , v. 32, p. 225-234.
- Criss, R.E., Champion, D.E., McIntyre, D.H., 1985, Oxygen isotope, aeromagnetic, and gravity anomalies associated with hydrothermally altered zones in the Yankee Fork mining district, Custer County, Idaho: *Economic Geology*, v. 80, p. 1277-1296.
- Criss, R.E., and Taylor, H.P., Jr., 1986, Meteoric hydrothermal systems. *In* Valley, J.W., Taylor, H.P., Jr., O'Neal, J.R., Stable isotopes in high temperature geological processes. *Rev. Mineral.* 16, 373-424.
- Criss, R.E., Singleton, M.J., Champion, D.E., 2000, Three-dimensional oxygen isotope imaging of convective fluid flow around the Big Bonanza, Comstock Lode mining district, Nevada: *Economic Geology*, v. 95, p. 131-142.
- Dobak, P.J., Arbonies, D., Hipsley, R., and Visher, M., 2002, Geology of the Storm gold deposit, *in* Thompson, T.B., Teal, L., and Meeuwig, R.O., eds., *Gold Deposits of the Carlin Trend: Nevada Bureau of Mines and Geology*, v. 111, p. 46-53.

- Dong, G, Morrison, G., and Jaireth, S., 1995, Quartz textures in epithermal veins, Queensland – classification, origin, and implication: *Economic Geology*, v. 90, p. 1841-1856.
- Emsbo, P., 1999, Origin of the Meikle high grade gold deposit from the superposition of Late Devonian Sedex and mid-Tertiary Carlin-type gold mineralization: Unpublished Ph.D. Dissertation, Golden, Colorado School of Mines, 394 p.
- Emsbo, P., Hutchinson, R.W., Hofstra, A.H., Volk, J.A., Bettles, K.H., Baschuk, G.J., and Johnson, C.A., 1999, Syngenetic Au on the Carlin trend: Implications for Carlin-type deposits: *Geology*, v. 27, p. 59-62.
- Emsbo, P., Hofstra, A.H., Lauha, E.A., Griffin, G.L., and Hutchinson, R.W., 2003, Origin of high-grade gold ore, source of ore fluid components, and genesis of the Meikle and neighboring Carlin-type deposits, northern Carlin trend, Nevada: *Economic Geology*, v. 98, p. 1069-1100.
- Engel, A.E.J., Clayton, R.N., Epstein, S., 1958, Variations in isotopic composition of oxygen and carbon in Leadville Limestone (Mississippi, Colorado) and its hydrothermal and metamorphic phases: *Journal of Geology*, v. 66, p. 373-424.
- Evans, D.C., 2000, Carbonate-hosted breccias in the Meikle mine, Nevada and Their relationship with gold mineralization: Unpublished Masters thesis, Colorado School of Mines, 266 p.
- Fortuna, J., Kesler, S.E., and Stenger, D.P., 2003, Source of iron for sulfidation and gold deposition, Twin Creeks Carlin-type deposit, Nevada: *Economic Geology*, v. 98, p. 1213-1224.
- Freidman, G.M., 1959, Identification of carbonate minerals by staining methods: *Journal of Sedimentary Petrology*, v. 29, p. 87-97.
- Friehauf, K.C., and Pareja, G.A., 1998, Can oxygen isotope halos be produced around high-temperature dolostone-hosted ore deposits?: Evidence from the Superior District, Arizona: *Economic Geology*, v. 93, p. 639-650.
- Garrels, R.M., and Dryer, R.M., 1952, Mechanism of limestone replacement at low temperatures and pressures: *Geological Society of America Bulletin*, v. 63, p. 325-380
- Gies, H., 1976, Zur Beziehung zwischen Photolumineszenz und chemismus natürlicher Karbonate: *Neues Jahrbuch für Mineralogie Abhandlungen*: v. 127, p. 1-46.

- Gregg, J.M., and Shelton, K.L., 1990, Dolomitization and dolomite neomorphism in the back reef facies of the Bonnetterre and Davis Formations (Cambrian), southeastern Missouri: *Journal of Sedimentary Petrology*, v. 60, p. 549-562.
- Groff, J.A., Heizler, M.T., McIntosh, W.C., Norman, D.I., 1997, $^{40}\text{Ar}/^{39}\text{Ar}$ dating and mineral paragenesis for carlin-type gold deposits along the Getchell Trend, Nevada; evidence for Cretaceous and Tertiary gold mineralization: *Economic Geology*, v. 92, p. 601-622.
- Gustafson, L.B. and Hunt, J.P., 1975, The porphyry copper deposit at El Salvador, Chile: *Economic Geology* v. 70, p. 857-912.
- Harlan, J.B., Harris, D.A., Mallette, P.M., Norby, J.W., Rota, J.C., and Sagar, J.J., 2002, Geology and mineralization of the Maggie Creek district: Nevada Bureau of Mines and Geology Bulletin 111, p. 115-142.
- Hauff, P.L., Kruse, F.E., Madrid, R.J., 1991, Defining gold ore zones using illite polytypes, *in* Raines, G.L., Lisle, R.E., Schafer, R.W., Wilkinson, W.H.: *Geology and Ore Deposits of the Great Basin*, Geological Society of Nevada, p. 239-247.
- Hall, C.M., Kesler, S.E., Simon, G., Fortuna, J., 2000, Overlapping Cretaceous and Eocene Alteration, Twin Creeks Carlin-Type Deposit, Nevada: *Economic Geology*, v. 95, no. 8, p. 1739-1752.
- Hedenquist, J.W., Arribas R., A., and Gonzales-Urien, E., 2000, Exploration for epithermal gold deposits, *in* Hagemann, S.G., and Brown, P.E., eds., *Gold in 2000: Reviews in Economic Geology*, v. 13, p. 245-277.
- Heitt, D.G., Dunbar, W.W. Thompson, T.B., and Jackson, R.G., 2003, Geology and Geochemistry of the Deep Star Gold Deposit, Carlin Trend, Nevada: *Economic Geology*, v. 98 p. 1107-1136.
- Hitzman, M.W., Routine staining of drill core to determine carbonate mineralogy and distinguish carbonate alteration textures: *Mineralium Deposita*, v. 34, n. 8, p. 794-798.
- Hofstra, A.H., 1994, Geology and genesis of the Carlin-type gold deposits in Jerritt Canyon district, Nevada: Unpublished Ph.D. dissertation, Boulder, University of Colorado, 791 p.
- Hofstra, A.H., and Cline, J.S, 2000, Characteristics and models for Carlin-type gold deposits: *in* *Reviews in Economic Geology*, v.13, p. 163-220.

- Hofstra, A.H., Leventhal, J.S., Northrop, H.R., Landis, G.P., Rye, R.O., Birak, D.J., and Dahl, A.R., 1991, Genesis of sediment-hosted disseminated gold deposits by fluid mixing and sulfidation: Chemical-reaction-path modeling of ore-depositional processes documented in the Jerritt Canyon District, Nevada: *Geology*, v. 19, p.36-40.
- Hofstra, A.H., Snee, L.W., Naeser, C.W., Stein, H.J., and Lewchuck, M., 1999, Age constraints on Jerritt Canyon and other Carlin-type gold deposits in the western United States—relationship to Mid-Tertiary extension and magmatism: *Economic Geology*, v. 94, p. 769-802.
- Horton, R. C., 1999, History of the Getchell gold mine: *Mining Engineering*, v. 51, p. 50-56.
- Hotz, P.E., and Willden, R., 1964, *Geology and mineral deposits of the Osgood Mountains quadrangle, Humboldt County, Nevada*: U.S. Geological Survey Professional Paper 431, 128 p.
- Ilchick, R.P., 1990, *Geology and geochemistry of the Vantage gold deposits, Alligator Ridge-Bald Mountain mining district, Nevada*: *Economic Geology*, v. 85, p. 50-75.
- Jackson, M., Lane, M., Leach, B., 2002, *Geology of the West Leeville Deposit*: Nevada Bureau of Mines and Geology Bulletin 111, p.106-114.
- Joraleman, P., 1951, The occurrence of gold at the Getchell mine, Nevada, *Economic Geology*, v. 46, p. 276-310.
- Kesler, S.E., Vennemann, T.W., Vazquez, R., Stenger, D.P., Frederickson, G.C., 1996, Application of large-scale oxygen isotope haloes to exploration for chimney-manto Pb-Zn-Cu-Ag deposits: *In* Coyner, A.R., Fahley, P.L., (Eds.), *Geology and ore deposits of the American Cordillera*, 1995 Proceedings vol., p. 1383-1396.
- Kesler, S.E., Fortuna, J., Ye, Z., Alt, J.C., Core, D.P., Zohar, P., Borhauer, J., and Chryssoulis, S.L., 2003, Evaluation of the role of sulfidation in deposition of gold, Screamer section of the Betze-Post Carlin-type deposit, Nevada: *Economic Geology*, v. 98, p. 1137-1157.
- Kuehn, C.A., 1995, Carlin gold deposit, Nevada: Origin in a deep zone of mixing between normally pressured and over pressured fluids: *Economic Geology*, v. 87, p. 1697-1721.
- Kuehn, C.A., and Rose, A.R., 1992, *Geology and geochemistry of wall-rock alteration at the Carlin gold deposit, Nevada*: *Economic Geology*, v. 87, p. 1697-1721.

- Larson, P.B., Zimmerman, B.S., 1991, Variations in delta (super 18) O values, water?rock ratios, and water flux in the Rico paleothermal anomaly, Colorado: Special Publication Geochemical Society, v. 3, p. 463-469.
- Longo, A.A., Cline, J.S., and Muntean, J.L., 2009, Using pyrite to track evolving fluid pathways and chemistry in Carlin-type deposits: *in* Ressel, M.W., Diverse Gold Deposits of the Osgood Mountains and Humboldt Range, North-Central, Nevada, Special Publication no. 49, p.63-65.
- Lovering, T.G., 1972, Jasperoid in the United States – its characteristics, origin, and economic significance: U.S Geological Survey Professional Paper
- Lowell, J.D., and Guilbert, J.M., 1970, Lateral and vertical alteration-mineralization zoning in porphyry ore deposits: *Economic Geology* v. 65, p. 373-408.
- Machel, H.G., Mason, R.A., Mariano, A.N., Mucci, A., 1991, Causes and measurements of luminescence in calcite and dolomite: *In* Barker, C.E., Kopp, O.C. (eds.), *Society of Economic Paleontologists and Mineralogists*, v. 25, p. 9-25, 172-173.
- Machel, H.G., 2000, Application of Cathodoluminescence to carbonate diagenesis: *In* Pagel, M., Barbin, V., Blanc, P., Ohnenstetter, D. (eds.), *Cathodoluminescence in Geosciences*: Springer, Berlin, p. 271-301.
- Madden-McGuire, D.J., and Marsh, S.P., 1991, Lower Paleozoic host rocks in the Getchell gold belt; several distinct allochthons or a sequence of continuous sedimentation?: *Geology*, v. 19, p. 489-492.
- Madrid, R. J. J., 1987, Stratigraphy of the Roberts Mountains allochthon in north-central Nevada: unpublished PhD thesis, Stanford University, 341 p.
- Masinter, R.A., 1990, Geology, wall-rock alteration, and gold mineralization of the Gold Bar deposit, Eureka County, Nevada, unpub Stanford University MS Thesis. p.118.
- Marlowe, K., Wood, K. and Muntean, J., 2007, The Getchell mine complex: Seven decades of mining and geology: *in* Johnston, M. K. (ed.), *Faults, folds, and mineral belts: regional structural systems, gold mineralization, and exploration potential in the Great Basin*, Geological Society of Nevada Special Publication No. 46, p. 127-134.
- McLachlan, C.D., Struhsacker, E.M., and Thompson, W.F., 2000, The gold deposits of Pinson Mining Company; a review of the geology and mining history through 1999, Humboldt County, Nevada: Part II, Geology and gold deposits of the

Getchell region, Crafford: Guidebook Series Society of Economic Geologists, v. 32, p. 207-223.

Mohling, J.W., 2002, Geology and gold mineralization of the Turf Deposit: Geology and mineralization of the Maggie Creek district: Nevada Bureau of Mines and Geology Bulletin 111, p. 91-105.

Muntean, J. L., Coward, M. P., and Tarnocai, C. A., 2007, Reactivated Palaeozoic normal faults: controls on the formation of Carlin-type gold deposits in north-central Nevada: Reis, A. C., Butler, R. W. H. and Graham, R. H. (eds.) "Deformation of the Continental Crust – The Legacy of Mike Coward," Geological Society, London, Special Publications, v. 272, p. 573-589.

Muntean, J.L., Cassinerio, M.D., Arehart, G.B., Cline, J.S., and Longo, A.A., 2009, Fluid pathways at the Turquoise Ridge Carlin-type gold deposit, Getchell District, Nevada: *in* Ressel, M.W., Diverse Gold Deposits of the Osgood Mountains and Humboldt Range, North-Central, Nevada, Special Publication no. 49, p.67-69.

Nabelek, P., 1991, Stable isotope monitors: Reviews in Mineralogy, v. 26, p. 395-436.

Neuser, R.D., Bruhn, F., Gotze, J., Habermann D., Richter, D.K., 1996, Kathodolumineszenz: Methodik und Anwendung. Zentralblatt Geologie und Palaontologie Teil I: p. 287-306.

Nevada Bureau of Mines and Geology, 2009, The Nevada Mineral Industry 2008: Special Publication MI-2008, p. 175.

Ohle, E.L., 1951, The influence of permeability on ore distribution in limestone and dolomite: Economic Geology, v. 46, p. 667-706 and 871-908.

Ohmoto, H., 1986, Stable isotope geochemistry of ore deposits: Reviews in Mineralogy, v. 16, p. 491-559.

O'Neal, J.R., Silberman, M.L., Fabbri, B.P., and Chesterman, C.W., 1973, Stable isotope and chemical relations during mineralization in the Bodie mining district, Mono County, California: Economic Geology, v. 68, p. 765-784.

Osterberg, M.W., and Guilbert, J.M., 1991, Geology, wall-rock alteration, and new exploration techniques at the Chimney Creek sediment-hosted gold deposit, Humboldt County, Nevada, *in* Raines, G.L., Lisle, R.E., Schaefer, R.W., and Wilkinson, W.H., eds., Geology and Ore Deposits of the Great Basin, Symposium Proceedings: Reno, Geological Society of Nevada, p. 805-821.

- Patterson, L.M., 2009, Hydrothermal Footprint of Carlin-type Gold Deposits at the District Scale: Jerritt Canyon Mining District, Elko County, Nevada: Unpublished M.S. dissertation, University of Nevada, Reno, 240 p.
- Pinckney, D.M., Rye, R.O., 1972, Variation of O (superscript 18)/O (superscript 16), C (superscript 13)/C (superscript 12), texture and mineralogy in the Hill Mine, Cave-in-District, Illinois: *Economic Geology*, v. 67, p.1-18.
- Raiswell, R. and Canfield, D.E., 1998, Sources of iron for pyrite formation in marine sediments: *American Journal of Science*, v. 298, p. 219-245.
- Radtke, A.S., Rye, R.O., and Dickson, F.W., 1980, Geology and stable isotope studies of the Carlin gold deposit, Nevada: *Economic Geology*, v. 75, p. 641-672.
- Reich, M., Kesler, S.E., Utsunoyiya, S., Palenik, C.S., Chryssoulis, S., and Ewing, R.C., 2005, Solubility of gold in arsenian pyrite: *Geochemica et Cosmochimica Acta*, vol. 69, p.2781-2796.
- Reid, W.P., 1969, Mineral staining tests: *Colorado School of Mines Mineral Industry Bulletin*. v. 12, n. 3 20p.
- Ressel, M.W., 2000, Summary of research on igneous rocks and gold deposits of the Carlin Trend, Nevada: Ralph J. Roberts Center for Research in Economic Geology Annual Research meeting-1999, University of Nevada Reno.
- Rye, R.O., 1985, A model for the formation of carbonate-hosted disseminated gold deposits based on geologic, fluid inclusion, geochemical, and stable isotope studies of the Carlin and Cortez deposits, Nevada: *U.S. Geological Survey Bulletin* 1646, p. 35-42.
- Seedorff, E., Dilles, J.H., Proffett, J.M., Einaudi, M.T., Zurcher, L., Stavast, W.J.A., Johnson, D.A., and Barton, M.D., 2005, Porphyry deposits; characteristics and origin of hypogene features, *in* Hedenquist, J.W., Thompson, J.F.H., Goldfarb, R.J., and Richards, J.P., eds., 100th Anniversary Volume: Society of Economic Geologists, Littleton, CO, p. 251-298.
- Sha, P., 1993, Geochemistry and genesis of sediment-hosted disseminated gold mineralization at the Gold Quarry mine, Nevada: Unpublished Ph.D. dissertation, University of Alabama, 228 p.
- Simmons, S.F., White, N.C., John, D.A., 2005, Geological characteristics of epithermal precious and base metal deposits, *in* Hedenquist, J.W., Thompson, J.F.H.,

Goldfarb, R.J., and Richards, J.P., eds., 100th Anniversary Volume: Society of Economic Geologists, Littleton, CO, p. 451-484.

- Simon, G., Kesler, S.E., and Chrysoulis, S., 1999, Geochemistry and textures of gold bearing arsenian pyrite, Twin Creeks, Nevada: Implications for deposition of gold in Carlin-type deposits: *Economic Geology*, v. 94, p. 405-422.
- Stenger, D.P., Kesler, S.E., Peltonen, D.R. and Tapper, C.J., 1998, Deposition of gold in Carlin-type deposits; the role of sulfidation and decarbonation at Twin Creeks, Nevada: *Economic Geology* vol. 93, p. 201-215.
- Taylor, H.P., Jr., 1971, Oxygen isotope evidence for large-scale interaction between meteoric ground waters and Tertiary granodiorite intrusions, western Cascade Range, Oregon: *Journal of Geophysical Research*, v. 76, p. 7855-7874.
- Taylor, H.P., Jr., 1973, ¹⁸O/¹⁶O evidence for meteoric-hydrothermal alteration and ore deposition in the Tonopah, Comstock lode, and Goldfield mining districts, Nevada: *Economic Geology*, v. 68, p. 747-764.
- Taylor, H.P., Jr., 1974, The application of oxygen and hydrogen isotope relations in hydrothermal alteration and ore deposition: *Economic Geology*, v. 69, p. 843-883.
- Taylor, H.P., 1979, Oxygen and Hydrogen isotope relationships in hydrothermal mineral deposits: *In* Barnes, H.L. (Ed.), *Geochemistry of hydrothermal ore deposits*: Wiley, New York, p. 236-277.
- Taylor, B.E., O'Neil, J.R., 1977, Stable isotope studies of metasomatic Ca-Fe-Al-Si skarns and associated metamorphic and igneous rocks, Osgood Mountains, Nevada: *Contributions to Mineralogy and Petrology*, v. 63, p. 1-49.
- Thompson, A.J.B., Hauff, P.L., Robitaille, A.J., *Alteration Mapping in Exploration: Application of short-wave infrared (SWIR) spectroscopy*: SEG Newsletter, no. 39, 1999.
- Tretbar, D., Arehart, G.B., and Christensen, J.N., 2000, Dating gold deposition in a Carlin-type gold deposit using Rb/Sr methods on the mineral galkhaite: *Geology*, v. 28, p. 947-950.
- Trotman, R.B., 2009, *Geology of the Storm Gold-silver Deposit Elko County, Nevada*: Unpublished M.S. dissertation, University of Nevada, Reno, 84 p.

- Vazquez, R., Vennemann, T.W., Kesler, S.E., Russell, N., 1998, Carbon and oxygen isotope halos in the host limestone, El Mochito Zn-Pb-(Ag) skarn massive sulfide-oxide deposit, Honduras: *Economic Geology*, v. 93, p. 15-32.
- Veizer, J., Hoefs, J., 1976, The nature of $^{18}\text{O}/^{16}\text{O}$ and $^{13}\text{C}/^{12}\text{C}$ secular trends in sedimentary carbonate rocks: *Geochimica et Cosmochimica Acta*, v. 40, p. 1387-1395.
- Veizer, J., Bruckschen, P., Pawellek, F., Diener, A., Podlaha, O.G., Carden, G.A.F., Jasper, T., Korte, C., Strausse, H., Azmy, K., Ala, D., 1997, Oxygen isotope evolution of Phanerozoic seawater: *Palaeogeography, Palaeoclimatology, Palaeoecology*, v. 132, p. 159-172.
- Warne, S.S.J., 1962, A quick field or laboratory staining scheme for the differentiation of the major carbonate minerals: *Journal of Sedimentary Petrology*, v. 32, p. 29-38.
- Wells, J.D. and Mullins T.E., 1973, Gold-bearing arsenian pyrite determined by microprobe analysis, Cortez and Carlin gold mines, Nevada: *Economic Geology*, v. 68, p. 187-201.
- Ye, Z., Kesler, S.E., Essene, E.J., Zohar, P.B., and Borhauer, J.L., 2002, Relation of Carlin-type gold mineralization of lithology, structure, and alteration: Screamer zone, Betze-Post deposit, Nevada: *Mineralium Deposita*, v.38, p. 22-38.

Appendix 1: 3370 N55°E Cross-section Fact Map

